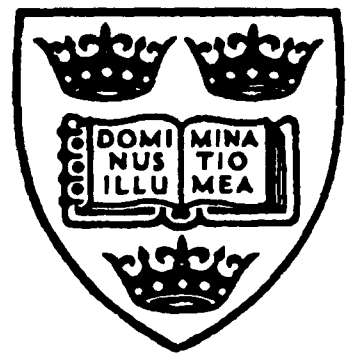
A Computational and Experimental Examination of Turbine Cooling Flows

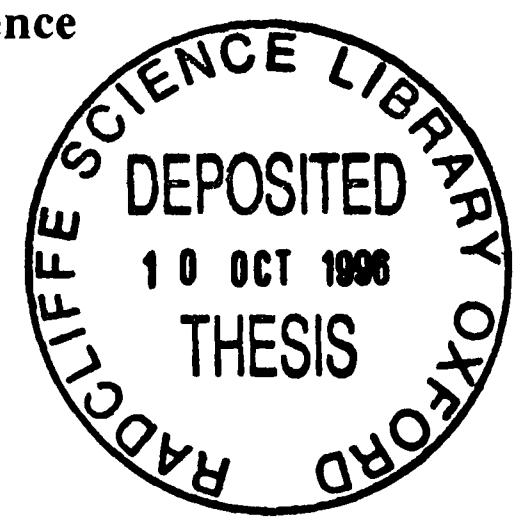
Carrie E. Allen
Queen's College

Trinity Term 1996



A Thesis Submitted in Partial Fulfillment of the Requirements for the Degree of Doctor of Philosophy at the University of Oxford

Department of Engineering Science
Parks Road
Oxford, U.K.
OX1 3PJ



A Computational and Experimental Examination of Turbine Cooling Flows

Carrie E. Allen
Queen's College

A Thesis Submitted in Partial Fulfillment of the Requirements for the Degree of Doctor of Philosophy at the University of Oxford, Trinity Term 1996.

ABSTRACT

Film cooling by means of holes is an essential cooling technique in modern gas turbine engines. This cooling technique is employed over endwalls, as well as on the surface of blades. Thus, there is a need for film cooling predictions in a three-dimensional setting. Currently only boundary layer codes are available for design purposes and they are difficult to apply to the three-dimensional case with secondary flows. Present advanced computation prediction methods are capable of solving the complete flow field in three dimensions with coolant flow. However, the spatial resolution that these methods require eliminate them as suitable options for design tools.

This study introduces a simpler description of the film cooling process which may be implemented in a code for design purposes. The parameters of turbulence enhancement, turbulence decay, and the coolant distribution at injection were optimized using existing experimental data. Finally, the code was employed in a three-dimensional setting with film cooling present.

An experimental study of the flow through cooling holes was also undertaken. Two unique geometries were later developed where a row of cooling holes exited into a vortex region where the flow was mixed before being injected from a slot. The cooling benefits of these geometries is apparent.

To Albert,

my best friend, my sanity, and my inspiration.

ACKNOWLEDGEMENTS

First and foremost, I would like to thank Professor Terry Jones for giving me the opportunity to study at Oxford. I have learned more than I thought was possible in my three years here and most of that was due to Terry. He was always enthusiastically armed with new approaches for me to try and new ways of thinking of particular problems that I had not thought of before.

I would also like to express my deepest gratitude to my co-advisor, John Chew. When I first came to Oxford all that I knew about CFD was what the initials stood for. Not only did he teach me everything from the ground up, but he always seemed willing to drop all that he was working on at a moment's notice to help me through some crisis with the code. The other members of the Theoretical Sciences Group at Rolls Royce plc, Derby were also very helpful in getting me started and allowing me to use their facilities.

Thanks are also in order for Dr. Peter Ireland. I consider him my third, unofficial advisor as he oversaw the experimental portion of this study. His enthusiasm for the work that I was doing was always apparent and infectious. I even found myself enjoying the endless wind tunnel tests in spite of it being the most frustrating part of my research.

The help of the members of the internal cooling group, specifically Dr. Zoulan Wang and David Gillespie, was invaluable. I called upon their extensive knowledge during every phase of the experimental work. Dr. Zoulan Wang and Steve Thorpe also deserve thanks for maintaining the CFD workstations and continually updating the code. It is because of them that the CFD part of my research was the least frustrating.

The fine workshop skills of Jeff Horton, Pat Timms and Leo Verling were called upon for the construction and assembly of the experimental rig. The assistance of Tony Simms and Terry Baker was also greatly appreciated in finding and assembling what always seemed to be "that last vital part" of the rig. Lorraine King was also always on hand with a quick and pleasant answer to whatever my current query happened to be.

I surely would not have made it through three years in England without the love, support, and never-ending encouragement in the form of care packages from my Mother and my grandparents. I hope that I can find a way to repay all that they have done and sacrificed for me that does not include supporting them for the rest of my life starting from the moment that I get my first job!

Last but not least, I owe a debt of gratitude that can never be repaid to my fiancé, Albert Hofeldt. I could not have asked for a better study partner, partner in crime and best friend. I persevered only because he kept reminding me that I was too stubborn to quit.

A trust fund that was set up by my late stepfather provided most of my financial support over the past several years. He deserves all the credit and the gratitude for the doors that are now open to me. Partial financial support was also provided by the Overseas Research Student (ORS) Scholarship.

Table of Contents

Title Page	1
Abstract	2
Dedication	3
Acknowledgements	4
Table of Contents	5
List of Figures	7
List of Tables	9
List of Graphs	10
Notation	13
Chapter 1. Introduction	17
1.1 Motivation for the Present Study	17
1.2 Milestones of the Present Study	17
1.3 Structure of Thesis	18
Chapter 2. CFD Basics	19
2.1 Introduction to CFD	19
2.2 CFD Literature Survey	19
2.2.1 Governing Equations	19
2.2.2 Turbulence Models	24
2.2.3 Wall Region Equations	27
2.3 Mechanics of CFD	29
Chapter 3. MEFP Basics	36
3.1 Introduction to MEFP	36
3.2 Mechanics of MEFP	36
Chapter 4. Film Cooling Overview	40
4.1 Introduction to Film Cooling	40
4.2 Hole Film Cooling Literature Survey	40
4.3 Slot Cooling Literature Survey	45
4.4 Film Cooling Modeling Literature Survey	48
4.5 Initial Film Cooling Model	58
Chapter 5. ILPT Flat Plate CFD Cases	61
5.1 Test Cases	61
5.2 Discussion of Results	69
5.2.1 Isentropic Mach Number Results	69
5.2.2 Unblown Heat Transfer Results	72
5.2.3 Film Cooled Heat Transfer Results	75
5.2.3.1 Strong Favourable Results	76

5.2.3.2 Mild Adverse Results 85
5.2.4 Effect of Coolant on Flow Field 94
5.2.5 Shear Stress Results 95
5.3 Conclusions 97
Chapter 6. Development of Film Cooling Model 99
6.1 Turbulence Augmentation 99
6.2 Mass Shed Ratio 101
6.3 Discussion of Results 102
6.4 Conclusions 120
Chapter 7. RT27A Turbine Blade CFD Cases 122
7.1. Test Cases 122
7.2 Discussion of Results 123
7.2.1 Non-Film Cooled Results 123
7.2.2 Film Cooled Results 125
7.3 Conclusions 141
Chapter 8. CHTT Turbine Blade CFD Cases 142
8.1 Test Cases 142
8.2 Discussion of Results 143
8.2.1 Non-Film Cooled Results 143
8.2.2 Film Cooled Results 144
8.3 Conclusions 165
Chapter 9. Film Cooling Experiments 166
9.1 Experimental Facility 166
9.2 Data Processing 173
9.3 Discussion of Results 175
9.3.1 Calibration Test Results 175
9.3.2 Non-Film Cooled Results 177
9.3.3 Film Cooling Hole Results 180
9.3.3.1 Comparison of Results 203
9.3.4 Slot Results 211
9.3.4.1 Vortex Slot Results 211
9.3.4.2 Trench Vortex Results 215
9.3.4.3 Comparison of Results 220
9.4 Conclusions 223
Recommendations for Further Work 225
Appendix 228
References 233

List of Figures

Figure 3.1	Sample Convergence Plot	39
Figure 4.1	Crawford Film Cooling Model	50
Figure 4.2	Schönung/Rodi Film Cooling Model	52
Figure 4.3	Coupled Film Cooling Flow	55
Figure 4.4	Complex Flow Within Film Cooling Hole	56
Figure 4.5	Complex Flow at Film Cooling Injection	57
Figure 4.6	Stripping Model	60
Figure 5.1	ILPT Test Plates	62
Figure 5.2	Strong Injection from Film Cooling Hole	66
Figure 5.3	Weak Injection from Film Cooling Hole	67
Figure 7.1	RT27A Cascade Geometry	123
Figure 8.1	CHTT Cascade Geometry	143
Figure 9.1	Experimental Test Section with Holes	167
Figure 9.2	Experimental Test Section with Slot	167
Figure 9.3	Basic Film Cooling Geometry	168
Figure 9.4	Vortex Slot Geometry	169
Figure 9.5	Trench Vortex Geometry	169
Figure 9.6	Vortex Slot Test Section Insert	170
Figure 9.7	Trench Vortex Test Section Insert	170
Figure 9.8	Test Section Schematic with Holes	172
Figure 9.9	Test Section Schematic with Slot	172
Figure 9.10	Raw Hue vs. Temperature Data	176
Figure 9.11	Smoothed Calibration Curve	176
Figure 9.12	Raw Temperature Signal with Curve Fit	178
Figure 9.13	Theoretical Nu_x vs. Re_x	180
Figure 9.14	G=0.2 at t=1.39 sec.	182
Figure 9.15	G=0.2 at t=58.03 sec.	182
Figure 9.16	G=0.4 at t=1.53 sec.	186
Figure 9.17	G=0.4 at t=5.65 sec.	186
Figure 9.18	G=0.4 at t=11.77 sec.	187
Figure 9.19	G=0.4 at t=28.85 sec.	187
Figure 9.20	G=0.4 at t=51.13 sec.	188
Figure 9.21	G=0.6 at t=3.96 sec.	192
Figure 9.22	G=0.6 at t=6.36 sec.	193
Figure 9.23	G=0.6 at t=11.96 sec.	193
Figure 9.24	G=0.8 at t=2.58 sec.	196

Figure 9.25	G=0.8 at t=3.30 sec.	196
Figure 9.26	G=0.8 at t=6.34 sec.	197
Figure 9.27	Coolant Separation	197
Figure 9.28	G=1.0 at t=2.29 sec.	200
Figure 9.29	G=1.0 at t=2.81 sec.	200
Figure 9.30	G=1.0 at t=4.01 sec.	201
Figure 9.31	η vs. Z/D	204
Figure 9.32	h/h_o vs. Z/D	205
Figure 9.33	Effectiveness Data at G=0.6	206
Figure 9.34	Heat Transfer Data at G-0.6	207
Figure 9.35	Heat Transfer Data at G=1.2	207
Figure 9.36	Comparative Hole Cooling Data	210
Figure 9.37	Video Capture of Vortex Slot Run	213
Figure 9.38	Video Capture of Trench Vortex Run (t=15.69 sec.)	217
Figure 9.39	Video Capture of Trench Vortex Run (t=33.73 sec.)	218

List of Tables

Table 1.1	Structure of Thesis	18
Table 5.1	Temperature Boundary Conditions	65
Table 5.2	ILPT Test Matrix (Weak Injection)	68
Table 5.3	ILPT Test Matrix (Strong Injection)	69
Table 5.4	Variation of n With Pressure Gradient	97
Table 6.1	S.F.P.G. Optimization Values	112
Table 6.2	M.A.P.G. Optimization Values	118
Table 6.3	Z.P.G. Optimization Values	120
Table 7.1	RT27A Film Cooling Parameters	126
Table 7.2	RT27A Test Matrix	127
Table 7.3	RT27A Optimization Values	140
Table 8.1	Temperature Boundary Conditions	145
Table 8.2	CHTT Film Cooling Parameters	146
Table 8.3	CHTT Optimization Values	149
Table 8.4	Discharge Coefficient Values	154
Table 8.5	Film Cooled CHTT Test Matrix	158
Table 9.1	Experimental Test Matrix (Holes)	181
Table 9.2	Comparative Hole Effectiveness Data	208
Table 9.3	Comparative Hole Heat Transfer Data	209
Table 9.4	Experimental Test Matrix (Vortex Slot)	212
Table 9.5	Experimental Test Matrix (Trench Vortex)	216
Table 9.6	Comparative Slot Effectiveness Data	221
Table 9.7	Comparative Slot Heat Transfer Data	221

List of Graphs

Graph 5.1	M.F.P.G. Isentropic Mach Number	70
Graph 5.2	S.F.P.G. Isentropic Mach Number	71
Graph 5.3	M.A.P.G. Isentropic Mach Number	72
Graph 5.4	M.F.P.G. Heat Transfer	73
Graph 5.5	S.F.P.G._data1 Heat Transfer	74
Graph 5.6	M.A.P.G._data1 Heat Transfer	75
Graph 5.7	S.F.P.G._data2 Heat Transfer	77
Graph 5.8	S.F.P.G._data3 Heat Transfer	78
Graph 5.9	S.F.P.G._data4 Heat Transfer	79
Graph 5.10	S.F.P.G._data8 Heat Transfer	80
Graph 5.11	S.F.P.G._data10 Heat Transfer	81
Graph 5.12	S.F.P.G._data5 Heat Transfer	82
Graph 5.13	S.F.P.G._data6 Heat Transfer	83
Graph 5.14	S.F.P.G._data11 Heat Transfer	84
Graph 5.15	S.F.P.G._data13 Heat Transfer	85
Graph 5.16	M.A.P.G._data2 Heat Transfer	86
Graph 5.17	M.A.P.G._data3 Heat Transfer	87
Graph 5.18	M.A.P.G._data8 Heat Transfer	88
Graph 5.19	M.A.P.G._data10 Heat Transfer	89
Graph 5.20	M.A.P.G._data4 Heat Transfer	90
Graph 5.21	M.A.P.G._data5 Heat Transfer	91
Graph 5.22	M.A.P.G._data11 Heat Transfer	92
Graph 5.23	M.A.P.G._data12 Heat Transfer	93
Graph 5.24	M.A.P.G._data13 Heat Transfer	94
Graph 5.25	S.F.P.G. Mach Number Comparison	95
Graph 5.26	S.F.P.G. y^+/y Comparison	96
Graph 6.1	A vs. X/D (S.F.P.G., G=0.15)	103
Graph 6.2	B vs. X/D (S.F.P.G., G=0.15)	104
Graph 6.3	A vs. X/D (S.F.P.G., G=0.25)	105
Graph 6.4	B vs. X/D (S.F.P.G., G=0.25)	105
Graph 6.5	A vs. X/D (S.F.P.G., G=0.35)	106
Graph 6.6	B vs. X/D (S.F.P.G., G=0.35)	107
Graph 6.7	A vs. X/D (S.F.P.G., G=0.59)	108
Graph 6.8	B vs. X/D (S.F.P.G., G=0.59)	108
Graph 6.9	A vs. X/D (S.F.P.G., G=0.75)	109
Graph 6.10	B vs. X/D (S.F.P.G., G=0.75)	110

Graph 6.11	A vs. X/D (S.F.P.G., G=1.20)	111
Graph 6.12	B vs. X/D (S.F.P.G., G=1.20)	111
Graph 6.13	A vs. X/D (M.A.P.G., G=0.15)	113
Graph 6.14	B vs. X/D (M.A.P.G., G=0.15)	114
Graph 6.15	A vs. X/D (M.A.P.G., G=0.25)	115
Graph 6.16	B vs. X/D (M.A.P.G., G=0.25)	115
Graph 6.17	A vs. X/D (M.A.P.G., G=0.35)	116
Graph 6.18	B vs. X/D (M.A.P.G., G=0.35)	117
Graph 6.19	Mass Shed Ratio vs. Injection Rate	119
Graph 7.1	Mach Number Correlation	124
Graph 7.2	Heat Transfer Coefficient Correlation	125
Graph 7.3	Original Build B h/h_o (G=0.92)	129
Graph 7.4	Optimized Build B h/h_o (G=0.92)	129
Graph 7.5	Original Build G h/h_o (G=1.07)	130
Graph 7.6	Optimized Build G h/h_o (G=1.07)	131
Graph 7.7	Original Build G h/h_o (G=1.44)	132
Graph 7.8	Optimized Build G h/h_o (G=1.44)	132
Graph 7.9	Original Build H h/h_o (G=0.71)	133
Graph 7.10	Optimized Build H h/h_o (G=0.71)	134
Graph 7.11	Original Build H h/h_o (G=1.07)	135
Graph 7.12	Optimized Build H h/h_o (G=1.07)	135
Graph 7.13	Original Build C h/h_o (G=0.36)	137
Graph 7.14	Optimized Build C h/h_o (G=0.36)	137
Graph 7.15	Original Build D h/h_o (G=0.36)	138
Graph 7.16	Optimized Build D h/h_o (G=0.36)	139
Graph 8.1	Film Cooled Heat Transfer Comparison	150
Graph 8.2	Heat Transfer Coefficient Comparison	152
Graph 8.3	Adiabatic Effectiveness Comparison	153
Graph 8.4	Updated Heat Transfer Comparison	155
Graph 8.5	Updated Adiabatic Effectiveness Comparison	156
Graph 8.6	MEFP Heat Transfer Comparison	157
Graph 8.7	Effect of Showerhead Region on Heat Transfer	160
Graph 8.8	Test Case #4 Heat Transfer Coefficient	161
Graph 8.9	Test Case #5 Heat Transfer Coefficient	162
Graph 8.10	Test Case #6 Heat Transfer Coefficient	163
Graph 8.11	Test Case #7 Heat Transfer Coefficient	164
Graph 9.1	Nusselt Number vs. Reynolds Number	179
Graph 9.2	η vs. X/D (G=0.2)	184

Graph 9.3	h/h_o vs. X/D (G=0.2)	185
Graph 9.4	η vs. X/D (G=0.4)	190
Graph 9.5	h/h_o vs. X/D (G=0.4)	191
Graph 9.6	η vs. X/D (G=0.6)	194
Graph 9.7	h/h_o vs. X/D (G=0.6)	195
Graph 9.8	η vs. X/D (G=0.8)	198
Graph 9.9	h/h_o vs. X/D (G=0.8)	199
Graph 9.10	η vs. X/D (G=1.0)	202
Graph 9.11	h/h_o vs. X/D (G=1.0)	203
Graph 9.12	Average Hole Cooling Data	211
Graph 9.13	Average η vs. X/D (Vortex Slot)	214
Graph 9.14	Average h/h_o vs. X/D (Vortex Slot)	215
Graph 9.15	Average η vs. X/D (Trench Vortex)	219
Graph 9.16	Average h/h_o vs. X/D (Trench Vortex)	220
Graph 9.17	Comparison of Cooling Schemes	222

NOTATION

a	velocity of sound
A^+	damping constant
A	area
A	represents ratio of film cooled to non-film cooled heat transfer produced by mixing of freestream and coolant
B	represents cooling effect of injection generated by temperature difference between freestream and coolant
CFD	computational fluid dynamics
CHTT	cold heat transfer tunnel
C_{ax}	axial chord
C_D	discharge coefficient
C_f	coefficient of friction
C_p	specific heat at constant pressure
C_v	specific heat at constant volume
D	diameter (of film cooling hole)
dr	diameter to pitch ratio
E	total energy per unit volume
f	coefficient of friction
g	acceleration due to gravity
G	injection rate
h	heat transfer coefficient
H	total enthalpy
ILPT	isentropic light piston tunnel

k	coefficient of thermal conductivity
k	turbulent kinetic energy
K	mass shed ratio
ℓ	mixing length
L	length
L	slot width
$\dot{m}$	mass flow
M	Mach number
M.A.P.G.	mild adverse pressure gradient
MEFP	Moore elliptic flow program
M.F.P.G.	mild favourable pressure gradient
MSR	mass shed ratio
Nu	Nusselt number
Nu/m	Nusselt number per unit length
P	static pressure
PD	penetration distance
PDE	partial differential equation
Pr	Prandtl number
q	heat flux
$\dot{q}$	heat transfer rate
r	radius
r	recovery factor
R	gas constant

Re	Reynolds number
RMS	root mean square
s	slot height
S	surface length
S.F.P.G.	strong favourable pressure gradient
t	time
T	temperature
TR	temperature ratio
u	velocity of flow (-x direction)
v	velocity of flow (-y direction), velocity
x	distance, streamwise distance
y	distance from wall
y^+	non-dimensional distance

GREEK SYMBOLS

α	angle of coolant jet with respect to surface
β	angle of coolant jet with respect to direction of freestream
γ	ratio of specific heats
δ	boundary layer thickness
ε	rate of dissipation of turbulent energy
η	effectiveness
κ	von Kármán constant
μ	coefficient of dynamic viscosity
ν	kinematic viscosity

ρ	density
τ	shear stress
Φ	velocity potential
Ψ	non-dimensional downstream distance
ω	vorticity

SUBSCRIPTS

aw	adiabatic wall
c	coolant
e	at edge of boundary layer
g	gas
i	injection
i	surface initial
i	inner
j	coolant jet
o	outer
r	recovery
t	total (as in total temperature, pressure, etc.)
T	turbulent
w	wall
x	in the -x direction
y	in the -y direction
∞	freestream

CHAPTER 1. INTRODUCTION

1.1 MOTIVATION FOR THE PRESENT STUDY

The aim of this study is to develop a model for coolant injection from holes to be implemented in a three-dimensional design code. The research presented here is meant to provide a thorough examination of the initial testing and improvement of this model when compared to corresponding experimental data. In an effort to measure the success of this computational model, its application in a three-dimensional setting is necessary. In addition, useful experimental data were sought for several different representative cooling geometries. It is hoped that the base of knowledge in the above areas can be increased, due to the fact that there is a need for successful computational examinations of practical turbine flows.

1.2 MILESTONES OF THE PRESENT STUDY

This work serves as a source of research that is being performed for the first time in its present context. Previous to this study, the film cooling routine that is implemented in the CFD code was virtually untested. Through the course of the work presented here, there has been a rigorous testing of this film cooling routine. Furthermore, improvements were later made to this routine based on an exhaustive survey of suggested improvement methods throughout the relevant literature. In short, due to this study the overall usefulness of the code has been improved.

Other ground breaking research has also been a part of this study. For instance, the results of the first fully three-dimensional film cooled turbine test case run with Rolls Royce's CFD code is presented here. Revolutionary experimental work includes the testing of two completely unique slot-hole hybrid cooling configurations.

1.3 STRUCTURE OF THESIS

Table 1.1 describes how the remainder of the thesis is structured with a short description of what is discussed in each chapter. While it is only loosely based on chronological order, it is certainly the most logical order for the presentation of the work in this study.

CHAPTER	CONTENTS
2	Basic introduction to CFD and discussion of different approaches to modeling of general fluid flow.
3	Description of main features of MEFP code used in present study.
4	Review of all literature pertaining to film cooling by means of holes and slots, including modeling of the film cooling process and discussion of MEFP film cooling model before improvement.
5	Complete presentation and discussion of all ILPT CFD work including results before and after improvement to film cooling model.
6	Description of techniques used to improve MEFP film cooling model and presentation of results of that improvement.
7	Complete presentation and discussion of all RT27A turbine blade CFD work.
8	Complete presentation and discussion of all CHTT turbine blade CFD work.
9	Complete presentation and discussion of all experimental hole and slot cooling work.

Table 1.1 Structure of Thesis

CHAPTER 2. CFD BASICS

2.1 INTRODUCTION TO CFD

CFD stands for Computational Fluid Dynamics. Making use of a CFD algorithm simply entails using a computer code to solve problems concerning fluid flow. It is a useful numerical technique because it is adaptable to a number of different problems, all with varying conditions. At the present time, the most widespread use of CFD is in the correlation of both theoretical and experimental results. It is conceivable that one day it may be used as the sole design tool in certain applications. Using CFD, a number of design options could be tested at reduced costs over even shorter time periods, and then implemented to even more stringent requirements. In fact, as the processing time of computing devices decreases, the storage capacity or memory of these devices increases, and the computer codes themselves improve, it is inevitable that CFD is destined to play an ever increasing role in engineering research and design.

2.2 CFD LITERATURE SURVEY

2.2.1 GOVERNING EQUATIONS

The theoretical development of CFD focuses on the derivation and solution of the governing equations of fluid flow. It is for this reason that many CFD codes are known as "Navier-Stokes solvers" after the Navier-Stokes equations that fully define fluid dynamics. There are, of course, other sets of equations that are commonly used to define fluid flow, but none are as thorough as the Navier-Stokes equations. Several sets of these equations, such as the aforementioned Navier-Stokes equations, are very complex and for a solution to be attempted they must be simplified and/or approximated. In fact, virtually all of the CFD codes that are in use today simplify and/or approximate the governing equations to some degree.

Goldsmith and Seddon **(ref.34)** have compiled one of the most comprehensive descriptions of the development of various models for use in CFD codes. Probably the oldest model to date is the potential flow model. This method, as is common with all methods, has both its advantages and its disadvantages. For instance, one advantage is that it is very simple. The governing equations for potential flow are one of the first things that are taught in any introductory aerodynamics lecture. However, the flow problems that can be solved using this model are very limited. The flow must be steady in time, inviscid, irrotational and isentropic. Another consequence of this model is that the potential flow solutions are only valid at high Reynolds numbers, and when the flow is perfectly attached. Not a single flow in nature follows all of these conventions. Eqn.2.1 shows the governing equation for compressible potential flow. For incompressible flow, Eqn.2.1 simply reduces to Laplace's Equation (Eqn.2.2).

$$\left(1-\frac{\Phi_x^2}{a^2}\right)\Phi_{xx}+\left(1-\frac{\Phi_y^2}{a^2}\right)\Phi_{yy}-2\frac{\Phi_x\Phi_y}{a^2}=0 \qquad \textbf{(2.1)}$$

$$\Phi_{xx}+\Phi_{yy}=0 \qquad \textbf{(2.2)}$$

The next model to be addressed uses the equations devised by Euler in 1755 as the governing equations for fluid flow. Like the potential flow equations, the Euler equations can only be used to analyze inviscid flow. However, the flow can be unsteady, rotational and non-isentropic. While the Euler model is more flexible and models a true flow more closely than the potential flow model, information regarding the boundary layer behavior is still unattainable. Euler analyses are most useful when called upon to look at the pressure distribution in a particular flow problem where information regarding the viscous effects of the flow is either not necessary, or is of secondary concern. It can be noted that the Euler equations are merely the Navier-Stokes equations with the viscous and heat conduction terms eliminated (Eqns.2.3-2.7).

$$\frac{\partial}{\partial x}(\rho u) + \frac{\partial}{\partial y}(\rho v) = 0 \tag{2.3}$$

$$\frac{\partial}{\partial x}(\rho u^2) + \frac{\partial}{\partial y}(\rho uv) = -\frac{\partial p}{\partial x} \tag{2.4}$$

$$\frac{\partial}{\partial x}(\rho uv) + \frac{\partial}{\partial y}(\rho v^2) = -\frac{\partial p}{\partial y} \tag{2.5}$$

$$\frac{\partial}{\partial x}(uE) + \frac{\partial}{\partial y}(vE) = -\frac{\partial}{\partial x}(up) - \frac{\partial}{\partial y}(vp) \tag{2.6}$$

$$E = \rho c_v T + \frac{1}{2}\rho\left(u^2 + v^2\right) \tag{2.7}$$

Prandtl developed the first method to deal with viscous or boundary layer effects in 1904, and the equations that he derived are appropriately called the boundary layer equations. Boundary layer analyses are most useful and accurate when used to analyze high Reynolds number flows where the overall pressure field of the flow is unaffected by the presence of the wall boundary layers. These equations are also ideal for analyzing flows that include jets, wakes, mixing layers, or flow in pipes and other internal passages. The common factor in all of these examples is that the primary flow direction can be easily identified. In this particular model, the flow must also be attached in the region directly next to the wall, or the streamwise velocity of the flow must be positive. The reason for this is because the diffusion terms from the Navier-Stokes equations have been neglected. In spite of this restriction, they remain the simplest way to incorporate viscous effects into flow analysis (Eqns.2.8-2.11).

$$\frac{\partial}{\partial x}(\rho u)+\frac{\partial}{\partial y}(\rho v)=0 \tag{2.8}$$

$$\frac{\partial}{\partial x}(\rho u^2)+\frac{\partial}{\partial y}(\rho uv)=-\frac{d}{dx}P_e+\frac{1}{Re}\frac{\partial}{\partial y}\left(\mu\frac{\partial u}{\partial y}\right) \tag{2.9}$$

$$\frac{\partial}{\partial x}(\rho uH)+\frac{\partial}{\partial y}(\rho vH)=-\frac{1}{RePr}\frac{\partial}{\partial y}\left(k\frac{\partial T}{\partial y}\right)+\frac{1}{Re}\frac{\partial}{\partial y}\left(\mu u\frac{\partial u}{\partial y}\right) \tag{2.10}$$

$$H=c_pT+\frac{1}{2}(u^2+v^2) \tag{2.11}$$

The most comprehensive equations for use in the analysis of fluid flow are the Navier-Stokes equations. They are simply the equations for the conservation of mass, momentum and energy respectively (Eqns.2.12-2.20). The energy equation (Eqn.2.15) must be included whenever a solution is required to a problem involving heat transfer. Within this large category of fluid flow models, however, there are even more direct simplifications of the Navier-Stokes equations. Some of these consist of the parabolized or the reduced Navier-Stokes equations, and the time-averaged or the Reynolds-averaged Navier-Stokes equations. These simplified sets of equations are faster and easier to solve than the full set of equations, while still giving quite an accurate picture of the flow. In the case of the parabolized Navier-Stokes equations, only the derivatives in the viscous and heat conduction terms are neglected. Once again, the criterion for these reduced models is that the flow must remain attached and exhibit no large regions of separation.

$$\frac{\partial \rho}{\partial t}+\frac{\partial}{\partial x}(\rho u)+\frac{\partial}{\partial y}(\rho v)=0 \tag{2.12}$$

$$\frac{\partial}{\partial t}(\rho u)+\frac{\partial}{\partial x}(\rho u^2)+\frac{\partial}{\partial y}(\rho uv)=-\frac{\partial p}{\partial x}+\frac{1}{Re}\left(\frac{\partial}{\partial x}\tau_{xx}+\frac{\partial}{\partial y}\tau_{xy}\right) \tag{2.13}$$

$$\frac{\partial}{\partial t}(\rho v)+\frac{\partial}{\partial x}(\rho uv)+\frac{\partial}{\partial y}(\rho v^2)=-\frac{\partial p}{\partial y}+\frac{1}{Re}\left(\frac{\partial}{\partial x}\tau_{xy}+\frac{\partial}{\partial y}\tau_{yy}\right) \tag{2.14}$$

$$\frac{\partial E}{\partial t}+\frac{\partial}{\partial x}(uE)+\frac{\partial}{\partial y}(vE)=-\frac{\partial}{\partial x}(up)-\frac{\partial}{\partial y}(vp)-\frac{1}{RePr}\left(\frac{\partial}{\partial x}q_x+\frac{\partial}{\partial y}q_y\right)$$

$$+\frac{1}{Re}\left(\frac{\partial}{\partial x}(u\tau_{xx}+v\tau_{xy})+\frac{\partial}{\partial y}(u\tau_{xy}+v\tau_{yy})\right) \tag{2.15}$$

$$\tau_{xx}=2\mu\frac{\partial u}{\partial x}-\frac{2\mu}{3}\left(\frac{\partial u}{\partial x}+\frac{\partial v}{\partial y}\right) \tag{2.16}$$

$$\tau_{yy}=2\mu\frac{\partial v}{\partial y}-\frac{2\mu}{3}\left(\frac{\partial u}{\partial x}+\frac{\partial v}{\partial y}\right) \tag{2.17}$$

$$\tau_{xy}=\mu\left(\frac{\partial u}{\partial y}+\frac{\partial v}{\partial x}\right) \tag{2.18}$$

$$q_x=-k\frac{\partial T}{\partial x} \tag{2.19}$$

$$q_y=-k\frac{\partial T}{\partial y} \tag{2.20}$$

In each of the sets of equations presented up to this point it can be seen that the number of unknowns exceeds the number of equations by one. Therefore, an additional

equation that does not add any more unknown parameters is needed to "close" the system of equations. This equation is the state equation. In most cases a perfect gas is assumed, so the equation that is needed to relate temperature, pressure and density takes the form of Eqn.2.21.

$$P = \rho RT \tag{2.21}$$

All of the previous methods increase in complexity (in the order that they were presented). As the complexity of these equations increase, the computing time required to solve the equations for the given flow conditions (at each grid point) also increases. For each individual application the advantages and disadvantages of each model must be weighed along with the issues of cost, efficiency, practicality, and the order of accuracy that is required of the solution.

2.2.2 Turbulence Models

Virtually every CFD code must also include another equation or set of equations: the turbulence model. There are three different types of turbulence models. They consist of the eddy viscosity models, the Reynolds stress models, and the "large eddy simulation" models. The most common option at the present time is to use an eddy viscosity model. Eddy viscosity models explain the effect of turbulence by simply assuming that it increases the viscosity and conductivity of the flow. These models all follow the Boussinesq convention (which he first suggested in 1877) **(ref.4)** which states that the turbulent shear stress is related to the mean rate of strain by an "eddy" or turbulent viscosity. Eqn.2.22 illustrates the relationship between the eddy shear stress, the turbulent viscosity, and the mean rate of strain. This eddy viscosity is proportional to a length scale multiplied by a velocity scale, thereby giving rise to a number of different eddy viscosity models. Eqn.2.23 shows the common turbulent viscosity equation for all eddy viscosity models where ν_T is the characteristic velocity scale of the turbulence and ℓ is the characteristic length scale of the turbulence. The subsequent

models are commonly classified according to the number of additional partial differential equations that must be solved in order to generate the modeling parameters.

$$-\rho\overline{u'v'} = \mu_T \frac{\partial \bar{u}}{\partial y} \tag{2.22}$$

$$\mu_T = \rho \nu_T \ell \tag{2.23}$$

One of the most common eddy viscosity models is the zero-equation Prandtl mixing length model (which he devised in the 1920's) **(ref.4)**. In the mixing length model, the length scale is proportional to some fraction of the local shear stress thickness, and can be thought of as the transverse distance (normal to the wall) over which a fluid particle is able to maintain its original momentum or vorticity. This model is useful because it is both the oldest and the simplest, but it is limited in that it encounters difficulties when attempting to switch from one kind of turbulent flow to another. This means that it has difficulty in accounting for varying turbulent length scales that can be found in different regions of the flow. It also encounters difficulty when faced with adverse pressure gradients. The turbulent viscosity for the mixing length model can be determined by solving Eqn.2.24 where $\bar{u}$ is the mean component of the instantaneous velocity. In this case, ℓ is the characteristic length of the turbulence, and $\ell\left|\frac{\partial \bar{u}}{\partial y}\right|$ is the characteristic velocity of the turbulence.

$$\mu_T = \rho \ell^2 \left|\frac{\partial \bar{u}}{\partial y}\right| \tag{2.24}$$

Prandtl and Kolmogorov first devised a one-equation turbulence model in the 1940's **(ref.4)**. Their motivation for devising this model was to find a way to deal with the case of fluid flow through pipes. The mixing length model is unable to deal with this case because at the centerline of a pipe there is effectively no velocity gradient.

Therefore, $\left|\frac{\partial \bar{u}}{\partial y}\right| = 0$, and the value of the turbulent viscosity would be zero. It is known that this is not true under practical circumstances, such as at the centerline of a pipe where the eddy viscosity can have a significant effect. They determined that the characteristic velocity scale of the turbulence should be proportional to the turbulent kinetic energy, k as defined in Eqn.2.25 for two-dimensional flow. The values of u′ and v′ are the fluctuating components of the instantaneous velocity. The turbulent viscosity is then determined by solving Eqn.2.26. In this equation, c_μ is a constant that is defined in conjunction with the length scale and usually takes on the value of 0.09.

$$k = \frac{1}{2}\left(\overline{u'}^2 + \overline{v'}^2\right) \qquad \textbf{(2.25)}$$

$$\mu_T = c_\mu \rho \ell \sqrt{k} \qquad \textbf{(2.26)}$$

A common two-equation model is the k-ε turbulence model first proposed by Harlow and Nakayama in 1968. It was later developed by Jones and Launder in 1972, and again in 1974 by Launder and Spalding (**ref.4**). The two-equation models are defined by the transport equations for the local length and velocity scales. Therefore the turbulence scales are dependent on the upstream "history" of the flow, as well as the local flow conditions. They do not encounter any of the difficulties of the previous, simpler models, like the ability to correctly predict flow parameters in the presence of adverse pressure gradients. However, as was noted previously with all advanced or more complex methods, there is a penalty of increased computer processing time. In this case, k is once again defined as the turbulent kinetic energy, and ε is defined as the rate of dissipation of turbulent energy. The turbulent viscosity for this model is determined by solving Eqn.2.27. Once again, c_μ is a constant and has a value of 0.09.

$$\mu_T = \rho c_\mu \frac{k^2}{\varepsilon} \qquad \textbf{(2.27)}$$

Each of the above models can be altered to include the effects of different flow conditions. For instance, additional terms or boundary conditions are needed if a particular flow problem is to include the effects of surface roughness, pressure gradients, and wall curvature, or if one wants to examine the effects of different levels of freestream turbulence. All of these flow conditions are found in a real turbine environment, therefore, it is imperative that a turbulence model is able to include the effects that each of these conditions produce.

There has been a generous amount of time and money devoted to the improvement of the current turbulence models. It is widely accepted that the turbulence model is one of the weakest parts of any CFD code due to the fact that turbulent flow is so complex. It is known that most of the models can predict two-dimensional flow with reasonable accuracy, but then become questionable when considering a three-dimensional flow problem. This is because existing turbulence models define turbulence that is constant in every direction (isotropic turbulence), or an eddy viscosity that is the same for all Reynolds stresses (isotropic eddy viscosity). In reality, turbulence is anisotropic. The current models are more capable of giving accurate predictions of flow phenomenon in the case of flows that are "well behaved", where the turbulence structure changes slowly over time and distance. They do not work as well when presented with rapid changes in the turbulence structure, such as regions of separation then re-attachment, or large gradients.

2.2.3 Wall Region Equations

Each of the above turbulence models only apply outside of the "wall region" of the boundary layer. The "wall region" occupies approximately twenty percent of the boundary layer thickness and includes the viscous sublayer which is next to the wall, as well as what is referred to as the log-law region. This region is thin and is characterized by the velocity distribution being independent of the external pressure distribution. If a particular computation is to include this region, then two options are currently available in order to determine the relevant parameters. The first option would be to use a low

Reynolds number turbulence model. Low Reynolds number turbulence models are essentially identical to the turbulence models addressed previously in this discussion, except for the fact that there are extra terms that are added to the equations to account for the mixing length varying throughout the boundary layer, especially close to the wall.

The second option is to use what is commonly referred to as a "law-of-the-wall" treatment that divides the boundary layer into two main regions: the inner wall region, and the outer wake-like region. It was first assumed that in the inner wall region, the mixing length scales according to the distance from the wall. Closest to the wall, the mixing length can be evaluated from Eqn.2.28 where κ is the von Kármán constant (which usually takes the value of 0.41) and y is the distance from the wall. At a point that is approximately twenty percent of the boundary layer thickness (at the boundary of the wall and the wake-like regions), the mixing length can then be evaluated from Eqn.2.29 where λ is a constant which usually takes on a value between 0.085 and 0.089 (depending on the literature) and δ is the boundary layer thickness. In the viscous sublayer, right next to the wall, the mixing length approaches zero.

$$\ell = \kappa y \tag{2.28}$$

$$\ell = \lambda \delta \tag{2.29}$$

In 1956, van Driest altered this approach to include a solution for the mixing length in the viscous sublayer (**ref.97**). He determined that Eqn.2.28 should be replaced with a different relation and that the mixing length in the inner wall region should be computed using Eqn.2.30 where A^+ is a damping constant which usually takes on a value of 26. The quantity in the brackets is commonly known as the van Driest damping function which accounts for the increased damping of the turbulence as

the wall gets closer. The mixing length in the outer wake-like region is still computed using Eqn.2.29. The switch from the inner equation to the outer equation occurs when the value generated by Eqn.2.30 exceeds that generated by Eqn.2.29.

$$\ell = \kappa y\left(1 - e^{-y^+/A^+}\right) \tag{2.30}$$

2.3 MECHANICS OF CFD

All of the equations given up to this point have been partial differential equations. Computers are unable to solve partial differential equations directly, so in order for a solution to be attempted they must be converted into a system of algebraic equations. This conversion process is called discretisation. The algebraic equations must then be coupled with the initial and boundary conditions for a given problem in order for a solution to be found. Discretisation also introduces a slight error, called truncation error, into the computation that is generally unavoidable when converting partial differential equations into their algebraic counterparts. Attempts should be made to make this error as small as possible, so that the final solution is as accurate as possible.

Discretisation can be carried out by means of several methods, such as the finite element method, the finite difference method, and the finite volume method. The method that is chosen depends on the problem being addressed and whether or not the equations being discretised include only time derivatives or spatial derivatives. For instance, equations involving only time derivatives are discretised almost exclusively by the finite difference method, whereas each of the methods has been used in the case of equations involving only spatial derivatives. For each of these methods, the computational domain is divided into a grid with a number of discrete points or nodes. Upon solution, all of these grid points or nodes adopt a value for each of the dependent variables.

The finite difference method uses a simple Taylor series expansion. Each derivative is rewritten to represent the difference in the value of the variable at different points in time or space. Eqn.2.32 shows a sample finite difference discretisation of a partial differential equation (Eqn.2.31) governing a variation in temperature T as a function of x (distance) and t (time). If it is assumed that $x=j\Delta x$ and $t=n\Delta t$ and if x_j is known at all points at time n, then Eqn.2.33 can be incremented by n and marched forward in time to determine the complete solution for all time and space.

$$\frac{\partial T}{\partial t}+u\frac{\partial T}{\partial x}-\alpha\frac{\partial^2 T}{\partial x^2}=0 \qquad \textbf{(2.31)}$$

$$\frac{T_j^{n+1}-T_j^n}{\Delta t}+\frac{u\left(T_{j+1}^n-T_{j-1}^n\right)}{2\Delta x}=\frac{\alpha\left(T_{j-1}^n-2T_j^n+T_{j+1}^n\right)}{\Delta x^2} \qquad \textbf{(2.32)}$$

$$T_j^{n+1}=T_j^n-\left(\frac{u\Delta t}{2\Delta x}\right)\left(T_{j+1}^n-T_{j-1}^n\right)+\left(\frac{\alpha\Delta t}{\Delta x^2}\right)\left(T_{j-1}^n-2T_j^n+T_{j+1}^n\right) \qquad \textbf{(2.33)}$$

In Eqn.2.32, there is a noticeable difference between the first order partial time derivative and the first order partial space derivative in their finite difference discretised forms. This discrepancy is due to the fact that there are different ways to carry out the differencing operation. There are forward, backward and central differences possible. The first order partial time derivative exhibits the forward difference option, and the first order partial space derivative exhibits the central difference option. Convenience and the desired level of accuracy dictate which option is used.

When using the finite difference method, truncation error arises when the higher order terms of the Taylor series expansion are neglected in the discretisation process. The cancellation of these terms is reasonable as it is impractical to include the large number of terms in a Taylor series expansion in every operation, especially when most

of these terms are very small. Each of the difference options mentioned in the previous paragraph has a level of accuracy associated with them according to which higher order terms are neglected in the final stages of the discretisation process. For instance, forward and backward differences are first-order accurate. This simply means that only the first order terms in the Taylor series expansion are retained. Central differences are second-order accurate which means that only the first and second order terms in the Taylor series expansion are retained.

The finite element method is more complicated and had its origins in structural mechanics. It is a technique that was once used almost exclusively to predict the values of stress and strain in solid structures. With this method, the entire computational domain is divided into a finite number of discrete elements or sub-domains. Each sub-domain is treated independently of the others and a simple variation of the dependent variable(s) is assumed over each. A variational technique is used to create discrete partial differential equations for each element. These equations must then be converted into their respective algebraic equations and the most common way of doing this is to use the Galerkin method. A series of equations will then exist for each sub-domain that describe the values of the variable(s) at the nodes or corner points. When all of these equations are finally brought together and solved simultaneously, it provides a complete description of how each flow parameter varies over the entire domain.

The finite volume method can be thought of a combination of the previous two methods. With this method, the computational domain is divided into a finite number of control volumes surrounding each grid point or node, as in the finite element method. It is generally most convenient to position the boundaries of the control volumes halfway between adjacent grid points. This ensures that the grid point is at the geometric center of each control volume if the grid spacing is constant. The value of a specific parameter at each grid point is then related to the values at opposing grid faces, and the value at each grid face is then related to the values at neighbouring grid points by means of a differencing technique, as in the finite difference method. Finally, the solutions to the

equations that are generated for each control volume can be brought together to give a complete flow description.

Partial differential equations can be classified into one of three categories. They may be elliptic, hyperbolic, or parabolic. If Eqn.2.34 is used to represent a typical partial differential equation, then Eqn.2.35 denotes an elliptic PDE, Eqn.2.36 denotes a hyperbolic PDE, and Eqn.2.37 denotes a parabolic PDE. Partial differential equations are categorized because each type of PDE requires a different number of initial and boundary conditions. The category that a given PDE falls into gives clues as to the nature of the flow problem, as well as suggesting a particular solution technique. For instance, elliptic PDEs are usually associated with steady state problems. Hyperbolic PDEs are usually associated with propagation problems without dissipation, whereas the parabolic PDEs deal with the propagation problems that include such dissipative mechanisms as viscous shear, and heat conduction.

$$A\frac{\partial^2 u}{\partial x^2}+B\frac{\partial}{\partial x}\left(\frac{\partial u}{\partial y}\right)+C\frac{\partial^2 u}{\partial y^2}+D\frac{\partial u}{\partial x}+E\frac{\partial u}{\partial y}+Fu+G=0 \qquad \textbf{(2.34)}$$

$$B^2-4AC<0 \qquad \textbf{(2.35)}$$

$$B^2-4AC>0 \qquad \textbf{(2.36)}$$

$$B^2-4AC=0 \qquad \textbf{(2.37)}$$

The category for each of the sets of governing equations of fluid flow can be determined. For instance, the potential flow equations and the Euler equations for steady flow are elliptic for subsonic flow. This means that the solution at any point depends on the conditions that were defined at every boundary of the computational domain, even the downstream boundaries. However, for supersonic flow, these same

equations are hyperbolic, meaning that the solution at any point depends only on the conditions defined at the upstream boundaries. The Euler equations for unsteady flow are also hyperbolic. Finally, the boundary layer equations are parabolic and the compressible Navier-Stokes equations are mixed hyperbolic-parabolic. These last two sets of equations can be solved by simply marching forward in the streamwise direction from the initial conditions.

As stated previously, the computational domain is divided into a grid with a number of discrete points or nodes. This is done so that the governing equations of the flow can be solved faster and easier. It is very difficult to solve for one particular parameter or variable at every point in the flow simultaneously, especially when all the changes that are possible in just one parameter in a given flow problem are considered. To facilitate this process, each parameter is solved at certain points in the flow only. A prediction can then be made of the value of each parameter at every point in the flow by the use of interpolation between the grid points. Special care must be taken when constructing the grid, however, because the improper choice of grid point or node location can lead to stability or convergence problems in the computation.

There is a tradeoff to consider between fine and coarse grid spacing when constructing any grid. A finer grid spacing would certainly provide more detailed information regarding the flow, but would increase the computing time significantly. Therefore, it is better to use the coarsest grid spacing possible in most cases. In most practical applications, it is also common to use a non-uniform grid density. A finer grid spacing would be used in regions where the flow parameters are changing rapidly or in areas of particular interest. Whereas, a coarser grid spacing would then be used to partition the rest of the computational domain.

There are two different types or forms of boundary conditions. They can be either Dirichlet boundary conditions or Neumann boundary conditions. In the first type, the exact values of the variables associated with each boundary are known. They are constants that can be substituted directly into the relevant equations. In the second type,

the derivatives of the variables associated with each boundary are known. This creates extra equations that must be solved to find the exact values of the variables.

Upon final manipulation of the governing equations, the solution must converge. This means that the approximate solution of the algebraic equations must approach the exact solution of the partial differential equations as the grid spacing approaches zero. It is clear that a significant factor in the construction of any CFD algorithm is that it is accurate, and that it will converge. Another important consideration is that it is stable. Stability requires that any simplifications or round-off errors in the computation also decay to zero. According to Lax's Equivalence Theorem, stability is said to be a sufficient and necessary condition for convergence.

There are two techniques that are used to either help a solution converge or to speed up the convergence of a solution. These techniques are called relaxation techniques. Under-relaxation is an interpolation scheme used to help convergence. It is employed when the values at any point are taking on an oscillatory pattern, or where the value of the parameter at each successive iteration appears to be overshooting the eventual solution. In the step change from T_j to T_{j+1} for instance, a new value between these two would be utilized in the next iteration. For non-linear problems, under-relaxation is often necessary for convergence. Over-relaxation is an extrapolation scheme used to accelerate convergence. If a certain pattern is noted in the step change from T_j to T_{j+1} for example, this trend can be anticipated. A "better guess" can then be made for the value of the parameter in the subsequent iteration.

The algebraic equations can either be solved directly or iteratively. It is most common in CFD to solve the algebraic flow equations in an iterative time marching scheme. The two types of time marching methods are point or explicit iterative methods and block or implicit iterative methods. In the explicit case, the set of algebraic equations is solved at single grid points in successive iterative sweeps. This option is used when the unknown value of one variable can be related to the known values of other variables. With this scheme, a solution can usually be found easily and directly.

Whereas in the implicit case, groups of grid points are solved together. This option is used when the unknown value of more than one variable is related to the known values of other variables. With this scheme, a system of several equations must be solved simultaneously if a solution for all of the unknown values is to be found.

Once again, in choosing between the above methods several factors must be taken into account. Implicit solution techniques tend to be more stable and can tolerate larger time steps in the time marching stage. However, they are also more difficult to implement and are considerably more expensive than explicit methods in terms of the cost of computation time, especially when complex three-dimensional flow problems are considered. Another consideration is that large time steps tend to increase the truncation error, and decrease the accuracy of the solution. In spite of this, the implicit method is currently favoured over the explicit method.

CHAPTER 3. MEFP BASICS

3.1 INTRODUCTION TO MEFP

MEFP stands for Moore Elliptic Flow Program. It is a computer code written in FORTRAN by Joan and John Moore of the Virginia Polytechnic Institute and State University that was programmed specifically to handle turbomachinery flow calculations. MEFP is capable of handling a wide range of flow conditions. The flow can be compressible or incompressible, subsonic or transonic, as well as, inviscid, laminar or turbulent. It has the capability to handle any flow problem ranging from simple two-dimensional jobs to complex three-dimensional jobs. The fact that it is an elliptic flow model also does not impose any restrictions on the flow direction that is employed in the problem. However, the code does encounter difficulties when asked to handle regions of abrupt separation, or separation and reattachment. It is also unable to handle flow problems where there is back flow at the exit plane.

3.2 MECHANICS OF MEFP

There are a number of options that are available concerning the grid input in MEFP. The code is able to interpret both uniform and non-uniform grids, as well as orthogonal and non-orthogonal grids. The grid points can be specified in either Cartesian or cylindrical coordinates. Furthermore, these coordinates can be either stationary or rotating. MEFP is unique in that the overall grid may pass through and include points in solid walls. The nature of each grid point is specified individually when setting up a job as to whether it is part of the flow field, on a wall surface, or a solid object.

In order to run the code, a complete dataset for each flow problem is required. The dataset consists of 13 different files that perform specific functions. For instance, the first two files define the geometry of the computational domain and the grid that is to be used. A subsequent file sets the values of particular constants, and defines the

initial and boundary conditions. The actual computation begins with a file that solves the continuity equation in order to generate the initial estimates of flow parameters that are to used a later time. During every pass or iteration in any given run, MEFP will update the pressure and velocity solutions, then use this information to solve the energy equation and any higher order turbulence models. During every second pass, MEFP will write the current values of all the parameters to a convergence file for later analysis, as well as update the parameters according to the prescribed relaxation. It is also possible to dictate which results are to be saved and printed in the final step, as well as specifying the computation of any new numerical data.

MEFP uses the Reynolds-averaged Navier-Stokes equations as the governing equations that define fluid dynamics. These equations are considered the most logical option when analyzing problems involving turbulent flow. In turbulent flow, the time and length scales of the motion are small, requiring an equally small grid scale and time step, which is simply impractical in most cases. This problem is solved by time-averaging or Reynolds-averaging the governing equations. The final product is arrived at by assuming that the local flow properties in both time and space are made up of a mean value (obtained over some time interval), as well as a fluctuating component, that are then time-averaged. The Reynolds-averaged Navier-Stokes equations are similar to the Navier-Stokes equations that were presented in Eqns.2.12-2.20 except for the substitution of a $\left(u' + \overline{U}\right)$ factor wherever a "u" appears (and the same for the other velocity components). Here u' is the fluctuating component of the velocity and $\overline{U}$ is the mean component of the velocity. New terms are created in both the momentum equation and the energy equation (a stress gradient and heat flux of the turbulent motion), which produces an extra unknown for the number of equations. An additional relation defining the turbulence model is needed to "close" the system of equations so that the number of unknowns once again equals the number of equations.

The code also includes a pressure correction algorithm. The momentum equations can only be solved initially when the pressure field is either completely defined or guessed at. If a guess is needed, it must be close to the final value or else the

resulting velocity components will not satisfy the continuity equation. Using a pressure correction algorithm is a simple way to improve the initial guess of the pressure field so that the resulting velocity components will get progressively closer to satisfying the continuity equation.

Unlike many CFD codes, MEFP is not a time marching code. Time marching codes solve for the relevant parameters or variables by knowing the initial conditions and gradually solving the flow conditions at every point by incrementing the time step. MEFP starts by making a guess at the flow parameters based on the initial conditions and the boundary conditions. A number of iterations follow and the final solution is arrived at when the value of the parameter no longer changes from iteration to iteration. This permits pass-to-pass changes in the flow parameters to be larger than with other methods, and also allows for convergence in fewer passes.

There are other options that can implemented in the code. For instance, with MEFP there are a number of different turbulence models that can be used. The mixing length model is the most common. However, there is also a one-equation q-l model, and a more complex two-equation k-ε model. The code also includes a film cooling subroutine that can be implemented with a few simple commands. This particular option is mentioned in detail in a later section and is the focus of this computational investigation.

At the end of each run, MEFP writes the output data to special files to be read and analyzed in other applications. Two such applications that were used are a convergence program called cvgce, and a three-dimensional output processor called GRAFFITI (which stands for Grid Rendering and Animation of Fluid Flow InformaTIon). Cvgce is very useful in that it can depict graphically whether or not a solution has converged. The criterion for convergence that is sought is a LOG RMS decrease in the relevant parameters of two orders of magnitude. Figure 3.1 shows a sample plot from cvgce. The convergence data that are shown are from the non-film cooled S.F.P.G. case over 400 passes with the relevant parameters being the heat

transfer, the static pressure and the velocity in two directions. GRAFFITI is very useful because it gives a complete picture of the flow behavior. It can perform a wide range of tasks from plotting contoured trends in any number of flow parameters over the entire computational domain, to showing the vectors depicting flow velocity at every grid point. It also proves to be quite useful when simply verifying the appearance of the test geometry with the accompanying grid.

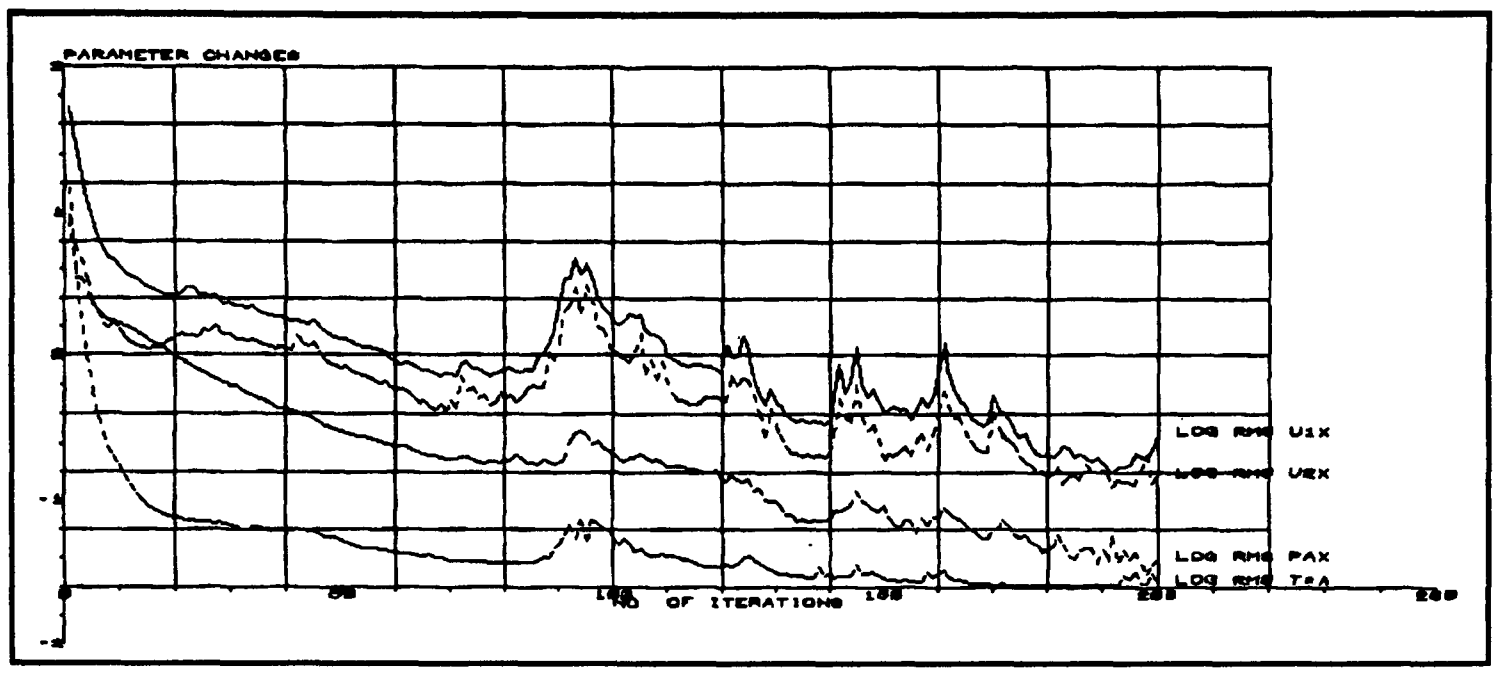


Figure 3.1 Sample Convergence Plot

MEFP, much like all other CFD codes, is not perfect. The results that it produces can not be expected to agree with every theoretical and experimental result. The results that it generates can only be as accurate as the equations that are used to define the flow. However, if a reasonable amount of time and effort are invested in constructing a detailed dataset, then MEFP has the potential to be a very powerful engineering design tool.

CHAPTER 4. FILM COOLING OVERVIEW

4.1 INTRODUCTION TO FILM COOLING

Over the years, engine manufacturers have made significant improvements in the thrust and the efficiency of gas turbine engines. With these improvements, however, come higher turbine inlet temperatures, which are beyond both the temperature and stress limits of current alloys. Therefore, it has become necessary to cool the high pressure turbine blades in all modern engines. Several techniques are currently being used to cool these blades, including film cooling. With this technique, a percentage of the air entering the compressor is ducted through the engine to the turbine blades. This air cools the inside of the blades by convection, and is then directed onto the blade surface through an array of discrete holes. This cool ejected air forms an insulating layer between the hot freestream and the surface of the blade, thereby reducing the gas-to-wall temperature difference, and the heat transfer to the blade. The cooling effect is greatest in the region directly downstream of the hole(s) and gradually diminishes further downstream as the coolant flow mixes with the hotter freestream.

This discussion of film cooling will deal almost exclusively with those methods that make use of holes, as opposed to slots. Even though film cooling through slots has been found to be the most effective technique, high thermal stresses and aerodynamic penalties make them an impractical choice in all modern gas turbine engines.

4.2 HOLE FILM COOLING LITERATURE SURVEY

Film cooling has been subject to a great deal of attention and the parameters affecting film cooling have been studied closely, both independently and in conjunction with each other. The most critical of these parameters include the injection geometry, the injection rate of the coolant flow, the density ratio of the coolant flow to that of the freestream, the surface pressure gradient, and the wall curvature. One set of parameters, however, may be discounted. It has been found by Liess (**ref.56**) that the

Reynolds number (in the range that is encountered in the gas turbine setting) has little effect on the adiabatic effectiveness where the effectiveness is defined according to Eqn.4.1 (It is worthwhile to note that the effectiveness is unity at the point of coolant injection where $T_{aw} = T_i$ and zero at a point far downstream of the cooling hole when $T_{aw} = T_\infty$). Ito et al. **(ref.46)** confirmed this result. It has also been found that the nature of the approach boundary layer has little effect on the heat transfer coefficient. Goldstein and Yoshida **(ref.36)** conducted film cooling tests where both a laminar and a turbulent boundary layer were studied. They reported that when comparing the two cases "very little difference" was found. Hay et al. **(ref.40)** used both a fully turbulent boundary layer and a transitional boundary layer, and reported that they found "hardly any difference" in the respective heat transfer coefficients. The reason for this insensitivity is that the turbulence introduced by the process of coolant injection causes the boundary layer to be turbulent with a thickness largely determined by the coolant mass addition.

$$\eta_{aw} = \frac{T_{aw} - T_\infty}{T_i - T_\infty} \tag{4.1}$$

The effects of differing coolant injection rates are very important, especially when they are looked at in the context of the downstream distance from the cooling hole. Goldstein et al. **(ref.37)** and Wilson et al. **(ref.96)** all confirmed with a simple analysis that there is a critical value for the injection rate, G, of 0.5 for all downstream distances when the coolant density equals that of the freestream. This critical value corresponds to a maximum effectiveness. Beyond this value, the effectiveness was found to decrease sharply, and the heat transfer coefficient was found to increase sharply. The authors attributed this effect to the increased boundary layer mixing that is induced by the coolant flow at injection rates exceeding this critical value.

Liess **(ref.56)** continued this work which resulted in some interesting findings. He found that the effectiveness decreases with increasing downstream

distance in the case of low injection rates, and increases with increasing downstream distance in the case of high injection rates. It is implied that low injection rates are those that are less than the critical value of G=0.5, and conversely, high injection rates are those that are greater than the critical value. Liess attributed this to the fact that at low injection rates the flow obviously has a low velocity, and a small velocity component normal to the wall. Therefore, the coolant flow is deflected by the freestream at the outset, and remains attached to the surface directly downstream of the cooling hole(s). There would be a high effectiveness closest to the hole with the effectiveness progressively decreasing as the downstream distance is increased as a result of the mixing with the freestream. At high injection rates, the flow has a high velocity, and a large velocity component normal to the wall. The coolant flow can penetrate farther into the freestream, hence the low effectiveness directly downstream of the cooling hole. However, the coolant flow is eventually deflected back to the surface by the freestream and the spreading of the coolant jet gives rise to the increased effectiveness farther downstream of the cooling hole(s). Liess surmised that the critical value of G=0.5 is the limiting value where the coolant flow is still attached to the surface directly downstream of the cooling hole. He confirmed this theory with flow visualization. The ideal situation for optimum cooling would be an injection rate of G=0.5 close to a film cooling hole, then shifting towards G=1.0 as the downstream distance is increased. He also found that the maximum effectiveness is found at higher values of G for increasing pressure gradients. These conclusions are drawn from experiments where the coolant and freestream densities are equal. Hence, the injection rate may be considered a scaling parameter.

The effects of pressure gradient on film cooling are well documented by Hay et al. **(ref.40)**. In the presence of mild adverse pressure gradients, the authors found little effect on the heat transfer coefficient at any injection rate. This, however, was not true for the favourable pressure gradient. The heat transfer coefficient was "significantly lowered" in this case, especially at low injection rates. They also found a definite variation in the heat transfer coefficient with injection rate. For a mild

favourable case, and an injection rate of G=0.5, it was found that the heat transfer coefficient was reduced to 70-80 percent of the value it exhibits with zero pressure gradient. As the injection rate is increased, the relevant values of heat transfer coefficient approach the values that are found in the case of zero pressure gradient. For a strong favourable case, the heat transfer coefficient was reduced to 45-70 percent of the value it exhibits with zero pressure gradient in the neighbourhood of the cooling hole and 20-60 percent of the value it exhibits with zero pressure gradient far downstream of the cooling hole. With increasing injection rate, the relevant values of heat transfer coefficient were also found to approach the values that are reported in the case of zero pressure gradient (although not nearly as much so as for the mild favourable case).

The effects of wall curvature on film cooling must also be examined because it represents a condition that is met in real gas turbine engines. Rastogi and Whitelaw **(ref.75)** were among the first to discover that the effectiveness increases with a convex wall and decreases with a concave wall. Ito et al. **(ref.46)** later quantified these findings. On the suction side of an actual blade, the authors determined that the effectiveness was the highest at a value of G=0.5 to 0.7. If the injection rate is increased beyond this range, the effectiveness decreases. At a value of G=1.5 to 2.0, the effectiveness increases once again. They said that this trend can be predicted by examining whether or not the coolant flow moves closer to or further from the surface. On the pressure side of an actual blade, the authors determined that the effectiveness is small at low injection rates because the pressure forces act to force the coolant flow away from the surface. They also determined that by increasing the injection rate, the effectiveness also increases. Intuitively, the data from the suction side and the pressure side should intersect at a value close to one.

Dring et al. **(ref.23)** examined the effects of rotation on film cooling. Using flow visualization, they found that the suction surface coolant trajectory was narrow, straight, and showed only slight radial displacement. Whereas, the pressure surface coolant trajectory was wider, displayed some noticeable curvature, and showed

significant radial displacement towards the tip of the blade of roughly 30° radially outward. It can be said that the coolant flow trajectories in these cases followed the three-dimensional inviscid flow over the blade. Further examination showed that the effectiveness patterns coincided with the flow visualization patterns, and that these patterns appeared insensitive to varying injection rates. In general, the authors found that the data from the suction surface were similar to that obtained for a flat plate. However, there were marked differences, both qualitatively and quantitatively, in the case of the pressure surface.

J. F. Muska et al. **(ref.66)** investigated the cumulative effect of film cooling from more than one row of holes. They found that the superposition principle first devised by Sellers in 1963 predicted the film cooling effectiveness with reasonable accuracy. In the first row of film cooling holes encountered, the effectiveness is solved using the conventional equation (Eqn.4.1). In all subsequent rows of film cooling holes, the film temperature from the previous upstream row of holes is used as the new freestream adiabatic wall temperature.

There are other significant effects that pertain to film cooling that need to be mentioned. For instance, Kadotani and Goldstein **(ref.50)** found that the turbulence level of the freestream influences the effectiveness. Increasing the turbulence level results in a slight decrease in effectiveness due to the fact that increased turbulence is associated with more efficient mixing of the coolant flow with the freestream. This essentially dilutes the coolant flow. Goldstein et al. **(ref.37)** found that the injection angle also influences the effectiveness. The effectiveness at an injection angle of 90° is considerably lower than at an injection angle of 35°. In fact, most film cooling studies are carried out at injection angles ranging from 25° to 35°. This is considered the optimum range because the coolant flow is injected closer to the wall with a smaller velocity component normal to the wall. Finally, Afejuku et al. **(ref.2)** found that a staggered configuration of cooling holes tends to generate higher effectiveness than an inline configuration of cooling holes. When all of these effects are combined, they

provide a comprehensive study of film cooling parameters which allow the turbine engineer to design for real engine representative conditions.

4.3 SLOT COOLING LITERATURE SURVEY

As stated previously, film cooling by means of slots has been found to be the most effective blade cooling technique, but it is not widely used because of other concerns. It has been found that higher values of effectiveness can be obtained with slots, as opposed to holes for the same injection rate. This is due to the fact that slot cooling simply provides a more efficient "blanket" of cooler air that covers the blade surface and protects it from the hotter freestream.

There are some factors that have been found to have very little effect on slot cooling performance. It is beneficial to single out those factors that have little influence, as well as those factors that have a significant influence, so that slot cooling effectiveness can be optimized more efficiently. Chin et al. **(ref.15)** determined that the level of mainstream turbulence is of "secondary nature" when considering the effect of various factors on slot cooling effectiveness. Seban **(ref.81)** found that the turbulence level has little effect on the relevant parameters as well. Seban also conducted tests at a wide range of Reynolds numbers. His results are similar to those of Metzger et al. **(ref.61)**, who found that the effect of varying the Reynolds number is "relatively small".

In general, slot cooling performance is dependent on one primary factor, geometry. Slot cooling is very much unlike cooling by means of holes, where the hole size and geometry, injection rate, pressure gradient, and curvature all have a significant influence on the cooling process. All of these elements may alter the value of the effectiveness or the heat transfer coefficient when cooling by means of slots, but are considered to have a secondary effect that is far less significant in comparison with altering the slot geometry. If the paper by Seban **(ref.81)** is consulted, then it is found that the maximum value of effectiveness is to be achieved when s, which he calls the

injection slot height, is the smallest. If the paper by Eckert and Birkebak **(ref.24)** is consulted, then it is found that better cooling performance is to be expected with wider slots. Eckert and Birkebak defined the slot geometry according to the non-dimensional parameter L/s, where L is the slot width at the exit of the slot and s is the slot height. They found that as the ratio L/s was increased, the value of the effectiveness also increased. Their explanation for these results was that less mixing between the freestream and the coolant occurs when the slots are wider. This is obviously more desirable because less mixing translates to a more effective coolant flow, where the dilution by the hotter freestream can be said to be at a minimum.

Research has also been carried out at varying injection angles ranging from normal injection to tangential injection. Intuitively, tangential injection is more effective than normal injection due to the fact that there is considerably less mixing of the coolant and the freestream. Therefore, the coolant can provide a more effective "film" of air to protect the surface of the blade. Any increase of the injection angle beyond what would be considered tangential injection would result in a decrease in the value of the effectiveness. Seban et al. **(ref.83)** showed that up to a 50 percent decrease in effectiveness is typical when comparing slot cooling results with normal injection to those results with tangential injection. Papell **(ref.70)** analyzed the effect of varying the injection angle through a wide range of angles. He found that for initially low values of effectiveness, changing the angle of injection does not noticeably change the final result. When the initial value of the effectiveness is 0.6 or higher, there is still very little change in the final result for small injection angles. However, the final result begins to decrease significantly as the injection angle is increased a substantial amount.

Effectiveness has been shown to alter slightly with varying injection rate. The pioneer in the field of slot cooling research is widely considered to be K. Wieghardt **(ref.95)**. In 1946, he found the maximum effectiveness occurs when the velocity of the freestream is approximately equal to the velocity of the injected flow. Chin et al. **(ref.15)** later confirmed this result and documented the changes in effectiveness over a wide range of velocity ratios. In this case, velocity ratio is defined as the velocity of the

injected flow divided by the velocity of the freestream. Their findings are as follows: the value of the effectiveness increases with increasing velocity ratio for $\left(\frac{U_i}{U_\infty}\right) < 1$, there is little change in the range of $1 \leq \left(\frac{U_i}{U_\infty}\right) \leq 2$, and the value of the effectiveness decreases when the velocity ratio is greater than two. The results documented by Seban **(ref.81)** are slightly different from those of Chin et al. Seban found that the effectiveness increases with increasing velocity ratio until the effectiveness reaches a maximum value at a velocity ratio of 0.90. There is then no change in the effectiveness until the velocity ratio reaches approximately 1.1, at which time the effectiveness begins to decrease. Even at very high velocity ratios, the effectiveness never decreases any more than the value it attained at a velocity ratio of 0.60. In any study of slot cooling where one set of final results were found to conflict or differ slightly from any other set of final results, the reason that is offered is almost always due to the slight differences in the slot geometries used in each investigation.

The effectiveness also changes according to the downstream distance from the slot. Seban **(ref.81)** reported that in each of his experimental runs, there was an initial, constant value of effectiveness that extended downstream of the slot. The limiting distance where the value of the effectiveness is a constant increases with increasing velocity ratio. In the area beyond this region of constant effectiveness, is a region where the effectiveness exhibits a "power law dependence on distance". Eckert and Birkebak **(ref.24)** also noticed a region where the effectiveness appeared to remain at a constant value of close to one. They determined that that region extended to a distance that was consistently about six times the slot height. Within this region, the surface of the blade or the wall sees only the coolant flow, as the freestream has not mixed thoroughly with the coolant and penetrated to that depth. They recognized a second region that begins at the downstream distance equal to six times the slot height and extends to a downstream distance between 20 and 100 times the slot height depending on the injection rate. Within this region, the freestream has thoroughly

mixed with the coolant and the freestream has penetrated to the depth of the surface of the blade or the wall. A third region exists beyond this one where it can be said that a "normal turbulent profile has been established".

4.4 Film Cooling Modeling Literature Survey

The previous efforts in film cooling modeling have been looked at in detail. This was done not only to consolidate the approaches that have been tried up to this point, but also to generate ideas for a new, and hopefully better approach. Most of the work that has been done in this area has been carried out in the last decade as the need for a satisfactory numerical prediction scheme has become more urgent. It is impractical to test experimentally every cooling hole geometry at a wide range of injection rates, temperature ratios, and density ratios in order to be able to predict the heat transfer at all points downstream of the hole(s) so that the design process can proceed. If a CFD code can predict all the relevant parameters with accuracy, then engineers can investigate new cooling configurations, or conditions with ease and speed. This kind of an approach would also be cheaper than the current experimental option. This discussion will look at general modeling principles, as well as the techniques that have been used in the two-dimensional boundary layer codes, and the three-dimensional codes that examine the entire flow field.

Inadequacies in the turbulence model that a particular code uses can also be blamed for poor prediction of the relevant film cooling parameters. This discussion does not address this factor. Instead, it is much simpler to look at the modeling of the film cooling process independently from the turbulence model in order to resolve the problems the are specific to this area.

The current methods all experience difficulty when analyzing the flow in the region of the film cooling hole, or directly downstream of the cooling hole. This is particularly true in the case of large injection rates, due to the highly three-dimensional nature of the flow in this area. It is imperative that the flow is well understood in this

region before an attempt at modeling is undertaken. S.W. Lee et al. (**ref.55**) tried to do just that. They determined that coolant flow is dominated by "turbulence" in the case of low injection rates, and by "inviscid vorticity dynamics" in the case of high injection rates. It was mentioned previously that the flow can be said to be essentially two-dimensional at low injection rates where the flow is attached to the surface of the wall at every point downstream of the cooling hole. The flow becomes very complex when there is separation from the wall at higher injection rates. There is a wake region where there may be backflow present. The authors determined that in this region, the streamwise velocity is very small and the pressure is lower than that of the freestream. As the injection rate continues to increase, the wake region downstream of the injection point grows proportional to the ratio of coolant velocity to that of the freestream velocity. In the wake region, there is also increased mixing of the crossflow, which moves inward and underneath the jet, with the downwash from the jet itself.

Ramette and Louis (**ref.74**) also made an attempt at describing the film cooling process in the region of the cooling hole. The injected cooling jet exhibits a kidney shaped bound vortex which increases in strength with increasing injection ratio. The entrainment of the freestream by the cooling jets is due in part to the existence of these contra-rotative vortices, as well as to the existence of turbulent mixing or diffusion. As stated previously, one or the other of these factors dominates the cooling process depending on the injection rate. Directly upstream of the film cooling hole, there is also a pressure increase due to the "blocking" effect that the injected jet creates. Around the edge of the hole, there is also a pressure drop. In general, the structure and the behavior of the injected jet is strongly dependent on the injection rate.

The industry standard for many years was the two-dimensional boundary layer code devised in 1976 by Crawford and Kays called STAN5. A simple film cooling subroutine called STANCOOL was added to the code in 1980 by Crawford, Kays, and Moffat (**ref.19**). Any three-dimensional effects were taken into account by the use of a turbulence augmentation model. This model was meant to simulate the "shear layer interaction within the boundary layer" by altering the eddy viscosity in the mixing

length turbulence model. The turbulence augmentation is at its maximum in the region of the cooling hole(s), and progressively decreases in the downstream direction. The code solves for the relevant parameters by marching forward in the streamwise direction. The calculation is stopped whenever a row of cooling holes is encountered. In this model, the coolant enters the freestream in stream tubes. The drag forces in the freestream "carry off" the injected flow and accelerate it. This process begins at the surface of the wall and continues until the amount of injected flow that is carried off or shed is equal to the injection rate per unit width of film cooled surface. Therefore, the injection process and the entrainment-diffusion or fluid mixing process are modeled together. This model gave accurate predictions except in the region of the film cooling hole(s), and in the case of high injection rates. Figure 4.1 shows a schematic of this film cooling model. Camci and Arts **(ref.12)** later altered STANCOOL and the augmented mixing length model in an effort to predict the heat transfer in the presence of film cooling in a curved environment along the suction side of a turbine blade.

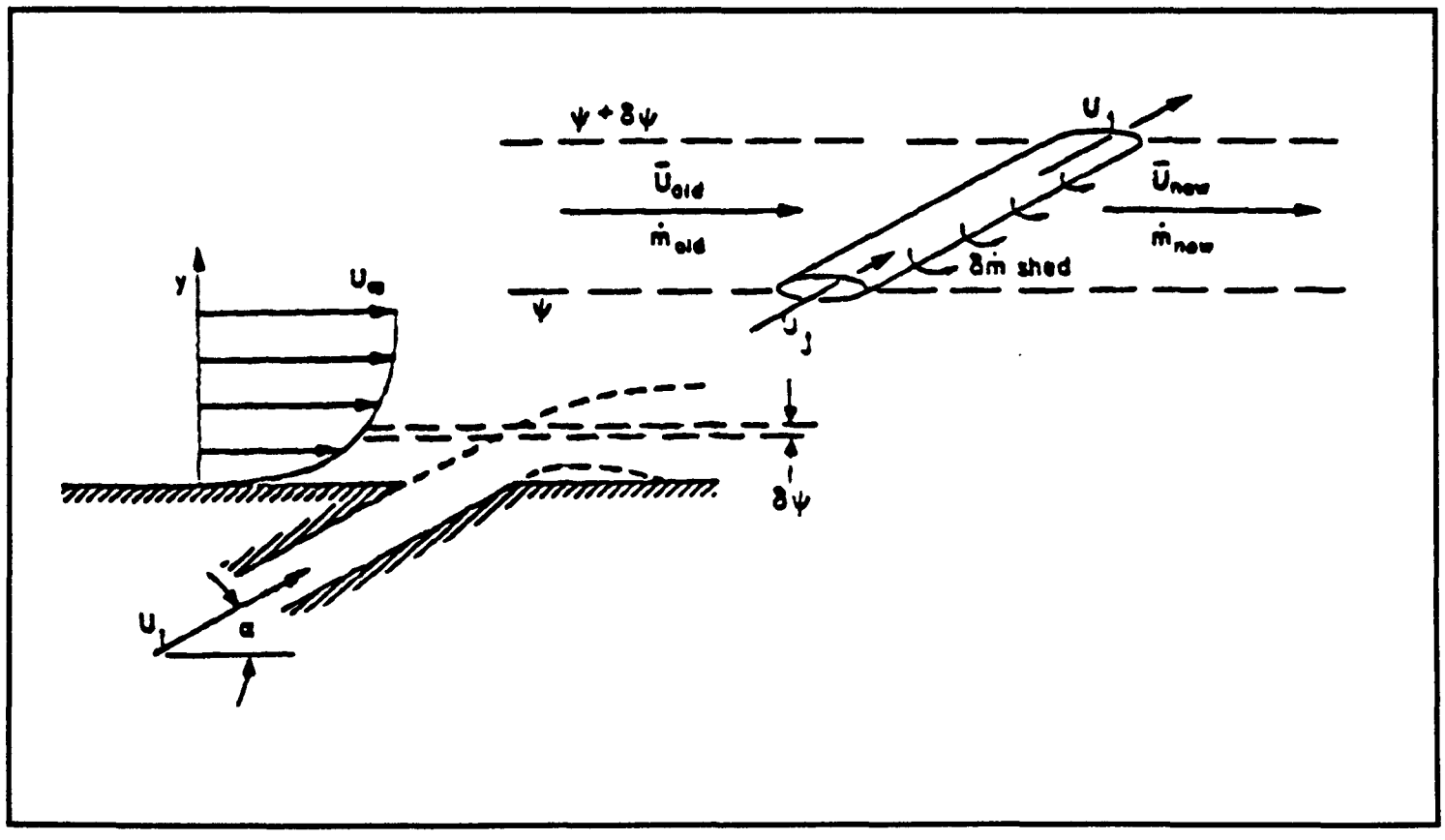


Figure 4.1 Crawford Film Cooling Model
(reference: "Full-Coverage Film Cooling" by M.E. Crawford et al., 1980)

Tafti and Yavuzkurt **(ref.88)** used a two-dimensional injection model with a low Reynolds number isotropic k-ε model boundary layer code in order to predict the

heat transfer on a turbine blade. The three-dimensional effects of film cooling were taken into account by including what the authors referred to as an "entrainment fraction" and an "entrainment enthalpy". A correlation between the entrainment fraction and the injection parameters was obtained by comparing the predictions to previously collected experimental data for film cooling from a single row of holes. This simple numerical approach gave accurate predictions in most cases, except at high injection rates where it under predicted the value of the Stanton number. The reliability of the results that were generated using this model were similar to the reliability of the results that were generated using other two-dimensional codes for prediction.

Schönung and Rodi **(ref.80)** also used a two-dimensional boundary layer code along with a k-ε turbulence model. They accounted for the three-dimensional nature of the flow in the neighbourhood of the film cooling hole by creating new boundary layer profiles after the point of injection. Any region of backflow was essentially skipped over. The newly created boundary layers were a combination of the approach boundary layer (before the injection point), and the flow profile from the injection itself. The flow profiles from the injection were based on three-dimensional, elliptic calculations for the specific flow conditions. The authors refer to this as the injection part of the model. The dispersion part of the model includes adding extra dispersion terms to the two-dimensional equations to account for the additional mixing brought about by the coolant injection. The results that were obtained were satisfactory. Differences between the experimental results and the computational results occurred when curvature effects were included (because the model does not take these into account), and at high injection rates, especially with relatively large cooling hole spacing. Figure 4.2 shows a schematic of this film cooling model. Haas et al. **(ref.38)** continued using this model and found that it gave reliable predictions of the relevant parameters under the influence of different coolant to freestream density ratios.

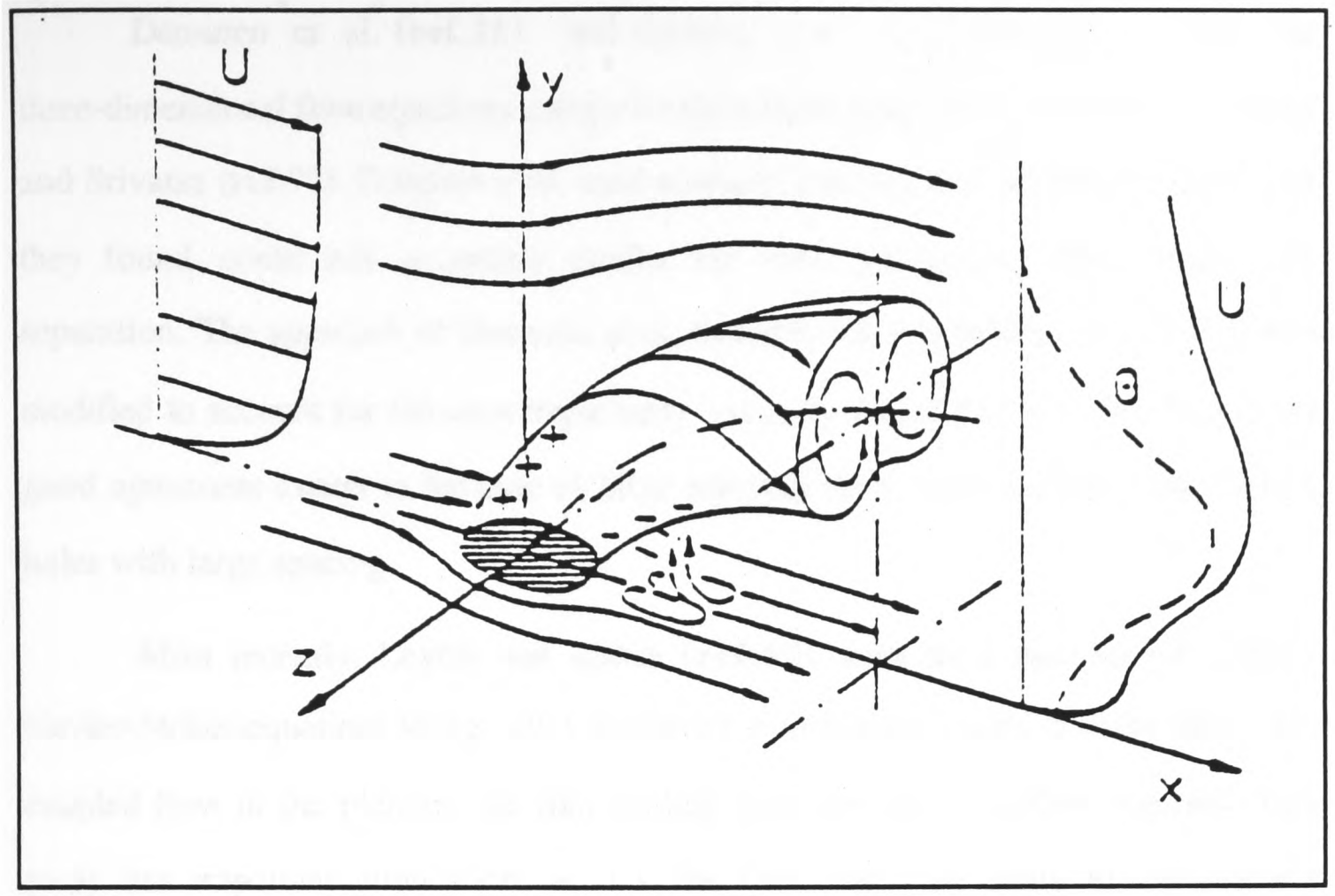


Figure 4.2 Schönung/Rodi Film Cooling Model (reference: "The Influence of Density Difference Between Hot and Cold Gas on Film Cooling by a Row of Holes" by W. Haas et al., 1987)

The flow field surrounding a film cooling hole is highly three-dimensional. Therefore, in order to generate truly accurate results, any CFD code must include a three-dimensional film cooling model, at least in the region of the cooling hole(s). Bergeles et al. **(ref.6)** employed one of the first three-dimensional models that included a semi-elliptic (or partially parabolic) treatment of the complex flow structure surrounding a film cooling hole. An elliptic, as opposed to a parabolic treatment, is necessary to resolve the three-dimensional aspects of the flow. However, using an elliptic method for the entire flow domain is impractical and costly, both in terms of time and money. The authors also used a k-ε turbulence model that was corrected for the anisotropic eddy viscosity. They reported good agreement, even in the neighbourhood of the film cooling hole(s). This good agreement was reported in cases when the injection rates ranged up to and including 0.5. After this point, major discrepancies were then reported.

Demuren et al. **(ref.21)** and Dibelius et al. **(ref.22)** also solved the three-dimensional flow equations using a locally elliptic method first developed by Rodi and Srivatsa **(ref.77)**. Dibelius et al. used a simple isotropic k-ε turbulence model that they found could not accurately predict the flow parameters when faced with separation. The approach of Demuren et al. included a k-ε turbulence model that was modified to account for the anisotropic eddy viscosity and diffusivity. They reported good agreement except in the case of large injection rates from multiple film cooling holes with large spacing.

Most recently, Leylek and Zerkle **(ref.57)** used three-dimensional, elliptic Navier-Stokes equations along with a standard k-ε turbulence model to fully define the coupled flow in the plenum, the film cooling hole, and the crossflow regions. This study has important implications as it is the first, and only study to the author's knowledge that addresses the fact that the flow emerging from a film cooling hole is coupled to the characteristics of the flow in the plenum, or the internal passages of a turbine blade. No current models take this effect into consideration. Their study also looked at the complex flow physics associated with this structure. With their results, a new understanding of this flow structure is now possible, and a new direction can be taken in the modeling of film cooling.

Figure 4.3 shows the complex, coupled flow associated with a film cooling hole. In the case of the top diagram, the injection rate is 0.5, and in the case of the bottom diagram, the injection rate is 2.0. Figure 4.4 shows the complex flow structure within a film cooling hole. The view that is presented is from the top, perpendicular to the direction of the freestream, looking down at the hole. Once again, in the case of the top diagram, the injection rate is 0.5, and in the case of the bottom diagram, the injection rate is 2.0. Figure 4.5 shows the flow structure with the accompanying temperature profile for the cases with injection rates of 0.5 and 2.0 respectively. The view that is presented is a section perpendicular to the freestream. In each of the figures, it is clear that the flow becomes more complex, and therefore, harder to define

with increasing injection rate. It can also be seen that with higher injection rates, the flow becomes more highly coupled, and the vortex structure of the flow strengthens.

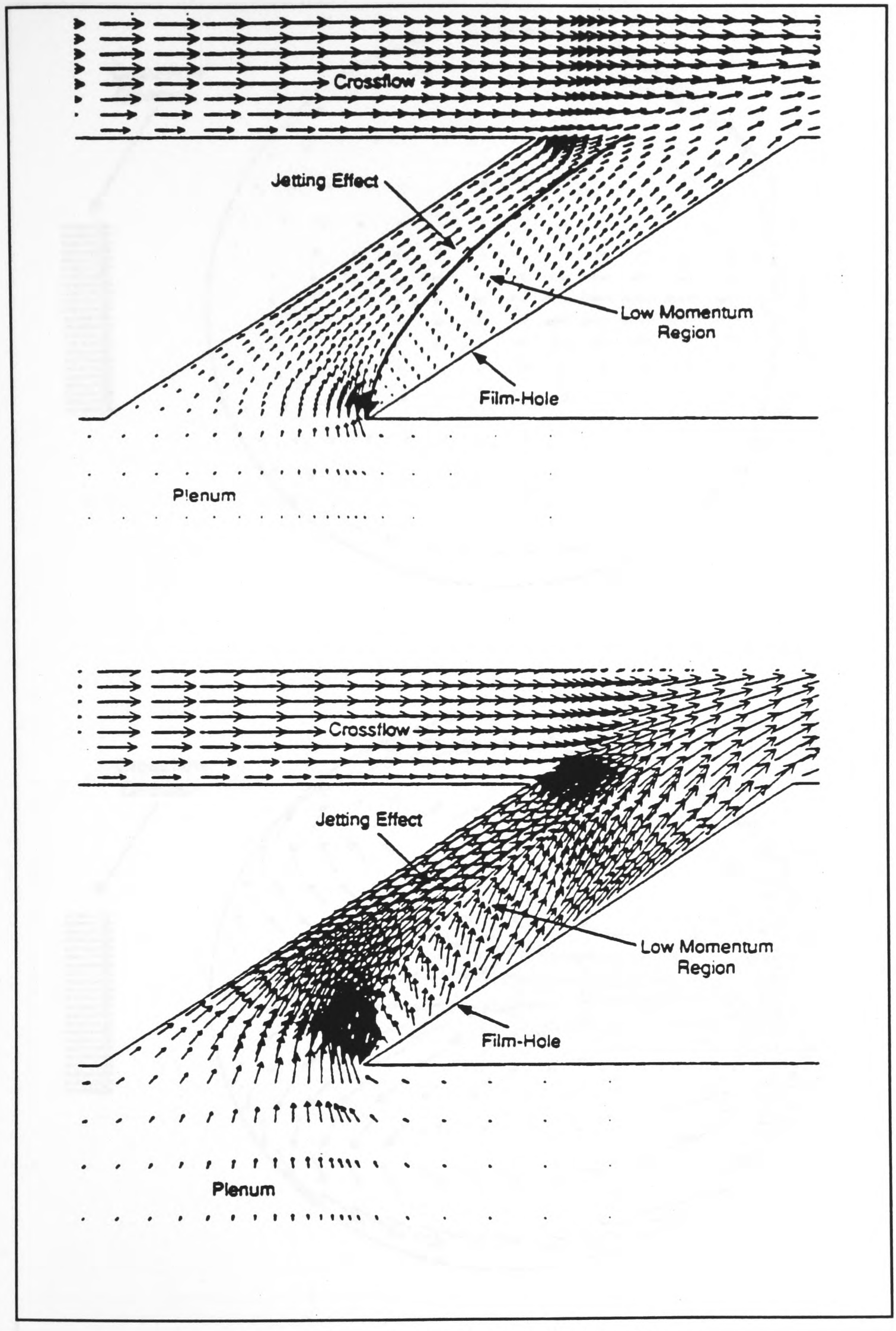


Figure 4.3 Coupled Film Cooling Flow
(reference: "Discrete-Jet Film Cooling" by J. Leylek and R. Zerkle, 1993)

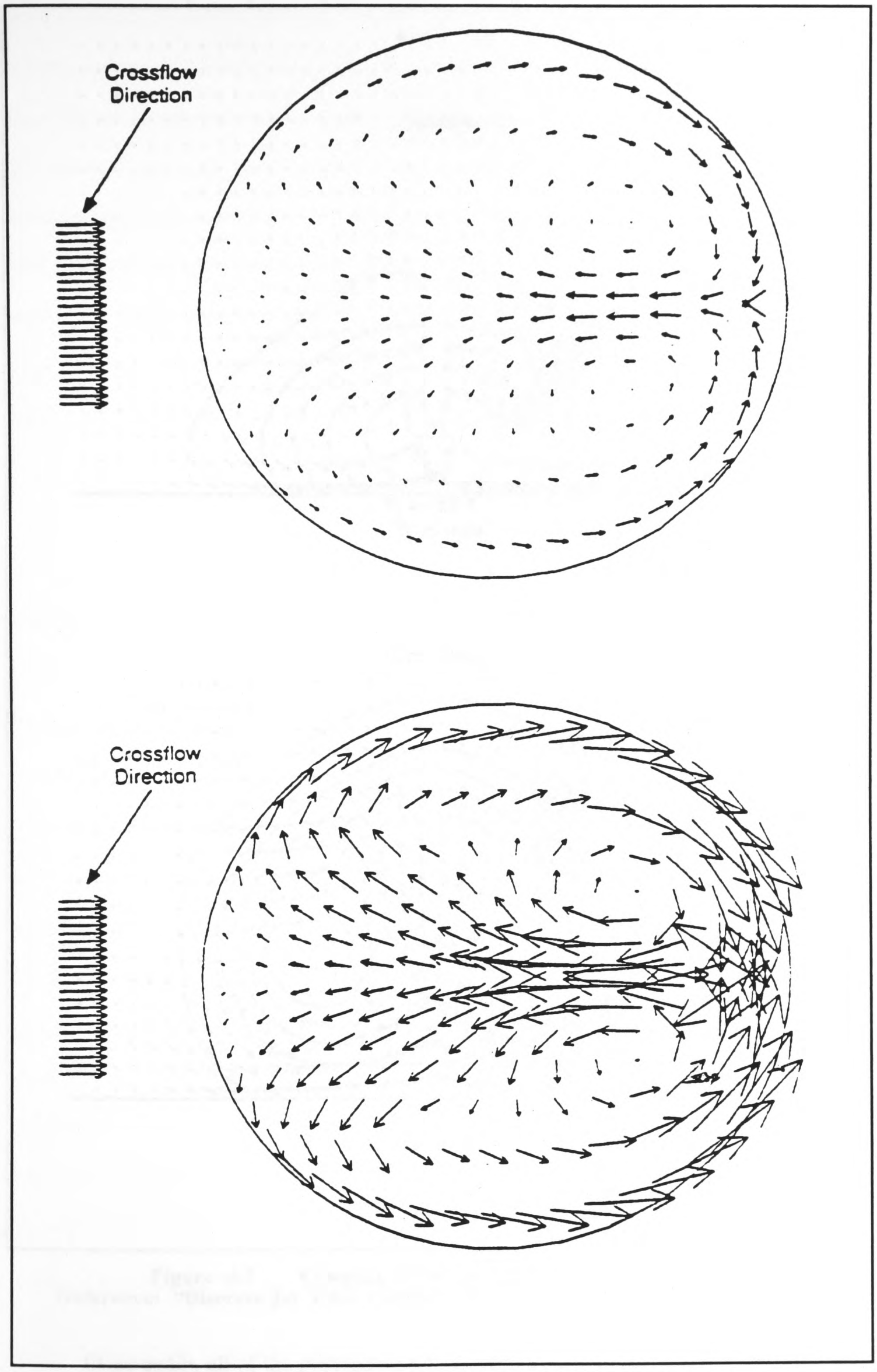


Figure 4.4 Complex Flow Within Film Cooling Hole
(reference: "Discrete-Jet Film Cooling" by J. Leylek and R. Zerkle, 1993)

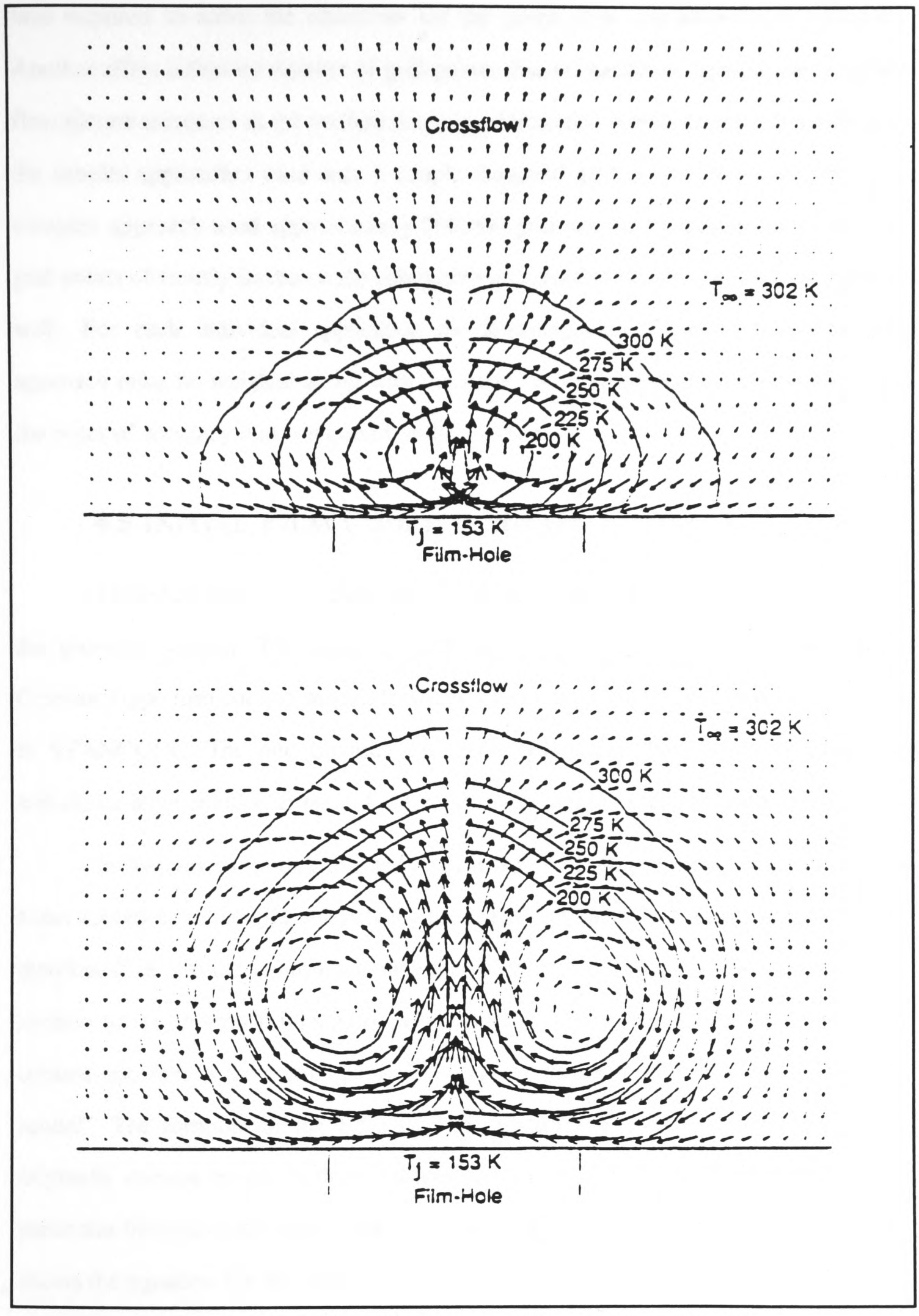


Figure 4.5 Complex Flow at Film Cooling Injection
(reference: "Discrete-Jet Film Cooling" by J. Leylek and R. Zerkle, 1993)

Once again, all of the previous methods increase in complexity in the order that they were presented. As the complexity of these approaches increase, the computing

time required to solve the equations for the given flow conditions also increases. Another effect is that the number of grid points that are needed to resolve the complete flow picture increases as the method that is used becomes more complex. For instance, the simpler approaches used only a couple thousand grid points. Whereas, the most complex approach used approximately 200,000 grid points. Increasing the number of grid points obviously increases the computing time needed to solve the flow problem as well. For each individual application the advantages and disadvantages of each approach must be weighed along with the issues of cost, efficiency, practicality, and the order of accuracy that is required of the solution.

4.5 Initial Film Cooling Model

There has been some discussion concerning the present film cooling model in the previous section. The computer code that was utilized in this analysis uses a Crawford type film cooling model. It is very similar to the model that was implemented in STANCOOL. The one obvious exception being that there were no additional turbulence augmentation terms in the code that was initially used in this investigation.

In the current model, injected coolant flow is averaged along rows of cooling holes according to the grid that is being used. The coolant flow is assumed to be evenly distributed in vertical control volumes that surround each grid point starting at the surface (at the point of injection). Momentum is conserved in the direction of the coolant injection in the computation. This type of model is referred to as a "stripping model". The formula for the mass shed ratio, that is the basis of this model, was originally derived by the Turbine Technology group of Rolls Royce **(ref.13)**. This particular formula is also used in the Rolls Royce boundary layer code Q253F. Eqn.4.2 shows the equation for the mass shed ratio. The subsequent equations (Eqns.4.3-4.5) are used to solve for the remaining unknown parameters. In the following equations, α is the angle of the coolant jet to the surface, β is the angle of the coolant jet to the freestream when projected on a plane parallel to the surface, dr is the cooling hole

diameter to pitch ratio for a row of cooling holes, U_∞ is the magnitude of the freestream, and U_j is the magnitude of the relative velocity between the coolant jet and the freestream and is assumed to be approximately parallel to the surface plane.

$$K = \frac{K_o}{\left(1+(1.62+4\sin\beta)\cos\alpha\left(U_j/U_r\right)^{1.45\cos\beta}\right)} \tag{4.2}$$

$$K_o = \frac{\eta}{(1-\eta)} \tag{4.3}$$

$$\eta = \frac{dr\sqrt{\left(\sin^2\beta+\cos^2\beta\sin^2\alpha\right)}}{\sin\alpha} \tag{4.4}$$

$$U_r = \sqrt{\left(U_\infty{}^2 - 2U_\infty U_j\cos\alpha\cos\beta + U_j{}^2\right)} \tag{4.5}$$

The mass shed ratio is further related to the penetration distance or the limiting height of the coolant injection by a few simple relations. It is assumed that into each initial control volume along a normal line (originating at the cooling hole and moving out into the freestream) that a total mass flow, $\dot{m}_{in}$, enters the control volume. Therefore, it can be assumed that a total mass flow, $\dot{m}_{out}$, must leave the control volume. Mass flow may enter the control volume from two sources, the freestream and the coolant injection. Upon exiting the control volume, the mass flow may be carried along with the freestream, in the same direction as the freestream. Alternatively, if the total amount of coolant mass flow has not been "shed", then its momentum will carry it to the next control volume in a vertical direction. Intuitively, the amount of coolant mass flow that enters the second control volume is the amount of coolant mass flow that entered the first control volume less the quantity of mass flow that was "shed" by the freestream. Figure 4.6 shows a detailed diagram of the stripping model. By

consulting this diagram, it is easy to determine the origin and relative magnitude of the mass flow that enters and exits each control volume. The penetration distance would then be the height of the last control volume into which any coolant had been injected. The aim of this model is to realistically distribute the coolant flow at the exit to a set of cooling holes rather than model the detailed characteristics of the coolant flow close to a set of holes.

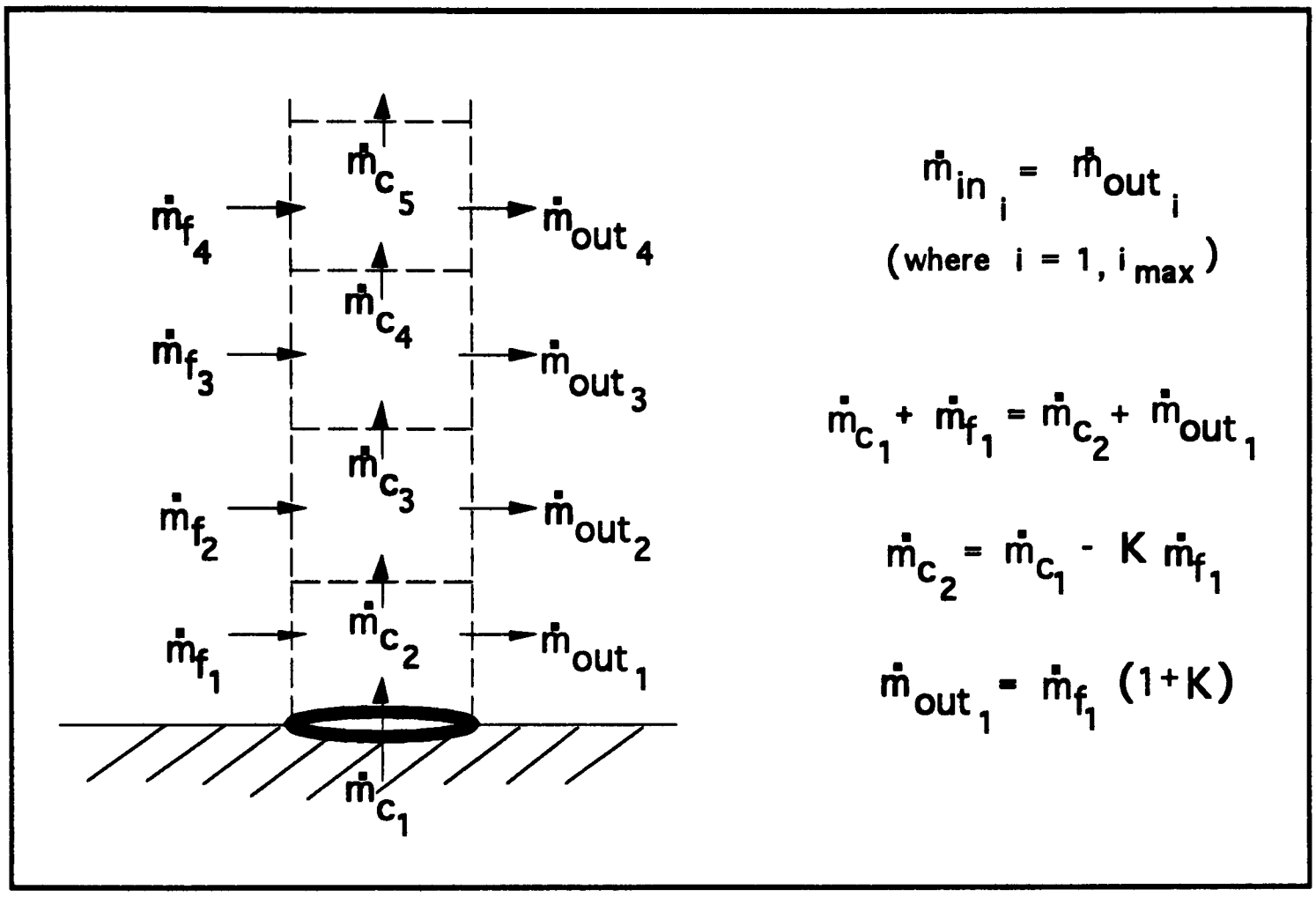


Figure 4.6 Stripping Model

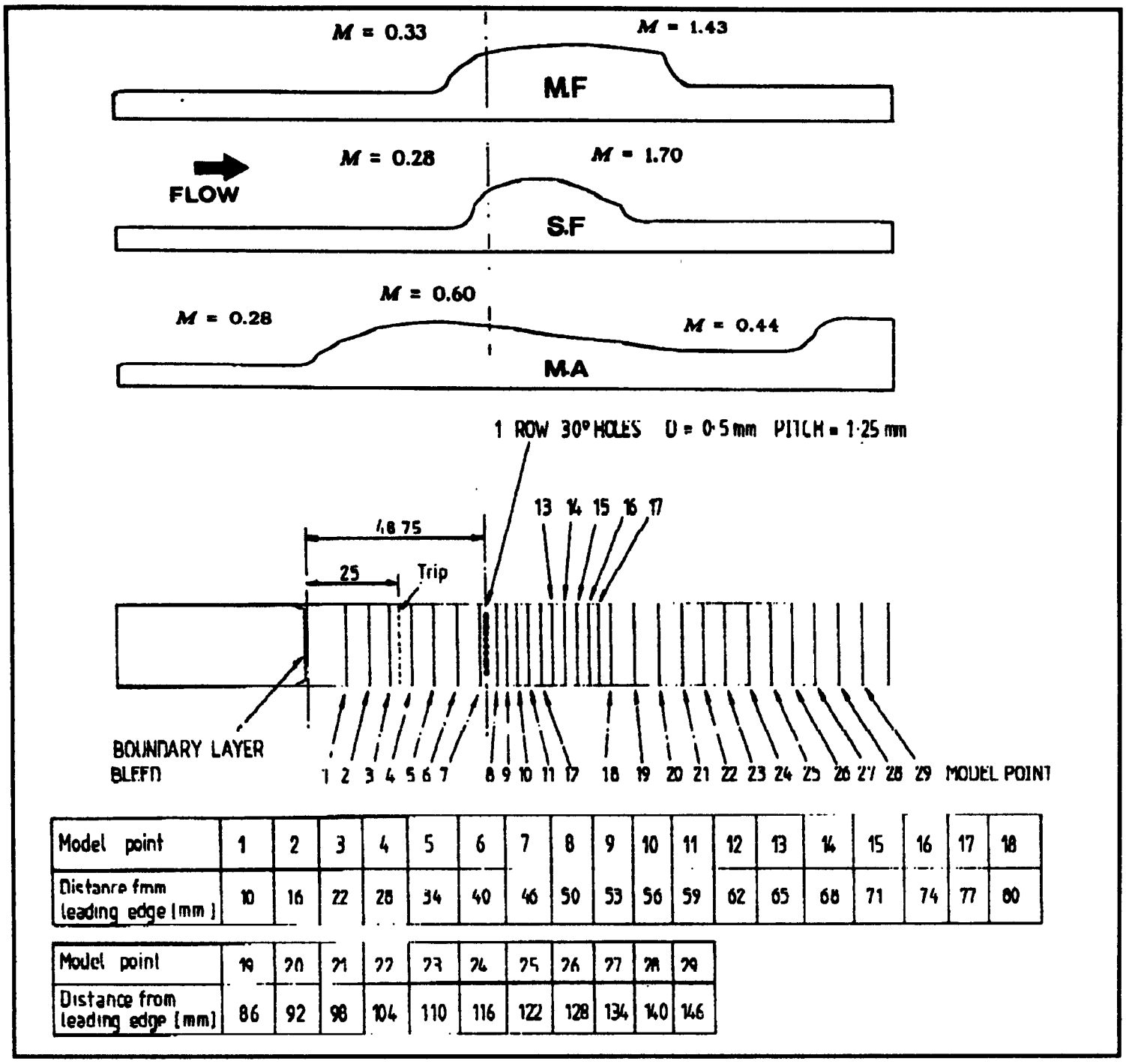
The present film cooling model also uses a Baldwin-Lomax turbulence model to determine the mixing length. It is a zero-equation model that is a slight variation on the basic mixing length model that was discussed in a previous section. Instead of using a mean velocity gradient as in Eqn.2.22, a mean vorticity is used.

CHAPTER 5. ILPT FLAT PLATE CFD CASES

5.1 TEST CASES

MEFP was used to calculate various flow parameters of the mild favourable, strong favourable, and mild adverse test cases from the ILPT. The channel geometry for each test case provided the boundary conditions for the flow field. Each test case was programmed to run for 400 passes which took approximately 6 hours on a Silicon Graphics Iris Indigo computer. This number of passes was chosen because it was found to give adequate convergence of the relevant parameters in all cases, while still maintaining as low a computing time as possible. In each case, the computation was started from the trip which was located 25mm aft of the boundary layer bleed or leading edge. This was chosen as the reference point because it can be said that after the flow encounters the boundary layer trip, the same turbulent boundary layer conditions exist for each plate. It was necessary to generate this turbulent boundary layer to simulate the conditions that exist in real turbine blades.

The boundary and initial conditions were chosen to coincide exactly with those used by Arnold Teekaram **(ref.89)** in his experimental ILPT testing, and the testing conditions that he chose were representative of those found in real gas turbine engines. Teekaram's data were chosen as the basis of comparison because he took extensive film cooled and non-film cooled heat transfer data, as well as isentropic Mach number data for all the different geometries. The ILPT cases also proved to be excellent examples of a simple flow problem with which to initially test the reliability of the code and the film cooling subroutine. The geometries of the plates which produced the varying pressure gradients were easy to input into MEFP because they were straightforward variations of a flat plate and their analysis demanded a simple, two-dimensional grid with only a couple thousand grid points. Figure 5.1 shows detailed profiles of the three ILPT test plates along with the relative trip, gauge, and injection plenum positions.



Model point	1	2	3	4	5	6	7	8	9	10	11	12	13	14	15	16	17	18
Distance from leading edge (mm)	10	16	22	28	34	40	46	50	53	56	59	62	65	68	71	74	77	80

Model point	19	20	21	22	23	24	25	26	27	28	29
Distance from leading edge (mm)	86	92	98	104	110	116	122	128	134	140	146

Figure 5.1 ILPT Test Plates
(reference: D. Phil. Thesis by Arnold J. Teekaram, 1989)

MEFP is able to calculate a number of different flow values, but only the isentropic Mach number and the heat transfer data are presented here. There are several reasons for this. By comparing the CFD Mach number data with the experimental Mach number data, a prediction can be made and confirmed involving both the velocity and pressure history over the entire test section. The heat transfer data also provided an important means of correlation, especially when looking at the film cooled test cases. Heat transfer is one of the most crucial parameters in turbine design, therefore, it is imperative that if MEFP is to be useful, it must be able to correctly predict these values.

Teekaram defined the non-film cooled heat transfer as the Nusselt number per unit length according to Eqn.5.2 where the heat transfer rate was defined according to

Eqn.5.1. The freestream recovery temperature T_{r_∞} was used in this definition instead of the typical stagnation temperature, because when viscous energy dissipation plays a significant role as it does in these test cases, the freestream recovery temperature is the relevant driving temperature. As a general rule, the influence of viscous energy dissipation is seen in high speed flows where M>0.5. The recovery temperature is related to the static temperature by Eqn.5.3. Eqn.5.4 shows the well known relation by which the static temperature is related to the stagnation temperature. The parameter r is the recovery factor and usually takes on a value of 0.87 for a turbulent boundary layer.

$$\dot{q} = h(T_{r\infty} - T_w) \tag{5.1}$$

$$Nu/m = \frac{\dot{q}/k}{T_{r\infty} - T_w} \tag{5.2}$$

$$\frac{T_{r\infty}}{T_\infty} = 1 + \frac{\gamma - 1}{2} M^2 r \tag{5.3}$$

$$\frac{T_{t\infty}}{T_\infty} = 1 + \frac{\gamma - 1}{2} M^2 \tag{5.4}$$

Teekaram described the film cooled heat transfer using a superposition model. He defined a ratio of the Nusselt number with coolant injection to that without coolant injection. This ratio (Eqn.5.5) is dependent on two parameters, A and B, which vary linearly with theta. Theta is a temperature ratio defined by Eqn.5.6 and is easily altered by changing the wall temperature. In all of the cases that were used for comparison, Teekaram chose 1.3 as the value for theta. This value was chosen because it is representative of real engine conditions.

$$\frac{Nu_{w/injection}}{Nu_{w/o\ \ injection}}(x) = A(x) + B(x)\theta \qquad (5.5)$$

$$\theta = \frac{T_{t\infty} - T_{ti}}{T_{r\infty} - T_w} \qquad (5.6)$$

The parameters A and B can be directly related to the heat transfer mechanisms associated with film cooling. For example, if the freestream temperature was equal to the coolant temperature, then A would represent the ratio of the film cooled heat transfer to the non-film cooled heat transfer produced by the mixing or entrainment of the two streams. B would then represent the "cooling effect" of the injection that is generated by the temperature difference between the freestream temperature and the coolant temperature. The conventional heat transfer coefficient and the film cooling effectiveness can also be related to the above expressions. Eqn.5.7 shows the equivalent expression for the cooling effectiveness.

$$\eta = \frac{T_{r\infty} - T_{aw}}{T_{t\infty} - T_{ti}} = -\frac{B}{A} \qquad (5.7)$$

Non-film cooled data were gathered for each of the three geometries, the mild favourable, the strong favourable, and the mild adverse. Film cooled data were only gathered for the strong favourable and the mild adverse test cases, as Arnold Teekaram only performed film cooling experiments with these geometries. As stated previously, the boundary and initial conditions, including different temperature ratios and injection rates, were chosen to coincide with those used by Teekaram in his ILPT experimental testing. The Reynolds number at the point of injection, where the Mach number was set to be 0.5 in each case, was 2.7E+07/m. He tested at two different temperature ratios (where temperature ratio in this case is defined as the total temperature of the injected flow divided by the total temperature of the freestream) of 0.82 and 1.21 (Eqn.5.8). He also tested at injection rates (where injection rate in this case is defined as the density of

the injected flow multiplied by the velocity of the injected flow divided by the density of the freestream divided by the velocity of the freestream) varying from 0.11 to 1.20 (Eqn.5.9). Table 4.1 shows the temperature boundary conditions for the non-film cooled and the film cooled test cases that were used in the experimental testing and the CFD analysis.

$$TR = \frac{T_{t_i}}{T_{t_\infty}} \tag{5.8}$$

$$G = \frac{\rho_i u_i}{\rho_\infty u_\infty} \tag{5.9}$$

FILM COOLING	TEMPERATURE RATIO (TR)	Tt_∞	Tti	Tw
NO	N/A	365 °K	N/A	300 °K
YES	0.82	365 °K	300 °K	315 °K
YES	1.21	280 °K	340 °K	326 °K

Table 5.1 Temperature Boundary Conditions

In the MEFP test runs, both temperature ratios were used and initially, only the weak injection rates were used. For the strong favourable case, this included injection rates up to, and including 0.35, and for the mild adverse case, this included injection rates up to, and including 0.25. The interval injection rates were chosen to correspond with the available experimental data. At higher injection rates, Teekaram found that the flow separated from the surface directly beyond the cooling holes and reattached at a later point downstream. The test cases with strong injection rates were analyzed after the study with the weak injection rates was complete. At the outset of this investigation,

it was unknown if MEFP would be able to give reliable or accurate results when presented with these test cases, not only because of the separation of the flow, but also because of the highly three-dimensional nature of the flow directly downstream of the cooling holes. It can be noted that the limiting injection rate for the mild adverse case is lower than the limiting injection rate for the strong favourable case, due to the fact that adverse pressure gradients tend to cause earlier injection jet separation. Figure 5.2 shows a schematic of a strong injection from a film cooling hole. The separation directly downstream of the cooling hole can be easily seen. Figure 5.3 shows a schematic of a weak injection from the same film cooling hole. It is clear that the weak injection causes less flow disruption and turbulence than the strong injection. Table 5.2 shows the ILPT test matrix that was used for all the weak injection rates as they were defined above. Table 5.3 shows the ILPT test matrix for the remaining strong injection rates as they were defined above.

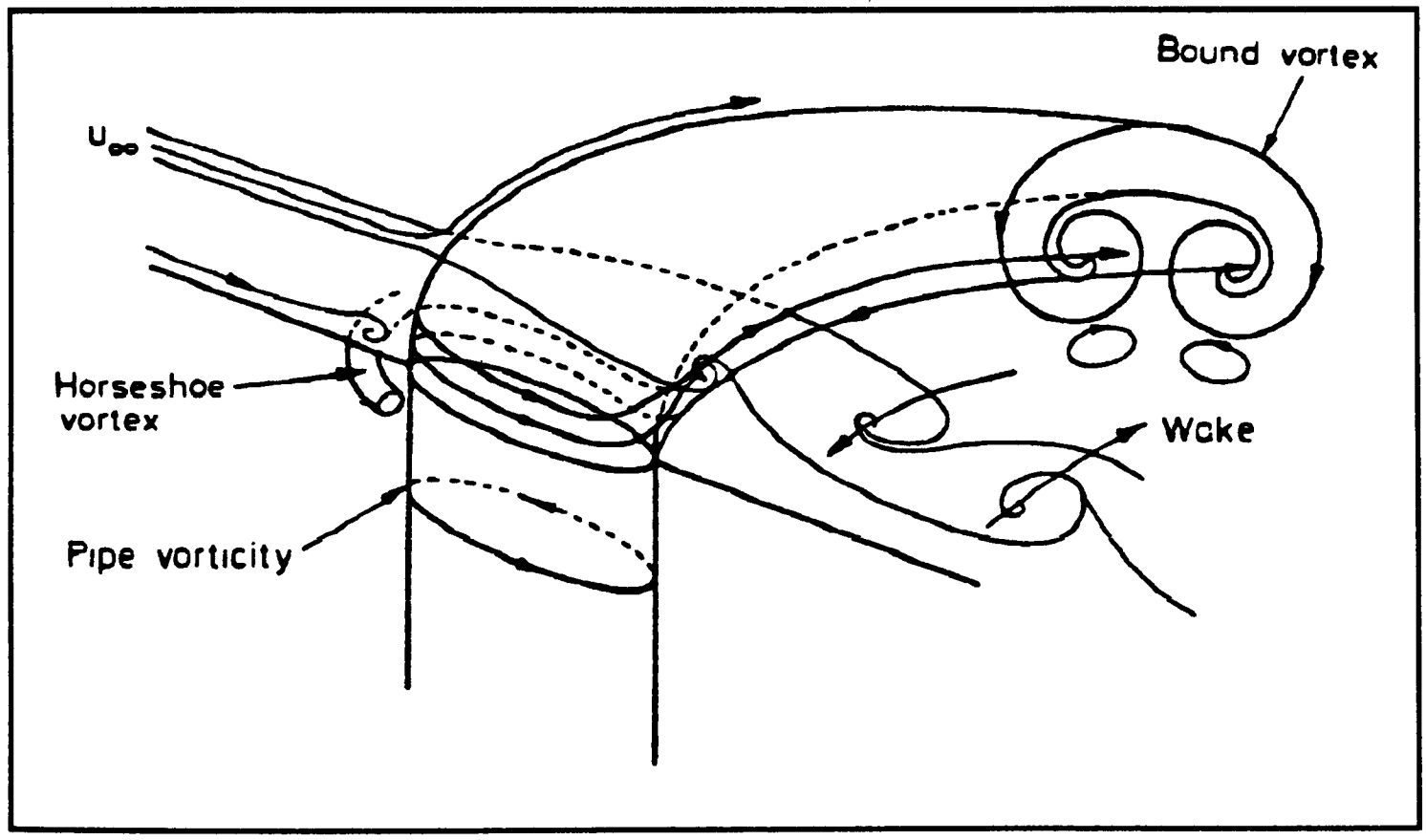


Figure 5.2 Strong Injection from Film Cooling Hole (reference: D. Phil. Thesis by Arnold J. Teekaram, 1989)

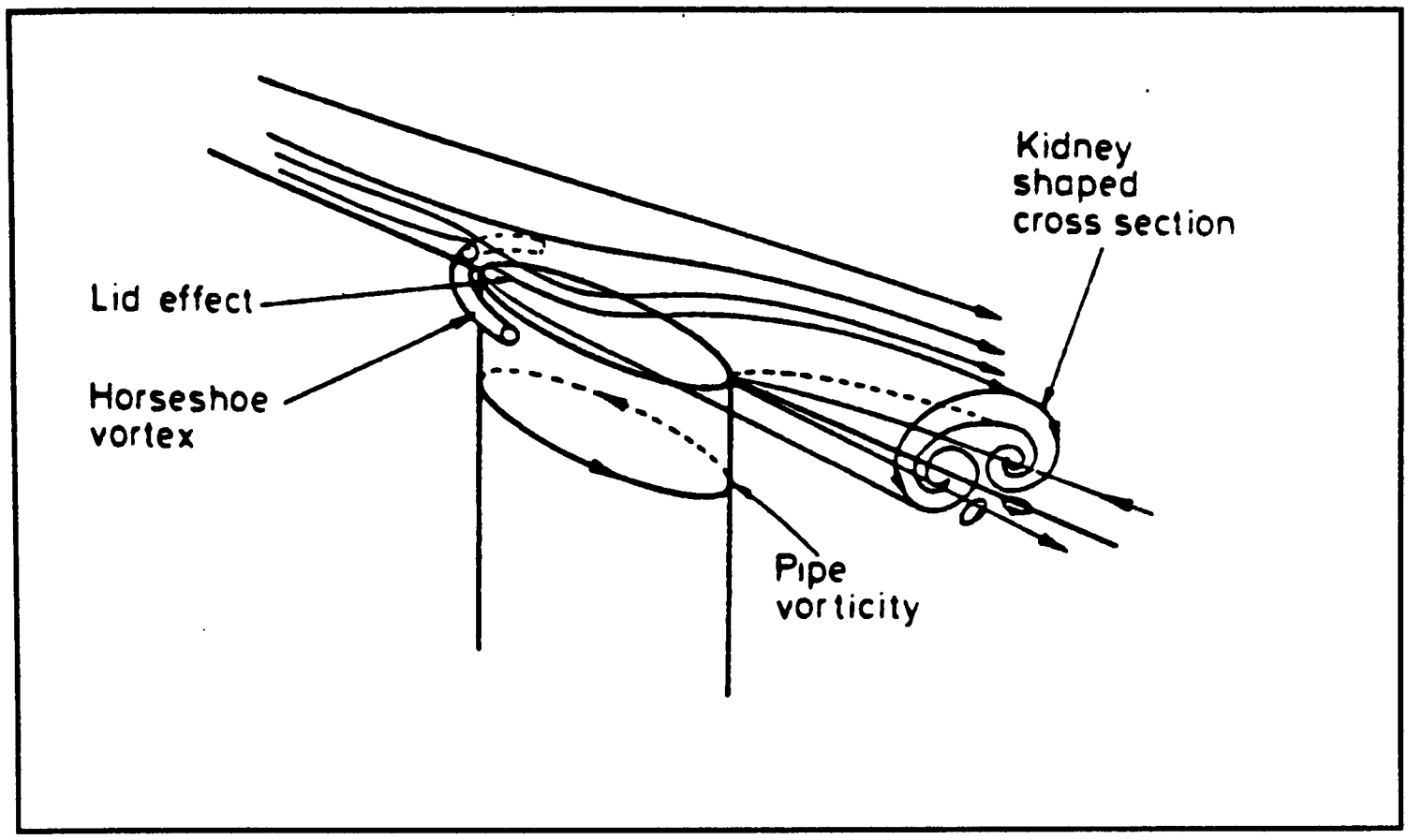


Figure 5.3 Weak Injection from Film Cooling Hole (reference: D. Phil. Thesis by Arnold J. Teekaram, 1989)

TEST CASE	TEMPERATURE RATIO (TR)	INJECTION RATE (G)
M.F.P.G. (non-film cooled)	N/A	N/A
S.F.P.G._data1 (non-film cooled)	N/A	N/A
S.F.P.G._data2	0.82	0.15
S.F.P.G._data3	0.82	0.25
S.F.P.G._data4	0.82	0.35
S.F.P.G._data5	1.21	0.11
S.F.P.G._data6	1.21	0.18
S.F.P.G._data7	1.21	0.25
M.A.P.G._data1 (non-film cooled)	N/A	N/A
M.A.P.G._data2	0.82	0.15
M.A.P.G._data3	0.82	0.25
M.A.P.G._data4	1.21	0.11
M.A.P.G._data5	1.21	0.18
M.A.P.G._data6	1.21	0.25

Table 5.2 ILPT Test Matrix (Weak Injection)

TEST CASE	TEMPERATURE RATIO (TR)	INJECTION RATE (G)
S.F.P.G._data8	0.82	0.59
S.F.P.G._data9	0.82	0.75
S.F.P.G._data10	0.82	1.20
S.F.P.G._data11	1.21	0.42
S.F.P.G._data12	1.21	0.55
S.F.P.G._data13	1.21	0.81
M.A.P.G._data7	0.82	0.35
M.A.P.G._data8	0.82	0.59
M.A.P.G._data9	0.82	0.75
M.A.P.G._data10	0.82	1.20
M.A.P.G._data11	1.21	0.42
M.A.P.G._data12	1.21	0.55
M.A.P.G._data13	1.21	0.81

Table 5.3 ILPT Test Matrix (Strong Injection)

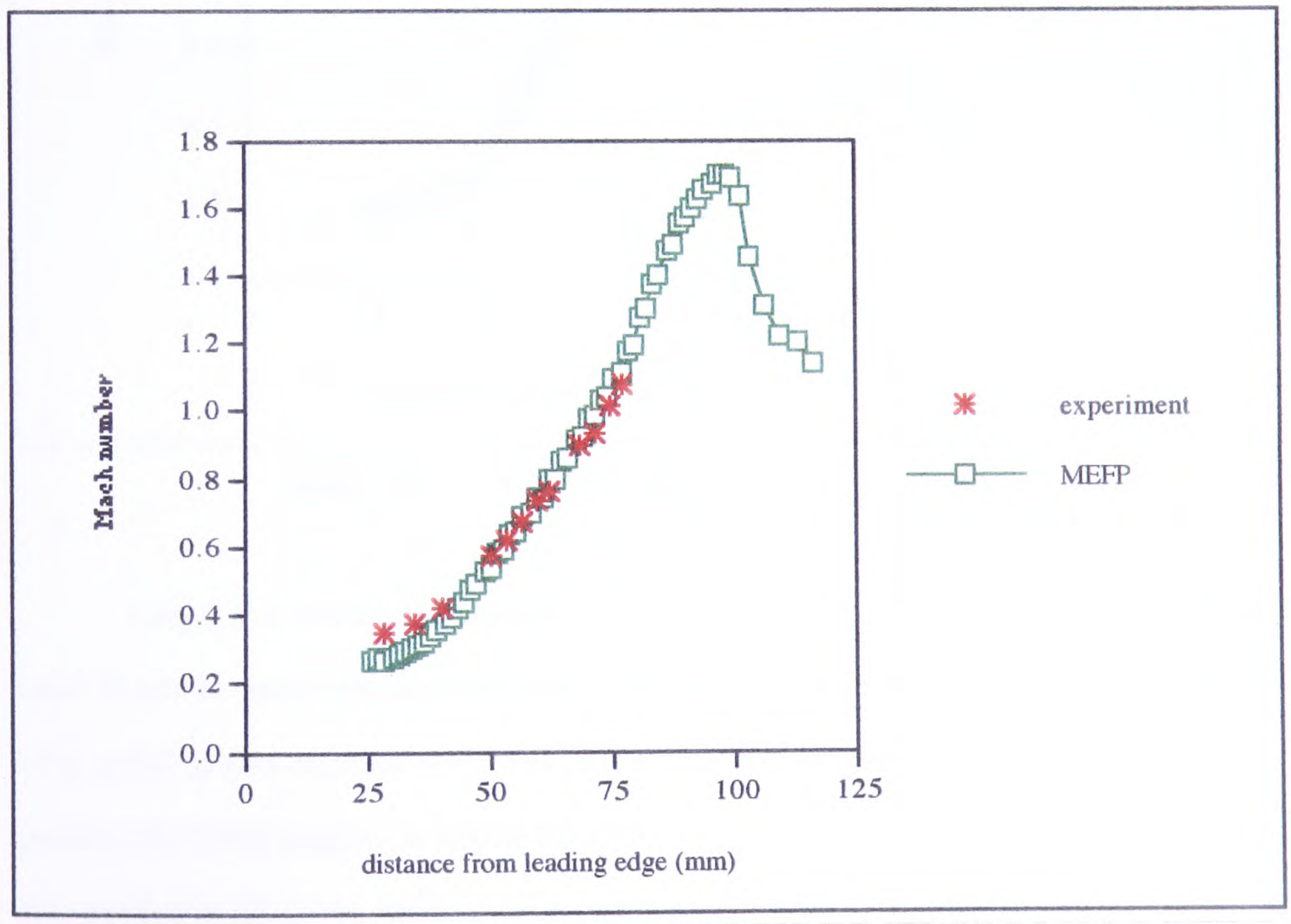
5.2 Discussion of Results

5.2.1 Isentropic Mach Number Results

The results that are addressed first are the isentropic Mach number graphs for each test case. These results are particularly important because if the agreement between the MEFP data and the experimental data is good, then it can be said that the code has computed the correct mass flow through the channel. However, if the agreement is not good, or is not within acceptable limits, then it can be said that the code has not

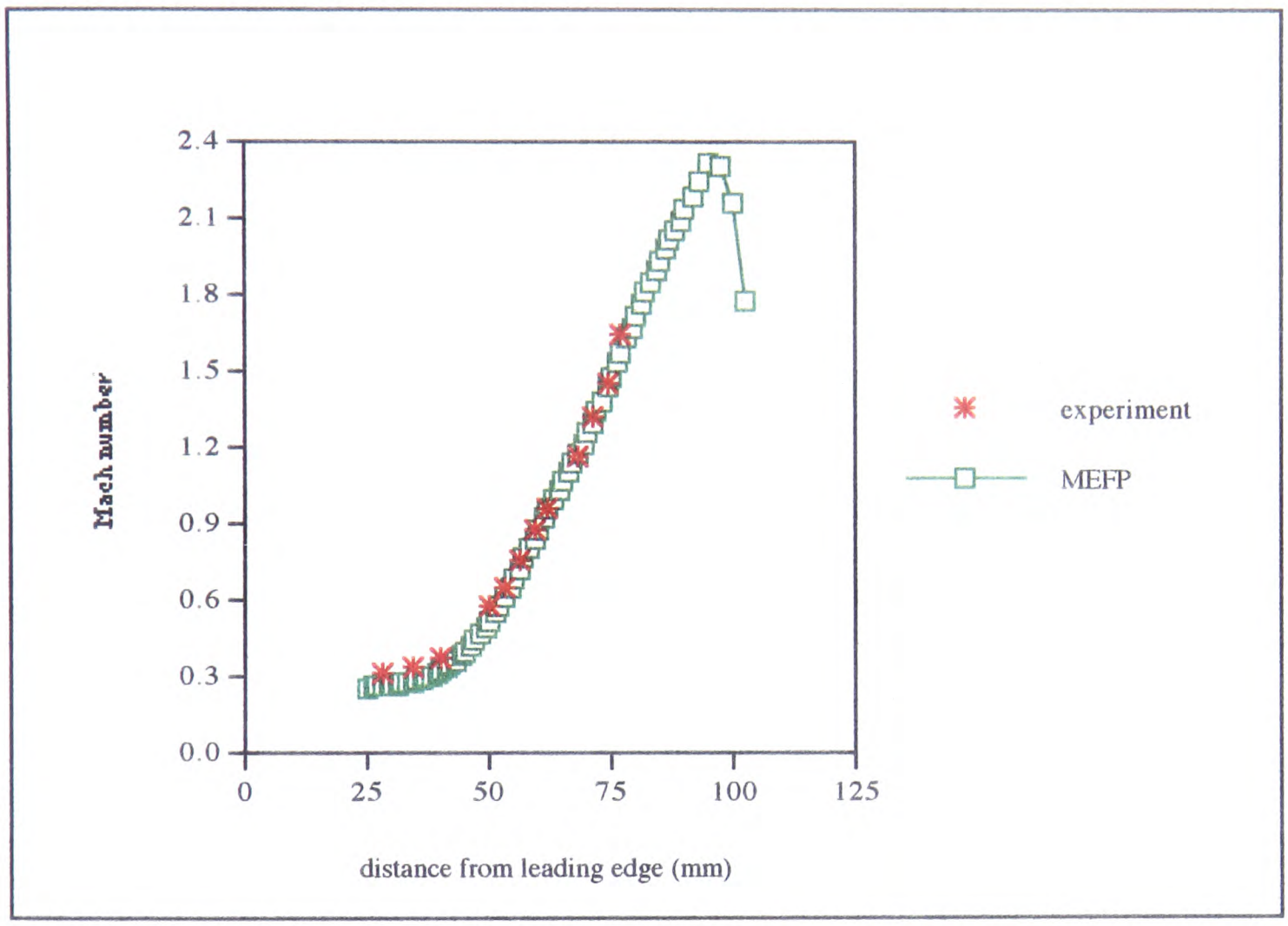
computed the correct mass flow through the channel. The code must be able to accurately predict the correct mass flow to be able to accurately predict all other relevant flow parameters, such as the heat transfer.

Graph 5.1 shows the isentropic Mach number data for the mild favourable test case. It can be seen that the agreement is very good. The point that shows the greatest discrepancy still predicts the Mach number to within Mach 0.0800. In order to get such agreement, it was necessary to increase the value of the backpressure. One of the requirements of matching the experimental flow field to the simulated CFD flow field was to ensure that the flow was choked at the throat. The increase of the backpressure was needed to satisfy this condition. Without this slight alteration, MEFP performs all of its computations assuming less mass flow than was present in the actual experiment. This graph also serves as a means of confirming the gentle upward slope of increasing Mach number that would be expected from a plate that produces this pressure gradient.



Graph 5.1 M.F.P.G. Isentropic Mach Number

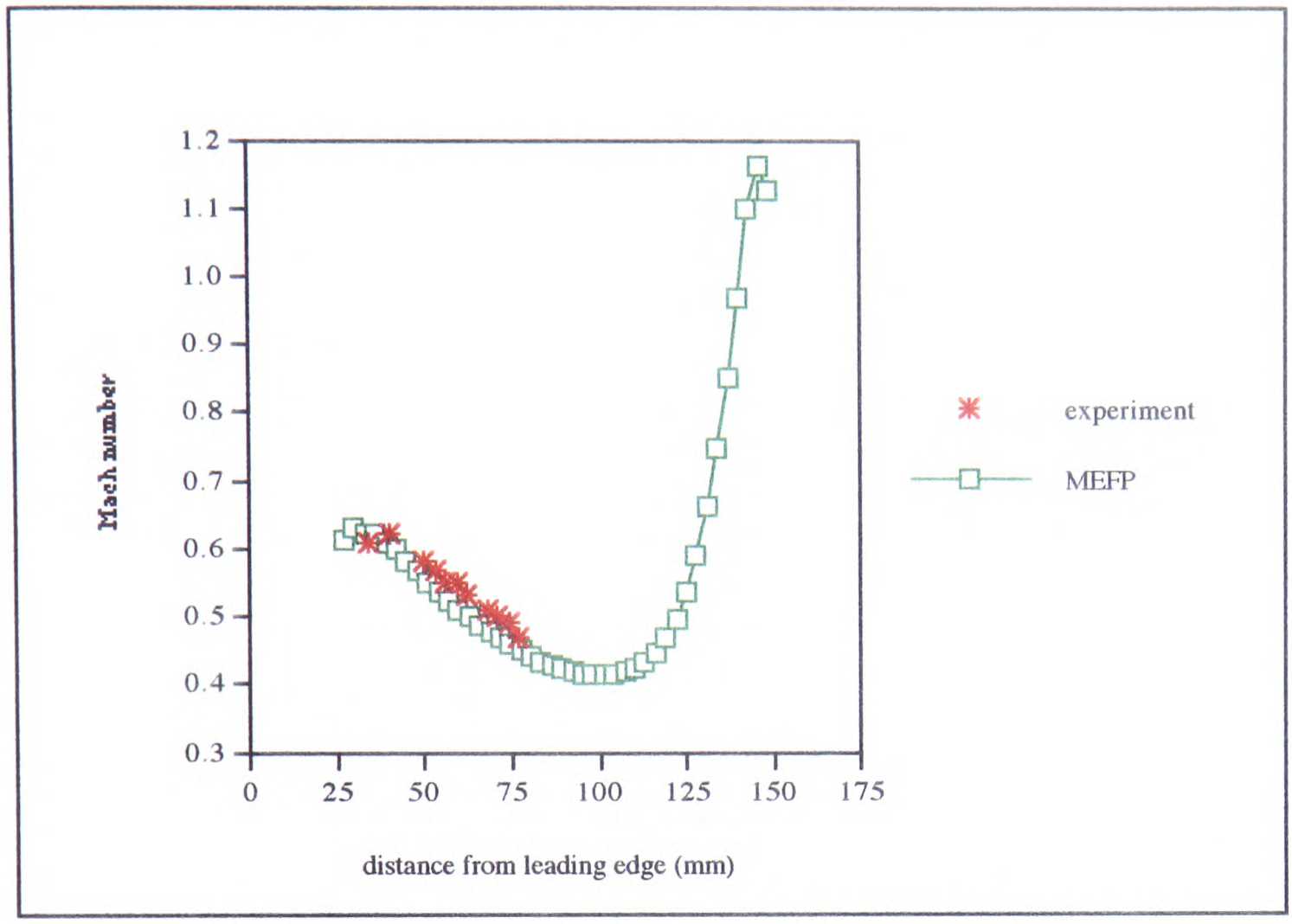
Graph 5.2 shows the isentropic Mach number data for the strong favourable test case. Once again, the agreement is very good. The point that shows the greatest discrepancy still predicts the Mach number to within Mach 0.0535. It would be expected that the slope in the strong favourable case would be steeper than the slope in the mild favourable case due to the greater acceleration that is needed in the flow to produce the stronger pressure gradient. This result is confirmed by comparing Graphs 5.1 and 5.2.



Graph 5.2 S.F.P.G. Isentropic Mach Number

Graph 5.3 shows the isentropic Mach number data for the mild adverse test case. It can be seen that the agreement between the experimental and MEFP results is very good in this case as well. The point that shows the greatest discrepancy still predicts the Mach number to within Mach 0.0391. An increase in the backpressure was also needed in all of the mild adverse test cases to ensure that the flow was choked at the throat. This plot serves as a means of confirming the gentle downward slope of

decreasing Mach number that would be expected from a plate that produces an adverse pressure gradient.



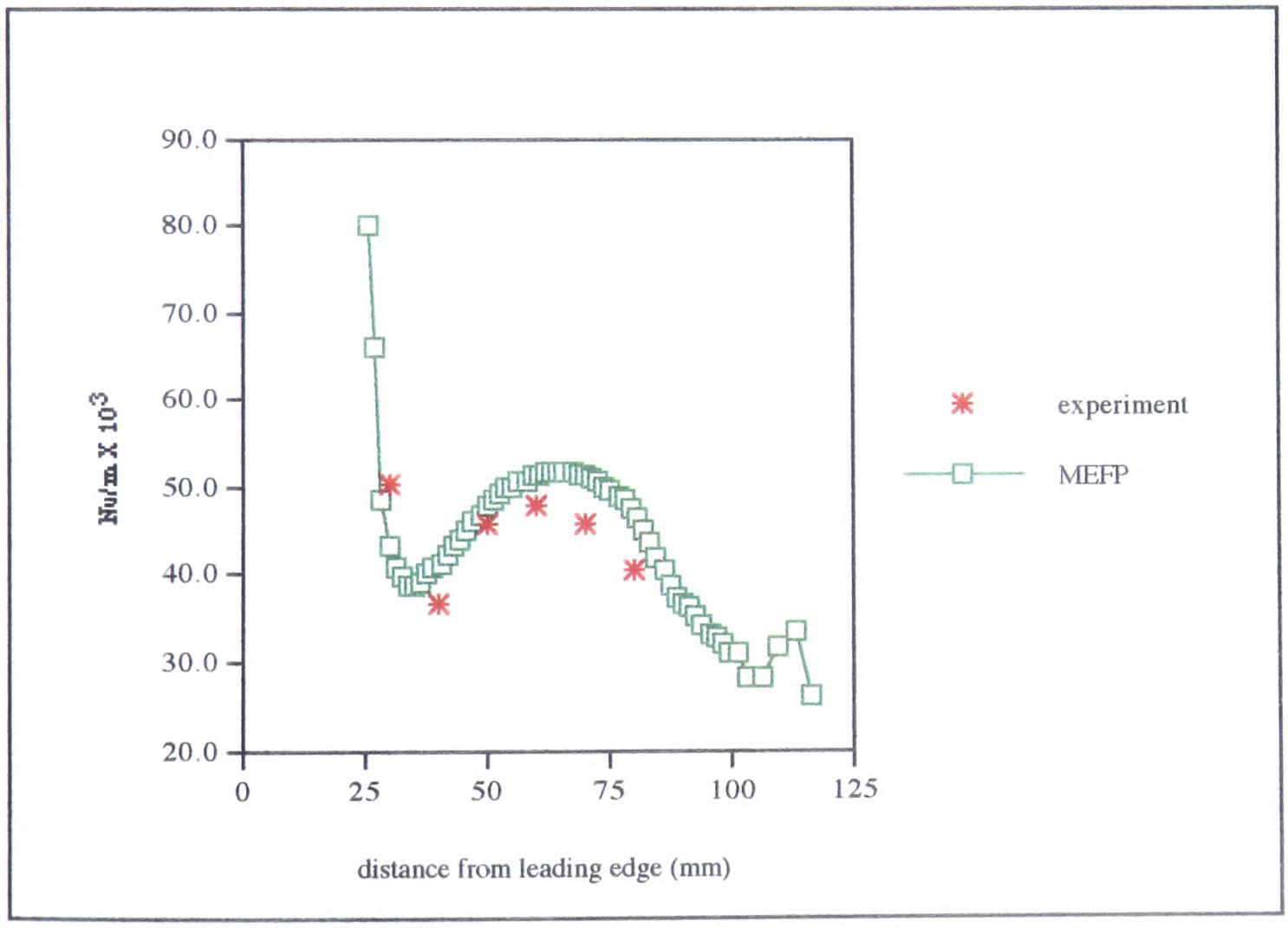
Graph 5.3 M.A.P.G. Isentropic Mach Number

5.2.2 Unblown Heat Transfer Results

Graph 5.4 shows the heat transfer data for the mild favourable case without coolant injection. The agreement between the MEFP data and the experimental data is acceptable. MEFP is certainly able to predict the correct trend in the Nusselt number, even if it does give a slight overestimation of the values particularly in the region from 60mm to 80mm downstream of the leading edge. The point that shows the greatest discrepancy still predicts the Nusselt number to within 11.8 percent of the experimental value. The high values of the Nusselt number at the outset are due to the fact that the computation is starting from the trip, where it is reasonable to assume that the boundary layer thickness will be at its smallest when compared to all other points downstream. The Nusselt number is highest in the region of the throat (around 60mm to 70mm

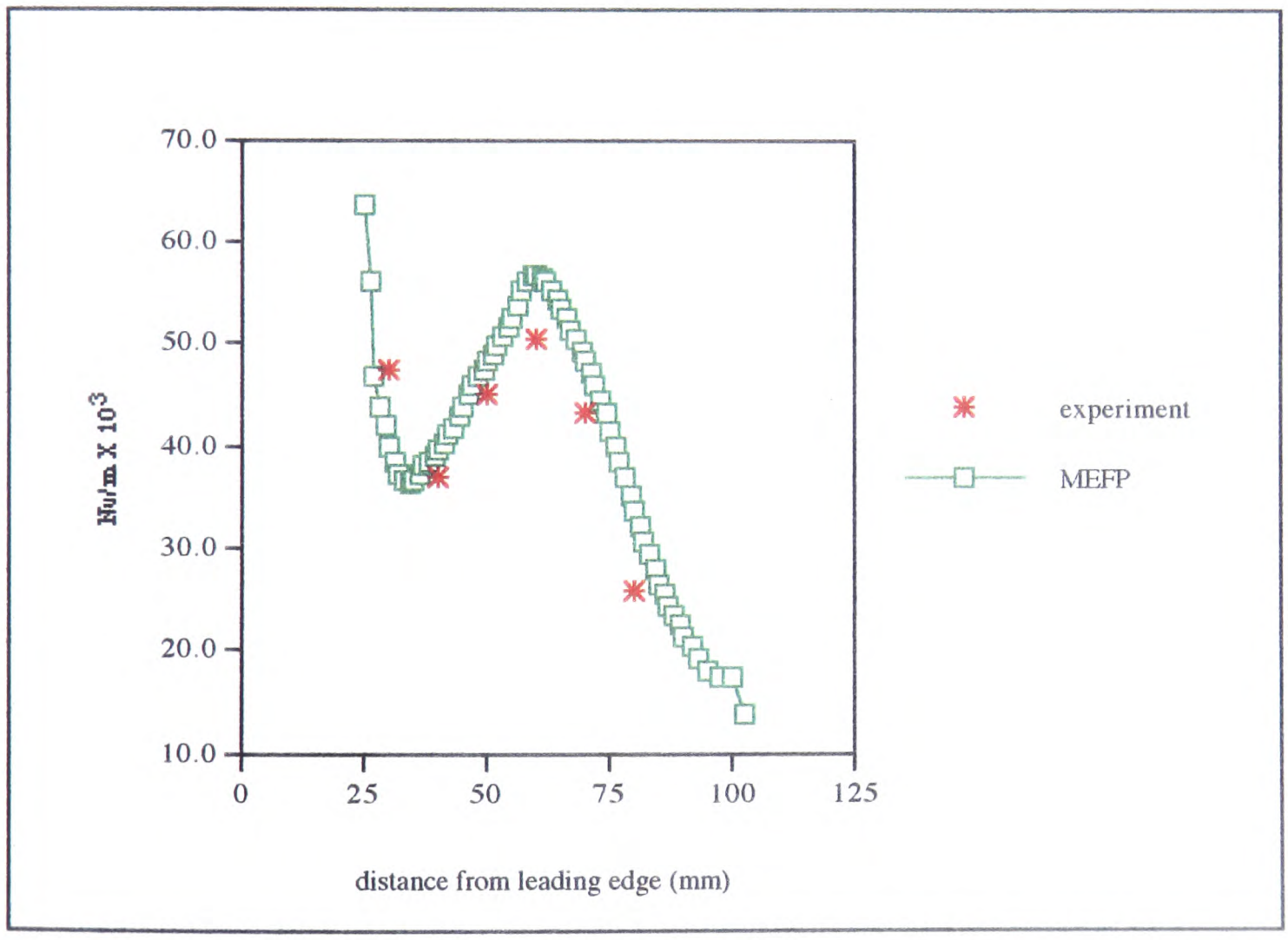
downstream of the leading edge). In the region beyond the throat, the Nusselt number decreases because the flow is supersonic.

Different techniques were employed throughout the prediction process to ensure that MEFP was able to correctly calculate the relevant parameters. For instance, near wall grid refinement was employed in this test case in order to better resolve the flow in the boundary layer, and to hopefully give better agreement. This did give limited improvement in the agreement between the MEFP results and the experimental results by approximately two percent in the regions that are either far upstream or far downstream of injection, and six percent in regions that are in the middle of the computational domain. While this did not change the results drastically, it can be said that it brought the agreement to within acceptable limits. Increased under-relaxation from 0.5 to 0.3 was also needed to eliminate some oscillatory behavior in the convergence data. This technique was described in an earlier section.



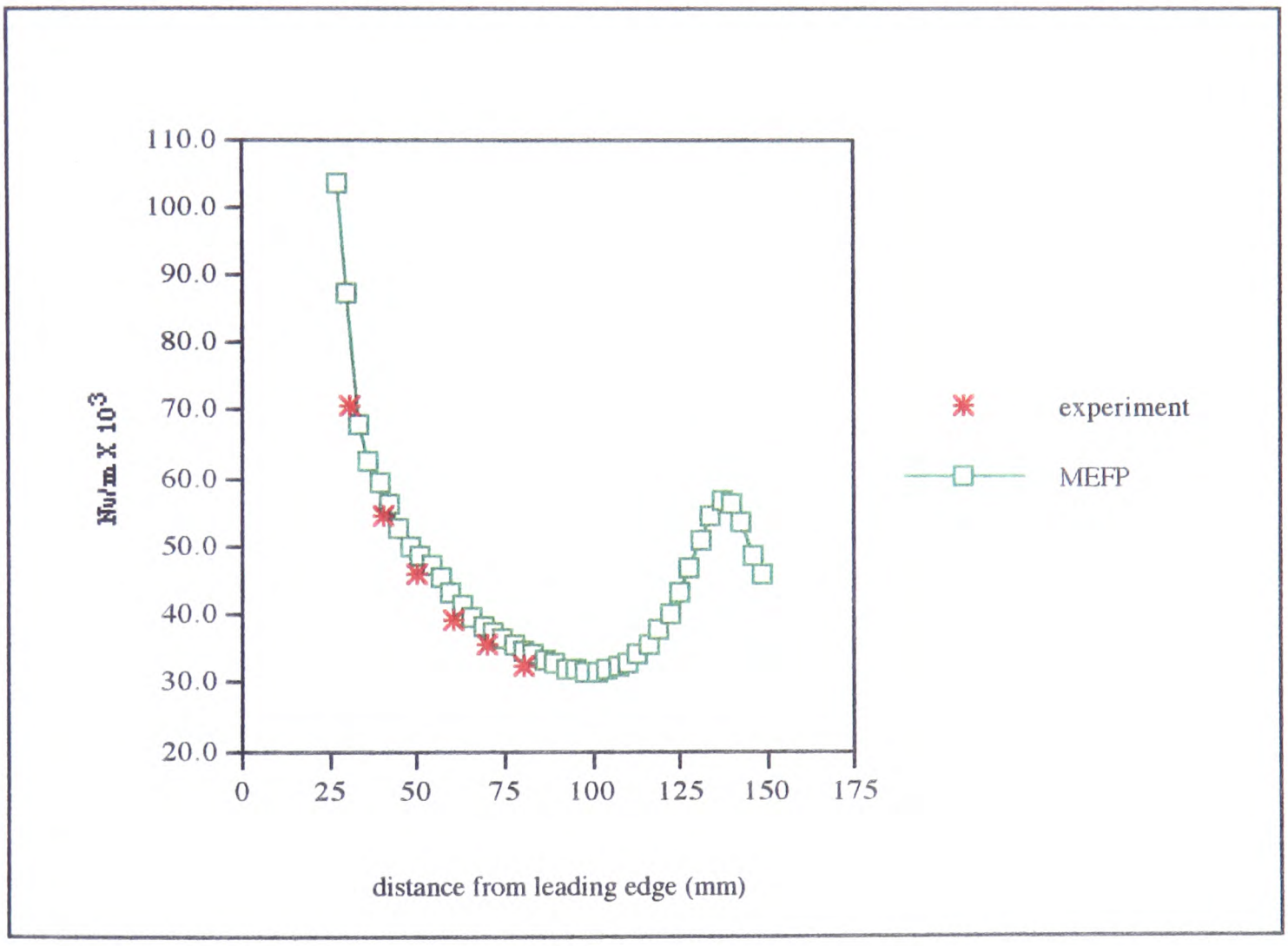
Graph 5.4 M.F.P.G. Heat Transfer

Graph 5.5 shows the heat transfer data for the strong favourable case without coolant injection. The agreement is very good, and the predicted trend is obviously correct. The MEFP results show only a slight overestimation of the Nusselt number in comparison with the experimental results. The point that shows the greatest discrepancy of 10.9 percent is 60mm downstream of the leading edge in the throat region. If this graph is compared with the graph for the mild favourable heat transfer, it can be seen that the peak value for the strong favourable case corresponds to higher value of Nusselt number (56.7 X 10^3 for the strong favourable case versus 51.7 X 10^3 for the mild favourable case). This is in fact, the expected outcome. Once again it can be said that the high values of the Nusselt number at the outset are due to the fact that the computation is starting from the trip. The values are highest in the region of the throat (around 60mm downstream of the leading edge) and then decrease when the flow becomes supersonic.



Graph 5.5 S.F.P.G._data1 Heat Transfer

Graph 5.6 shows the heat transfer data for the mild adverse case without coolant injection. The agreement is very good, and the predicted trend is obviously correct. The MEFP results show only a slight overestimation of the Nusselt number in comparison with the experimental results. In fact, the point that shows the greatest discrepancy is only 3.2 percent higher than the experimental value. The result shown in the graph can be explained by noting that the high values of Nusselt number at the outset are due to the fact that the computation is starting from the trip. The Nusselt number then "decreases monotonically", due to the combined effects of the boundary layer growth in the downstream direction, and the deceleration in the flow that the plate produces.



Graph 5.6 M.A.P.G._data1 Heat Transfer

5.2.3 Film Cooled Heat Transfer Results

The results that are presented in this section consist of all the film cooled ILPT test runs that were examined in this analysis. The results were collected at two different pressure gradients, two different temperature ratios, and numerous injection rates.

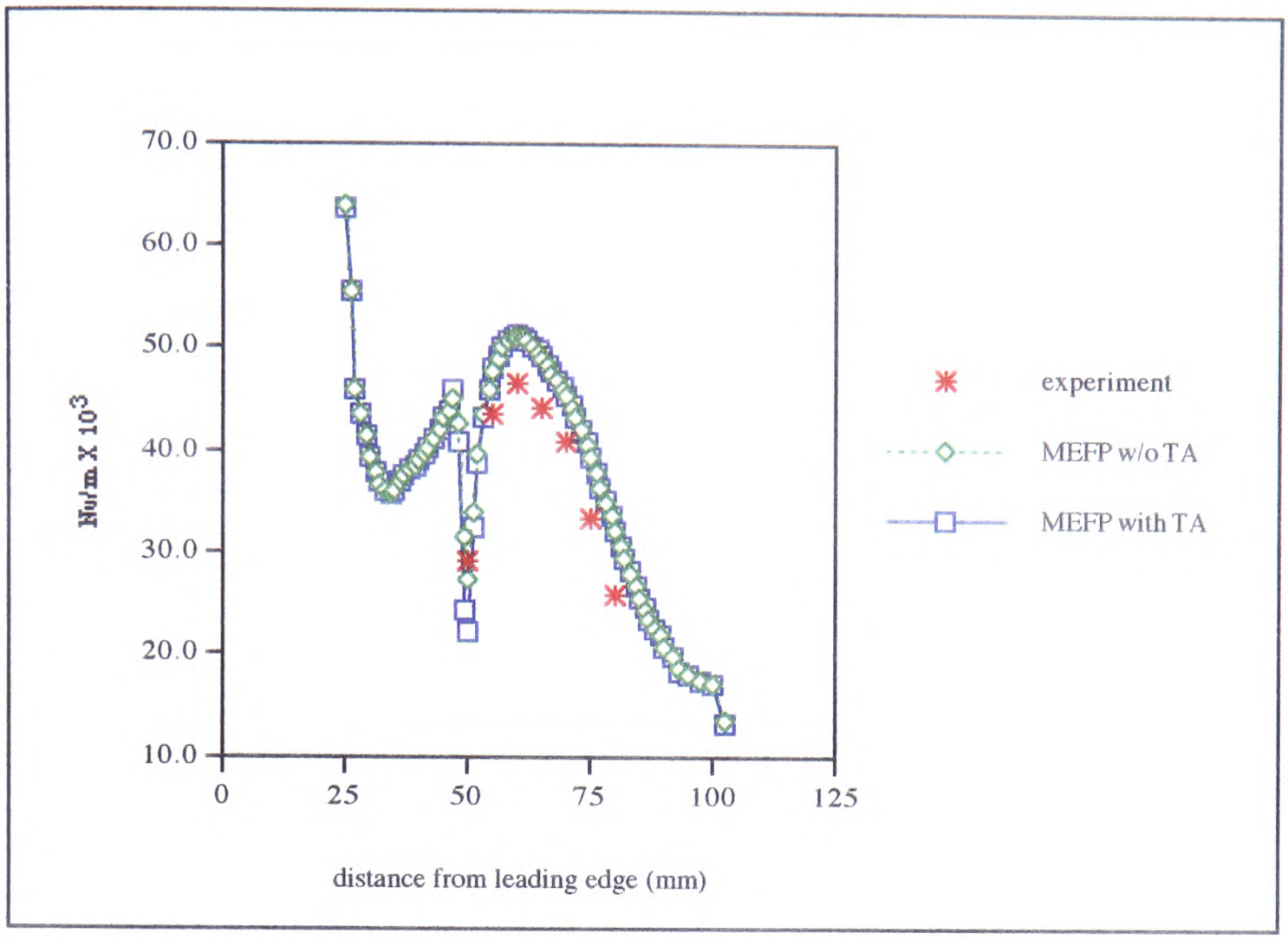
Where possible, the data that are shown here clearly illustrate the improvement that was achieved in the predictions using the improved film cooling model in comparison with the initial film cooling model and the experimental results. Where there is one set of MEFP data, it is the initial prediction that is depicted before any improvements were carried out. Where there are two sets of MEFP data, the initial prediction is designated "w/o TA" or without turbulence augmentation. The prediction that uses the improved film cooling model is designated "w/TA" or with turbulence augmentation. This simply means that the improved film cooling model includes an estimation of the turbulence augmentation due to the coolant injection, a realistic turbulence decay, and an improved distribution of the coolant flow at injection. The changes that were made in the development and improvement of the film cooling model will be discussed in detail in future chapters.

5.2.3.1 STRONG FAVOURABLE RESULTS

Graph 5.7 shows the heat transfer data for a strong favourable case with coolant injection (G=0.15, TR=0.82). It can be seen that the agreement is very good, and that the predicted trend is obviously correct. In this case, it is clear that the point of injection is around 50mm downstream of the leading edge. This is the point where the Nusselt number decreases drastically (40.9 percent local decrease). The MEFP results also show a slight overestimation of the Nusselt number downstream of the coolant injection in comparison with the experimental results. The point that shows the greatest discrepancy of 9.5 percent is 60mm downstream of the leading edge, but all of the other points show much better agreement.

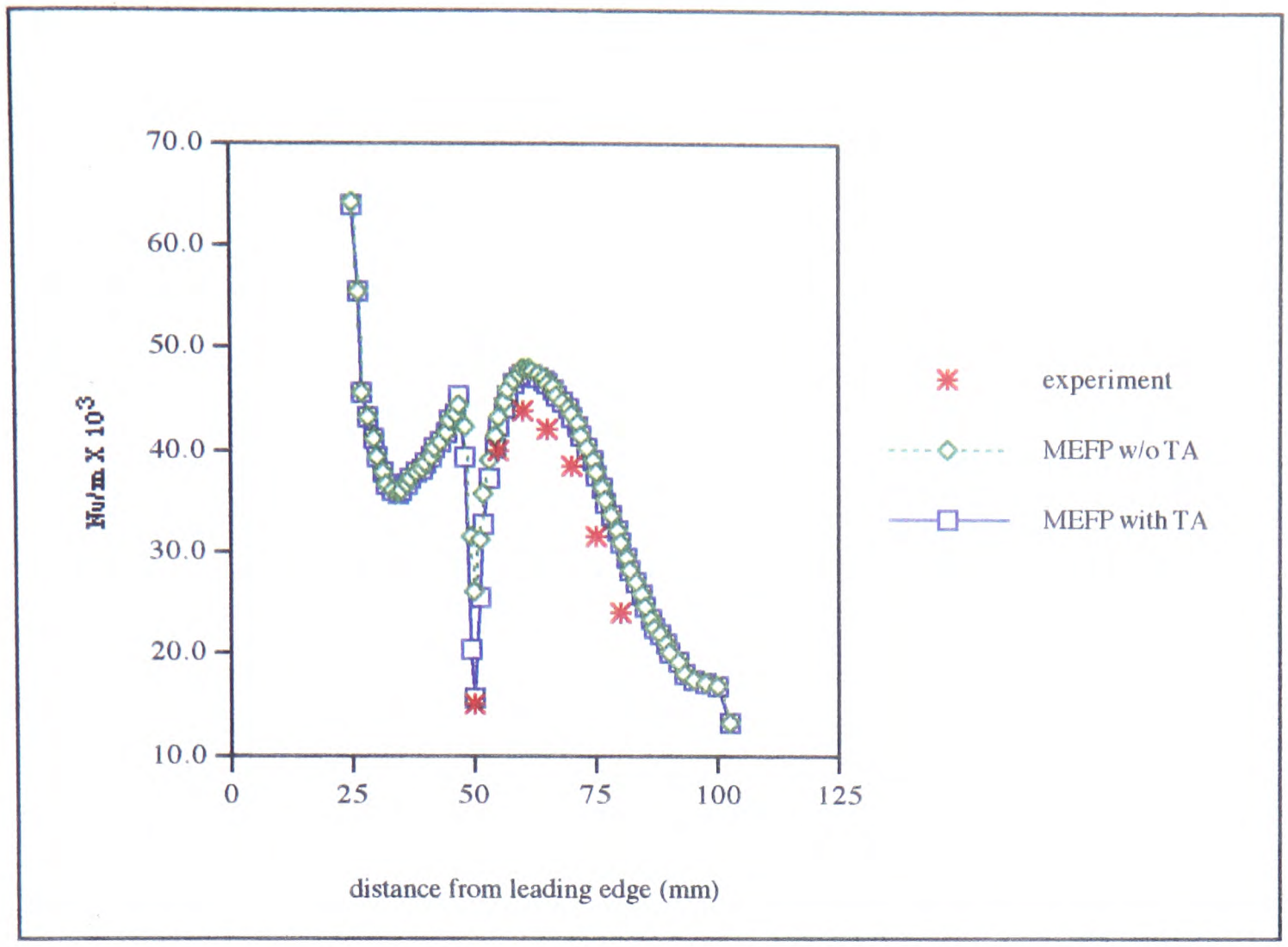
This is one of the datasets that was looked at in the development and improvement of the film cooling model that is described in detail in the next chapter. The original prediction of the Nusselt number at the injection point is more accurate than the "improved" prediction with the addition of turbulence augmentation. A reason for this may be because this is a test case with a low injection rate. Most of the improvements that were made to the film cooling model are better suited to a higher

injection rate where the flow is more disturbed by the coolant injection. The coolant flow at this injection rate would make no significant change to the turbulence level at the injection point. Therefore, a prediction, such as the original one, that does not include the effects of increased turbulence would generate more accurate results.



Graph 5.7 S.F.P.G._data2 Heat Transfer

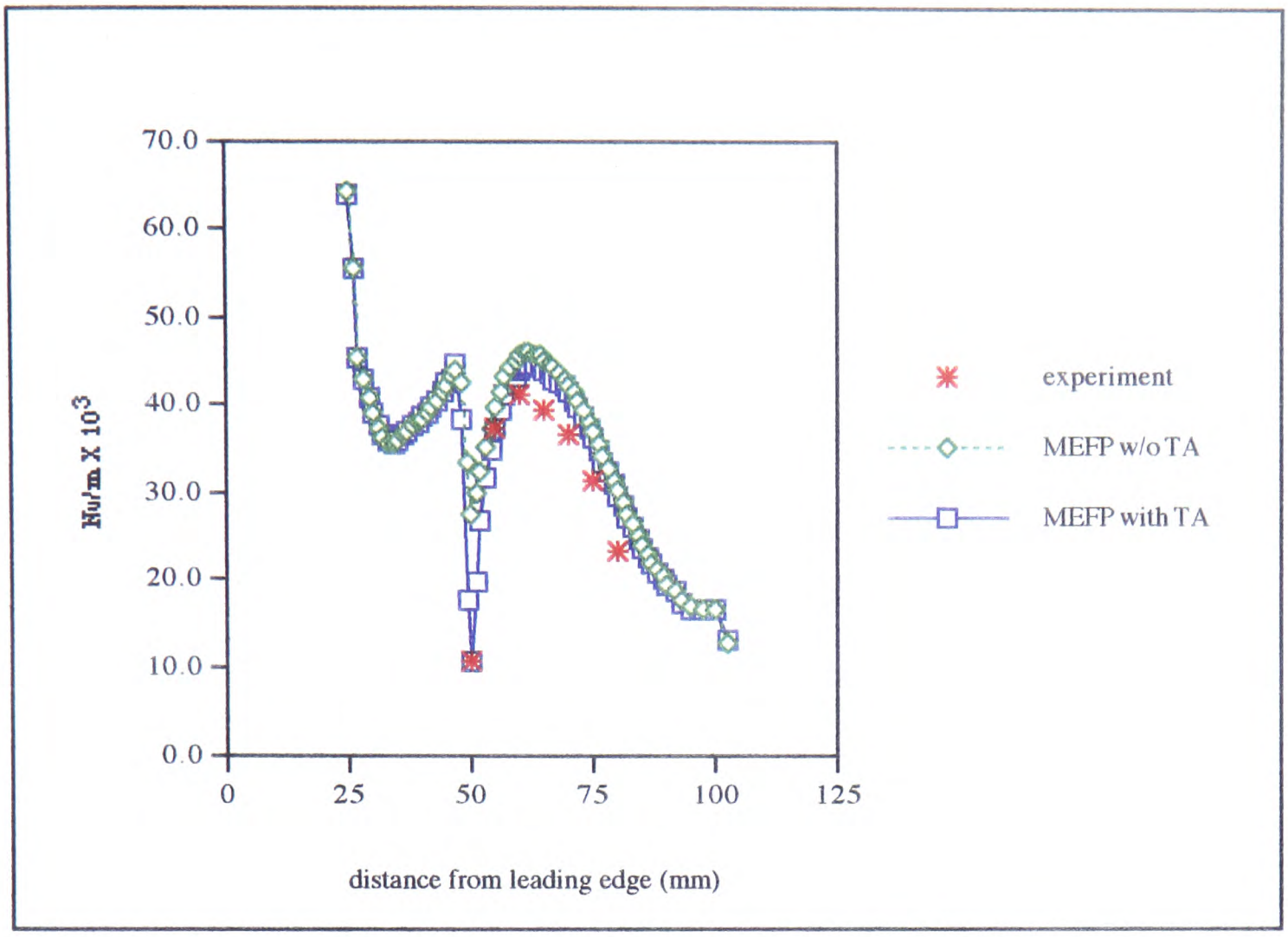
Graph 5.8 shows the heat transfer data for a strong favourable case with coolant injection (G=0.25, TR=0.82). Once again, it can be seen that the agreement is very good, and that the predicted trend is correct. At the point of coolant injection, MEFP predicts that there is a 42.5 percent local decrease in the Nusselt number. The injection point was predicted much more accurately when turbulence augmentation was included than in the previous case because this test case exhibits a higher injection rate. The MEFP results also show a slight overestimation of the Nusselt number downstream of the coolant injection in comparison with the experimental results. The point that shows the greatest discrepancy is only 7.5 percent higher than the experimental value.



Graph 5.8 S.F.P.G._data3 Heat Transfer

Graph 5.9 shows the heat transfer data for a strong favourable case with coolant injection (G=0.35, TR=0.82). Once again, it can be seen that the agreement is good, and that the predicted trend is correct. At the point of coolant injection, MEFP predicts that there is a 38.0 percent local decrease in the Nusselt number. The MEFP prediction at the injection point corresponds exactly to that of the experimental data when the effects of the increased turbulence from the injected flow are included. The MEFP results show an overestimation of the Nusselt number downstream of the coolant injection in comparison with the experimental results in this case as well. It is at this injection rate that the "improved" film cooling model begins to give a more accurate representation of the Nusselt number in the downstream direction as well as at the injection point. The reason for this will be given in the next chapter when the improvements to the film cooling model are examined in detail. The point that shows the greatest discrepancy in the original prediction is 9.1 percent higher than the

experimental value, but with the improved prediction, the greatest discrepancy is only 7.9 percent higher than the experimental value.

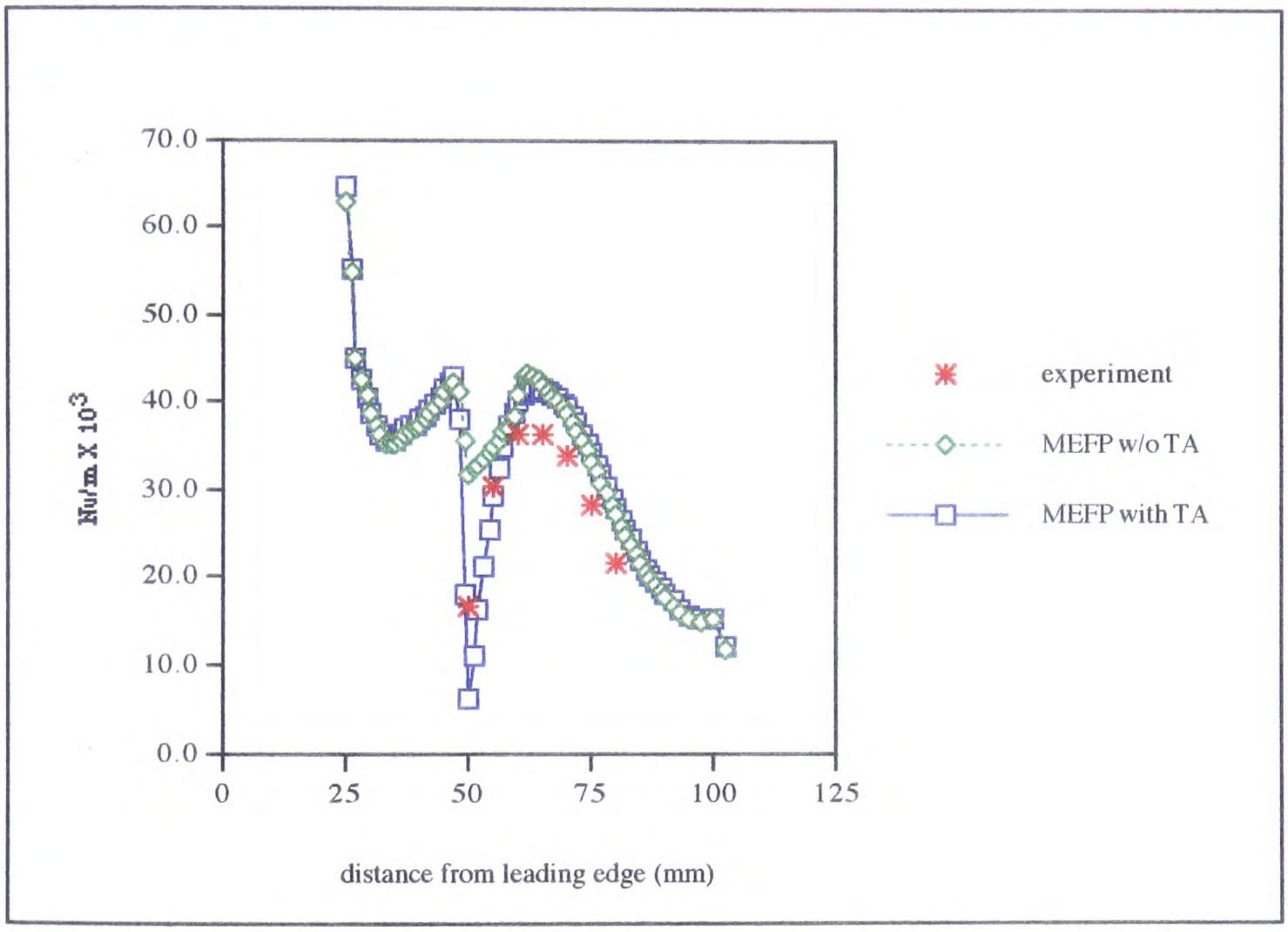


Graph 5.9 S.F.P.G._data4 Heat Transfer

It will now be shown that the concern that was expressed at the time of the initial exposure to the code concerning the higher injection rates was completely unfounded. It was determined at an early stage that the code was able to deal with what could be characterized as strong injection rates. Therefore, this was an area that never had to be addressed in the development and improvement of the film cooling model. Once again, comparisons are made between Teekaram's experimental heat transfer data and the predictions from MEFP.

Graph 5.10 shows the heat transfer data for a strong favourable case with coolant injection (G=0.59, TR=0.82). It can be seen that the agreement is reasonable. The predicted trend is correct, except in the area of the throat where MEFP overpredicts the value of the Nusselt number regardless of whether the initial film cooling model or the "improved" film cooling model was used. In the neighbourhood of the film cooling

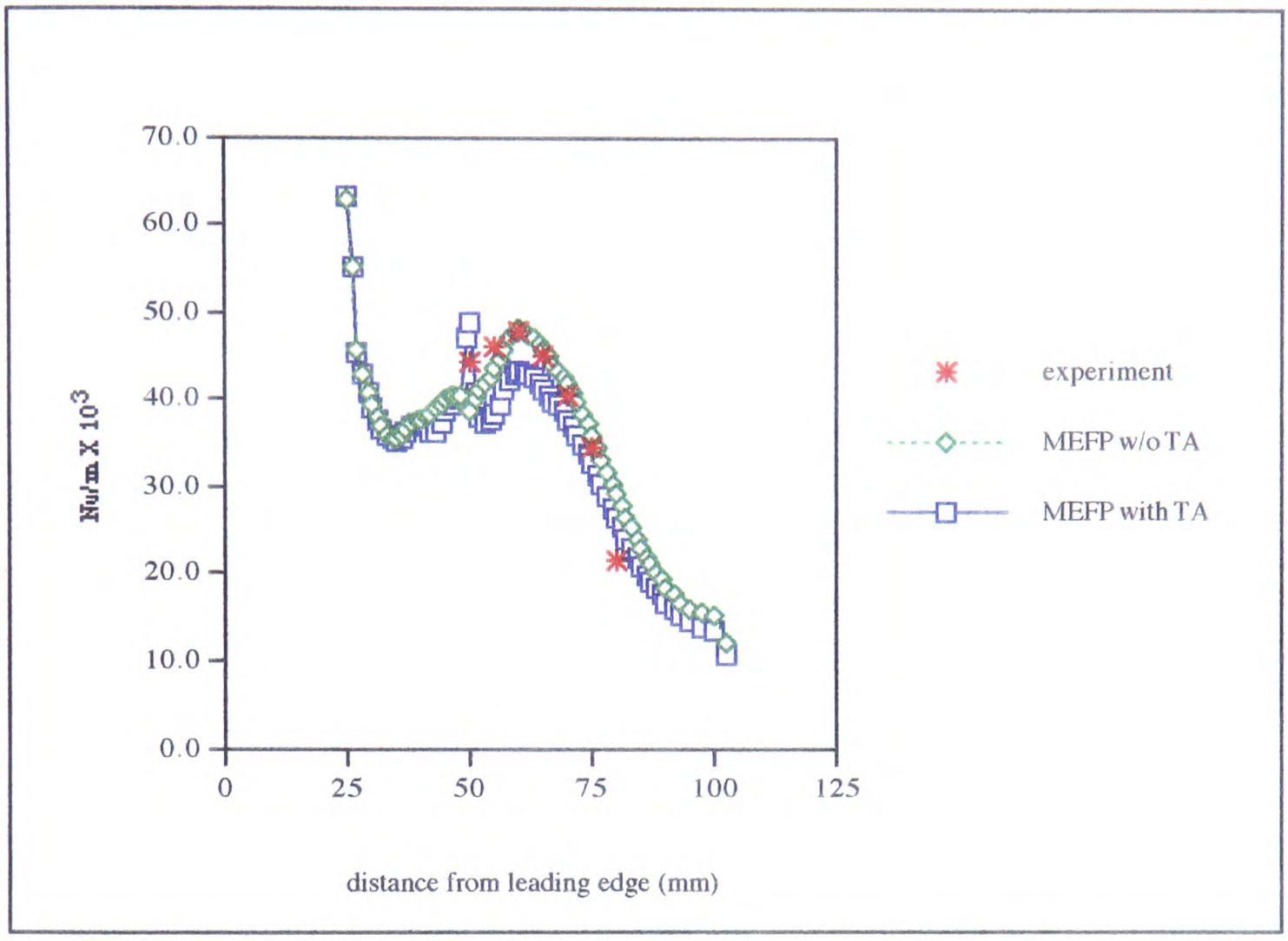
hole neither film cooling model was able to generate accurate results. It is interesting to note that the results that are depicted on this graph, which can be characterized as a strong injection rate, look slightly different from the graphs that were previously presented with the weak injection rates. In the region downstream of the cooling hole, it can be seen that the Nusselt number is noticeably and consistently lower in this case than in the previous cases. This can be explained by considering the effects of the separation or the "lifting off" of the coolant jet at the injection point with a reattachment of the coolant jet at some point downstream of the cooling hole. In other words, the coolant flow is now being slightly more effective farther downstream of the cooling hole(s), as opposed to directly beyond the cooling hole(s).



Graph 5.10 S.F.P.G._data8 Heat Transfer

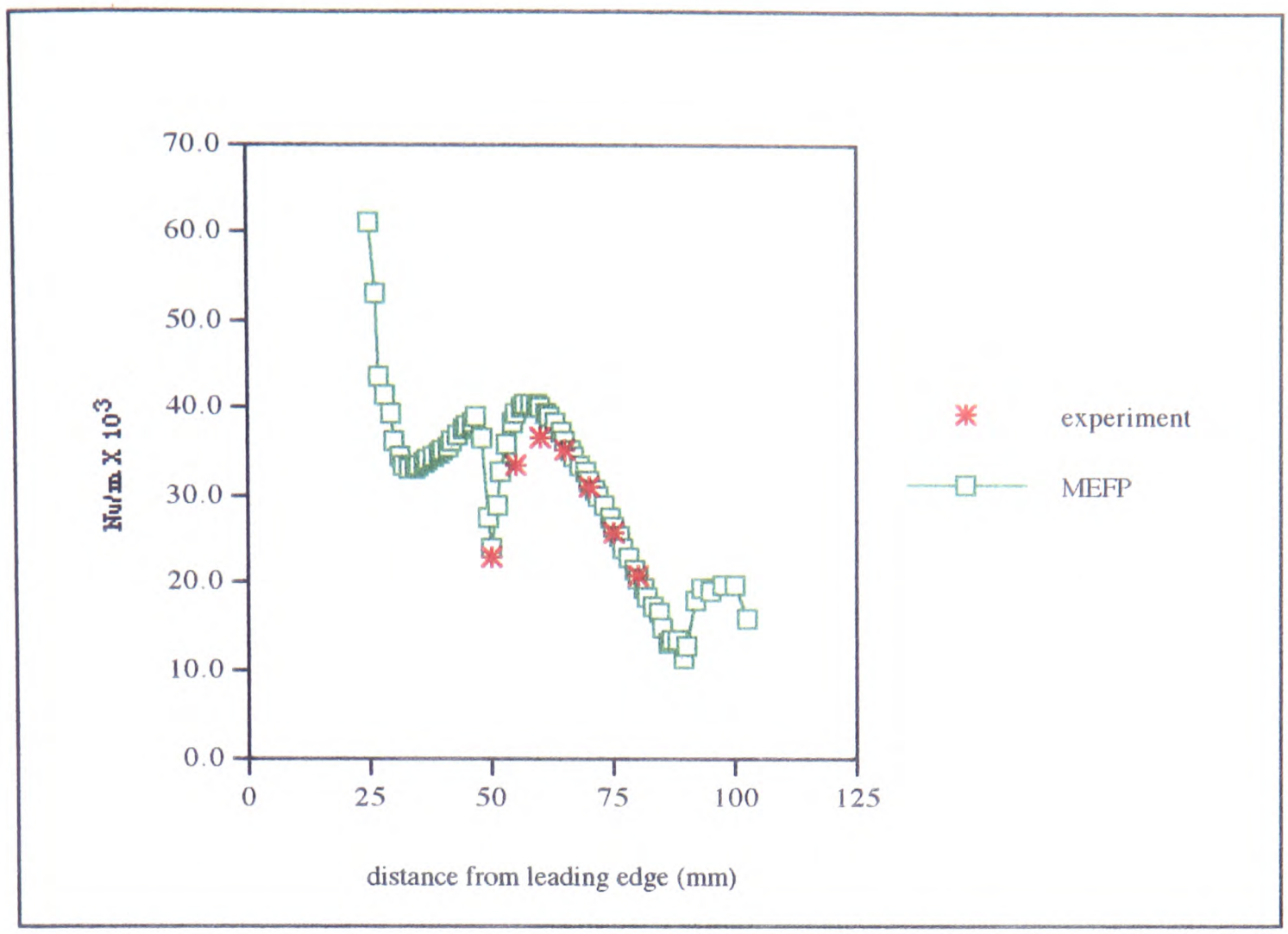
Graph 5.11 shows the heat transfer data for a strong favourable case with coolant injection (G=1.20, TR=0.82). The predicted trend is correct, and the agreement that is achieved with the initial film cooling model appears to be better in some areas than the agreement achieved with the improved film cooling model. It can be seen that

there is no local decrease in the Nusselt number directly after the film cooling hole, rather there is a slight increase in the Nusselt number. This increase is caused by the turbulence that the separated coolant flow generates in the neighbourhood of the cooling hole(s). The Nusselt number then decreases downstream of the cooling hole(s). This result can be explained by considering the effects of the coolant jet separating from the surface beyond the cooling hole and reattaching at a later point downstream.



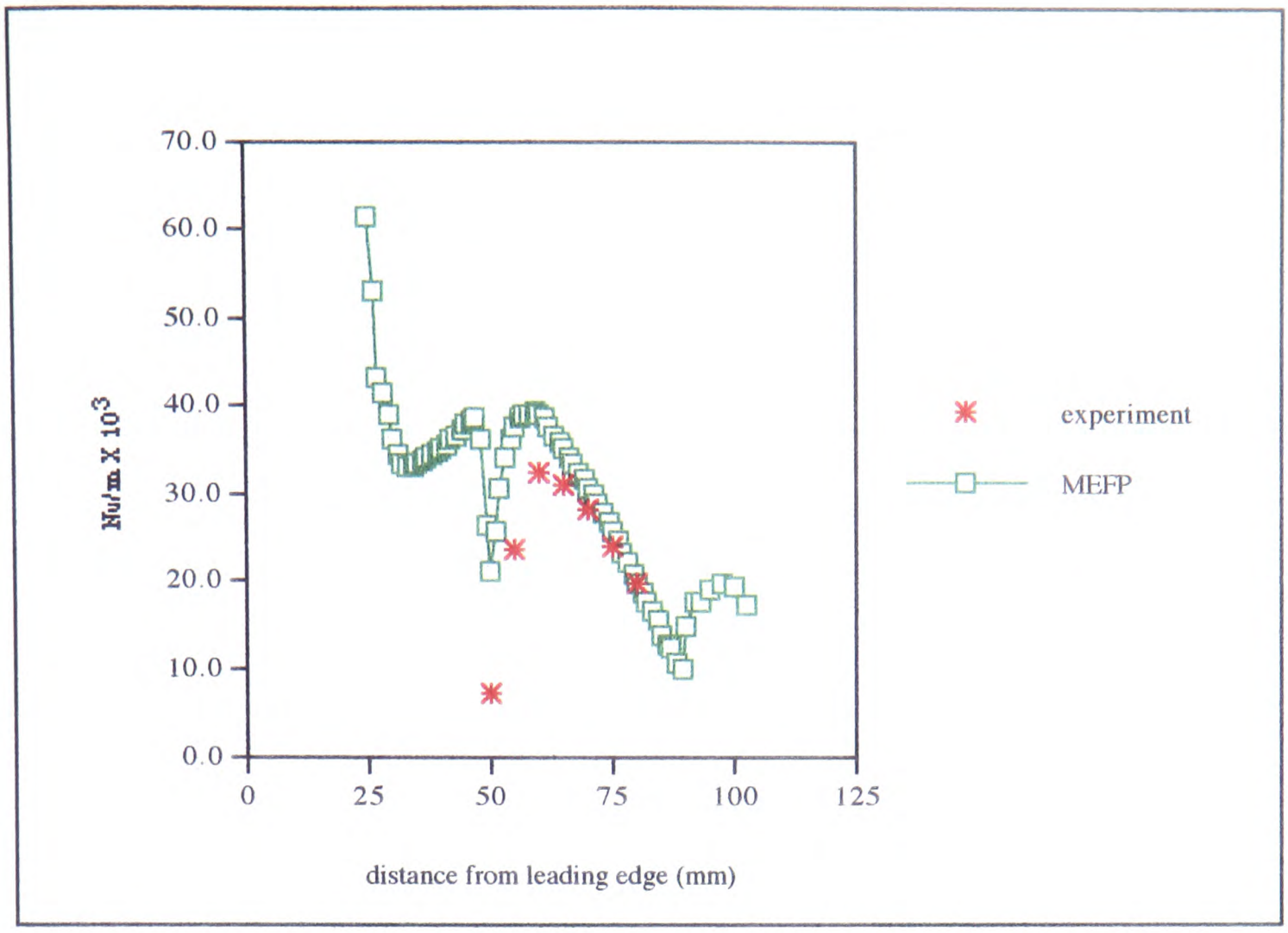
Graph 5.11 S.F.P.G._data10 Heat Transfer

Graph 5.12 shows the heat transfer data for a strong favourable case with coolant injection (G=0.11, TR=1.21). The agreement is still consistently good, and MEFP is able to correctly predict the trend in the Nusselt number. At the point of coolant injection, the prediction is quite accurate and there is a 42.3 percent local decrease in the Nusselt number. The point that shows the greatest discrepancy in this test case is 60mm downstream of the leading edge and is 4.7 percent higher than the experimental value.



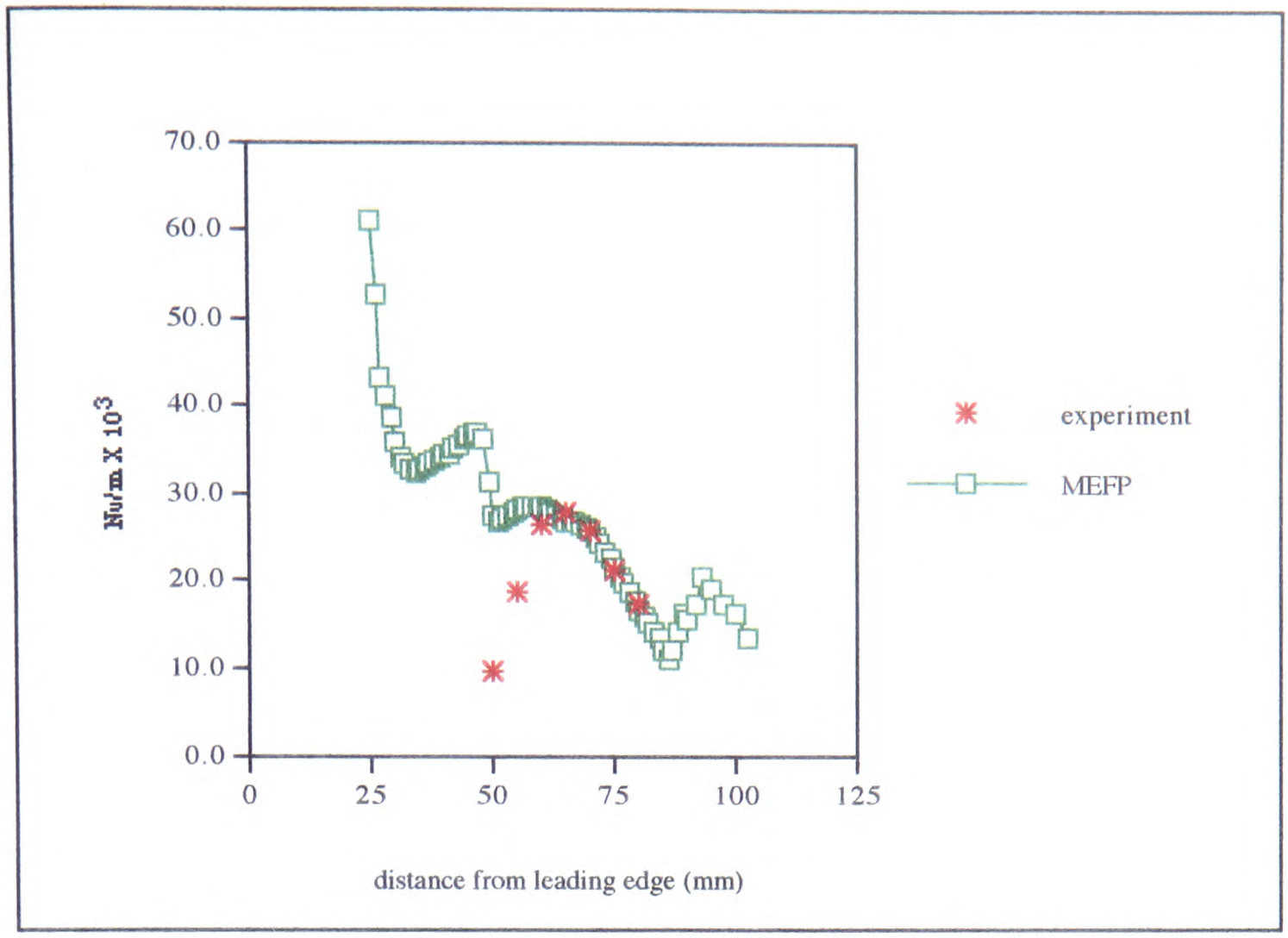
Graph 5.12 S.F.P.G._data5 Heat Transfer

Graph 5.13 shows the heat transfer data for a strong favourable case with coolant injection (G=0.18, TR=1.21). The trend in the Nusselt number is still predicted reasonably well. However, at the point of coolant injection, the code does not predict the value for the Nusselt number accurately. This would suggest that the highly three-dimensional nature of flow near the point of injection begins to effect the predictions at a lower injection rate at the temperature ratio of 1.21, than for the temperature ratio of 0.82. The point that shows the greatest downstream discrepancy in this test case is located 60mm downstream of the leading edge and is 19.5 percent higher than the experimental value.



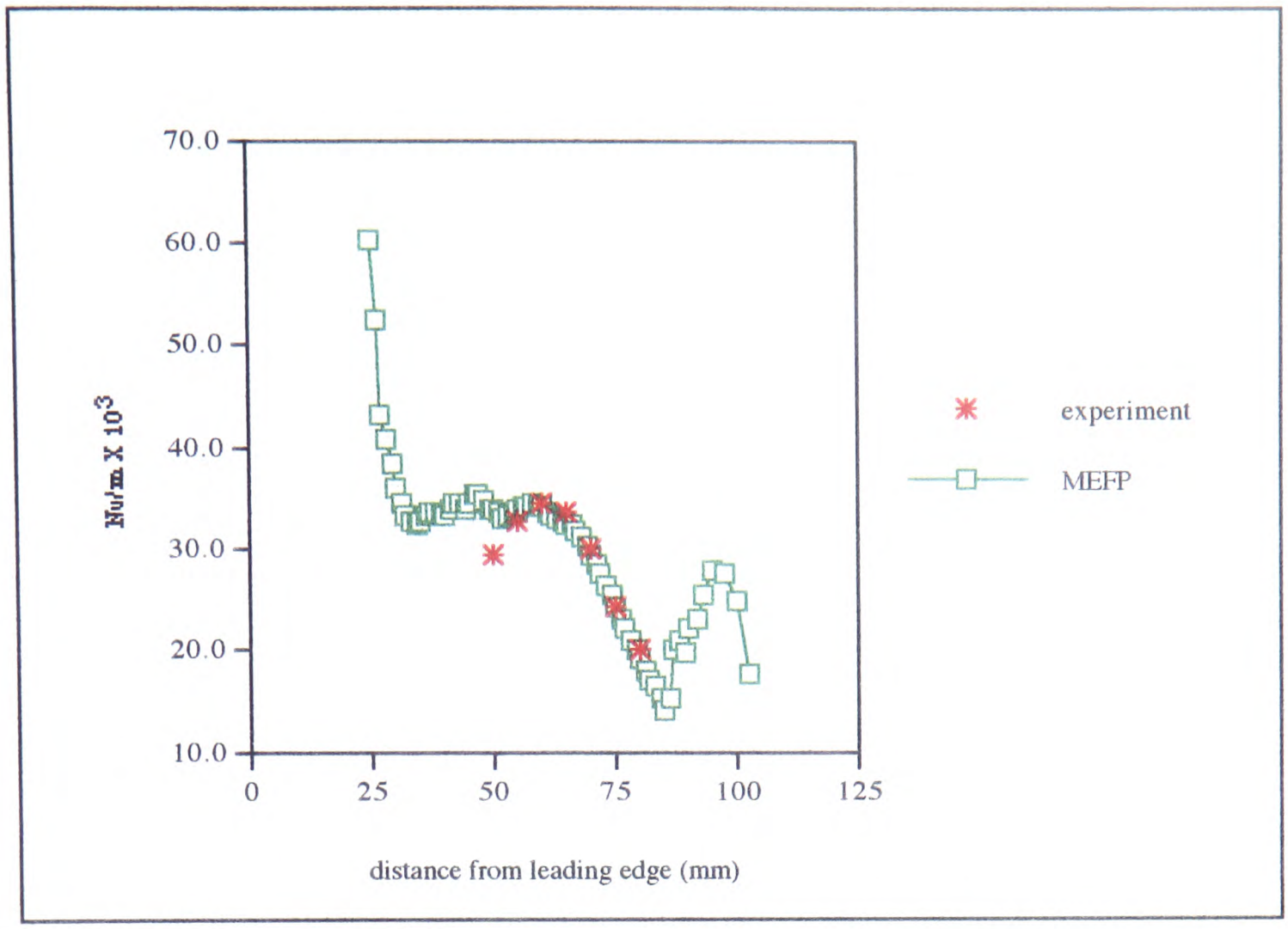
Graph 5.13 S.F.P.G._data6 Heat Transfer

Graph 5.14 shows the heat transfer data for a strong favourable case with coolant injection (G=0.42, TR=1.21). The agreement and the predicted trend are only accurate from the point that is 60mm downstream of the leading edge in the area of the throat. In the neighbourhood of the film cooling hole, MEFP does not correctly predict the cooling effect of injection. It is interesting to note that the experimental values of the Nusselt number downstream of the point of injection are lower than those found in the previous two plots. MEFP has also begun to predict the early signs of coolant jet separation.



Graph 5.14 S.F.P.G._data11 Heat Transfer

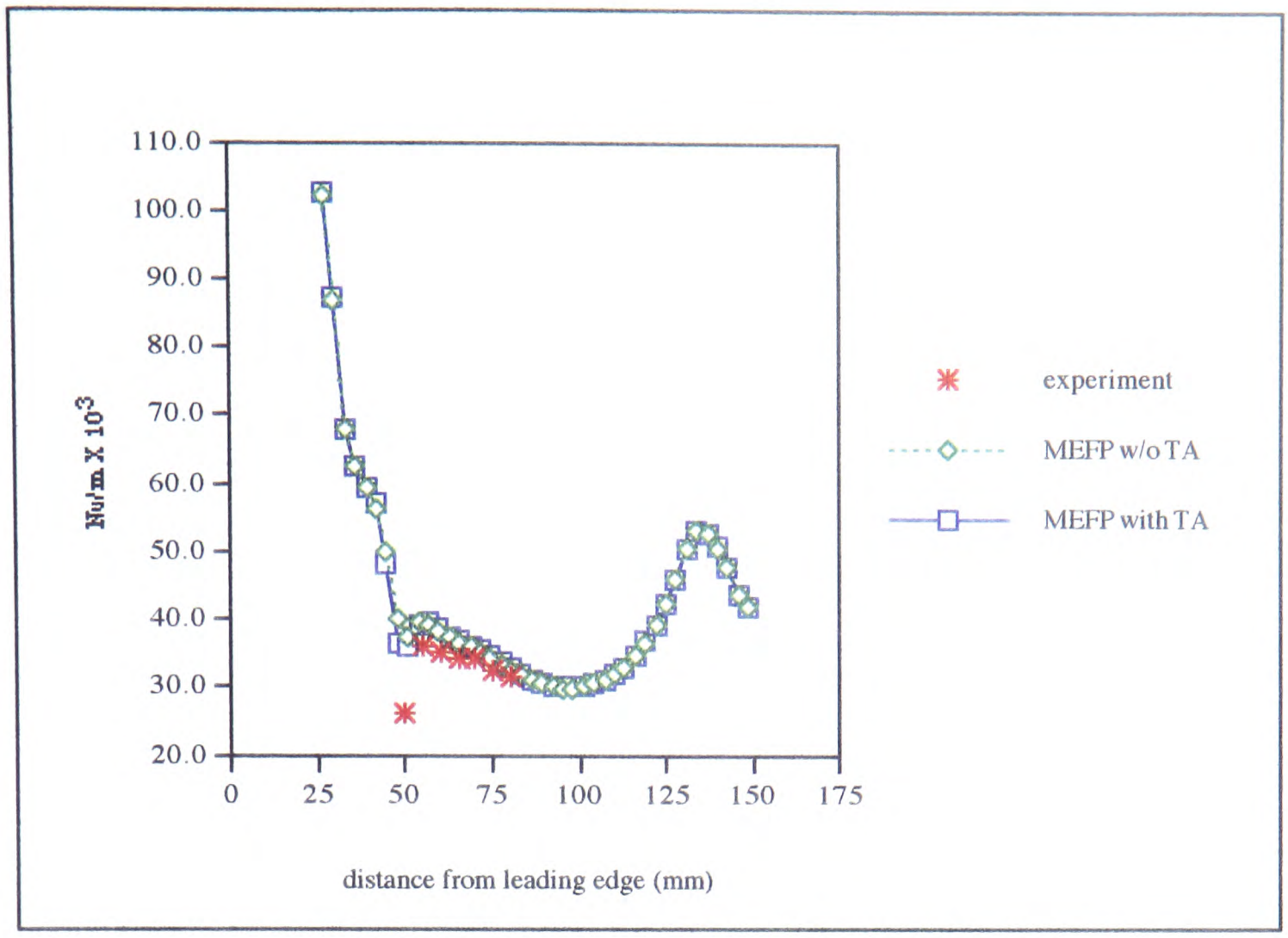
Graph 5.15 shows the heat transfer data for a strong favourable case with coolant injection (G=0.81, TR=1.21). It can be seen that the agreement is very good, and that the predicted trend is correct. The predictions are obviously much better than in the previous case with the lower injection rate. This is particularly true directly after the point at which separation is to occur. In fact, the point that shows the greatest discrepancy is only 10.7 percent higher than the experimental value. The fact that there is almost no local decrease in the Nusselt number at the point of injection would indicate that separation has occurred in this test case.



Graph 5.15 S.F.P.G._data13 Heat Transfer

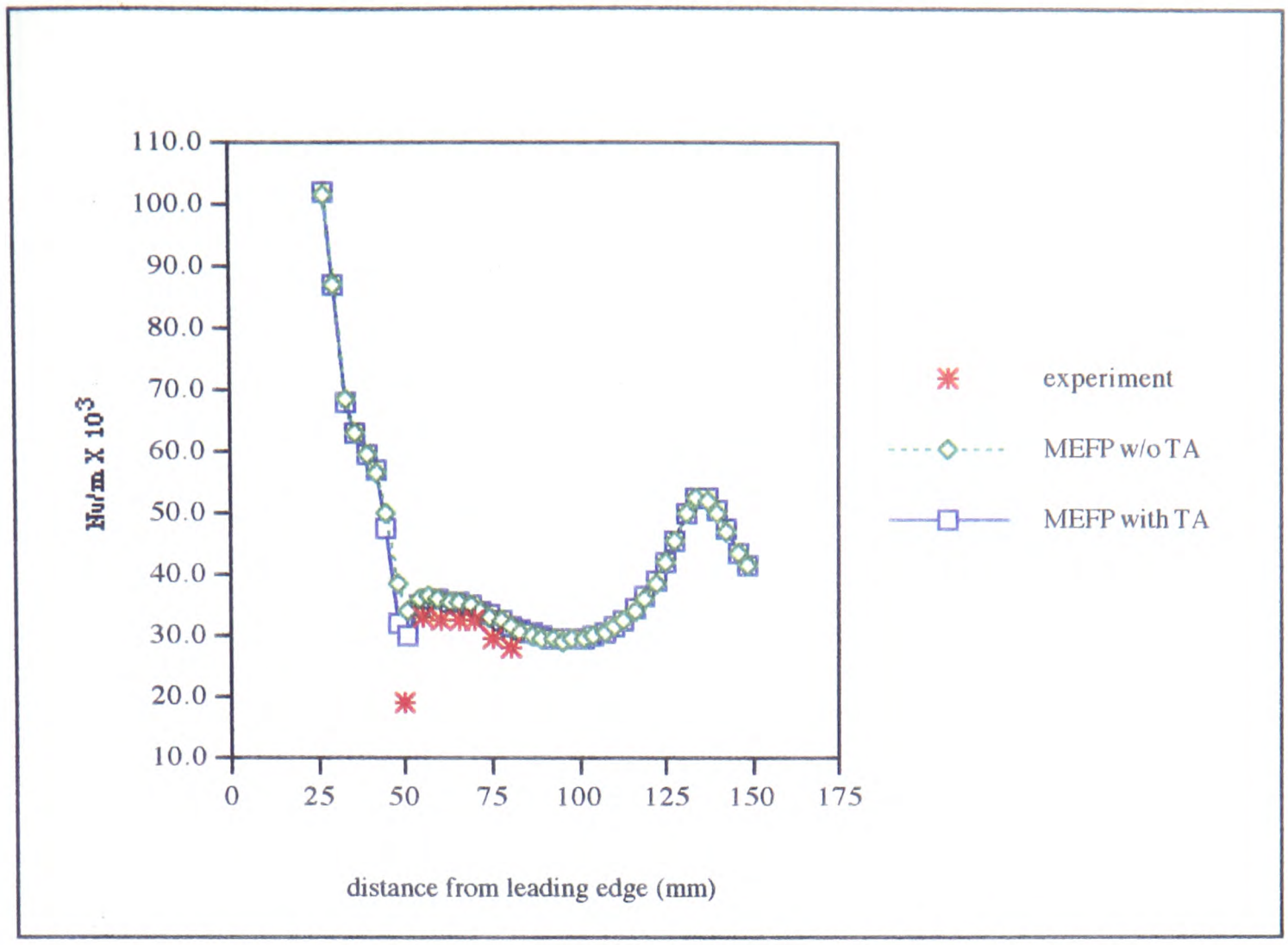
5.2.3.2 Mild Adverse Results

Graph 5.16 shows the heat transfer data for a mild adverse case with coolant injection (G=0.15, TR=0.82). It can be seen that the agreement is good, and that the predicted trend is correct. The agreement at the point of injection is not very good, even when the improved film cooling model is implemented. It can be seen that it is more difficult to determine the local reduction of the Nusselt number due to injection for the mild adverse case than for the strong favourable case at comparable injection rates. There is no large, drastic reduction in the neighbourhood of the film cooling hole, as was seen previously. The MEFP results show a very slight overestimation of the Nusselt number downstream of the coolant injection in comparison with the experimental results. This effect is very minor as the point that shows the greatest discrepancy is only 6.1 percent higher than the experimental value.



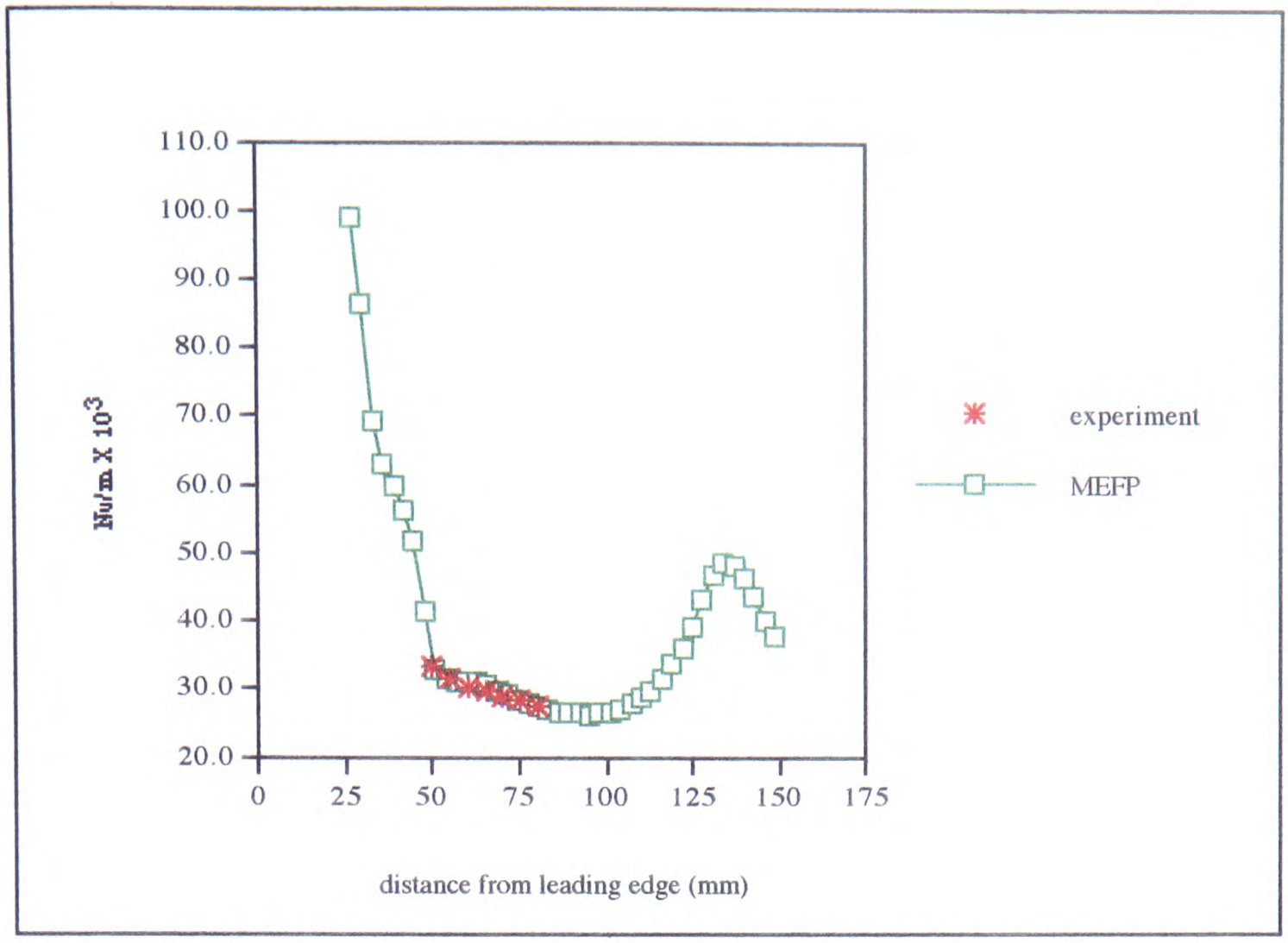
Graph 5.16 M.A.P.G._data2 Heat Transfer

Graph 5.17 shows the heat transfer data for a mild adverse case with coolant injection (G=0.25, TR=0.82). It can be seen that the agreement is good, and that the predicted trend is correct. The agreement at the point of injection is not very good in this case either. However, it can be seen that the improved film cooling model improves the prediction at this point slightly more than it did in the previous test case. The MEFP results show a slight overestimation of the Nusselt number downstream of the coolant injection in comparison with the experimental results. The point that shows the greatest discrepancy is 9.1 percent higher than the experimental value.



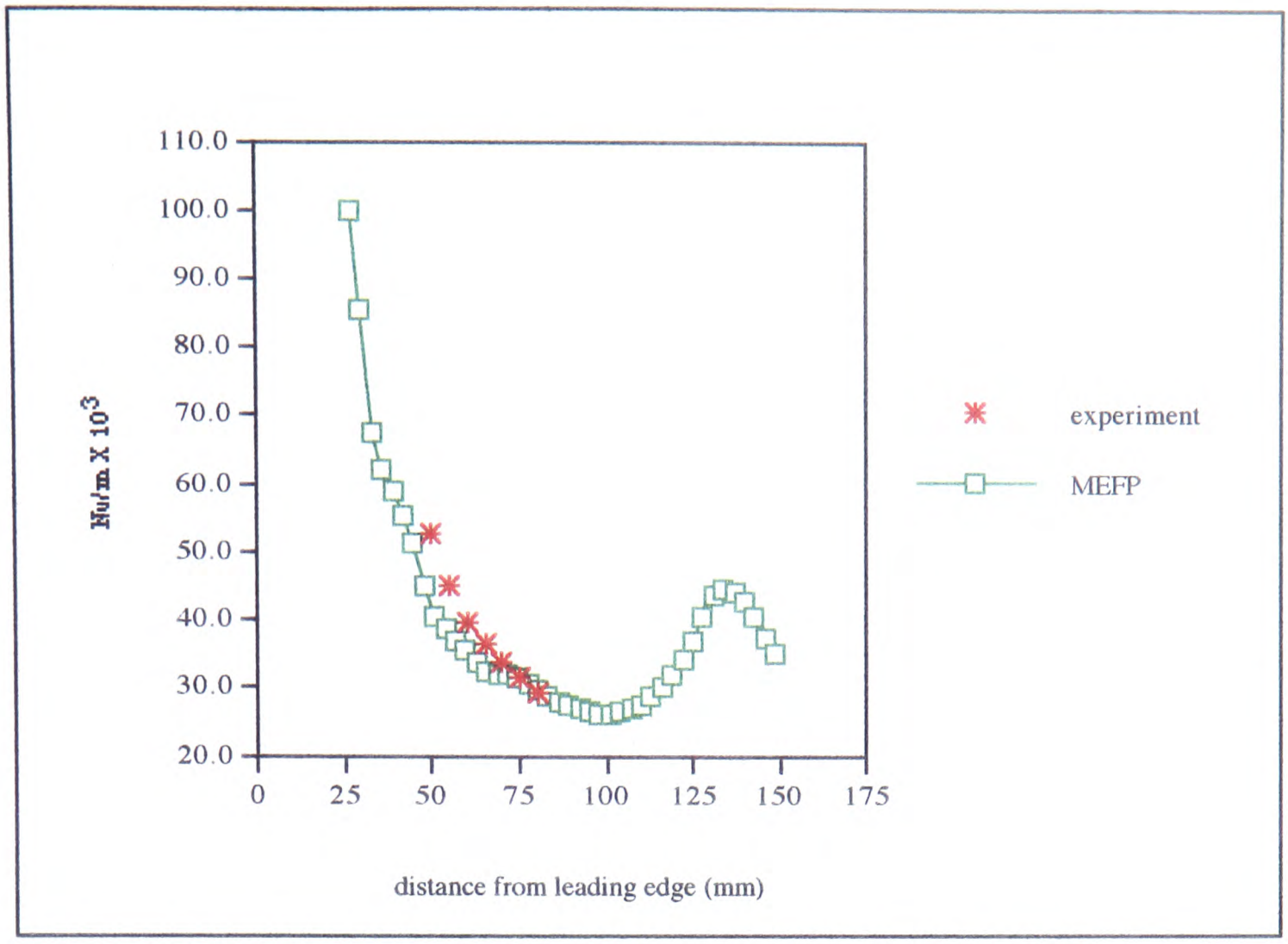
Graph 5.17 M.A.P.G._data3 Heat Transfer

Graph 5.18 shows the heat transfer data for a mild adverse case with coolant injection (G=0.59, TR=0.82). It is clear that the agreement is very good, and that the predicted trend is correct. There is no discrepancy between the MEFP results and the experimental results. In all of the mild adverse cases with the strong injection rates and a temperature ratio of 0.82, the under-relaxation was further decreased from the value of 0.3 that was needed for the cases with the weak injection rates to 0.2. This was done to eliminate some oscillatory behavior in the convergence data.



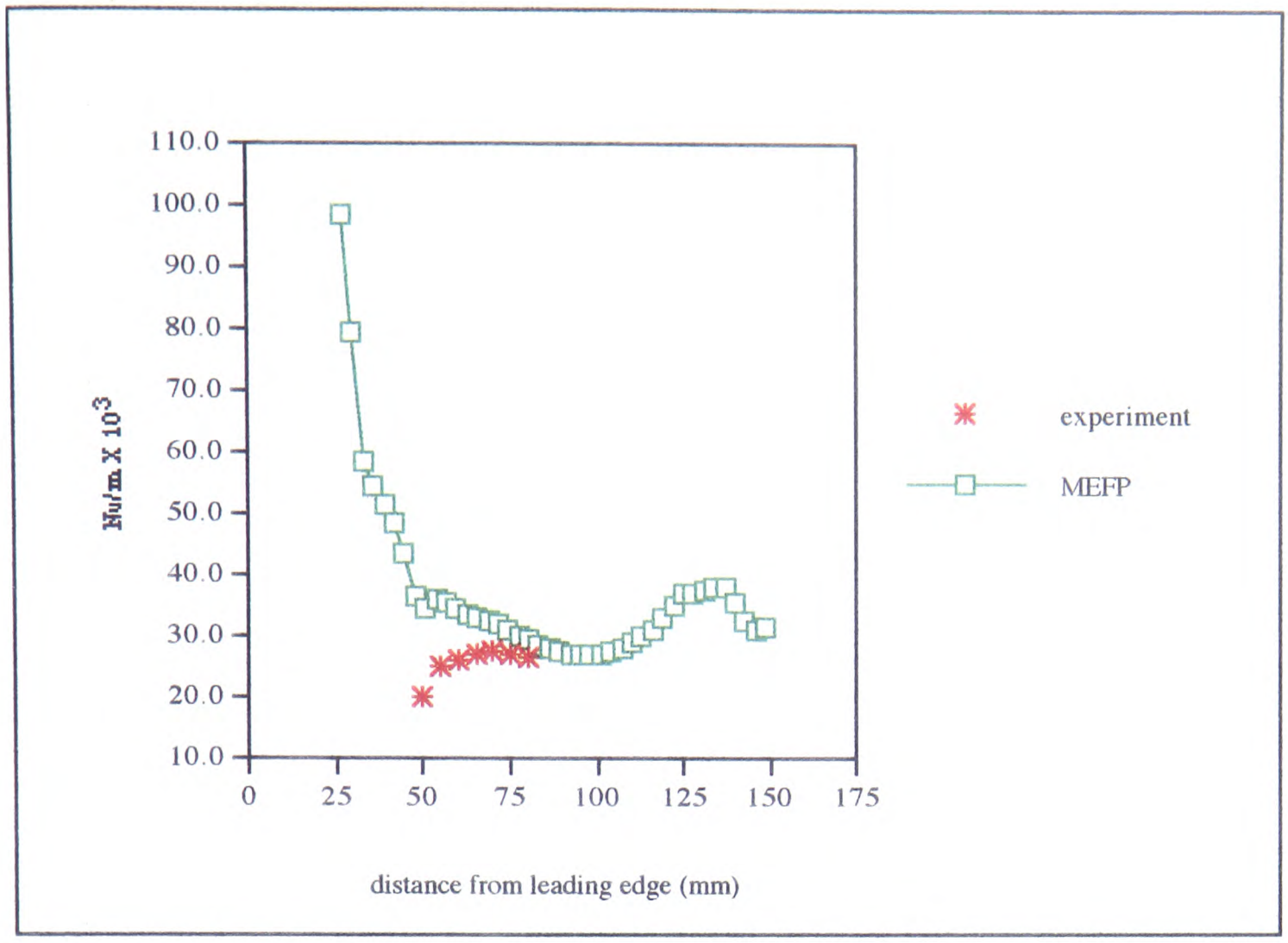
Graph 5.18 M.A.P.G._data8 Heat Transfer

Graph 5.19 shows the heat transfer data for a mild adverse case with coolant injection (G=1.20, TR=0.82). The agreement is very good and the predicted trend is correct. The point that shows the greatest discrepancy is only 1.9 percent lower than the experimental value. It can be seen that there is essentially no local decrease in the Nusselt number. Once again, this can be attributed to the separation of the coolant jet directly downstream of the cooling hole(s).



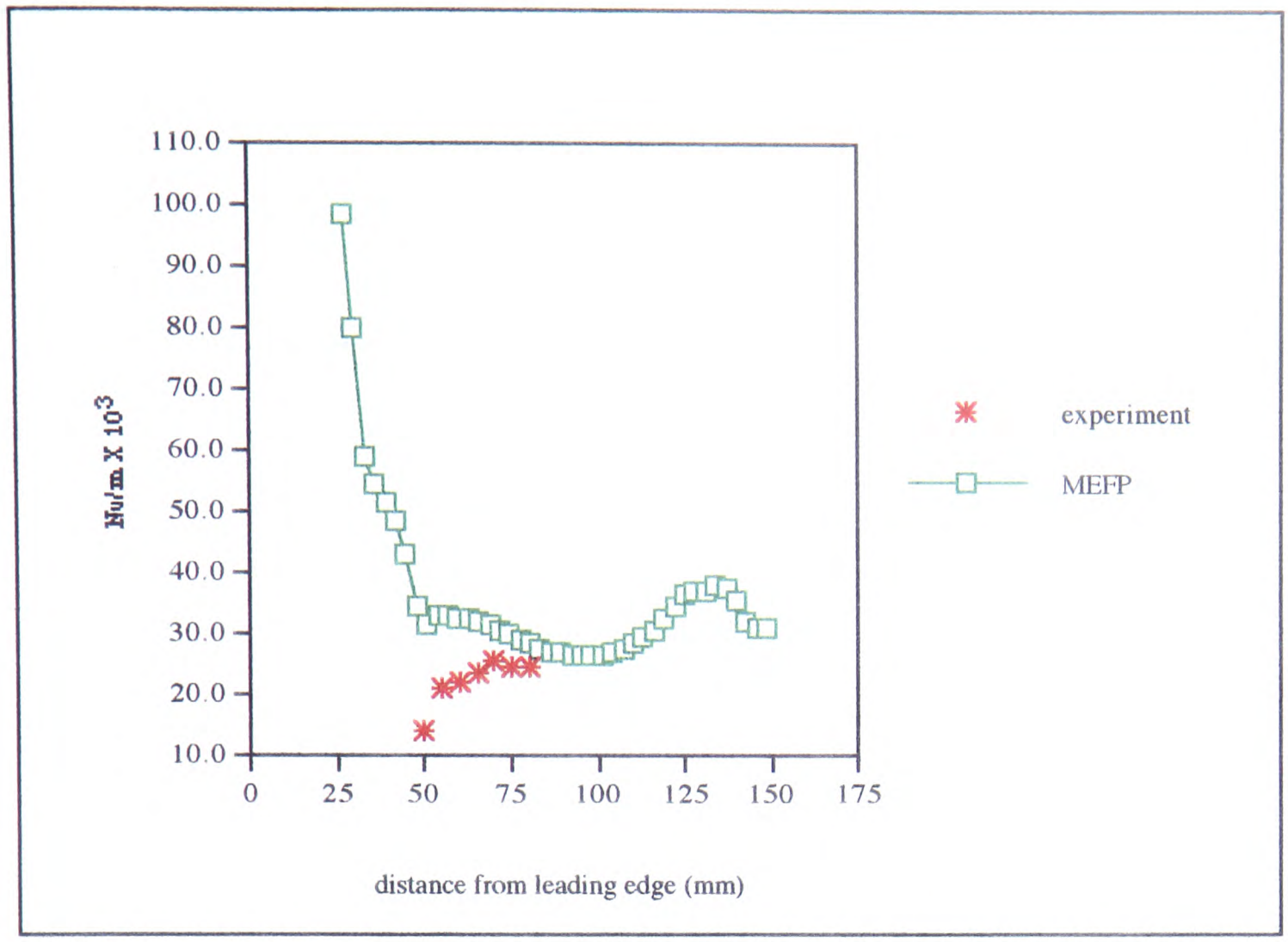
Graph 5.19 M.A.P.G._data10 Heat Transfer

Graph 5.20 shows the heat transfer data for a mild adverse case with coolant injection (G=0.11, TR=1.21). It can be seen that the agreement is not very good, and that MEFP is not even able to correctly predict the trend in the Nusselt number. It was stated in a previous section that the mixing length turbulence model encounters difficulty when faced with adverse pressure gradients, and that MEFP used the mixing length turbulence model for all of these computations. In every test case up to this point, the agreement between the MEFP data and the experimental data has been quite acceptable. It can be said that it was within reasonable limits of error. It would appear as if the code has encountered difficulty when presented with an adverse pressure gradient at a high temperature ratio of 1.21.



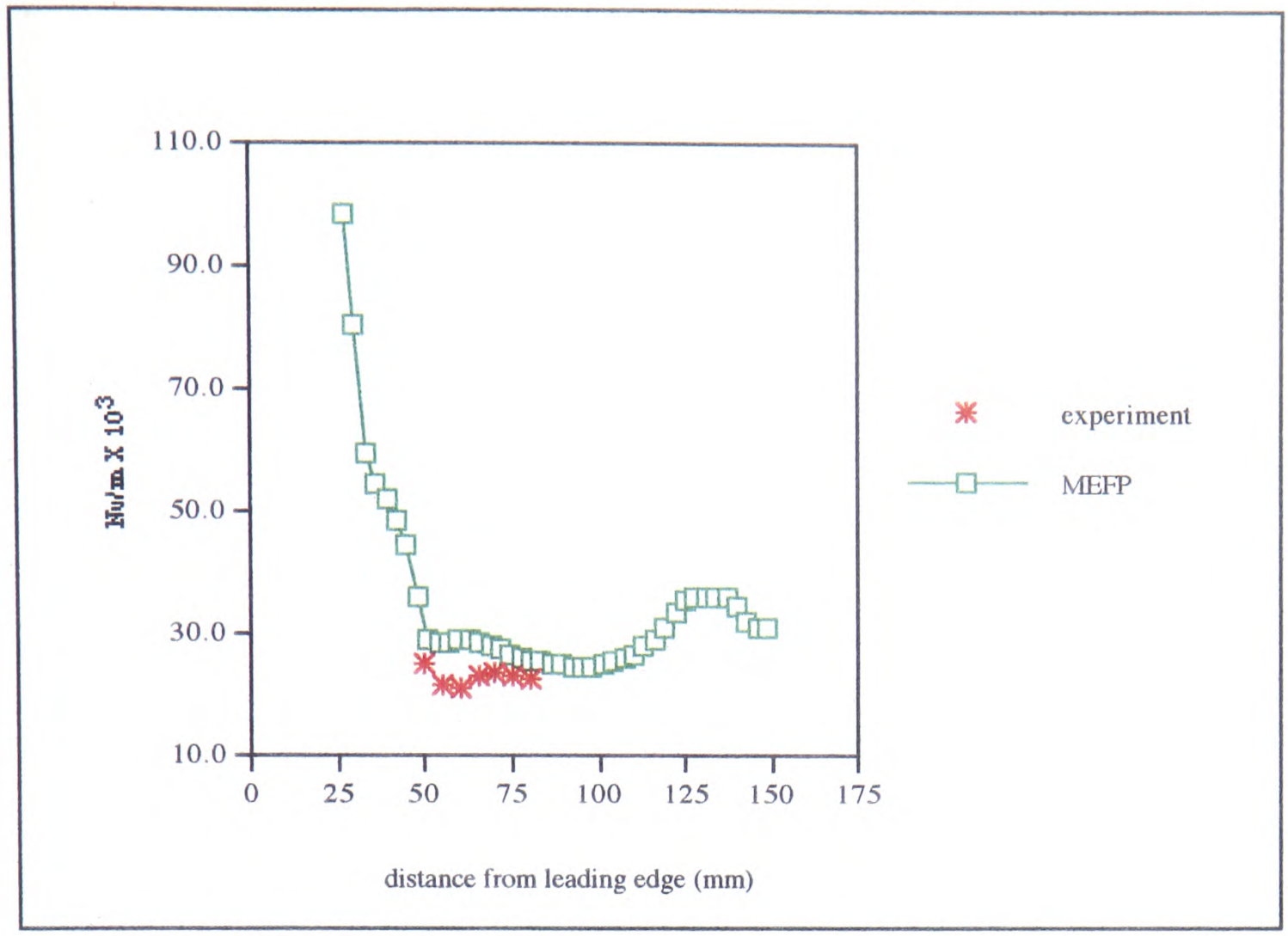
Graph 5.20 M.A.P.G._data4 Heat Transfer

Graph 5.21 shows the heat transfer data for a mild adverse case with coolant injection (G=0.18, TR=1.21). The same incorrect predictions that were found in the previous test case can be found here. The only difference is that it looks as if the agreement is even worse when the code is presented with an even higher injection rate, as it is in this case.



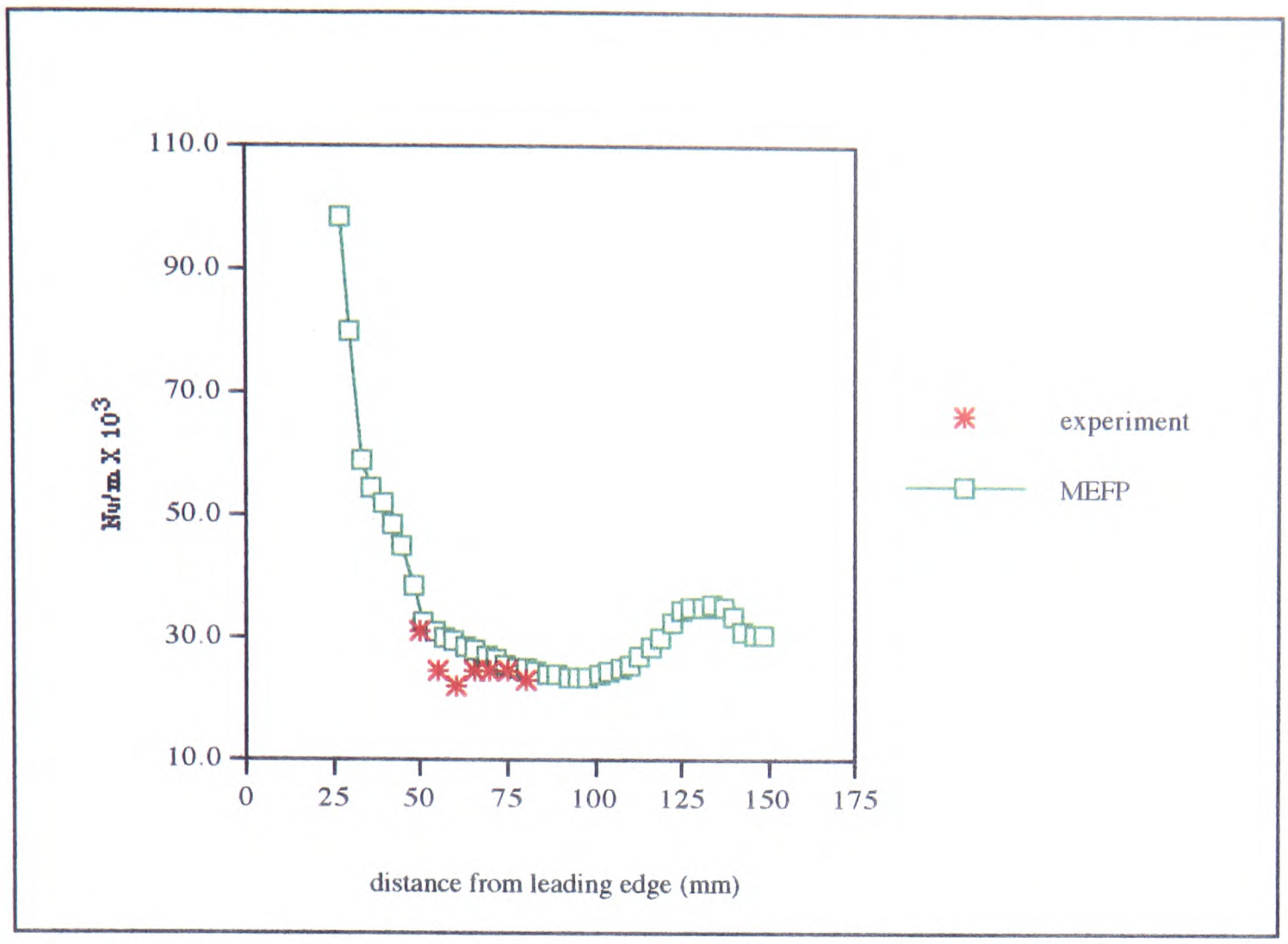
Graph 5.21 M.A.P.G._data5 Heat Transfer

Graph 5.22 shows the heat transfer data for a mild adverse case with coolant injection (G=0.42, TR=1.21). It can be seen that the agreement is not very good, and that MEFP was not even able to correctly predict the trend in the Nusselt number. This is not very surprising, because the code had difficulty in predicting the Nusselt number for the mild adverse case at the temperature ratio of 1.21 for the weak injection rates. In each of the following cases (Graphs 5.22, 5.23 and 5.24), there were also convergence problems in the computation. A value for the under-relaxation of 0.05 was needed, as was 500 passes in order to achieve the required two orders of magnitude decrease in the LOG RMS of the relevant parameters.



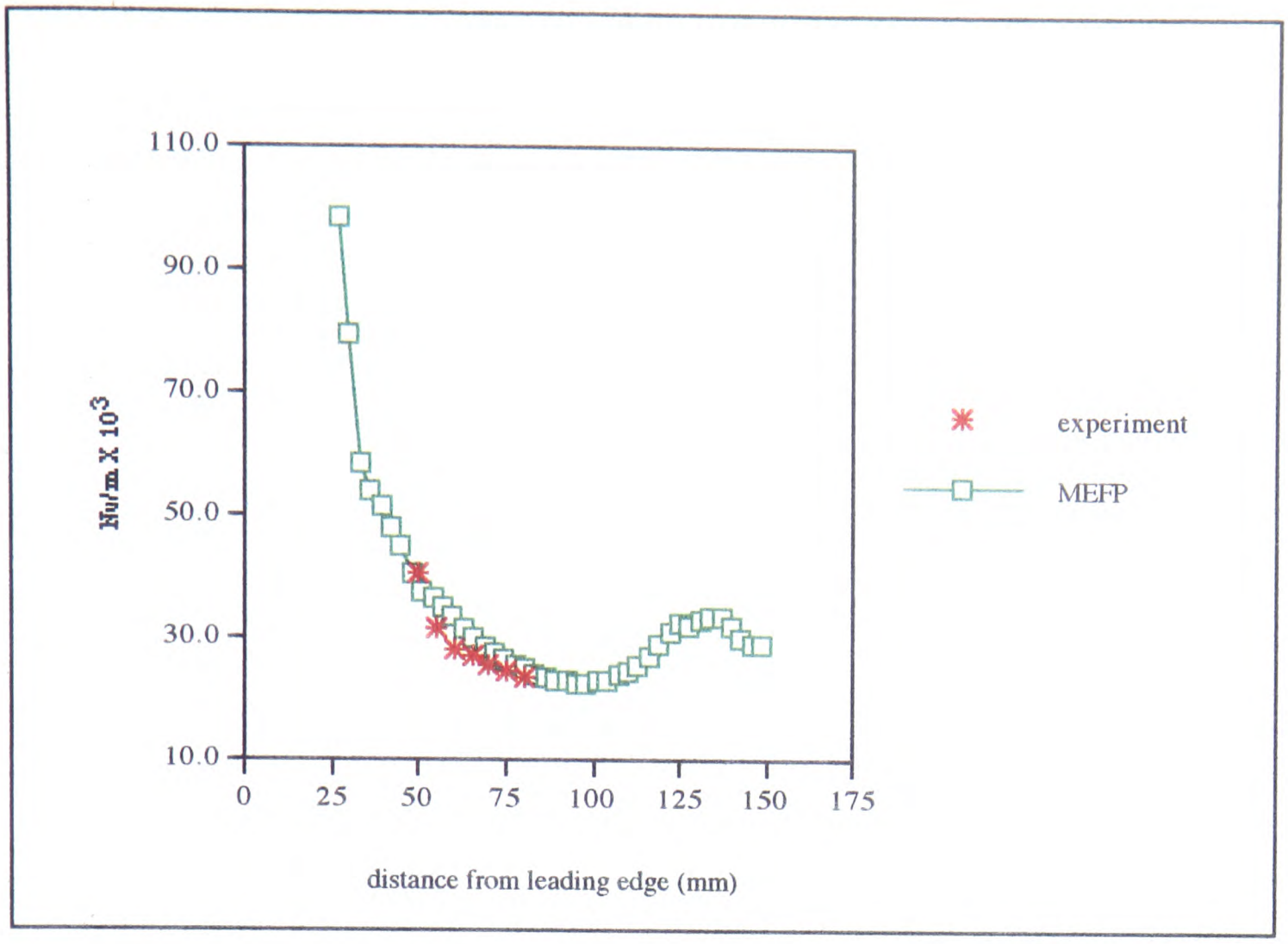
Graph 5.22 M.A.P.G._data11 Heat Transfer

Graph 5.23 shows the heat transfer data for a mild adverse case with coolant injection (G=0.55, TR=1.21). It can be seen that the agreement is not very good, and that the trend in the Nusselt number is not accurately predicted. The same incorrect predictions that were found in the previous test case can be found here.



Graph 5.23 M.A.P.G._data12 Heat Transfer

Graph 5.24 shows the heat transfer data for a mild adverse case with coolant injection (G=0.81, TR=1.21). At the highest injection rate for this temperature ratio, it can be seen that the agreement is very good, and that the predicted trend is correct. The point that shows the greatest discrepancy is only 9.1 percent higher than the experimental value. It is interesting to note that for the weak injection rates at this temperature ratio, the agreement got worse as the injection rate increased. Whereas for the strong injection rates, the agreement got better as the injection rate increased. Once again, it can be seen that there is no local decrease in the Nusselt number at the injection point due to the separation of the coolant flow from the surface directly beyond the cooling hole(s).



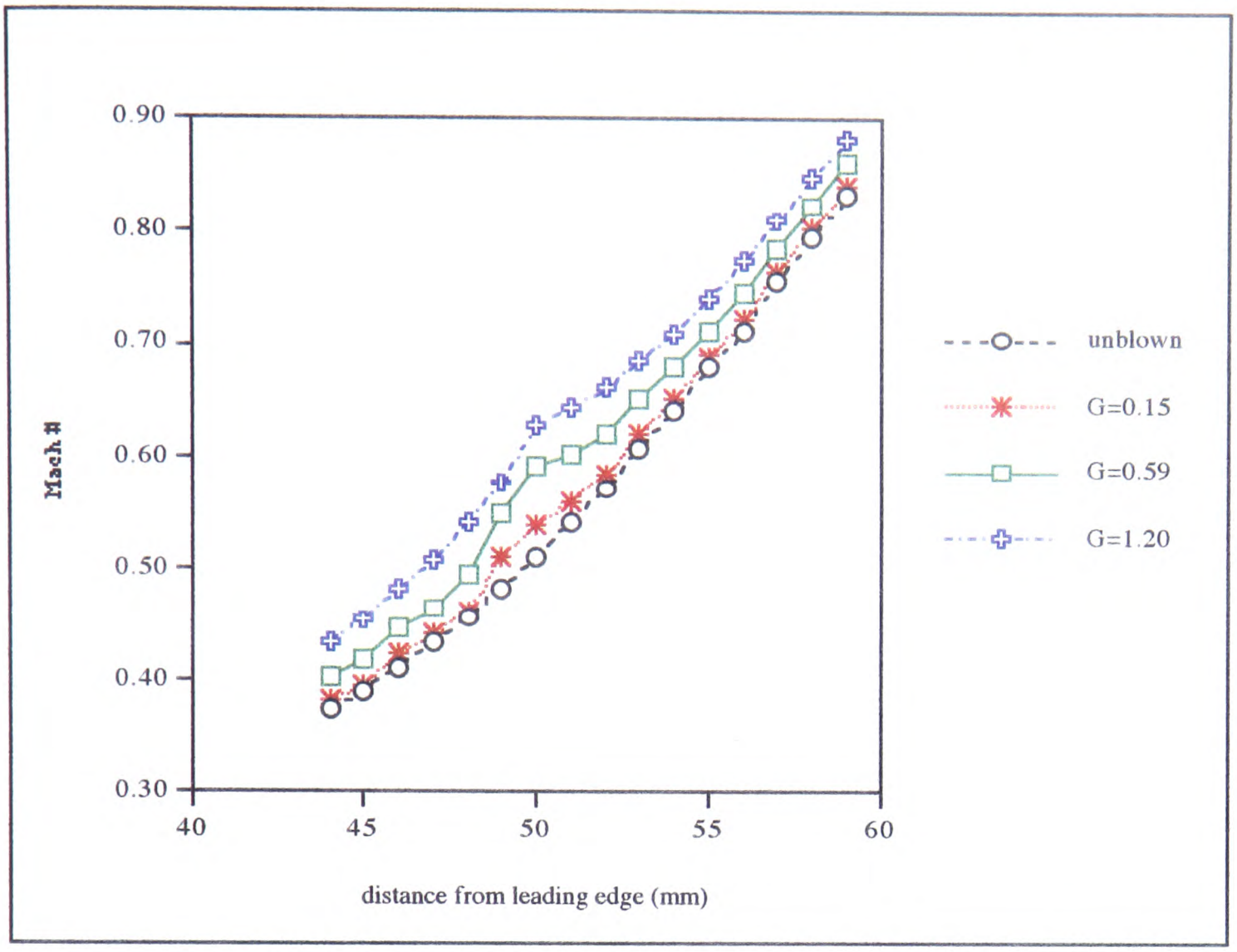
Graph 5.24 M.A.P.G._data13 Heat Transfer

5.2.4 Effect of Coolant on Flow Field

The strong favourable Mach number data that were presented previously were collected only for the unblown or non-film cooled test case. Here, a comparison is made between this data and the Mach number data that were collected for three other test cases with a low, medium, and high injection rate. This comparison was carried out in order to confirm that MEFP was not predicting any large discrepancies that could not be explained. The strong favourable test case was chosen for this comparison because the results at this pressure gradient were consistently the most reliable.

Graph 5.25 shows the results of this comparison. It can be seen that the data are consistent, and that it illustrates the expected trends. For instance, the injection point (which is located 48.75mm downstream of the leading edge) can be located clearly by the sudden increase in Mach number. It would be expected that this local increase in Mach number would be the most noticeable at the highest injection rate. If the plot is consulted, this fact can be confirmed. An upstream influence of the coolant injection

can also be noted in the data. This upstream influence is seen to increase with increasing injection rate, which is the expected outcome.



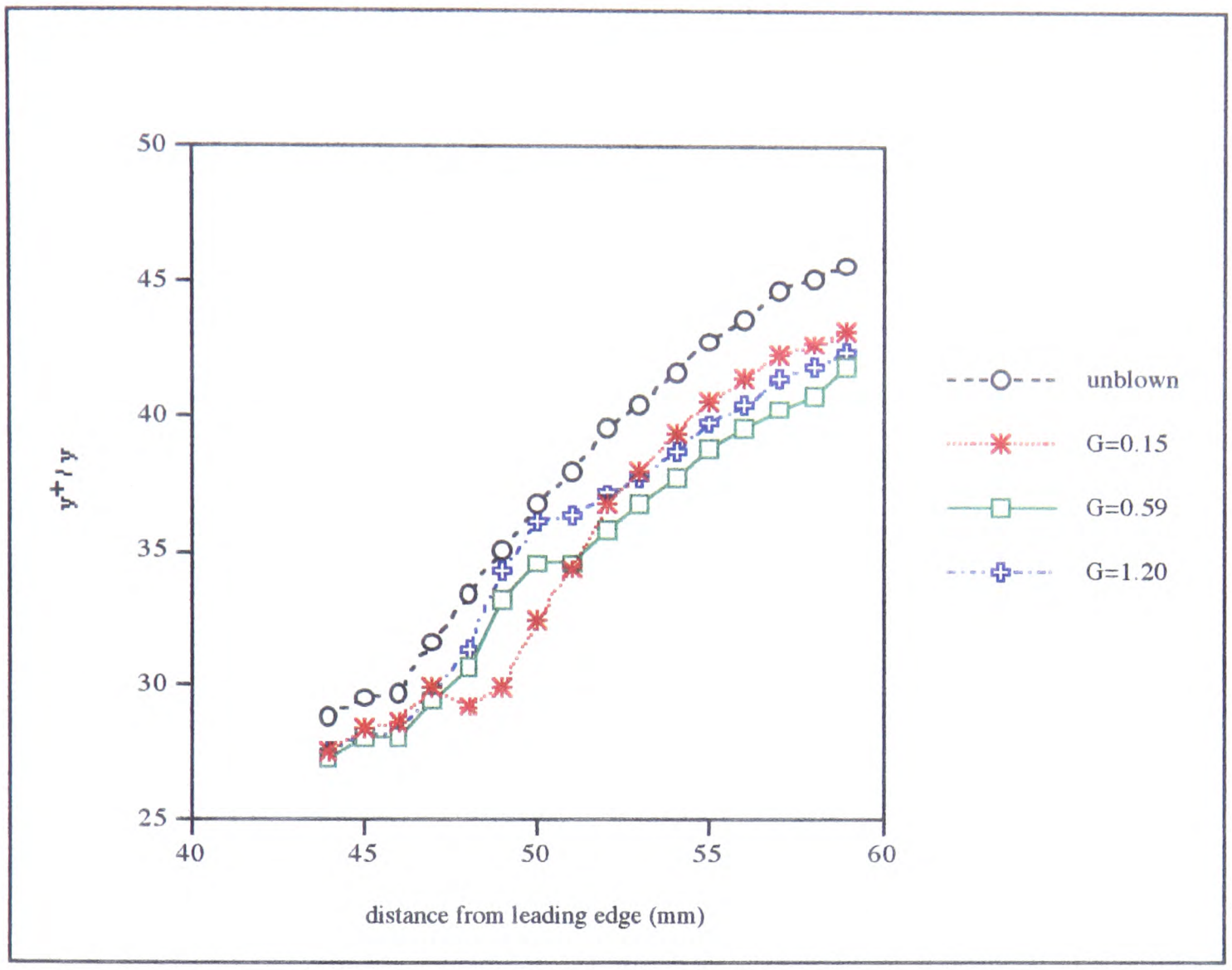
Graph 5.25 S.F.P.G. Mach Number Comparison

5.2.5 Shear Stress Results

The paper by Jones and Walton (**ref.49**) can be used to confirm the fact that MEFP is correctly predicting yet another important parameter, the skin friction in a film cooling situation. It is convenient to define the skin friction according to Eqn.5.10. It can be said that the expression $\frac{y^+}{y}$ is simply proportional to the square root of the shear stress. Jones and Walton found that at low injection rates, the injected fluid shields the surface or the wall from the shear of the freestream. This result can be confirmed by consulting Graph 5.26 where the value of the shear stress at an injection rate of 0.15 is less than that of the unblown case at the point of injection. They also

found that at high injection rates, such as G=0.59 and G=1.20, the process of coolant injection generates high shear stress at values greater than that of the unblown case.

$$\frac{y^+}{y} = \frac{1}{\nu}\sqrt{\frac{\tau}{\rho}} = \frac{u_\infty}{\nu}\sqrt{\frac{C_f}{2}} \qquad \textbf{(5.10)}$$



Graph 5.26 S.F.P.G. y^+/y Comparison

In Graph 5.26, the unblown data do not match that of the film cooled data in the regions before and after injection as would be expected. This is due to the different wall temperature that was used in the non-filmed cooled test case in comparison to the wall temperature that was used in the film cooled test cases (see Table 5.1). It is known that the Nusselt number varies non-linearly with the gas-to-wall temperature ratio "due to compressibility effects and variations in gas properties with temperature through the boundary layer" (**ref.28**). One method for accounting for this discrepancy is to

describe the behavior of the Nusselt number according to Eqn.5.11 where Nu_{cp} is the Nusselt number under constant gas properties and n is a constant. The value of n changes with pressure gradient according to Table 5.4. If a calculation is performed using the relevant gas and wall temperatures as defined in Table 5.1 and the value of n for a favourable pressure gradient as defined in Table 5.4, then it can be proven that the departure of the unblown data in Graph 5.26 is not due to erroneous MEFP prediction.

$$Nu = Nu_{cp}\left(\frac{T_w}{T_g}\right)^n \qquad (5.11)$$

PRESSURE GRADIENT	n
zero	-0.25
favourable	-0.43
mild adverse	-0.29

Table 5.4 Variation of n With Pressure Gradient

5.3 CONCLUSIONS

It was stated earlier that the ILPT test cases provided an excellent starting point for the initial verification of the film cooling routine in MEFP. By consulting the data presented here, it can be said that both MEFP and the film cooling routine were successful at accurately predicting flow phenomena. Due to the success that has been achieved in this analysis, the code can now be applied to more complex flow problems and test cases. Successful predictions of Mach number and Nusselt number were made at various locations and in varying pressure gradients. The MEFP predictions were within reasonable agreement with the experimental results in all but a few cases.

By consulting the Nusselt number plots, certain expected trends can be confirmed. These trends are the same regardless of temperature ratio or pressure

gradient. For instance, a lower value of the Nusselt number would be expected directly after the point of injection in the film cooled test cases in comparison with the non-film cooled test cases. This fact is easily verified by consulting the plots of test cases with low injection rates. Strong injection rates are characterized by separation of the coolant flow from the wall or surface directly downstream of the cooling hole. As the injection rate increases beyond the injection rate at which separation occurs, then the coolant is "lifted off" more and more from the surface. The coolant, therefore, becomes less and less effective in the region directly beyond the point of injection. It would also be expected that far downstream of the cooling hole(s), all of the values of the Nusselt number would merge as the coolant flow mixes with the freestream. This, too, is easily verified. Teekaram demonstrated all of these trends in his thesis (**ref.89**), and MEFP confirms these results.

CHAPTER 6. DEVELOPMENT OF FILM COOLING MODEL

There were particular problem areas that were addressed in the development and the improvement of the film cooling model. It was found through this investigation and other investigations by Rolls Royce that under certain circumstances, MEFP is unable to correctly predict certain flow phenomena. It was determined through this investigation that the code encountered difficulty when presented with adverse pressure gradients, especially at a temperature ratio of 1.21. It was also found that the code was unable to give reliable or accurate results when predicting the heat transfer in the neighbourhood of the film cooling hole, or directly downstream of the film cooling hole. The illustration and discussion of these results is presented in a previous section. A separate Rolls Royce investigation discovered that the code encountered difficulty when presented with leading edge film cooling (both pressure and suction surfaces near the stagnation point) involving actual turbine blading. These problem areas were deemed to have had a significant enough effect on the results that MEFP generates with film cooling present to necessitate changes in the film cooling model.

6.1 TURBULENCE AUGMENTATION

The first step in the development and the improvement of the film cooling model was to add the turbulence augmentation that is present in other similar computer codes like STANCOOL, but was neglected in MEFP. A turbulence augmentation model is meant to account for the effects of increased turbulence in the presence of film cooling by altering the mixing length. The turbulence augmentation should have its maximum value in the vicinity of the film cooling holes and should decrease exponentially as the downstream distance from the film cooling holes increases. A set of expressions was derived to add the necessary turbulence according to the above description. In Eqns.6.1 and 6.2, ℓ' / ℓ is the new mixing length with the addition of turbulence augmentation divided by the old mixing length without the addition of turbulence augmentation. The

old mixing length without the addition of turbulence augmentation is simply defined according to Eqn.2.28. The two constants, k_1 and k_2 control the magnitude of the augmentation and the axial decay of the turbulence augmentation respectively. Eqn.6.1 is valid in the region where $y < PD/2$ and Eqn.6.2 is valid in the region where $y \geq PD/2$.

$$\ell'/\ell = 1 + e^{(-k_2 x/PD)}\, k_1 \qquad \textbf{(6.1)}$$

$$\ell'/\ell = 1 + e^{(-k_2 x/PD)}\, 2k_1\left(1 - \frac{y}{PD}\right) \qquad \textbf{(6.2)}$$

The constants k_1 and k_2 effect the turbulence augmentation in different ways. The constant k_1 changes the magnitude of the turbulence augmentation local to the point of injection. Whereas, the constant k_2 determines the decay of the mixing length with downstream distance. It can be seen from Eqn.6.1 that k_2 scales with the parameter $\frac{PD}{x}$ which means that when the penetration distance is very small (low injection rates), then k_2 must also be very small to have any effect. Furthermore, as k_2 is decreased, its effects can be seen even further downstream. At high injection rates the value of k_2 does not need to be as small for any noticeable change to occur in the value of the heat transfer.

The turbulence augmentation model that Crawford adopted in STANCOOL is slightly different from the turbulence augmentation model used in MEFP. For instance, both the Crawford model and the model used in MEFP employ an exponential damping function. The function that is used in STANCOOL (and the constant for decay) is based on the boundary layer thickness, whereas it can be seen that the above functions are based on the penetration distance, which can not necessarily be assumed to be equal to the boundary layer thickness.

The two constants, k_1 and k_2, were easily set to any particular value in MEFP. The values were set in the datasets avoiding the need to alter the code itself. If the magnitude and the decay of the turbulence augmentation was to be left unaltered, then the value of k_1 would be set equal to zero. Under this initial condition, the MEFP results were then compared to Teekaram's experimental results **(ref.89)**. If it was determined that the agreement between the computational prediction and the experimental results could be improved, then each factor was altered individually until one value was found for each to give the optimum agreement with the corresponding experimental results.

It is more appropriate to attempt to correlate the mechanisms that define heat transfer as opposed to the actual value of the heat transfer. So the parameters A and B, which are "functions of the mainstream and injection fluid dynamics" and are discussed in detail in a previous section, were used for this purpose. These parameters were plotted according to X/D position so the value of each of the parameters could be easily determined at any downstream point and compared to the corresponding experimental results.

Unfortunately, Teekaram **(ref.89)** only provided experimental results for the twelve injection rates at the temperature ratio of 0.82 with a strong favourable pressure gradient and a mild adverse pressure gradient. Therefore, the problems that the code had in correctly predicting the relevant parameters at the temperature ratio of 1.21 could not be addressed with this particular scheme. Also, the high injection rates at a mild adverse pressure gradient did not lend themselves to accurate optimization via this method, so those results are not presented here.

6.2 Mass Shed Ratio

The film cooling model uses a constant mass shed ratio (Eqn.4.2). Therefore, it was decided in conjunction with Rolls Royce to first work with the existing mass shed ratio to see if any improvements could be made before it was abandoned altogether.

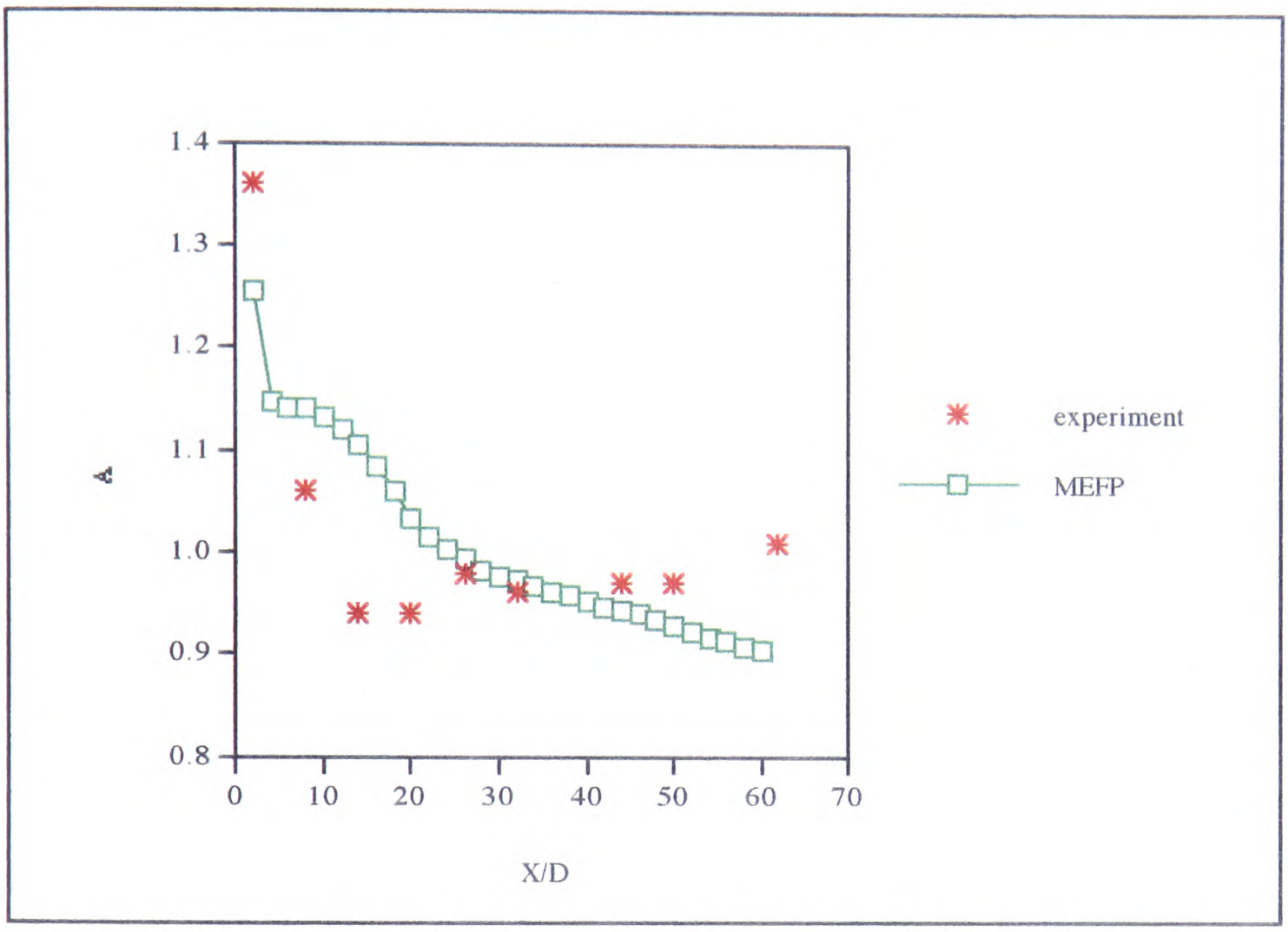
Keeping this constraint in mind, the mass shed ratio could be altered simply by multiplying it by some factor. In this way, a constant expression was maintained for all conditions. The initial verification of the code and its film cooling model was carried out on a set of test cases where $\beta=0$ (Eqns.4.2-4.5). Therefore, the mass shed ratio could be changed by merely altering the cooling hole pitch to diameter ratio that is defined individually in each dataset. Different values for the cooling hole pitch to diameter ratio were tried in each of the twelve cases and an optimum value of the constant mass shed ratio was generated according to the best correlation of the experimental and computational values of both A and B.

It may be obvious to say that by changing the constants in the turbulence augmentation model, the state of the turbulence augmentation in the neighbourhood of the cooling hole(s) and therefore, the mixing length were changed profoundly. The effect that changing the constant mass shed ratio has on the mixing length may not be as obvious. For example, increasing the mass shed ratio, distributes the coolant closer the wall or the surface. Hence, the penetration distance of the coolant is decreased. The velocity gradient normal to the wall would increase due to the increased velocity very close to the wall. This has the end effect of decreasing the mixing length.

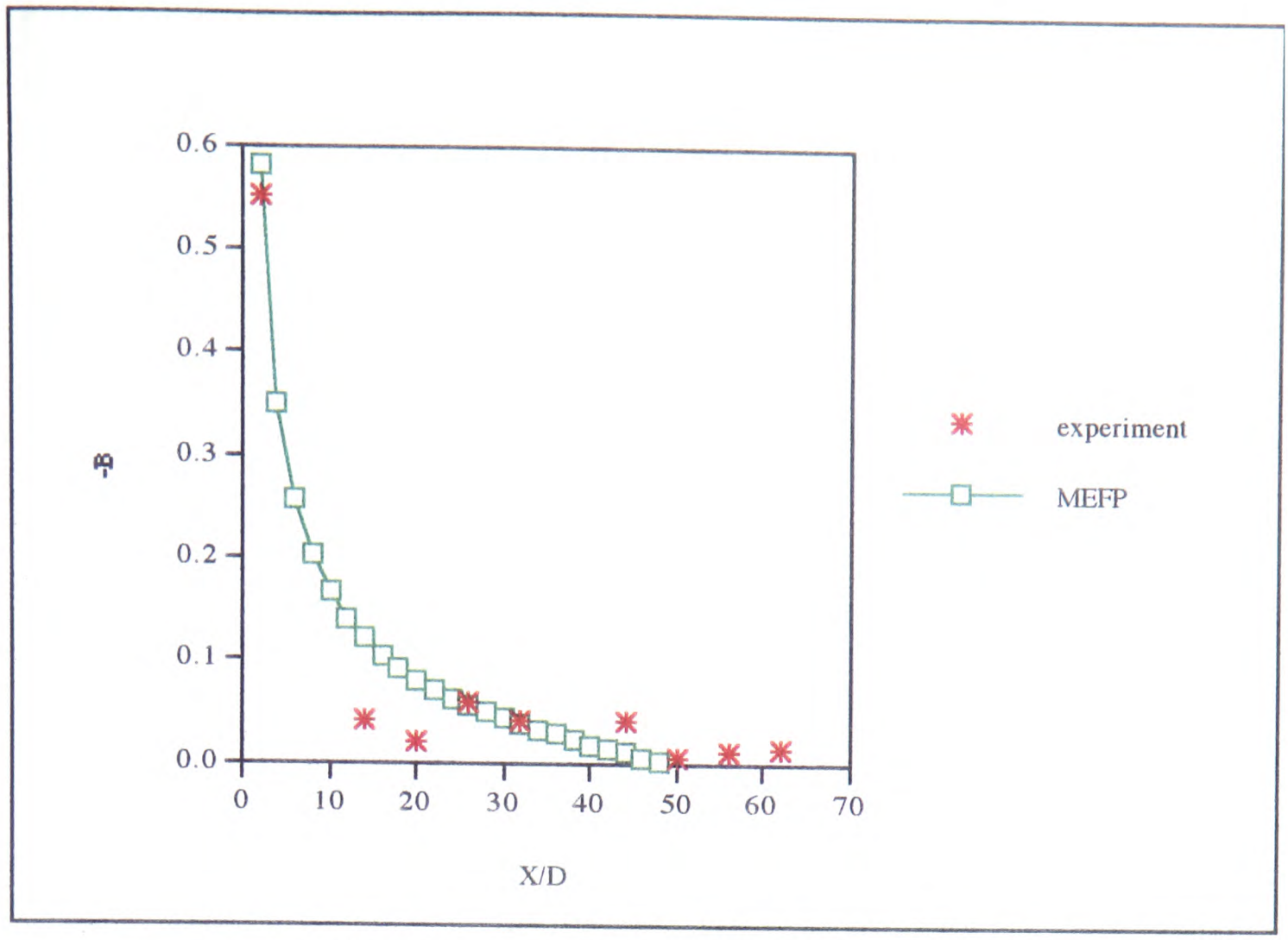
6.3 Discussion of Results

Graphs 6.1 and 6.2 show the A and B data for the lowest injection rate with a strong favourable pressure gradient. What is depicted in these two graphs is the best fit of the MEFP data to the experimental data that was achieved for both the A and B parameters. More specifically, it can be said that throughout this investigation values of k_1 and k_2 were selected to give the best joint prediction, as opposed to the best individual prediction. For instance, the first experimental data point on the A plot is not predicted very accurately, which would indicate that the magnitude of the turbulence augmentation should be increased. However, the first experimental data point on the B plot is slightly overshot by the MEFP data, which would indicate that the magnitude of

the turbulence augmentation should be slightly decreased. The graphs would also indicate that a reduction of the axial decay factor was in order to improve both the A and B predictions. A decrease in k_2 was actually found to produce little change in the relevant parameters and show no improvement beyond what it shown here. This may explain why no improvement was made in the Nusselt number prediction downstream of the injection point in Graph 5.7.

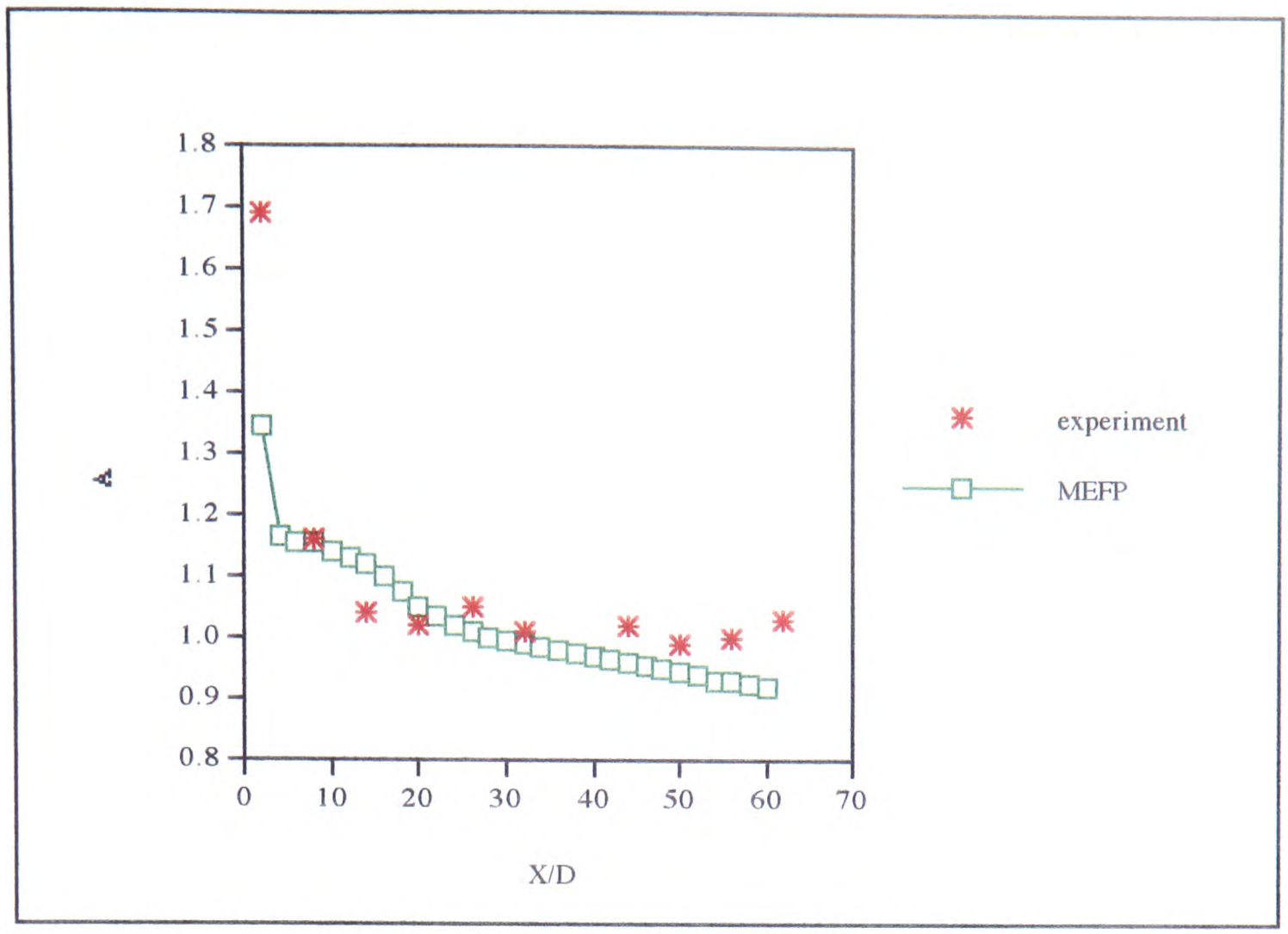


Graph 6.1 A vs. X/D (S.F.P.G., G=0.15)

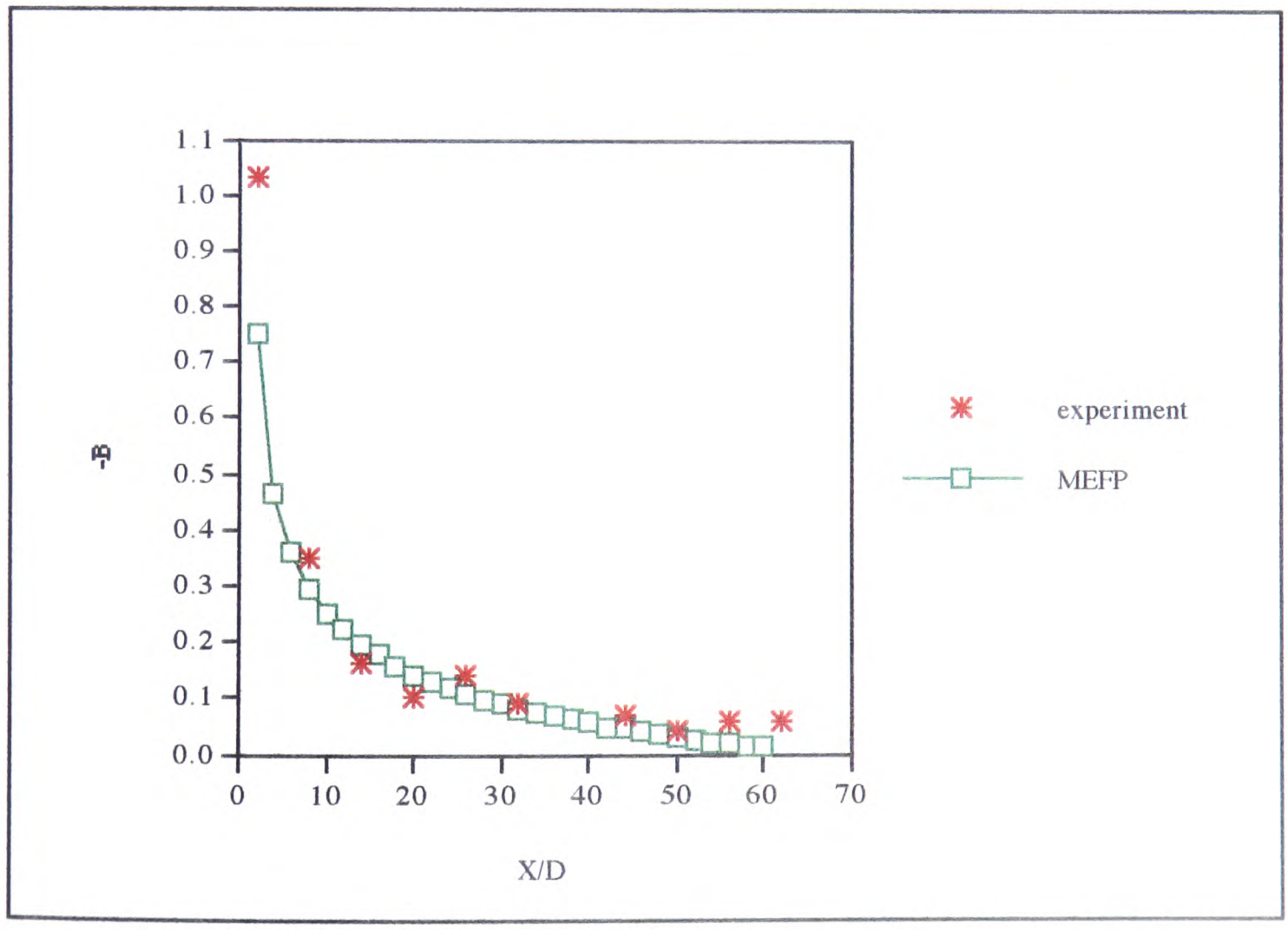


Graph 6.2 B vs. X/D (S.F.P.G., G=0.15)

Graphs 6.3 and 6.4 show the A and B data for the injection rate of 0.25 with a strong favourable pressure gradient. The first data point on both graphs is not predicted accurately, which would indicate that k_1 should be increased even higher than the current value. Such a change was found to produce little change in the relevant parameters and show no improvement beyond what it shown here. Interestingly enough, it can be seen from Graph 5.8 that this level of augmentation was sufficient to accurately predict the Nusselt number at the injection point.

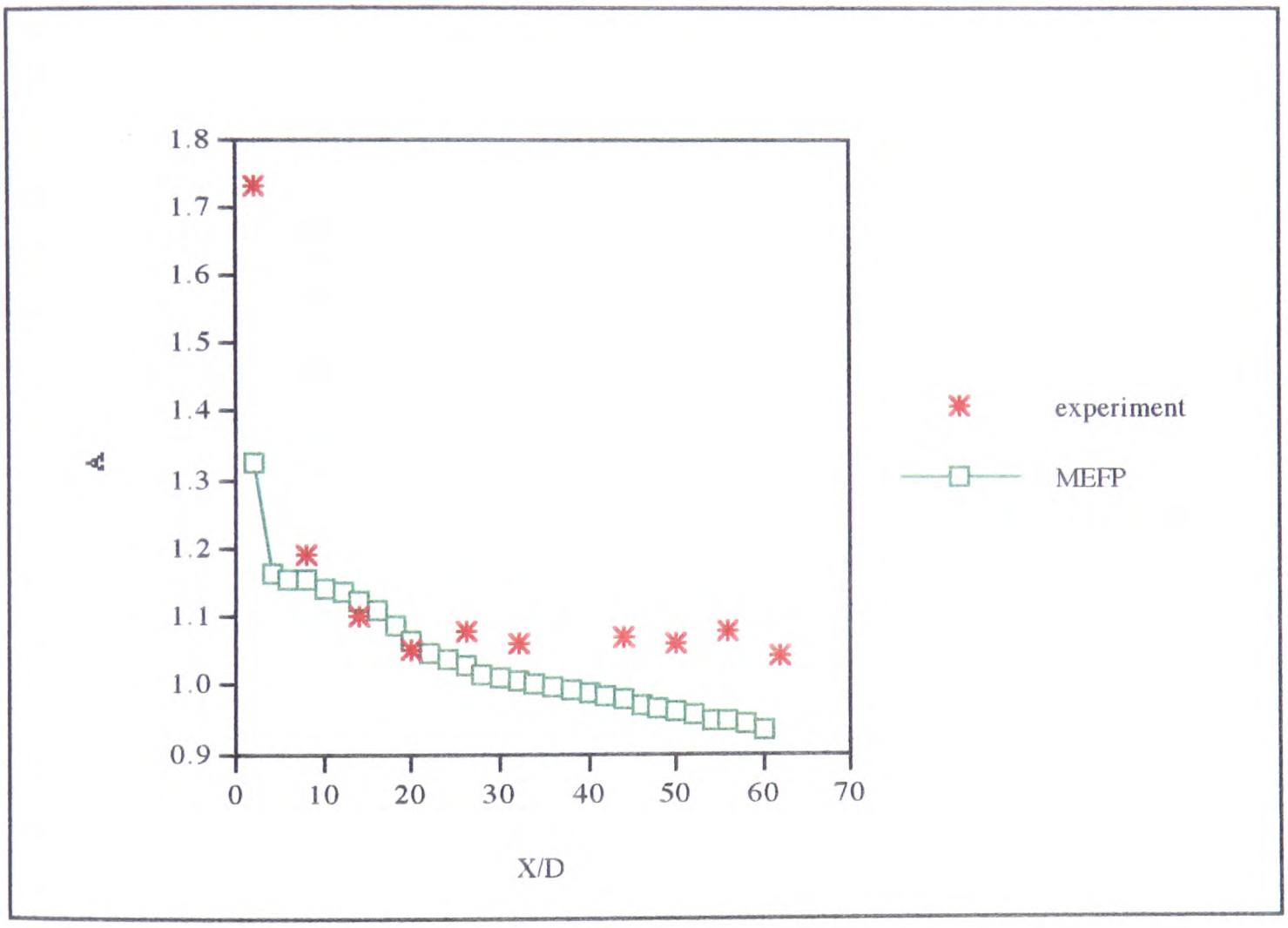


Graph 6.3 A vs. X/D (S.F.P.G., G=0.25)

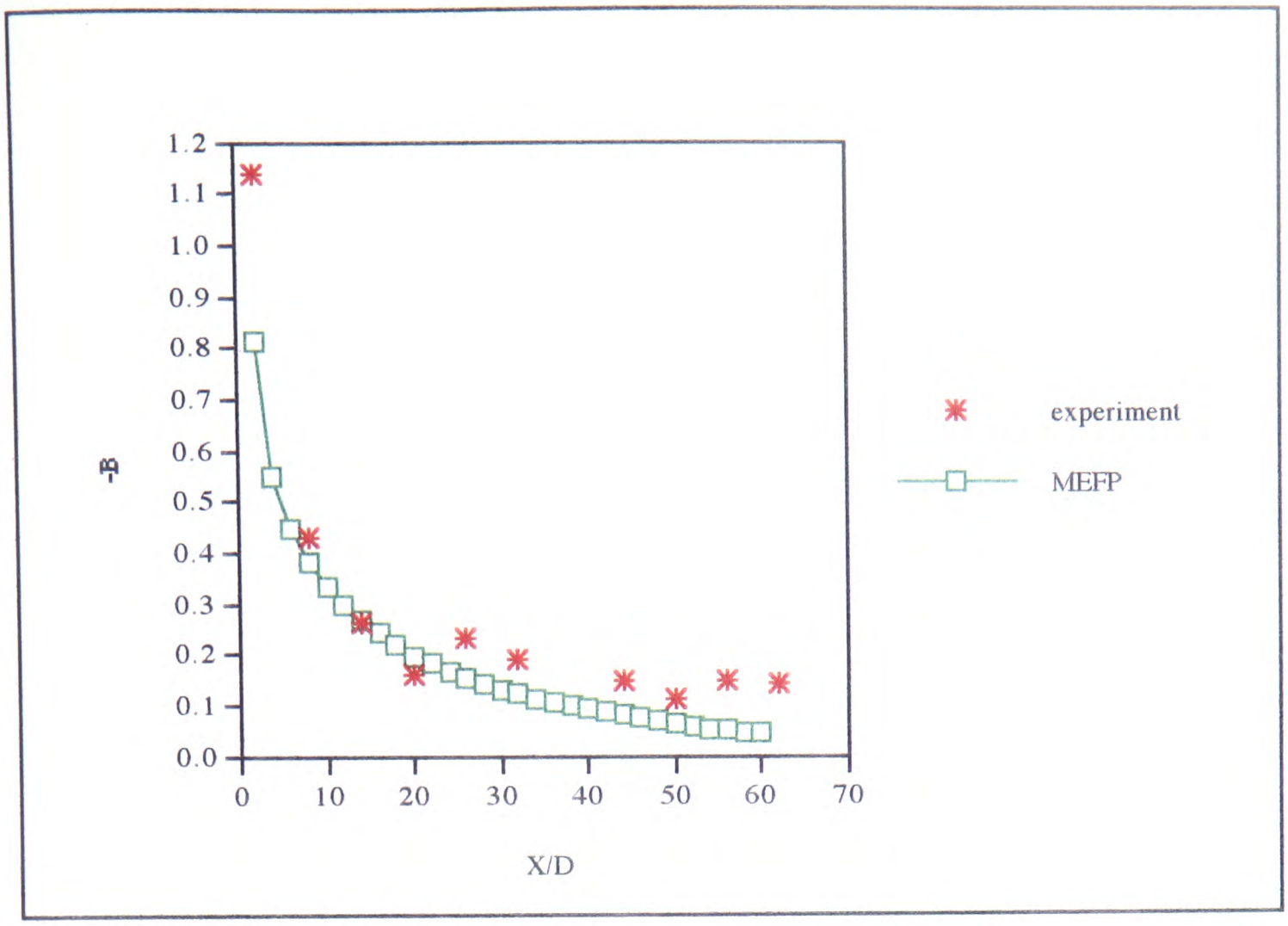


Graph 6.4 B vs. X/D (S.F.P.G., G=0.25)

Graphs 6.5 and 6.6 show the A and B data for the injection rate of 0.35 with a strong favourable pressure gradient. Once again, the first data point on both graphs is not predicted accurately, which would indicate that k_1 should be increased but such a change was found to produce no improvement. However, if Graph 5.9 is consulted then it can be confirmed that this level of augmentation was sufficient to accurately predict the Nusselt number at the injection point. Here too, the downstream points are predicted quite accurately on both plots, and corresponding improvements can be seen in the Nusselt number prediction particularly immediately downstream of the injection point. It is in this region that the A and B experimental and MEFP data are the most similar.

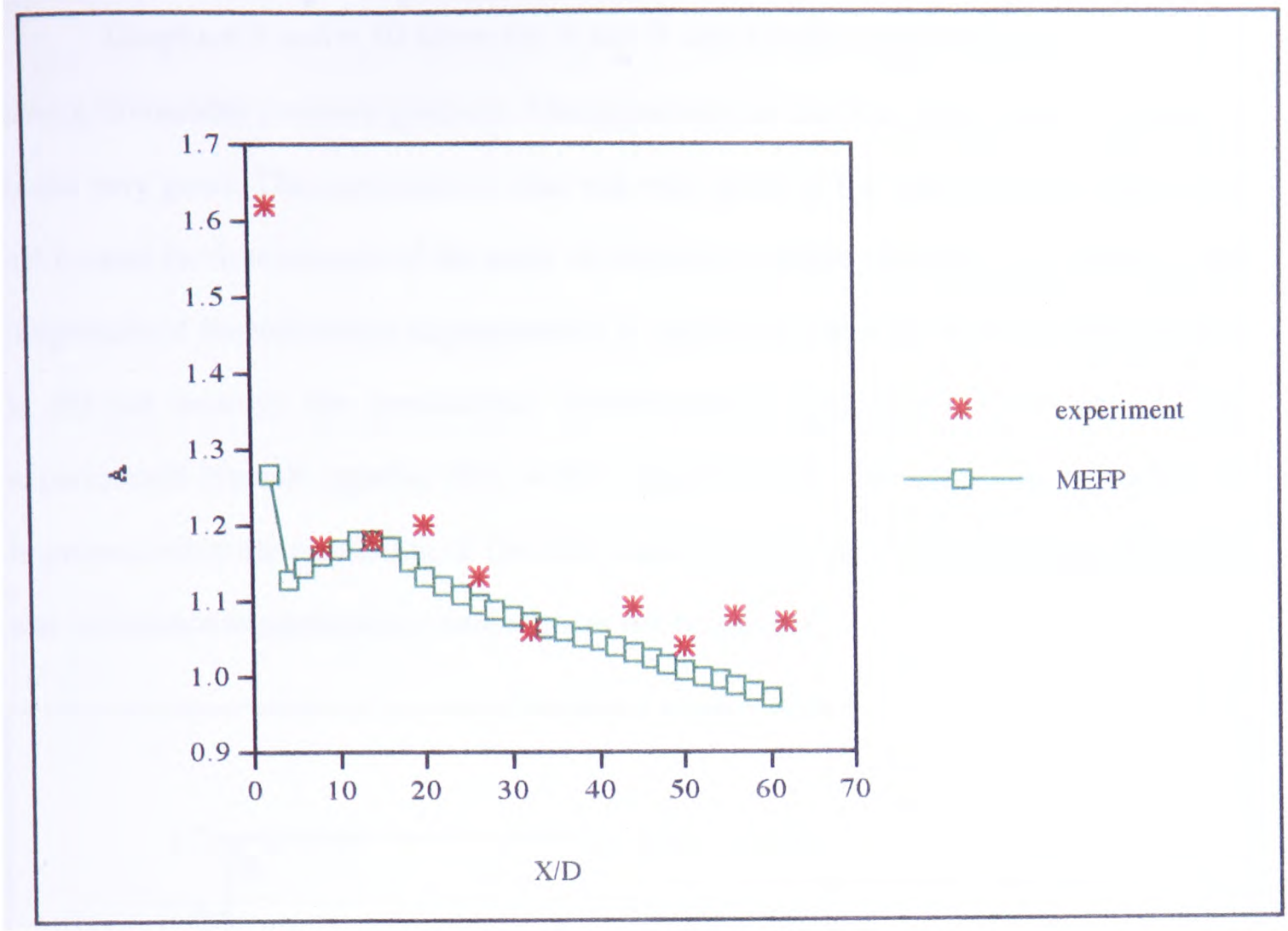


Graph 6.5 A vs. X/D (S.F.P.G., G=0.35)

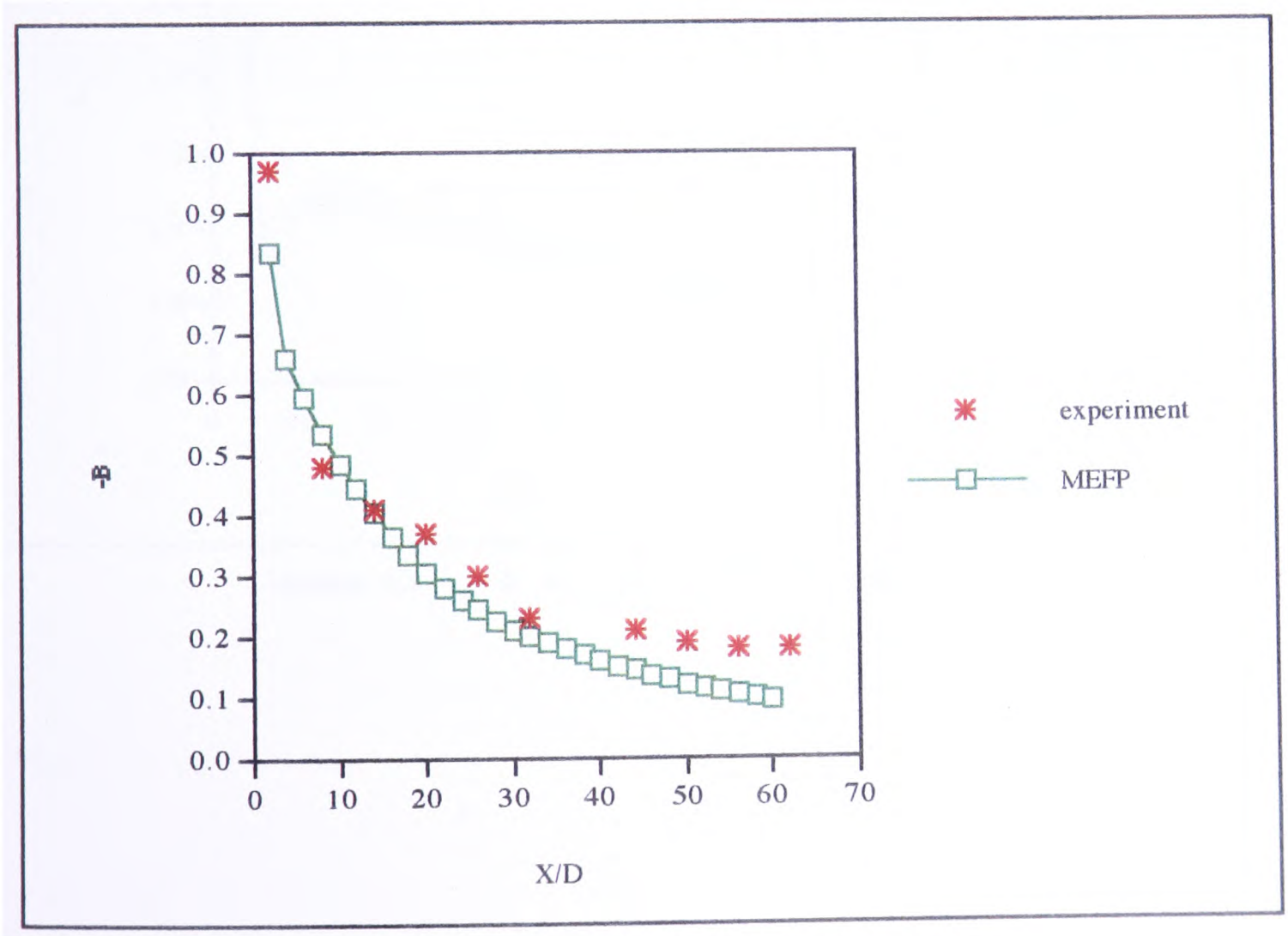


Graph 6.6 B vs. X/D (S.F.P.G., G=0.35)

Graphs 6.7 and 6.8 show the A and B data for the injection rate of 0.59 with a strong favourable pressure gradient. The first data points on both the A and B plots are not predicted accurately, which would indicate that k_1 should be increased but such a change was found to produce no improvement. In fact, if Graph 5.10 is consulted it can be seen that the new film cooling model has overcompensated and overshot the value of the Nusselt number at the injection point. The downstream points on the A and B plots are predicted with reasonable accuracy in this case. There is a departure of the MEFP and experimental points at the end of the X/D range which corresponds to the approximate location of the largest departure of the MEFP and experimental points on the Nusselt number plot.

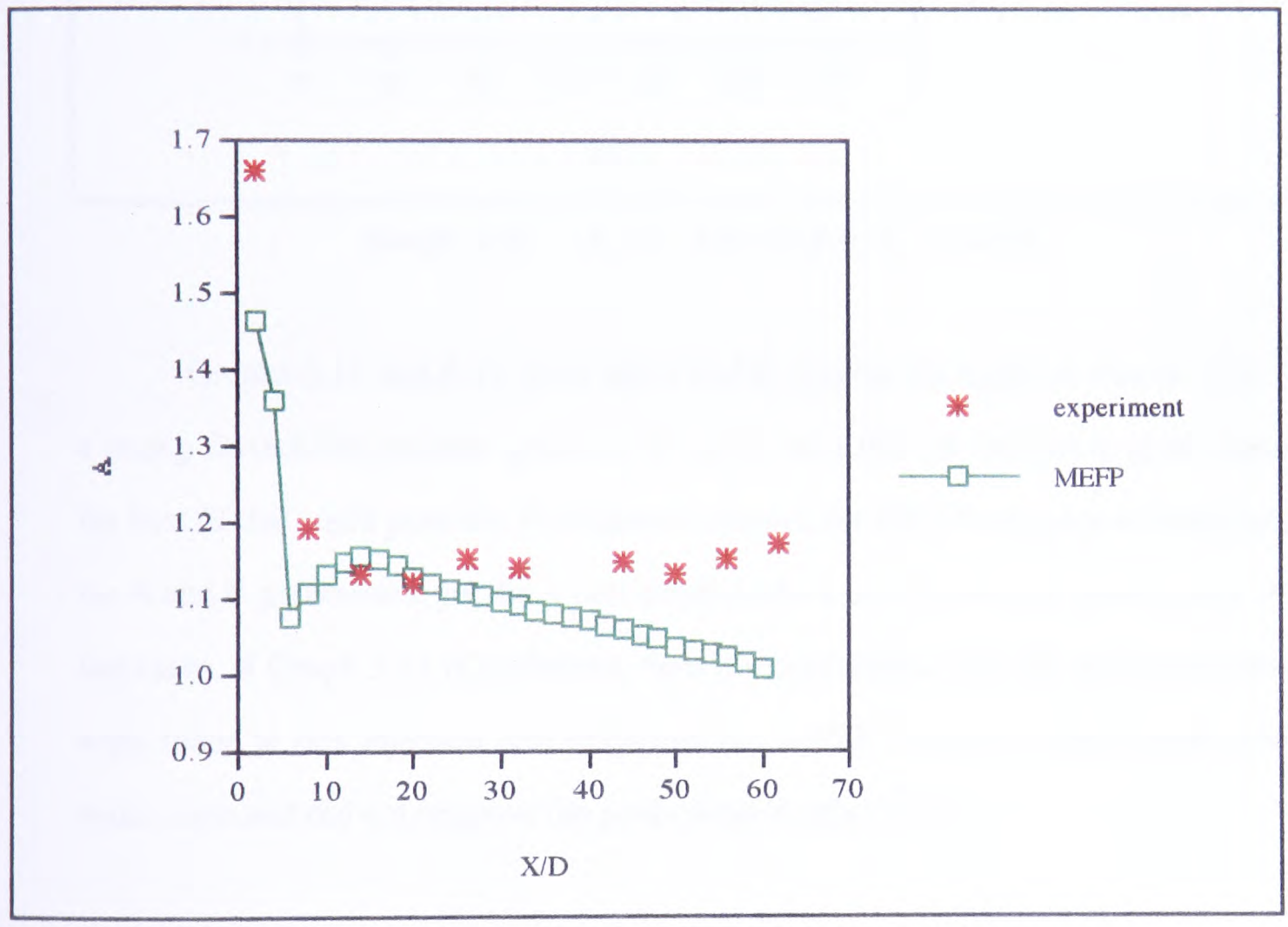


Graph 6.7 A vs. X/D (S.F.P.G., G=0.59)

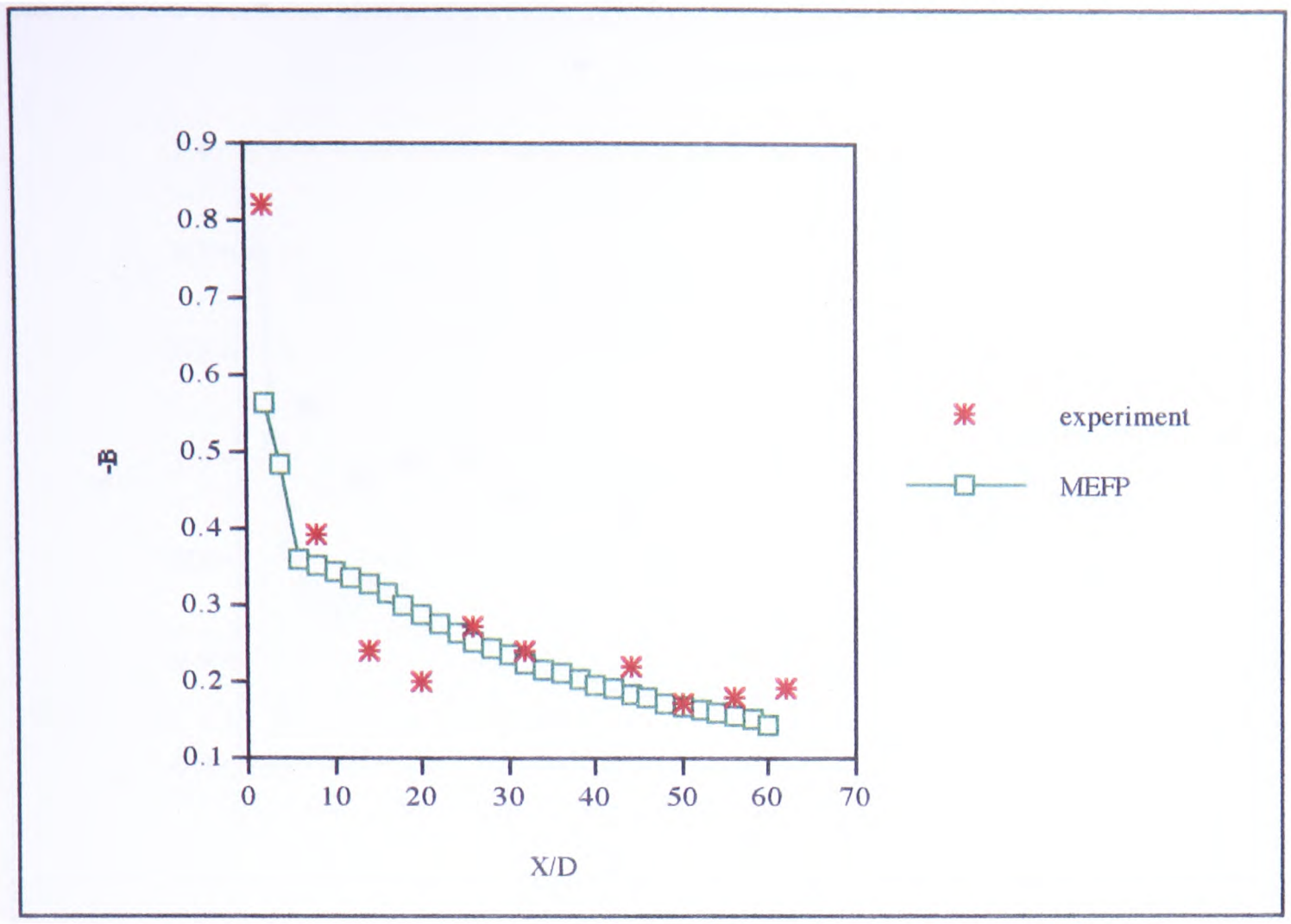


Graph 6.8 B vs. X/D (S.F.P.G., G=0.59)

Graphs 6.9 and 6.10 show the A and B data for the injection rate of 0.75 with a strong favourable pressure gradient. The agreement of the first data point in both plots is not very good. The agreement is also not very good in the case of the A values that are located far downstream of the point of injection. Further changes in the value of the magnitude of the turbulence augmentation, k_1 and in the value of the axial decay factor, k_2 did not improve the correlations. Unfortunately, Teekaram did not provide any experimental Nusselt number data at this injection rate. Therefore, any measure of improvement in the prediction of the heat transfer using the optimized mass shed ratio and turbulence augmentation constants can not be gauged.

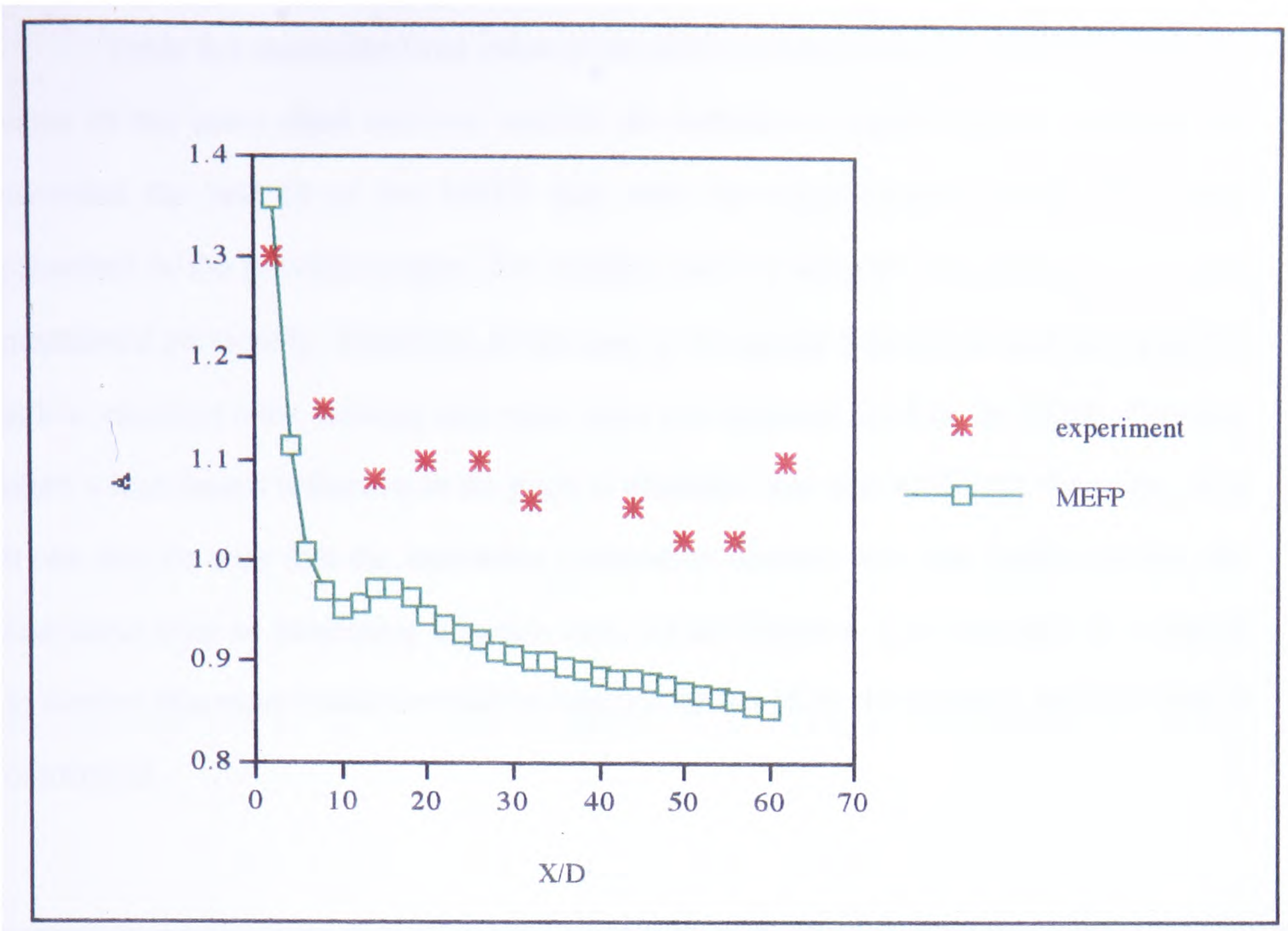


Graph 6.9 A vs. X/D (S.F.P.G., G=0.75)

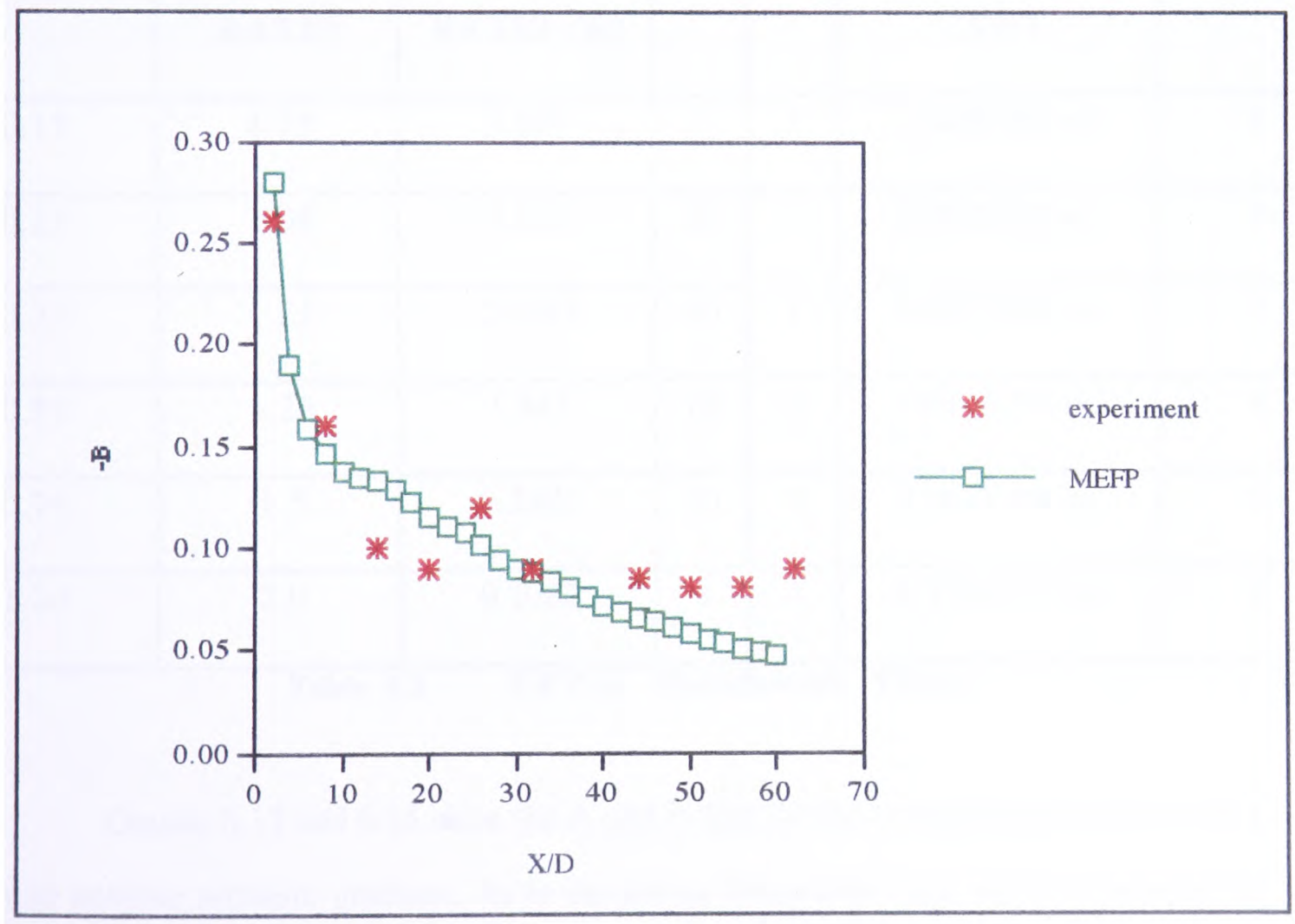


Graph 6.10 B vs. X/D (S.F.P.G., G=0.75)

Graphs 6.11 and 6.12 show the A and B data for the injection rate of 1.20 with a strong favourable pressure gradient. It can be said that the following plots represent the best fit that could possibly be achieved between the MEFP and experimental data for the A and B parameters, yet the A plot displays the worst correlation seen in any of the test cases. If Graph 5.11 is consulted, then it would appear that the improvements that were made at this injection rate improved the MEFP Nusselt number predictions in some areas and did not improve the predictions in other areas.



Graph 6.11 A vs. X/D (S.F.P.G., G=1.20)



Graph 6.12 B vs. X/D (S.F.P.G., G=1.20)

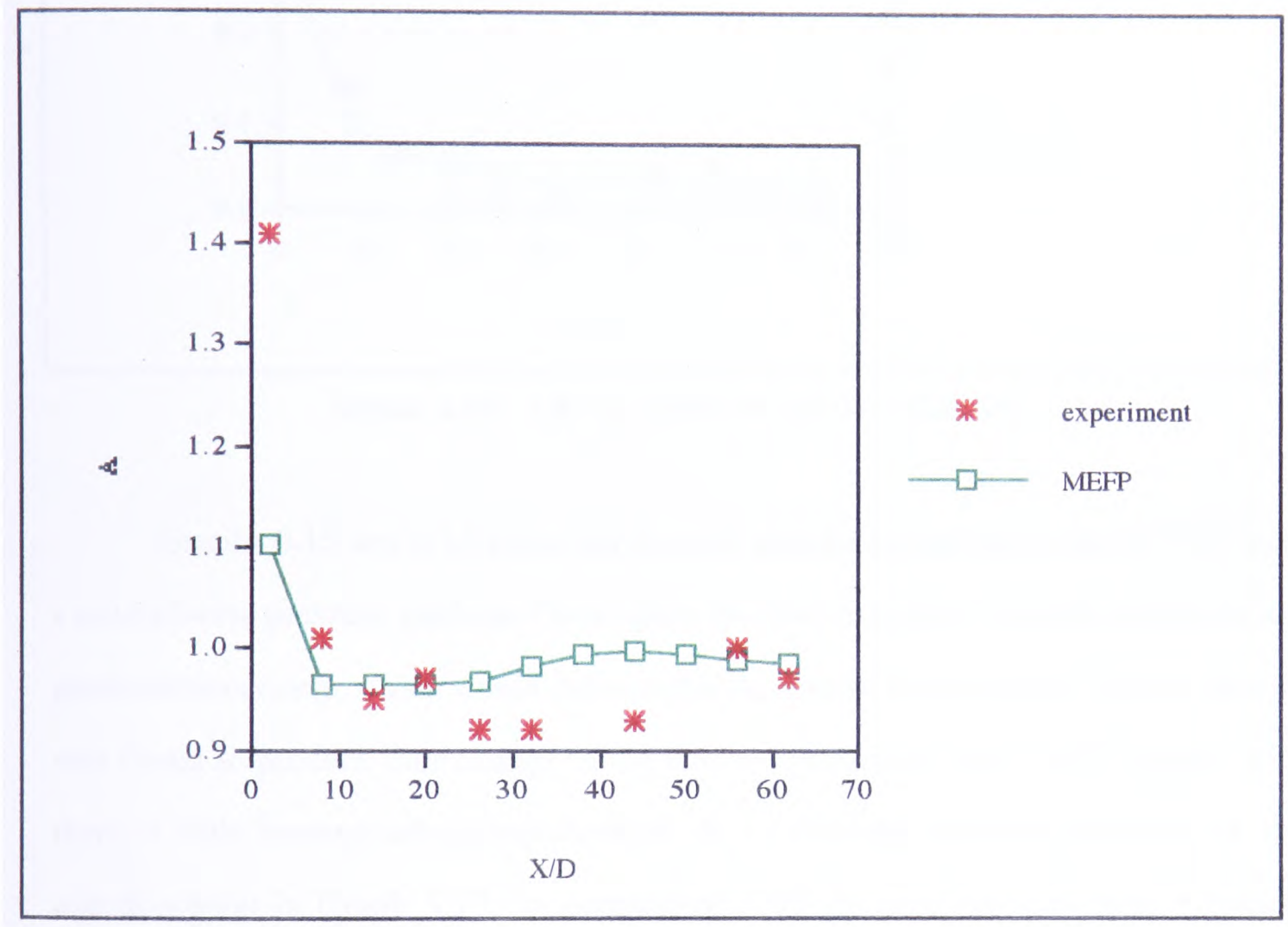
Table 6.1 shows the final value of the pitch to diameter ratio, which controls the value of the mass shed ratio, as well as the turbulence augmentation constants that provided the best fit of the MEFP data with the experimental data for the cases presented in the previous pages. The original pitch to diameter ratio was 2.5, as was mentioned previously. Therefore, in the case of the strong favourable pressure gradient at low injection rates, halving this value gave the optimum fit. For the higher injection rates, a less drastic reduction in the pitch to diameter ratio was sufficient. From the table it can also be seen that the increasing penetration distance and grid point number are consistent with an increasing injection rate. As the injection rate increases, it is logical to assume that more coolant would be injected farther from the surface, and this fact is confirmed.

INJECTION RATE (G)	PITCH TO DIAMETER RATIO	MASS SHED RATIO (K)	k_1	k_2	PENETRATION DISTANCE (PD)	GRID PT. #
0.15	1.25	3.669	1	1	2.542E-05 m.	2
0.25	1.25	3.293	10	1	5.084E-05 m.	3
0.35	1.25	2.8585	10	1	5.084E-05 m.	3
0.59	1.25	1.861	10	1	1.017E-04 m.	4
0.75	1.5	0.5505	10	1	4.067E-04 m.	6
1.20	2.0	0.2082	1	1	1.271E-03 m.	8

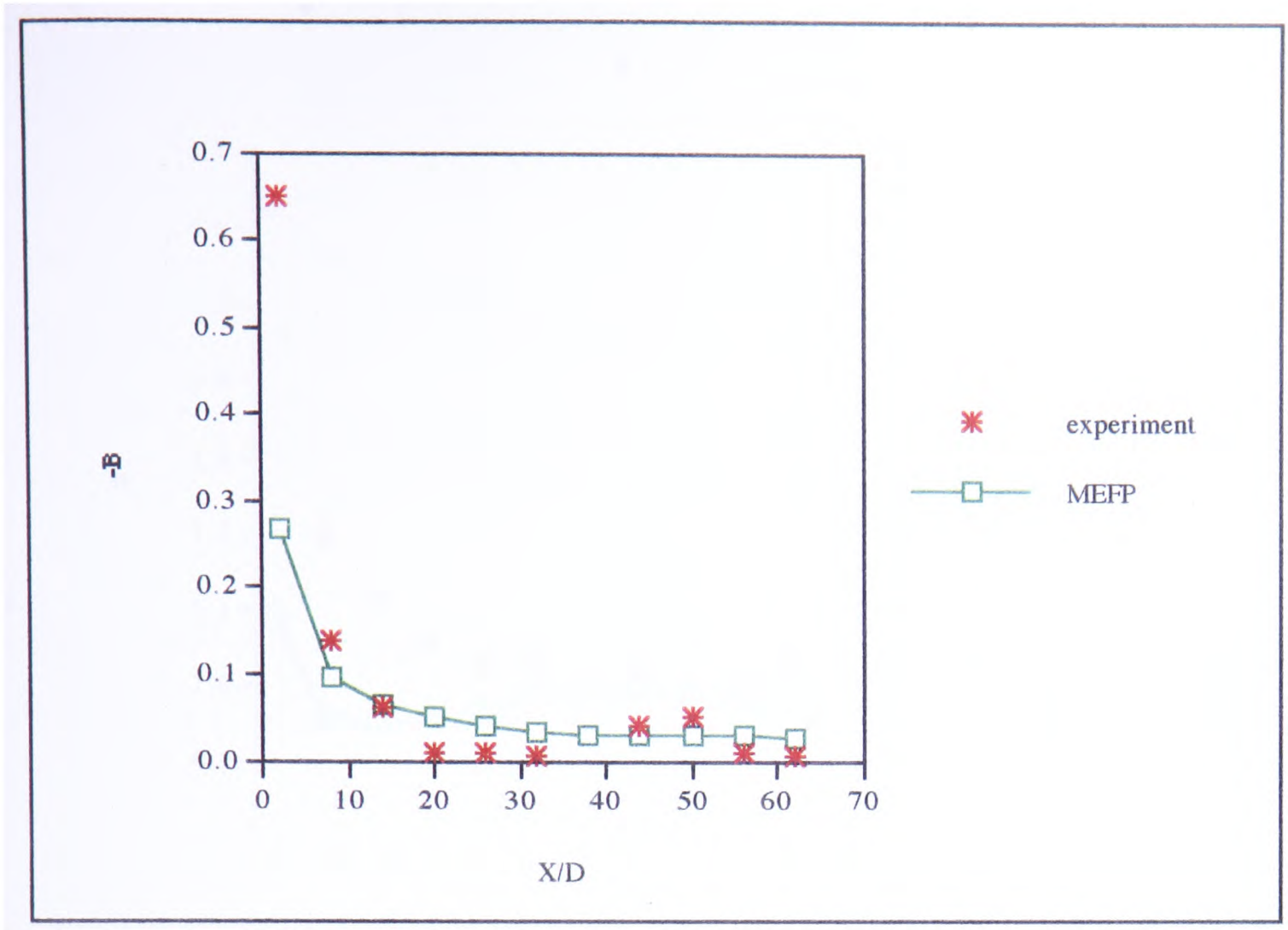
Table 6.1 S.F.P.G. Optimization Values

Graphs 6.13 and 6.14 show the A and B data for the lowest injection rate with a mild adverse pressure gradient. As in the strong favourable case, what is depicted in these two graphs is the best fit of the MEFP data to the experimental data that was achieved for both the A and B parameters. The first data point on both graphs is not

predicted accurately, which would indicate that k_1 should be increased even higher than the current value. Such a change was found to produce little change in the relevant parameters and show no improvement beyond what is shown here. This would explain why there is little corresponding improvement in the Nusselt number prediction at the injection point in Graph 5.16. The downstream points are predicted quite accurately and there is a corresponding agreement between the MEFP and experimental predictions in the Nusselt number.

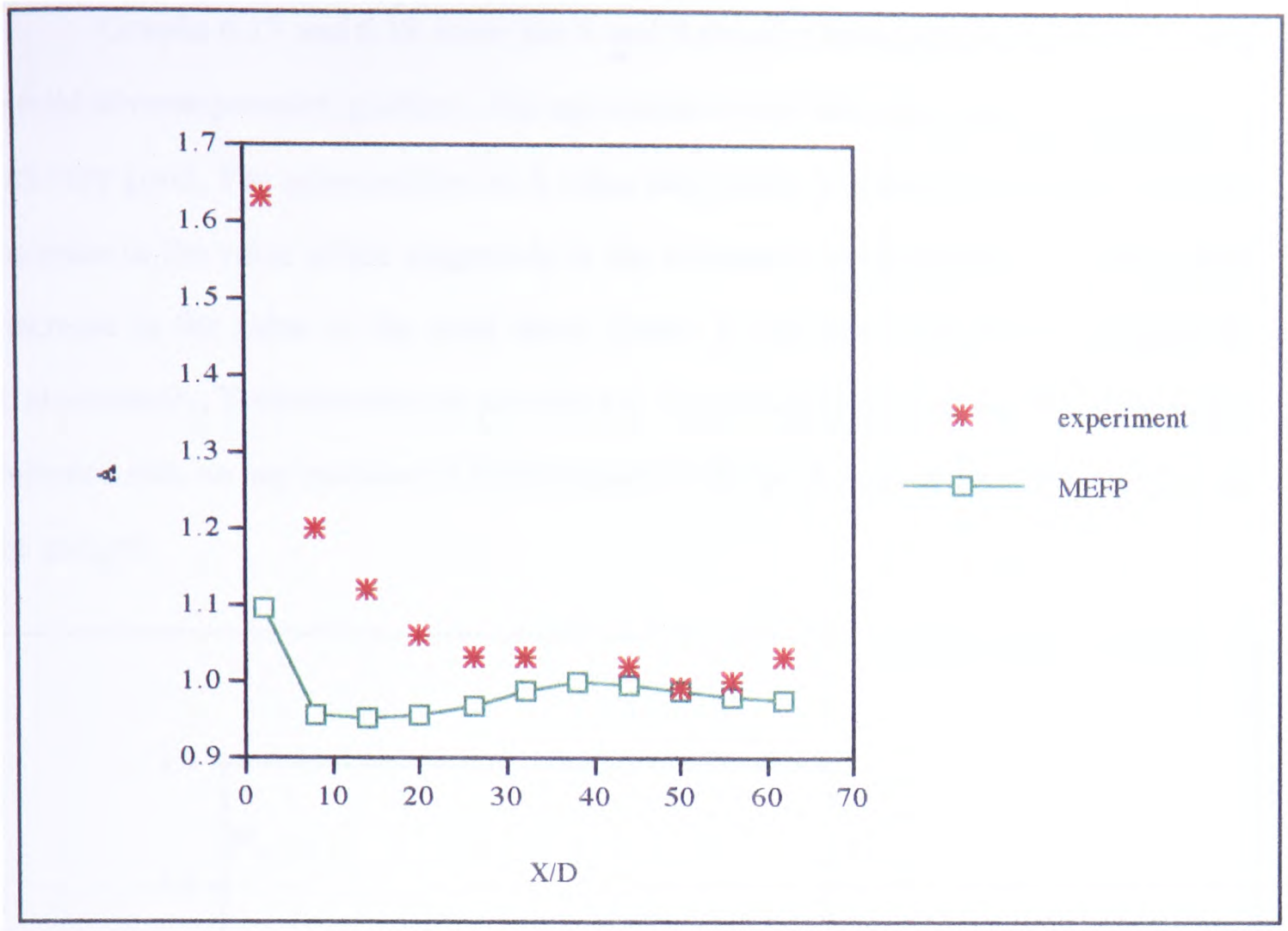


Graph 6.13 A vs. X/D (M.A.P.G., G=0.15)

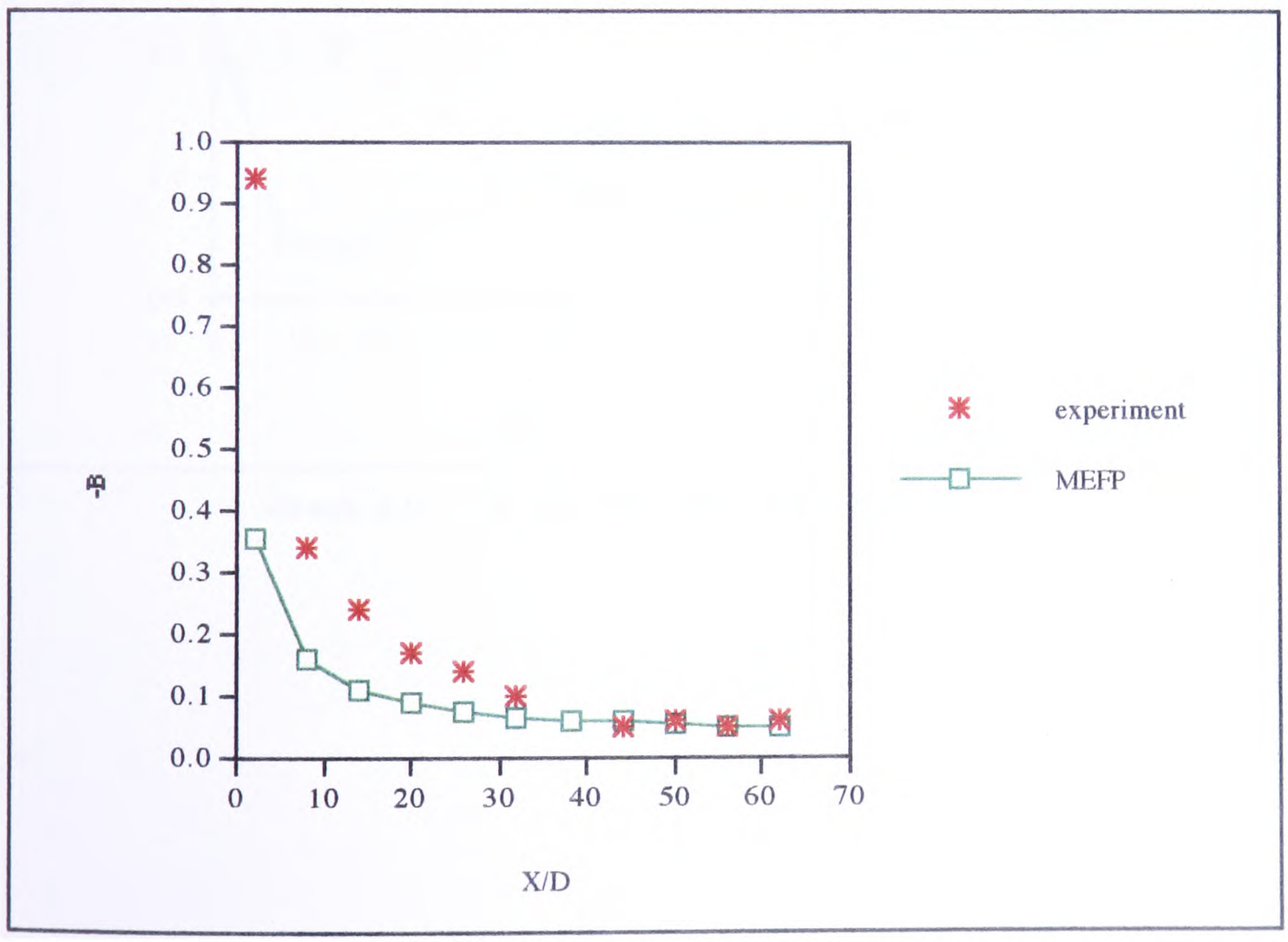


Graph 6.14 B vs. X/D (M.A.P.G., G=0.15)

Graphs 6.15 and 6.16 show the A and B data for the injection rate of 0.25 with a mild adverse pressure gradient. Once again, the first data point on both graphs is not predicted accurately, which would indicate that k_1 should be increased. Such a change was found to produce little change in the relevant parameters and would explain why there is little corresponding improvement in the Nusselt number prediction at the injection point in Graph 5.17. In comparison with the previous test case, a greater improvement can be seen in the prediction of the Nusselt number at the injection point with the improved film cooling model. Whereas, the downstream points do not appear to be as accurate as in the previous case, which a reduction in the axial decay factor should rectify. No change was noted in the A or B values with a reduction in the value of k_2 and the Nusselt number remained unchanged downstream of the injection point.

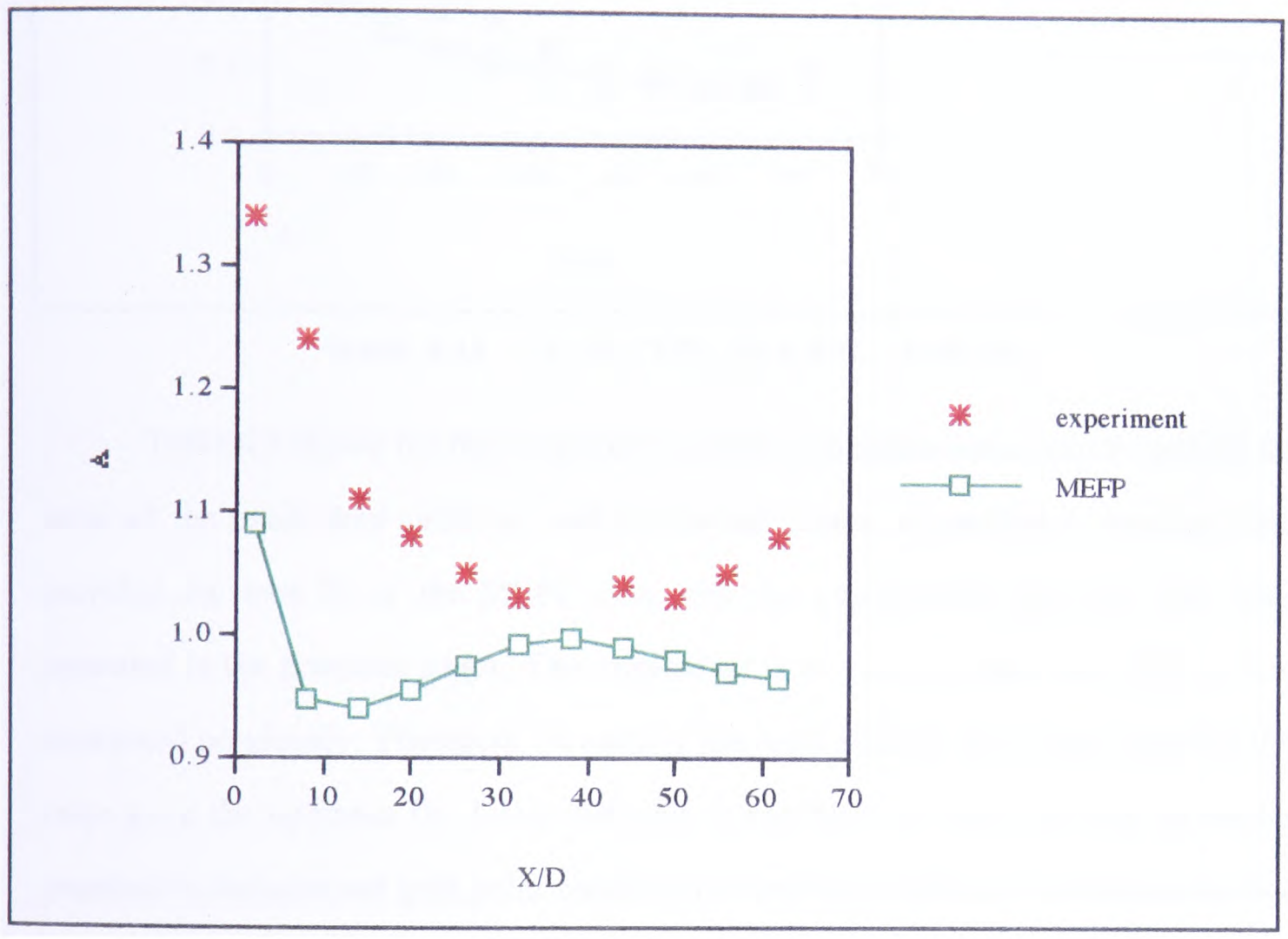


Graph 6.15 A vs. X/D (M.A.P.G., G=0.25)

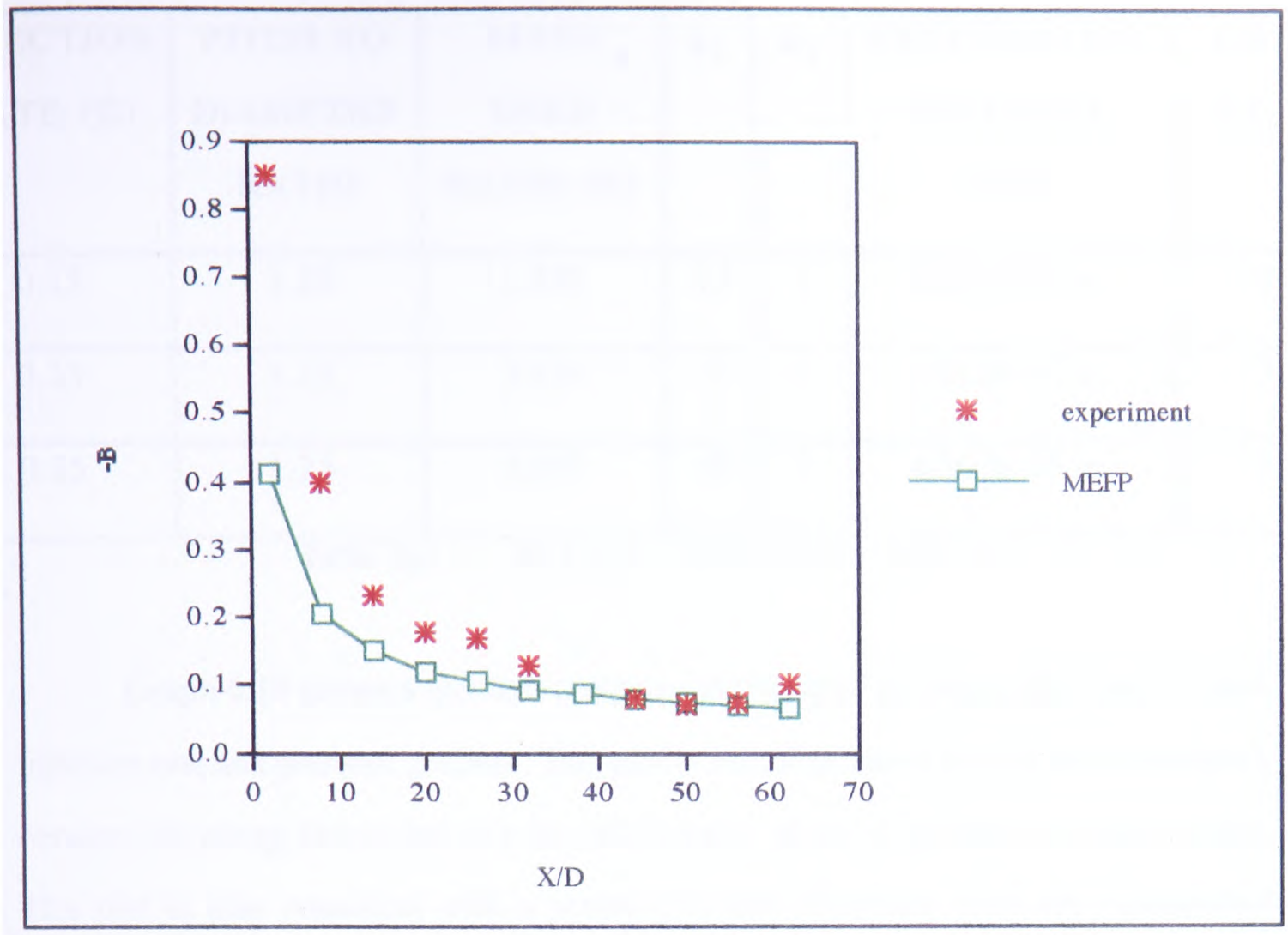


Graph 6.16 B vs. X/D (M.A.P.G., G=0.25)

Graphs 6.17 and 6.18 show the A and B data for the injection rate of 0.35 with a mild adverse pressure gradient. The agreement of the first data point in both plots is not very good. The agreement in the A value data points is also not very good. Further increase in the value of the magnitude of the turbulence augmentation, k_1 and further decrease in the value of the axial decay factor, k_2 did not improve the correlations. Unfortunately, Teekaram did not provide any experimental Nusselt number data at this injection rate, so any measure of improvement in the prediction of heat transfer can not be gauged.



Graph 6.17 A vs. X/D (M.A.P.G., G=0.35)



Graph 6.18 B vs. X/D (M.A.P.G., G=0.35)

Table 6.2 shows the final value of the pitch to diameter ratio, which controls the value of the mass shed ratio, as well as the turbulence augmentation constants that provided the best fit of the MEFP data with the experimental data for the cases presented in the previous pages. The original pitch to diameter ratio was 2.5, as was mentioned previously. Therefore, in each of the mild adverse test cases, halving this value gave the optimum fit. From the table it can also be seen that the increasing penetration distance and grid point number are consistent with an increasing injection rate. It is logical to assume that more coolant would be injected farther from the surface as the injection rate increases, and this fact is confirmed. These results are also comparable to the results seen previously for the strong favourable pressure gradient.

INJECTION RATE (G)	PITCH TO DIAMETER RATIO	MASS SHED RATIO (K)	k_1	k_2	PENETRATION DISTANCE (PD)	GRID PT. #
0.15	1.25	3.738	10	1	2.281E-05 m.	2
0.25	1.25	3.438	10	1	4.562E-05 m.	3
0.35	1.25	3.083	10	1	4.562E-05 m.	3

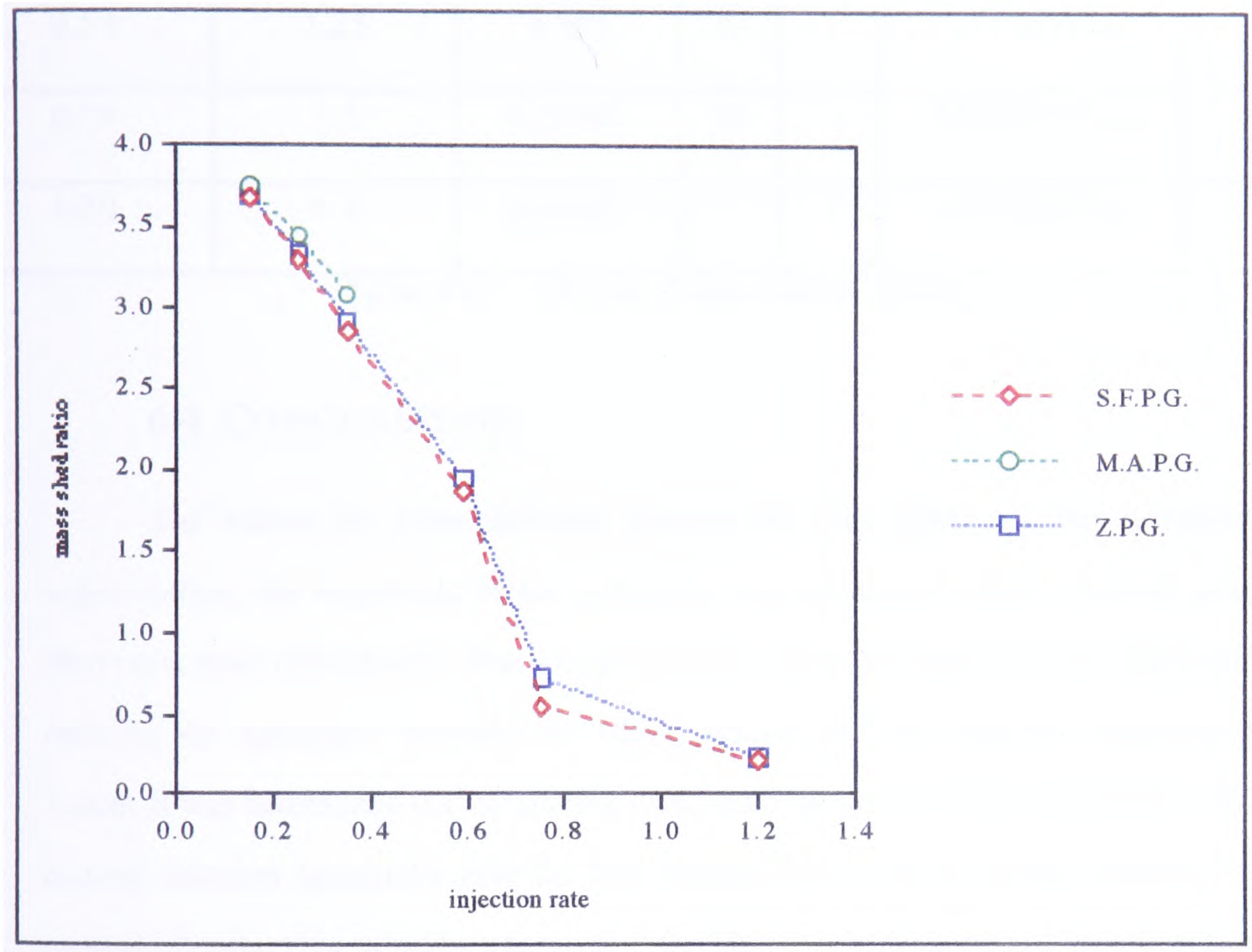
Table 6.2 M.A.P.G. Optimization Values

Graph 6.19 shows a plot that compares the value of the mass shed ratio at each injection rate and pressure gradient. This plot is useful in that it proves the consistency between the strong favourable and the mild adverse pressure gradient test case results. This plot is also consistent with a similar plot that Crawford **(ref.19)** constructed based on his results. The similarities and differences between the Crawford film cooling model and the film cooling model that was used in this investigation were discussed previously.

Finally, the plot confirms what is intuitively expected to happen when the penetration distance increases. With high injection rates, the coolant is injected farther from the surface or the wall than is the case with low injection rates. In other words, the coolant would be carried into a larger number of vertical grid points from the surface or the wall at a high injection rate than at a low injection rate. The mass flow that is "shed" from each consecutive vertical grid point is smaller at high injection rates because the coolant is spread over more grid points. This effect is the dominant factor in determining the trend of mass shed ratio with injection rate regardless of the fact that with increasing injection rate there is more mass flow to be "shed" (which would indicate that with higher injection rates come higher values of mass shed ratio).

Graph 6.19 also includes the mass shed ratio data at each injection rate for the zero pressure gradient test case. This test case was selected and carried out at the end of this investigation. Its sole purpose was to confirm that MEFP predicted the expected

results. The zero pressure gradient data would be expected to fall between the data from the strong favourable pressure gradient test case and the data from the mild adverse pressure gradient test case. It is clear that the plot of the MEFP predictions confirm this result. Table 6.3 shows the final optimization values of the pitch to diameter ratio, the mass shed ratio, the penetration distance of the coolant, and the turbulence augmentation constants that provided the best fit of the MEFP data with the zero pressure gradient experimental data.



Graph 6.19 Mass Shed Ratio vs. Injection Rate

INJECTION RATE (G)	PITCH TO DIAMETER RATIO	MASS SHED RATIO (K)	k_1	k_2	PENETRATION DISTANCE (PD)	GRID PT. #
0.15	1.25	3.6815	1	1	4.424E-05 m.	2
0.25	1.25	3.3245	10	1	4.424E-05 m.	2
0.35	1.25	2.912	10	1	8.848E-05 m.	3
0.59	1.25	1.943	10	1	1.77E-04 m.	4
0.75	1.5	0.71855	10	1	3.539E-04 m.	5
1.20	1.8	0.23635	1	1	1.416E-03 m.	7

Table 6.3 Z.P.G. Optimization Values

6.4 CONCLUSIONS

The values for three different factors, the axial decay of the turbulence augmentation, the magnitude of the turbulence augmentation, and the constant mass shed ratio, were individually altered in an attempt to find the value for each that would optimize the agreement between the MEFP results and the available experimental results. It was determined that by altering these three factors, the heat transfer in a film cooling situation (especially near the film cooling holes) can be greatly altered. The method of optimizing the values for each of the above factors was made by inspection, was identical in each case, and proved to be relatively easy in spite of being time consuming. From the results that were presented here, it is evident that this method was successful and did in fact provide the best possible means for improving and developing the existing film cooling model in MEFP.

The analysis of the behavior that the alteration of the two turbulence augmentation constants produced in many different numerical combinations at each injection rate and pressure gradient also provided valuable insight into how this particular film cooling model makes predictions. Changes in the turbulence

augmentation constants, k_1 and k_2, did produce the desired effects that were described earlier, but they also produced some effects that were not expected as well. For instance, when the magnitude of the turbulence augmentation was left unaltered and the axial decay factor was either increased or decreased, then the desired effects were easily generated exactly in the way that was described earlier in this chapter. However, when the magnitude of the turbulence augmentation was increased, an unforeseen secondary effect was produced. When the first data point on the A and B plots was raised by an increase in k_1, then the second data point also increased a small amount in the comparison to the first point. The third data point would also increase a very small amount. In short, an increase in the value of k_1 would also generate the equivalent response to a decrease in k_2 when in fact, no such decrease was programmed in the dataset.

The introduction of the turbulence augmentation routine and the optimization of the constant mass shed ratio was a successful approach for the purpose of improving and developing the film cooling model in MEFP. Significant improvements were made in the prediction of the two factors that define heat transfer, A and B, as well as the Nusselt number predictions that were seen in the previous chapter. Of primary importance were the improvements made in the predictions of the relevant parameters in the neighbourhood of the film cooling hole(s). The eventual success in this area exceeded all initial projections. The only area that did not meet with much success in improvement were some of the traditional problem areas that were discussed at the outset of this chapter. Further future development of this film cooling model or possibly the development of a more advanced film cooling model can improve the predictions for the mild adverse pressure gradient test cases at high injection rates.

CHAPTER 7. RT27A TURBINE BLADE CFD CASES

7.1 TEST CASES

The RT27A test cases served as an effective transition between the ILPT test cases where the geometry of interest was a flat plate and the CHTT test cases where the geometry was a complex, fully three-dimensional turbine blade. Each test case was programmed to run for 400 passes which took approximately 6 hours on a Silicon Graphics Indigo2 computer. This number of passes was chosen because it was found to give adequate convergence of the relevant parameters in all cases, while still maintaining as low a computing time as possible. Surface data of the relevant parameters were collected on the suction surface and the pressure surface from the leading edge to the trailing edge of the blade.

All of the MEFP test results were compared to the experimental data that Horton **(ref.44)** collected. Therefore, the boundary and initial conditions were chosen to coincide exactly with those used by him in his experimental testing. He provided Mach number and heat transfer coefficient data for the non-film cooled test case and heat transfer enhancement ratio data for the film cooled test cases. The heat transfer enhancement ratio that is referred to here is defined as the film cooled heat transfer coefficient divided by the non-film cooled heat transfer coefficient. Figure 7.1 shows a scale representation of the RT27A turbine blade. The locations on the blade surface that are marked and designated by the letters correspond to the film cooling locations. Horton referred to these different cooling schemes as "Builds", and they will be referred to as such from this point on. During Horton's experimental testing, the coolant flow was only present at one location or along one row of holes at a time, except in the case of the leading edge cooling (Build A), or the combination cooling schemes (Build J and Build E).

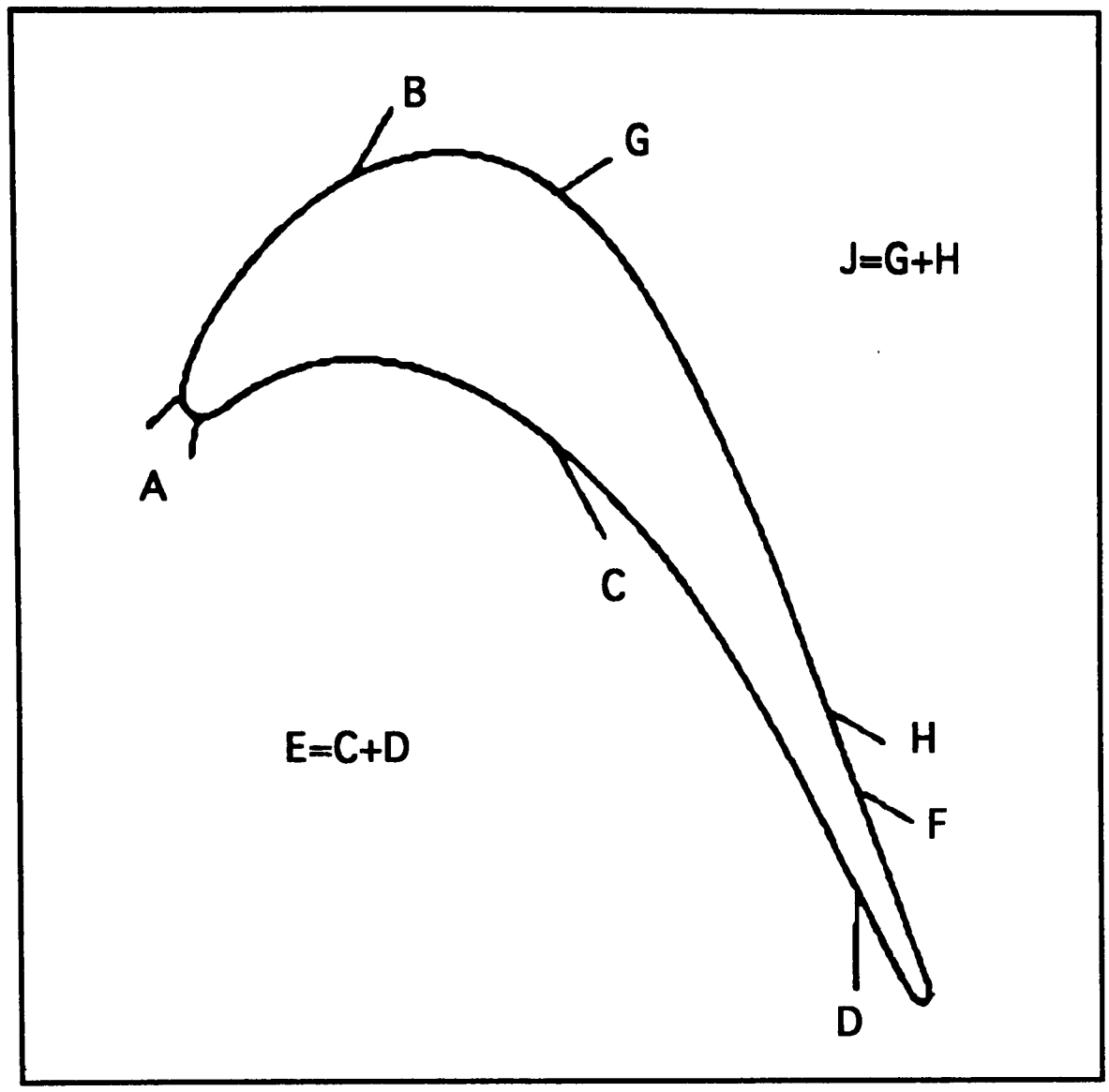


Figure 7.1 RT27A Cascade Geometry
(reference: D. Phil. Thesis by F.G. Horton, 1985)

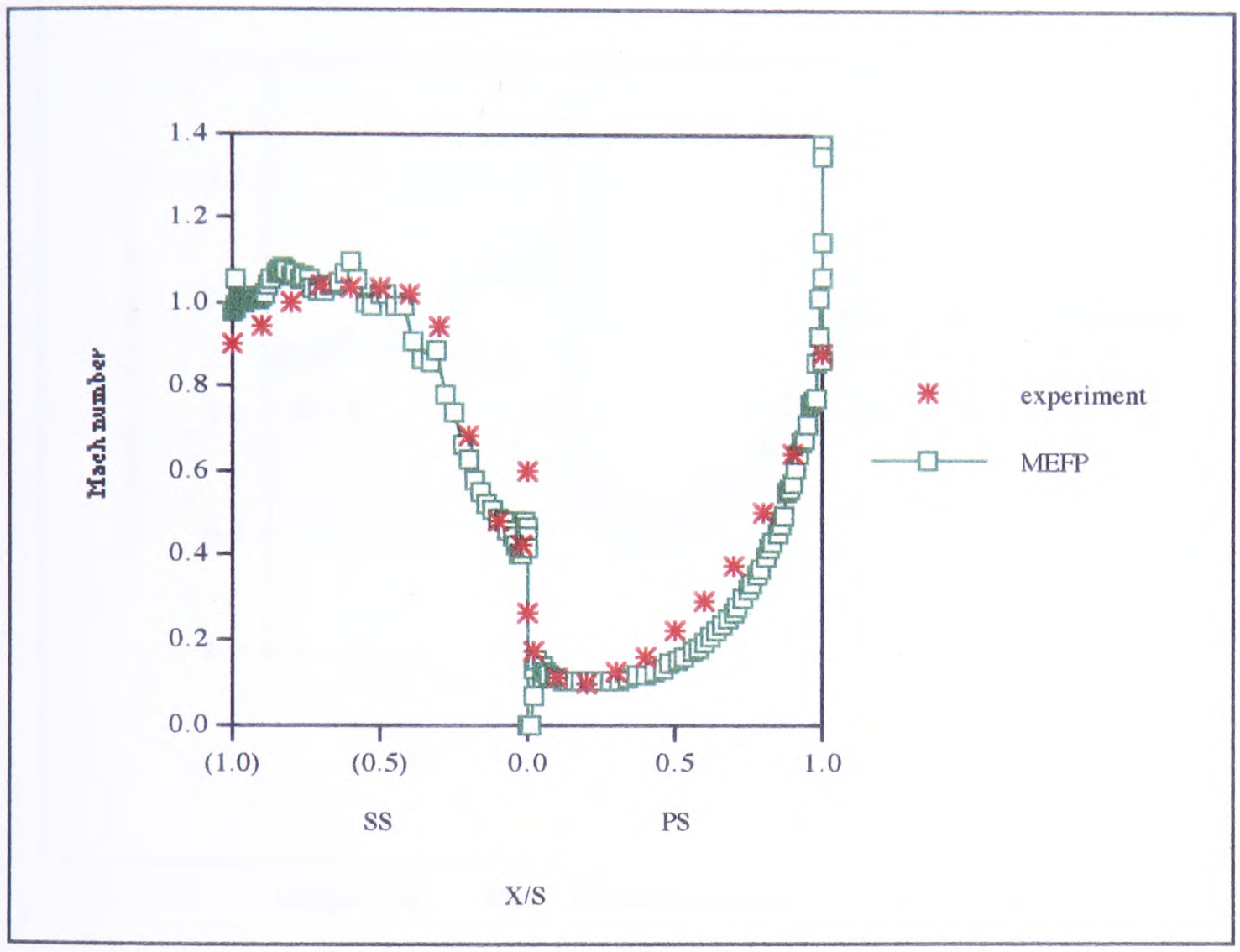
7.2 Discussion of Results

7.2.1 Non-Film Cooled Results

Horton chose to define the heat transfer coefficient in a different way than Teekaram, whose data were presented earlier. Teekaram **(ref.89)** used the recovery temperature in his definition which can be confirmed in Eqn.5.1. Horton did not define the heat transfer coefficient in this way, and instead defined it according to Eqn.7.1. The MEFP output was programmed to match Horton's definition in an effort to correlate the MEFP results with the experimental results.

$$h = \frac{\dot{q}}{(T_{t\infty} - T_w)} \qquad (7.1)$$

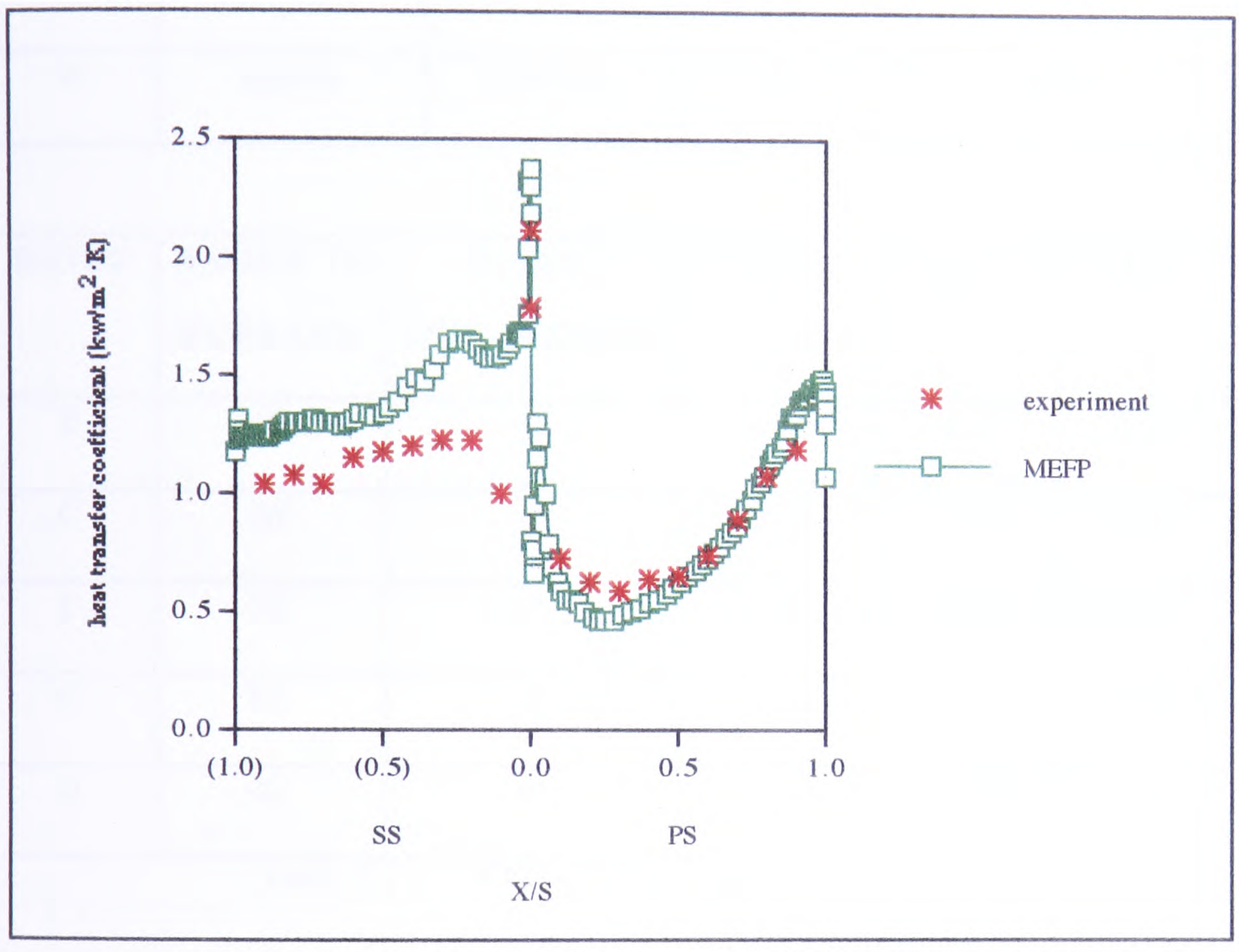
Graph 7.1 shows the Mach number correlation data for the non-film cooled test case. The agreement that is demonstrated in this plot is very important. As was stated previously, the code must be able to accurately predict the Mach number if it is to have any hope of accurately predicting all other relevant flow parameters, such as the heat transfer. It can be seen that MEFP does in fact, successfully predict the value of the Mach number at all positions along the suction surface and the pressure surface of the blade.



Graph 7.1 Mach Number Correlation

Graph 7.2 shows the heat transfer coefficient data for the non-film cooled test case. It can be seen that the prediction is accurate and shows the correct trend on the pressure surface of the blade. However, on the suction surface of the blade the prediction is not very accurate, even though the MEFP data and the experimental data exhibit similar trends. Near the trailing edge of the blade on the suction surface, the error is on the order of 20 percent. This error increases in the upstream direction toward

the leading edge. One source of this error lies in the fact that for simplicity, MEFP defined the flow as fully turbulent over the entire suction surface of the blade from the leading edge to the trailing edge. In reality and under experimental conditions, the flow was initially laminar, then transitional, followed by fully turbulent. This fact explains why the difference between the MEFP data and the experimental data is greater near the leading edge than the trailing edge.



Graph 7.2 Heat Transfer Coefficient Correlation

7.2.2 Film Cooled Results

Table 7.1 shows the values of the relevant film cooling parameters for the five different Builds that were selected for the MEFP film cooling testing. These Builds were selected based solely on the criterion that there was sufficient experimental data provided by Horton **(ref.44)** for the purpose of comparison with the MEFP results.

BUILD	SURFACE	HOLE DIAMETER	# OF HOLES	PITCH TO DIAMETER RATIO
B	suction	0.64 mm.	21	3.0
C	pressure	0.64 mm.	14	4.55
D	pressure	0.64 mm.	14	4.55
G	suction	0.64 mm.	14	4.55
H	suction	0.64 mm.	14	4.55

BUILD	ANGLE TO SURFACE	RADIAL INCLINATION	LOCAL MACH #	X/C_{ax}	X/S
B	40°	0°	0.80	0.25	0.23
C	30°	0°	0.15	0.5	0.37
D	30°	0°	0.5	0.85	0.77
G	55°	0°	0.98	0.5	0.39
H	30°	0°	1.02	0.82	0.74

Table 7.1 RT27A Film Cooling Parameters

Table 7.2 shows the injection rates that were selected for the testing of each Build. These injection rates were chosen based on the values that are representative of those found in real gas turbine engines. Furthermore, the injection rates were also chosen based on the ILPT results that were presented earlier.

The pressure surface of a turbine blade is commonly represented by a mild adverse pressure gradient on a flat plate, and the suction surface of a turbine blade is commonly represented by a strong favourable pressure gradient on a flat plate. The selected injection rates for Build C and Build D, which are both located on the pressure surface, corresponded to the lowest injection rate that Horton tested and the upper limit

of the code's capability. For the Builds that are located on the suction surface, the injection rates were selected based on the fact that in real turbine engines, injection rates tend to be on the order of one or higher, with slightly lower injection rates near the trailing edge.

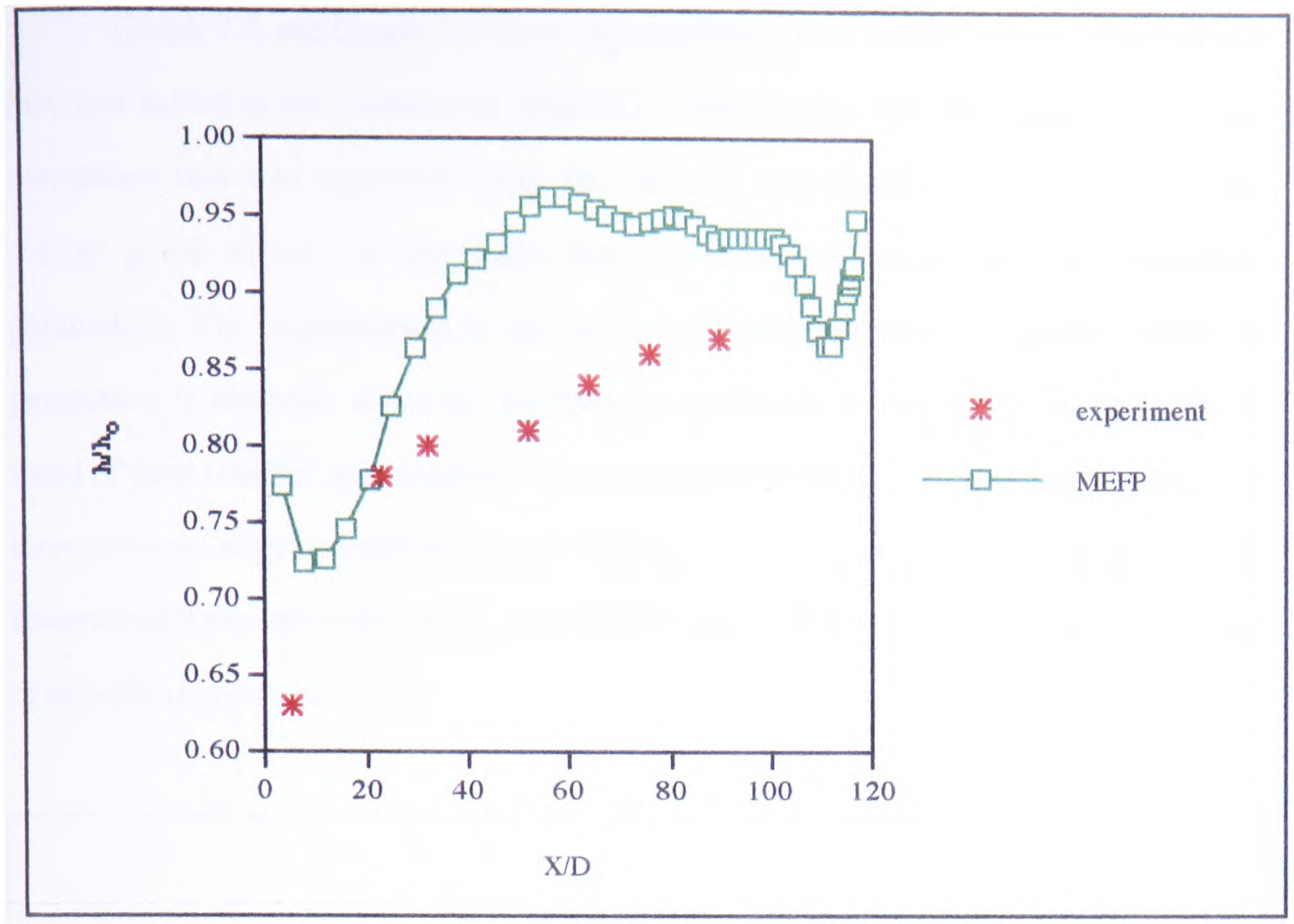
BUILD	INJECTION RATE (G)
B	0.92
C	0.36
D	0.36
G	1.07 1.44
H	0.71 1.07

Table 7.2 RT27A Test Matrix

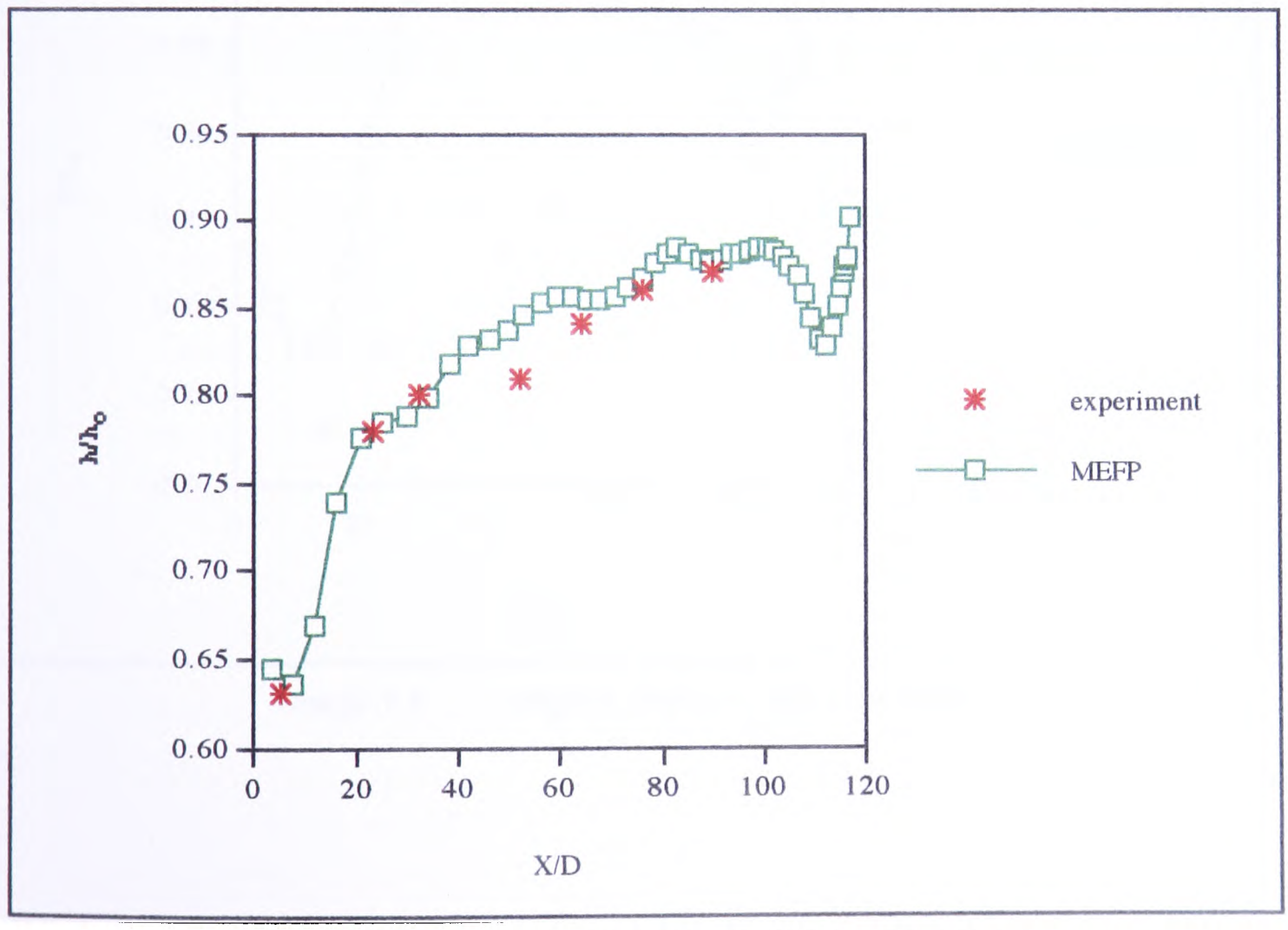
Each of the test cases that are presented here were first run with the exact experimental parameters that were reported in Tables 7.1 and 7.2. It was found that in each of the cases, the correlation between the experimental data and the MEFP data was not very good. Of course, in some cases the correlation was better than in the others. Improvement in the correlation of these test cases was sought by using the ILPT mass shed ratio optimization values, as well as the optimized turbulence augmentation constants. Great time and effort was spent finding the optimal mass shed ratio for a wide range of injection rates at different pressure gradients. This exercise was undertaken not to only to prove that the ILPT predictions could be improved by altering the mass shed ratio and adding turbulence augmentation, but also to eventually put the optimized values to use by improving the MEFP predictions in more complex test cases with film cooling present.

The improvement of the MEFP predictions consisted of estimating what an appropriate value of the mass shed ratio would be based on the corresponding ILPT data. A new value of the pitch to diameter ratio was computed by selecting a new value of the mass shed ratio according to pressure gradient and injection rate. It was stated previously that the strong favourable pressure gradient data were relevant to the suction surface and the mild favourable pressure gradient data were relevant to the pressure surface. Further minor improvements or alterations in the pitch to diameter ratio were needed in a small number of the cases. The discussion and examination of the relative success of this "first guess" in the optimization of the mass shed ratio is presented later in this section.

Graph 7.3 shows the heat transfer enhancement ratio correlation between Horton's experimental data and the MEFP data using the original experimental parameters. Graph 7.4 shows the heat transfer enhancement ratio correlation between Horton's experimental data and the MEFP data using the optimized film cooling parameters. It can be seen that the improvement between the two graphs is quite remarkable. The agreement seen in Graph 7.4 using the optimized parameters is very good, especially very close to the point of injection. It is very encouraging to see that MEFP was able to predict the heat transfer enhancement ratio correctly over the entire length of the blade's suction surface.

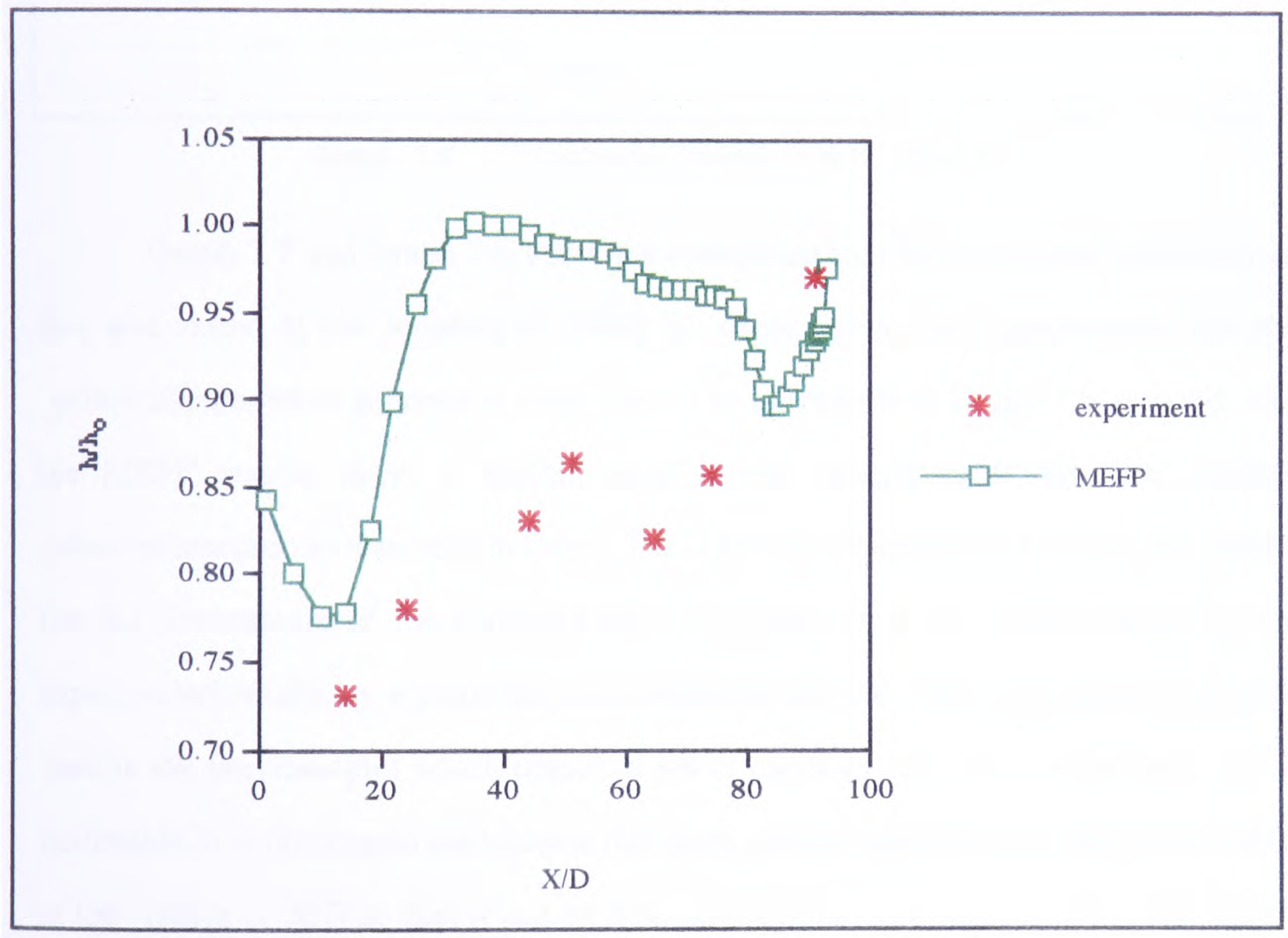


Graph 7.3 Original Build B h/h_o (G=0.92)

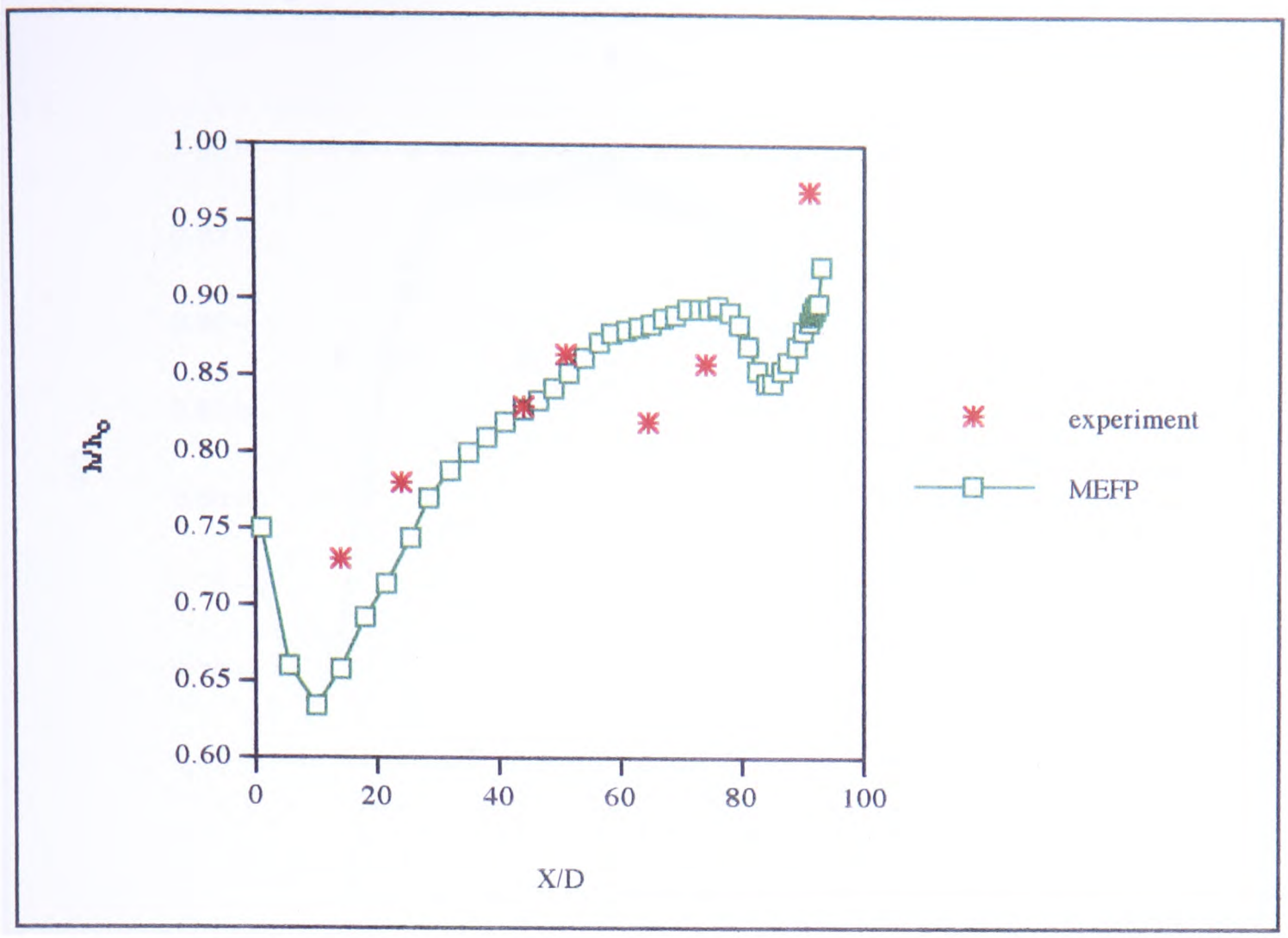


Graph 7.4 Optimized Build B h/h_o (G=0.92)

Graph 7.5 and Graph 7.6 show the correlation data for the lowest injection rate that was tested at the location of Build G. Once again, the first graph shows the correlation that was achieved using the original experimental parameters, and the second graph shows the correlation that was achieved using the final, optimized parameters. The improvement in the accuracy of the predictions with the optimized parameters is obvious. It can be said that the agreement is very good, and the overall trend of heat transfer enhancement ratio is correct in Graph 7.6. It is unfortunate that there were no experimental data points taken at a low value of X/D so that it can be determined if the low value of h/h_o that MEFP reports directly downstream of the point of injection is correct.

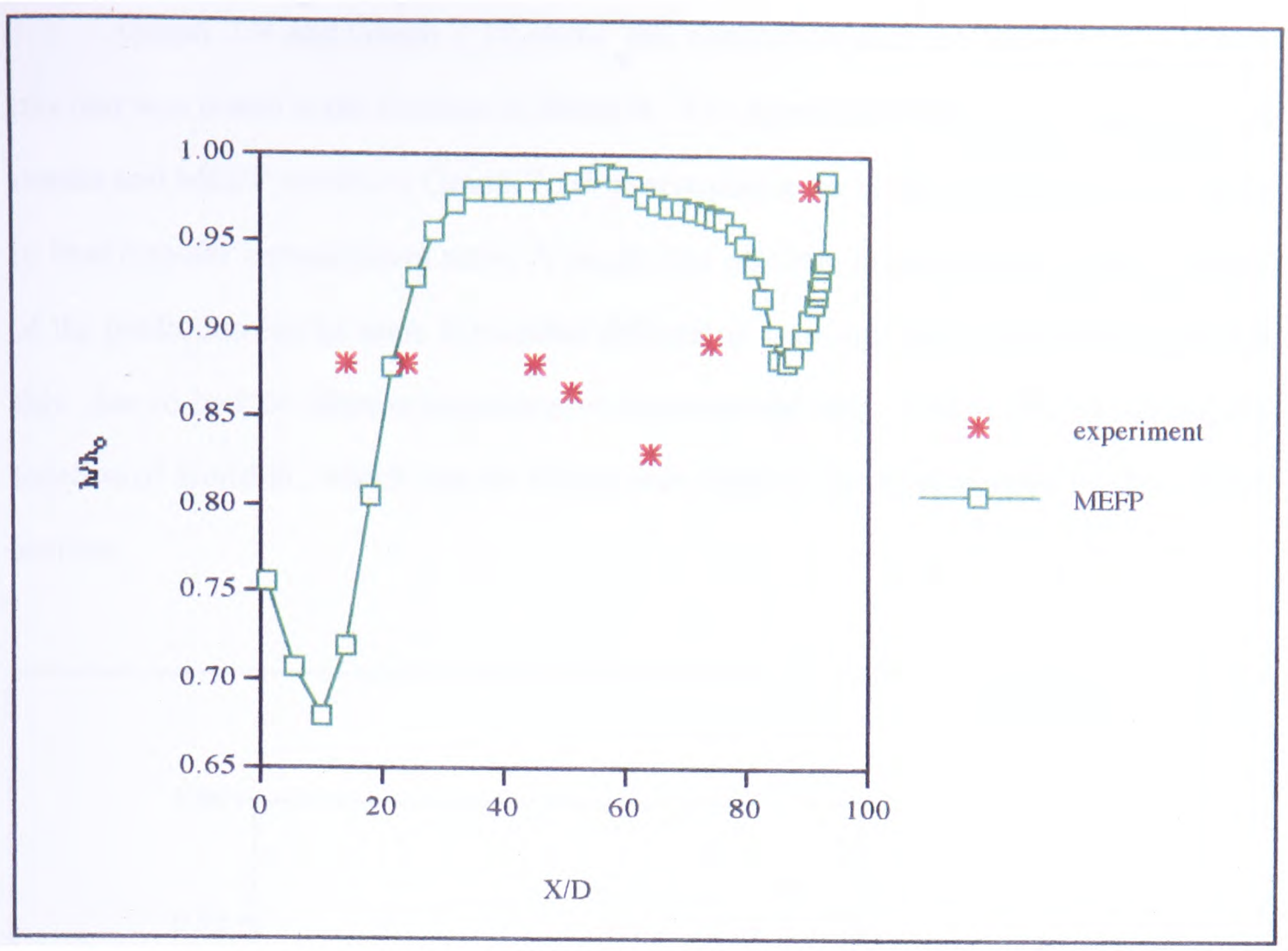


Graph 7.5 Original Build G h/h_o (G=1.07)

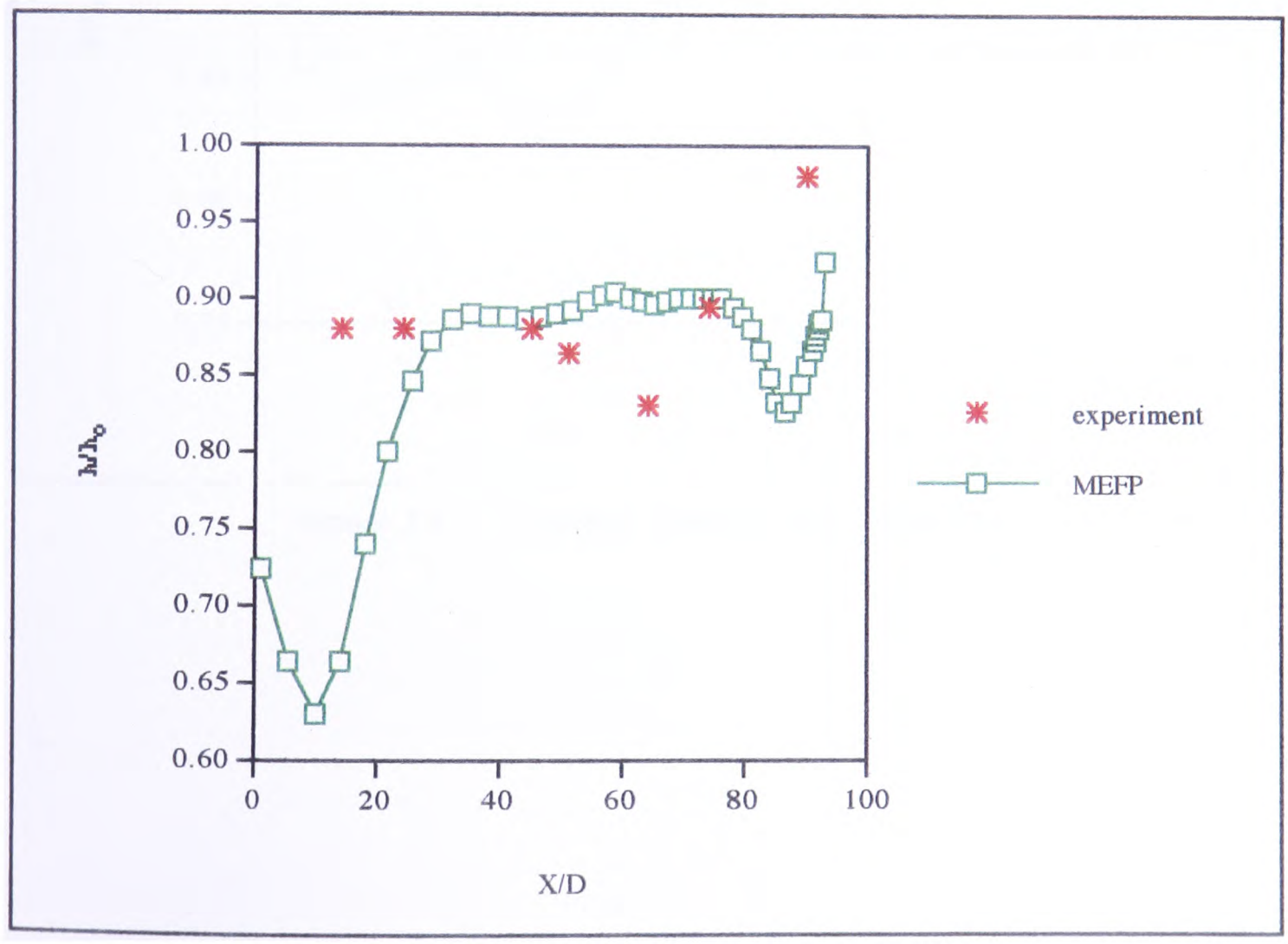


Graph 7.6 Optimized Build G h/h_o (G=1.07)

Graph 7.7 and Graph 7.8 show the correlation data for the highest injection rate that was tested at the location of Build G. Once again, the improvement that the optimized parameters generate is very clear. The agreement in Graph 7.8 is good, and the MEFP results show a similar trend in the prediction of the heat transfer enhancement ratio as was seen in Graph 7.6. The only discrepancy between the results lies far downstream of the cooling holes. It appears as if the MEFP results lag the experimental results by a particular and consistent amount. This discrepancy was also seen in the previous plot which depicts a lower injection rate, but was perhaps not as noticeable. It is once again unfortunate that there were no experimental data points taken at low values of X/D so that it can be determined if the low value of h/h_o that MEFP reports directly downstream of injection is correct.

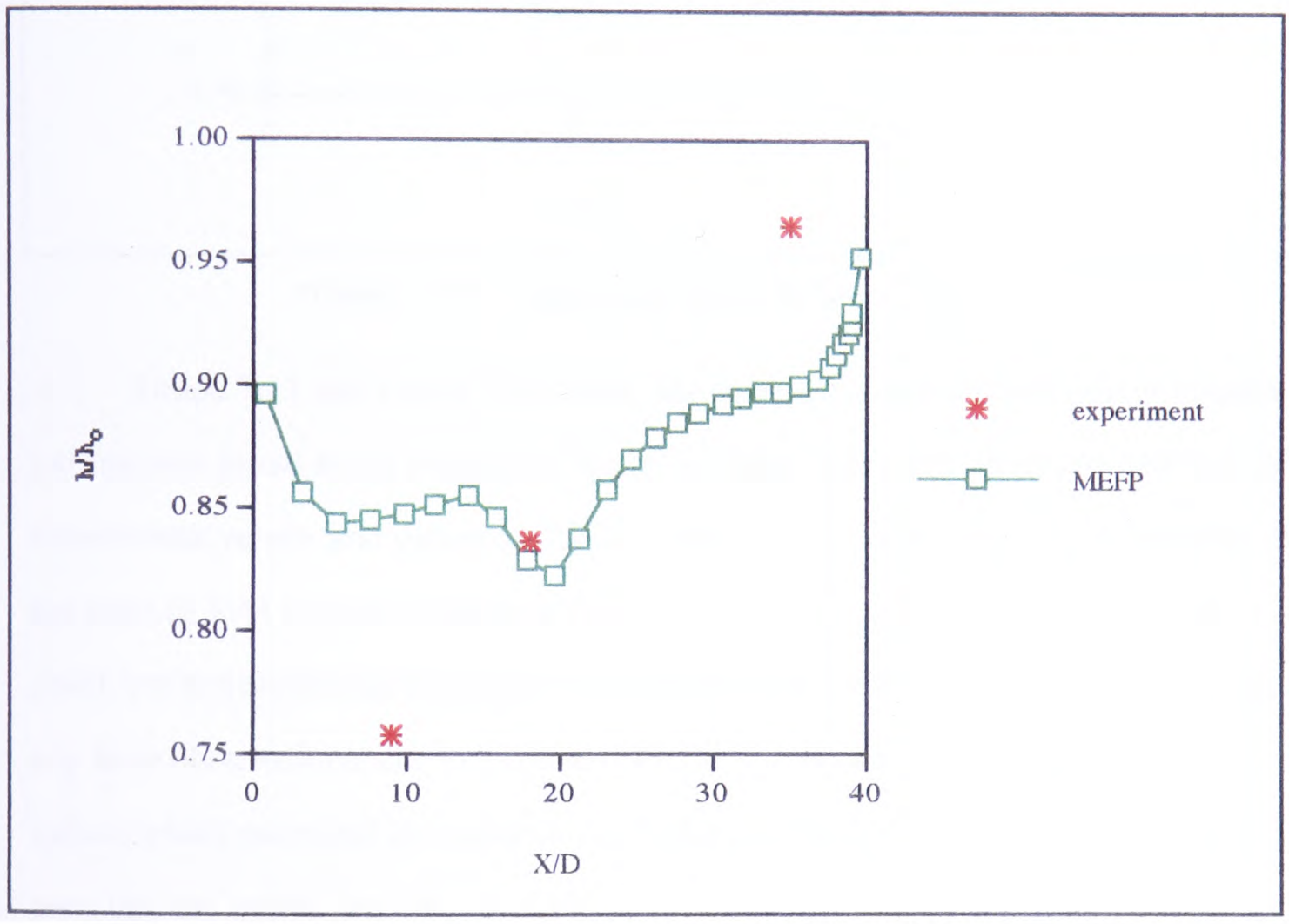


Graph 7.7 Original Build G h/h_o (G=1.44)

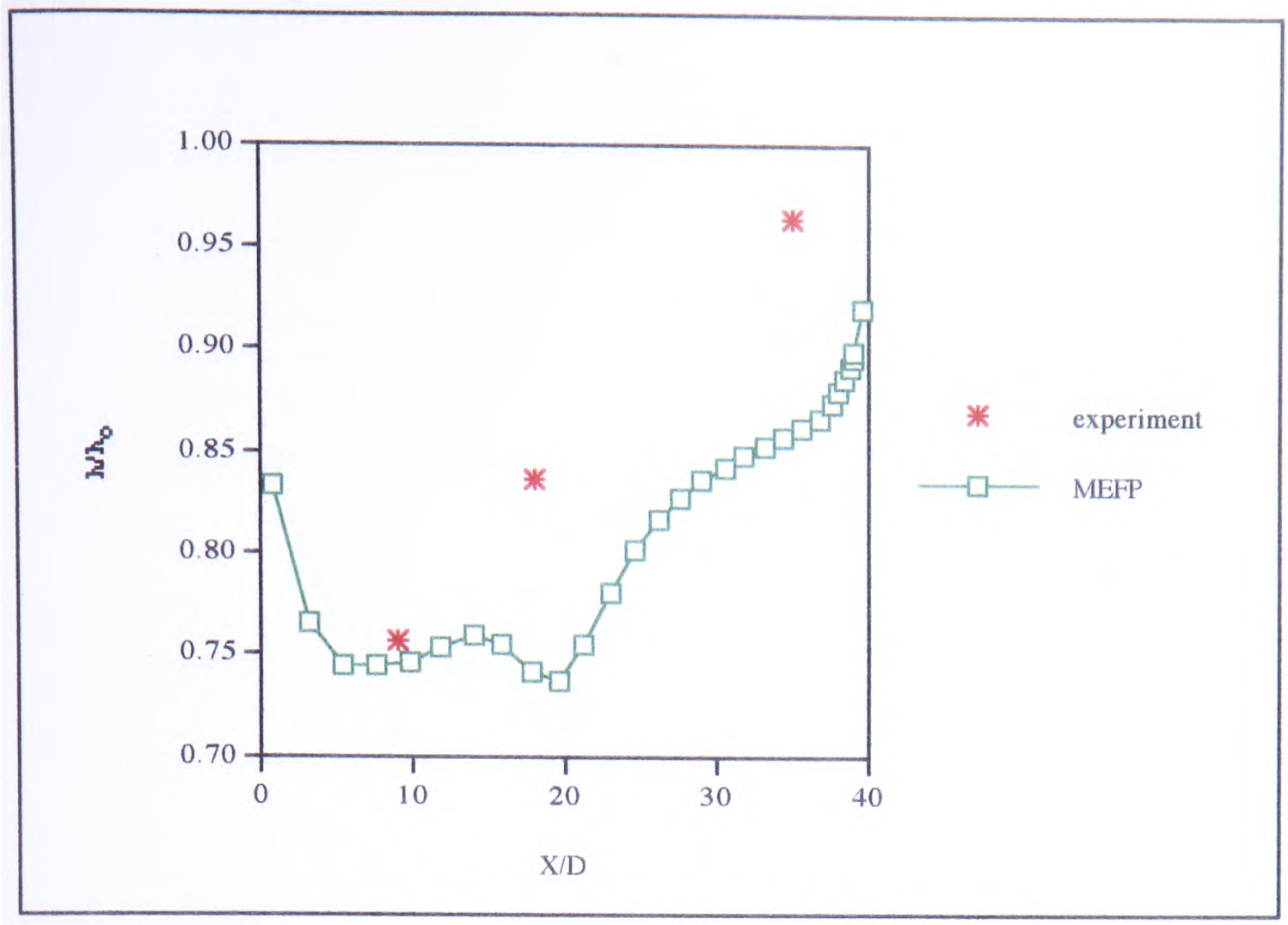


Graph 7.8 Optimized Build G h/h_o (G=1.44)

Graph 7.9 and Graph 7.10 show the correlation data for the lowest injection rate that was tested at the location of Build H. The agreement between the experimental results and MEFP results in Graph 7.10 is acceptable, as is the prediction of the trend in heat transfer enhancement ratio. A small, but obvious improvement in the accuracy of the prediction can be seen. It is rather difficult to draw any more conclusions beyond this, due to lack of more comprehensive experimental data. This is due in part to the location of Build H, which can be found very close to the trailing edge of the suction surface.

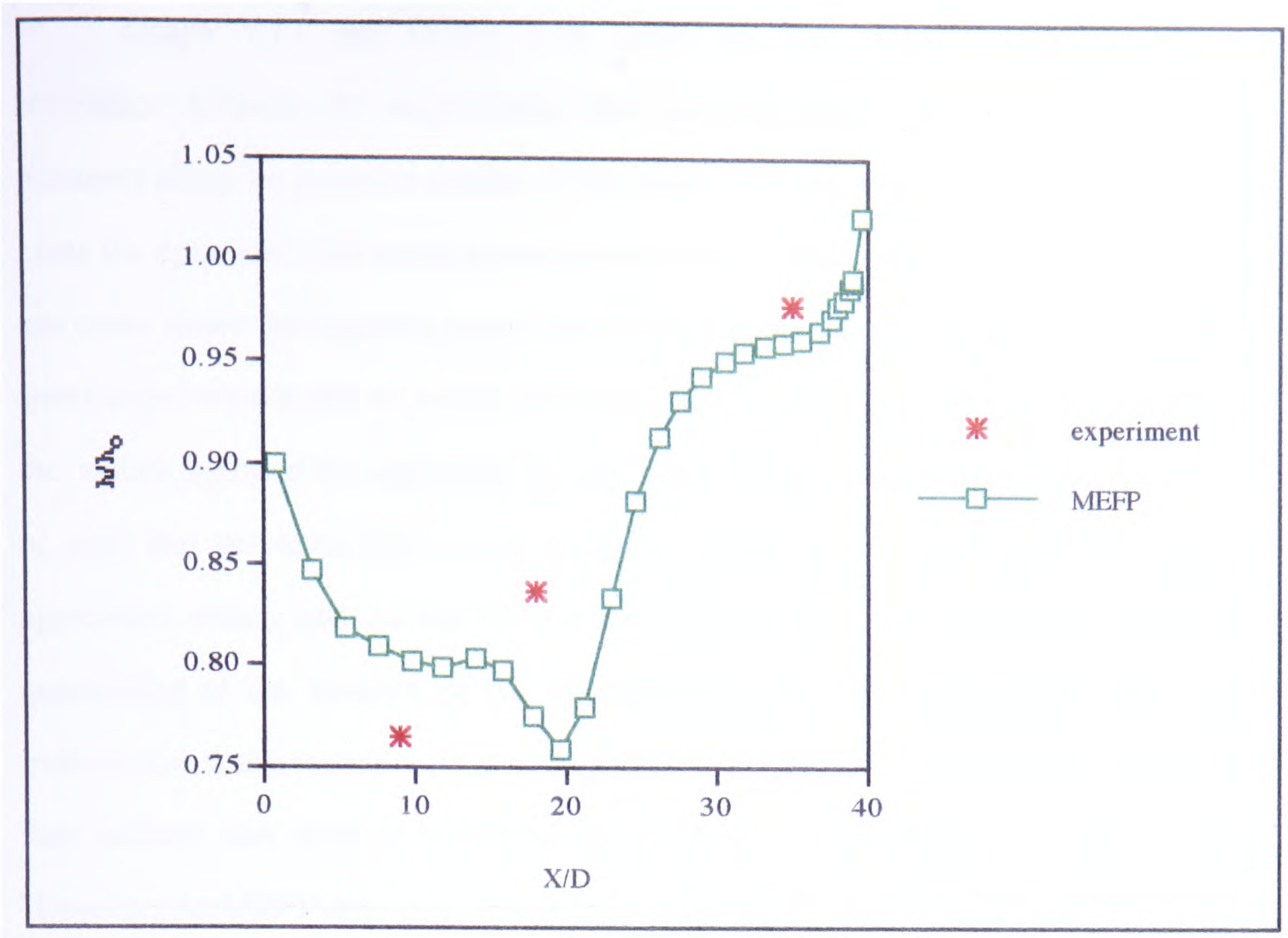


Graph 7.9 Original Build H h/h_o (G=0.71)

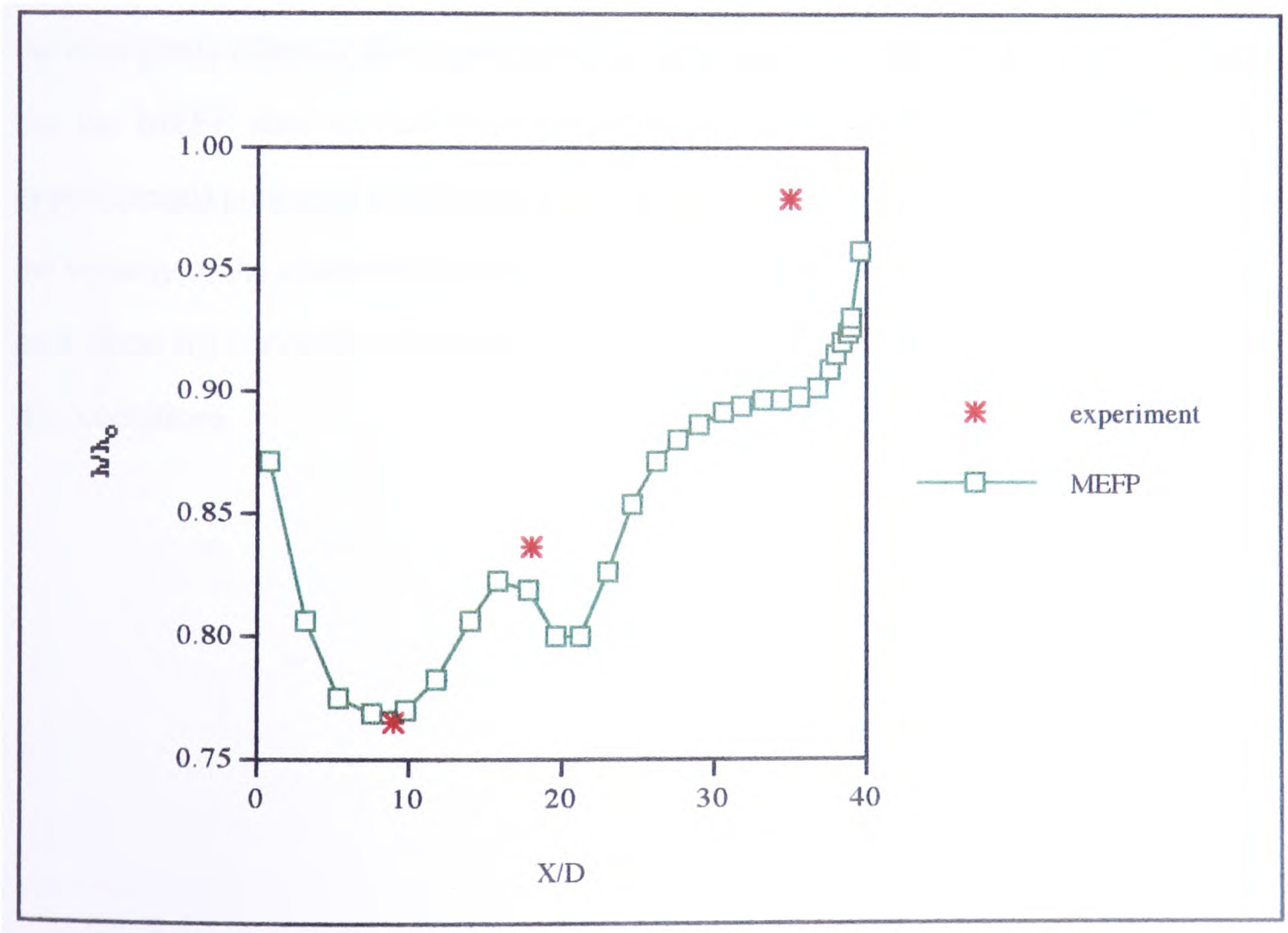


Graph 7.10 Optimized Build H h/h_o (G=0.71)

Graph 7.11 and Graph 7.12 show the correlation data for the highest injection rate that was tested at the location of Build H. Once again, the agreement between the experimental results and optimized MEFP results is acceptable, as is the prediction of the trend in heat transfer enhancement ratio. As in the previous test case, there is a small, but noticeable improvement in the experimental correlation. It is difficult to make any more observations, due to position of Build H near the trailing edge of the suction surface which prevented the collection of further experimental data. However, it can be seen that the trends depicted in Graphs 7.10 and 7.12 are very similar, which is obviously the expected outcome.

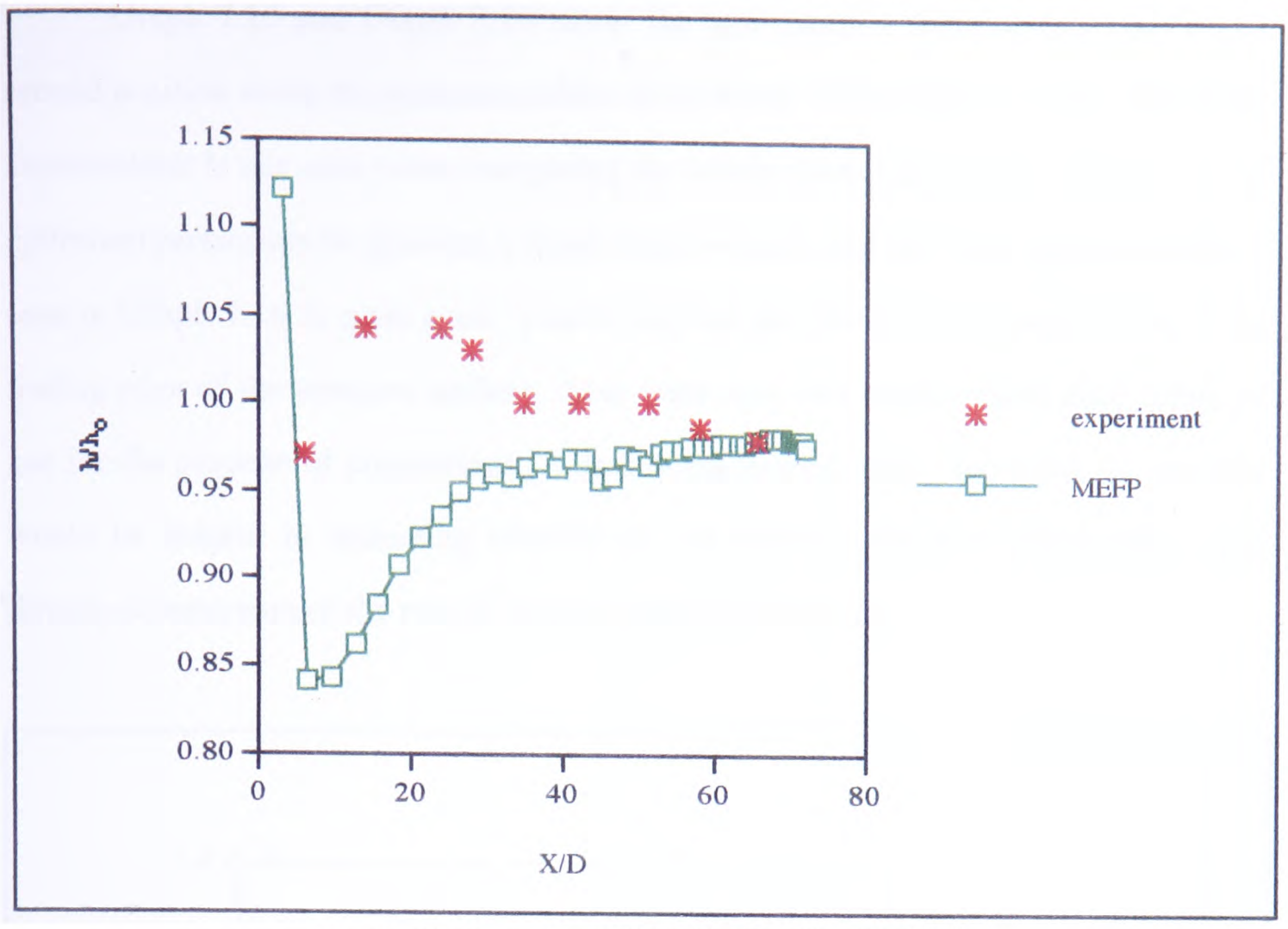


Graph 7.11 Original Build H h/h_o (G=1.07)

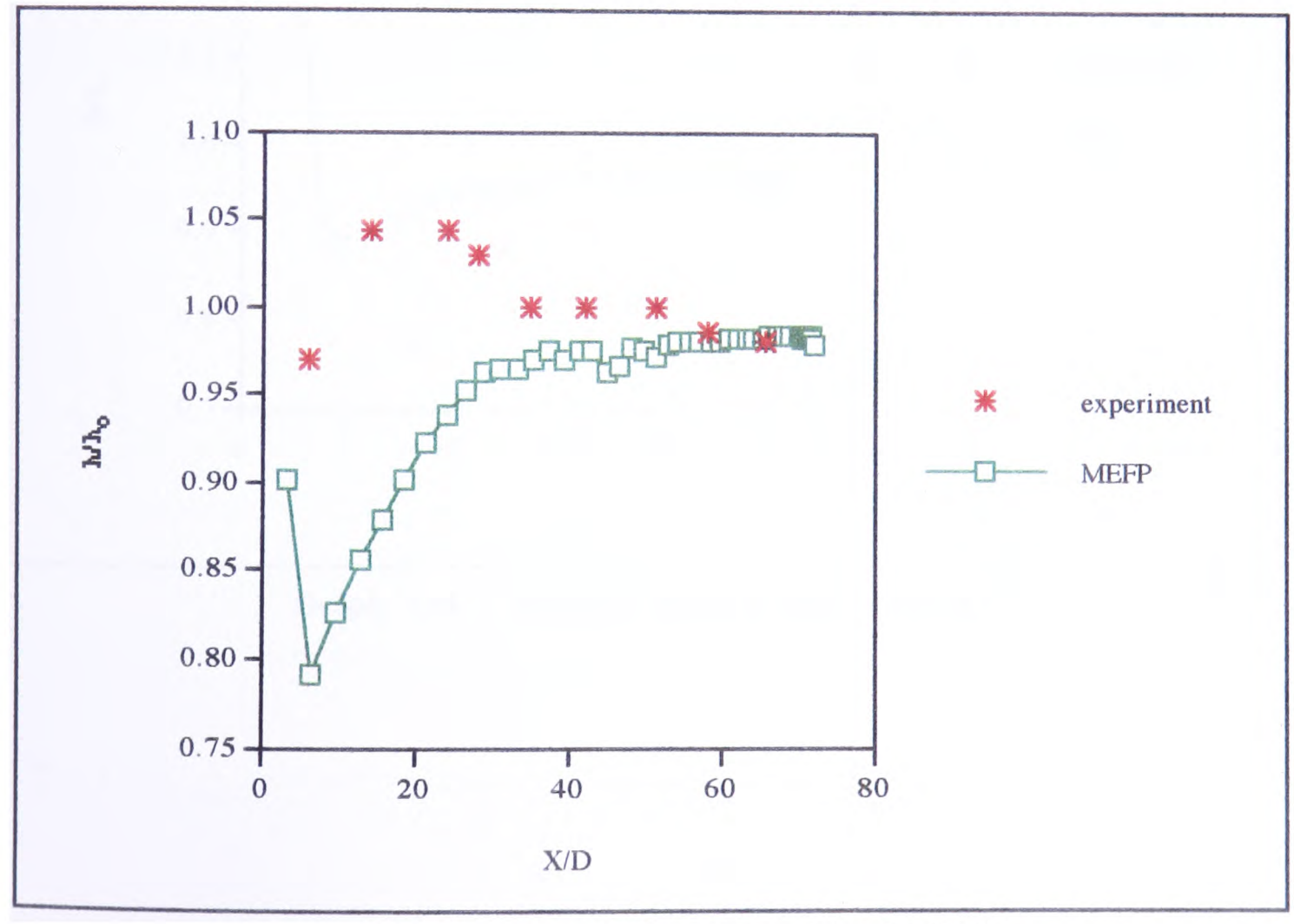


Graph 7.12 Optimized Build H h/h_o (G=1.07)

Graph 7.13 and Graph 7.14 show the heat transfer enhancement ratio correlation between the experimental data and the MEFP data at the first of two positions along the pressure surface of the blade. The improvement that is achieved by using the optimized film cooling parameters is not as obvious as it was in the previous test cases where the injection points were located on the suction surface of the blade. A small improvement can be noted, however, and it can be seen that far downstream of the coolant injection the agreement is very good. Close to the point of injection, it can be seen that the agreement is not as good. There is no explanation for this poor agreement, which leads to one of two conclusions. The first conclusion would be a questioning of the veracity of the experimental data. The experimental data would indicate that at this location, there is no benefit from the film cooling at all. In fact, the data indicate that there is a definite disadvantage to the addition of film cooling. However, the MEFP data show that there is some benefit from the film cooling close to the point of injection with the effect gradually decreasing in a downstream distance until there is little benefit far downstream of the injection. Not only would this appear to be the most likely effect of film cooling at this particular location on the pressure surface, but the MEFP data are the most consistent with the other data (both MEFP and experimental) presented in this study. The second conclusion would be a questioning of the veracity of the computational data. Build C is located on the pressure surface in an area where the curvature of the blade could have a significant effect on the accuracy of the predictions.

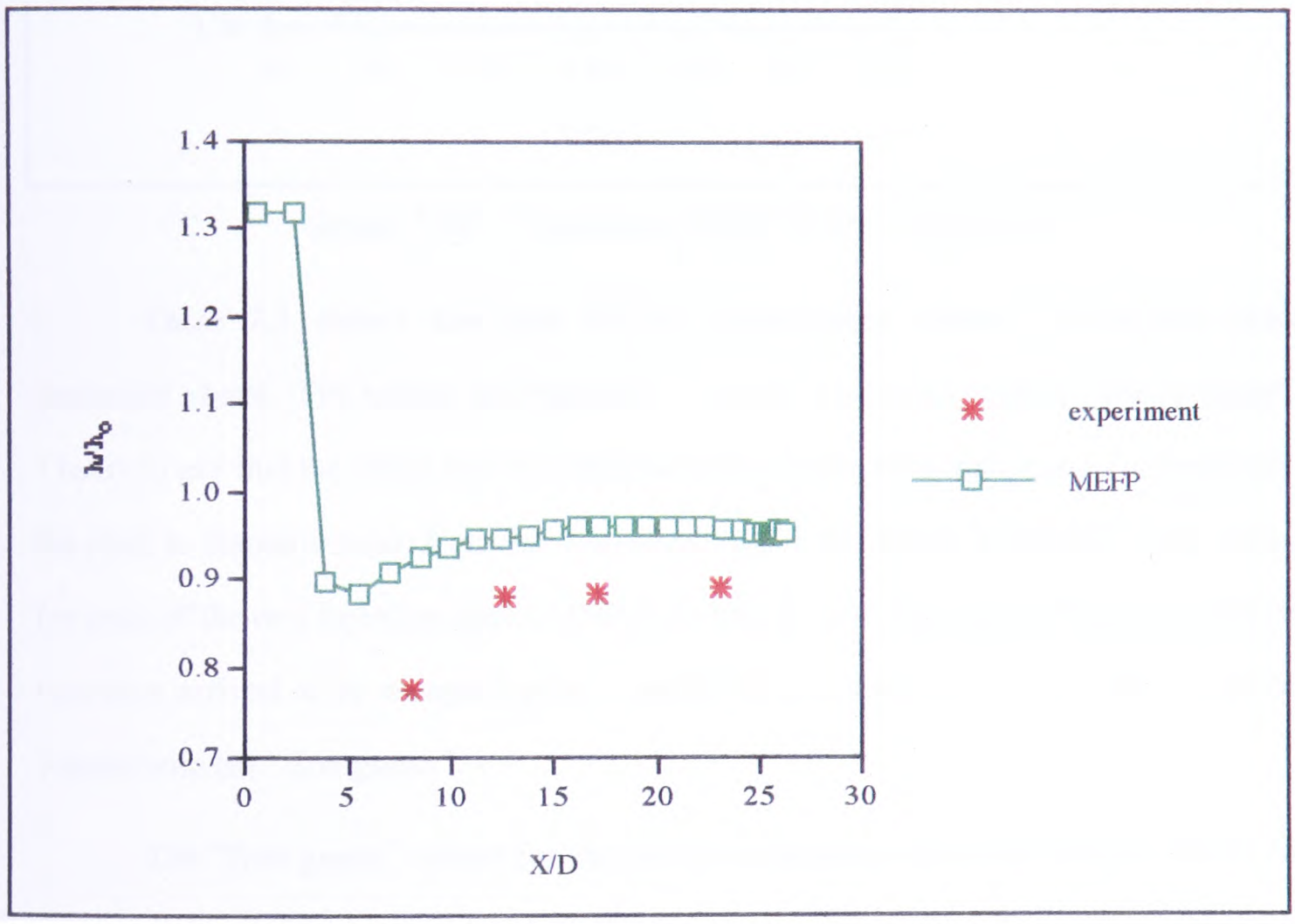


Graph 7.13 Original Build C h/h_o (G=0.36)

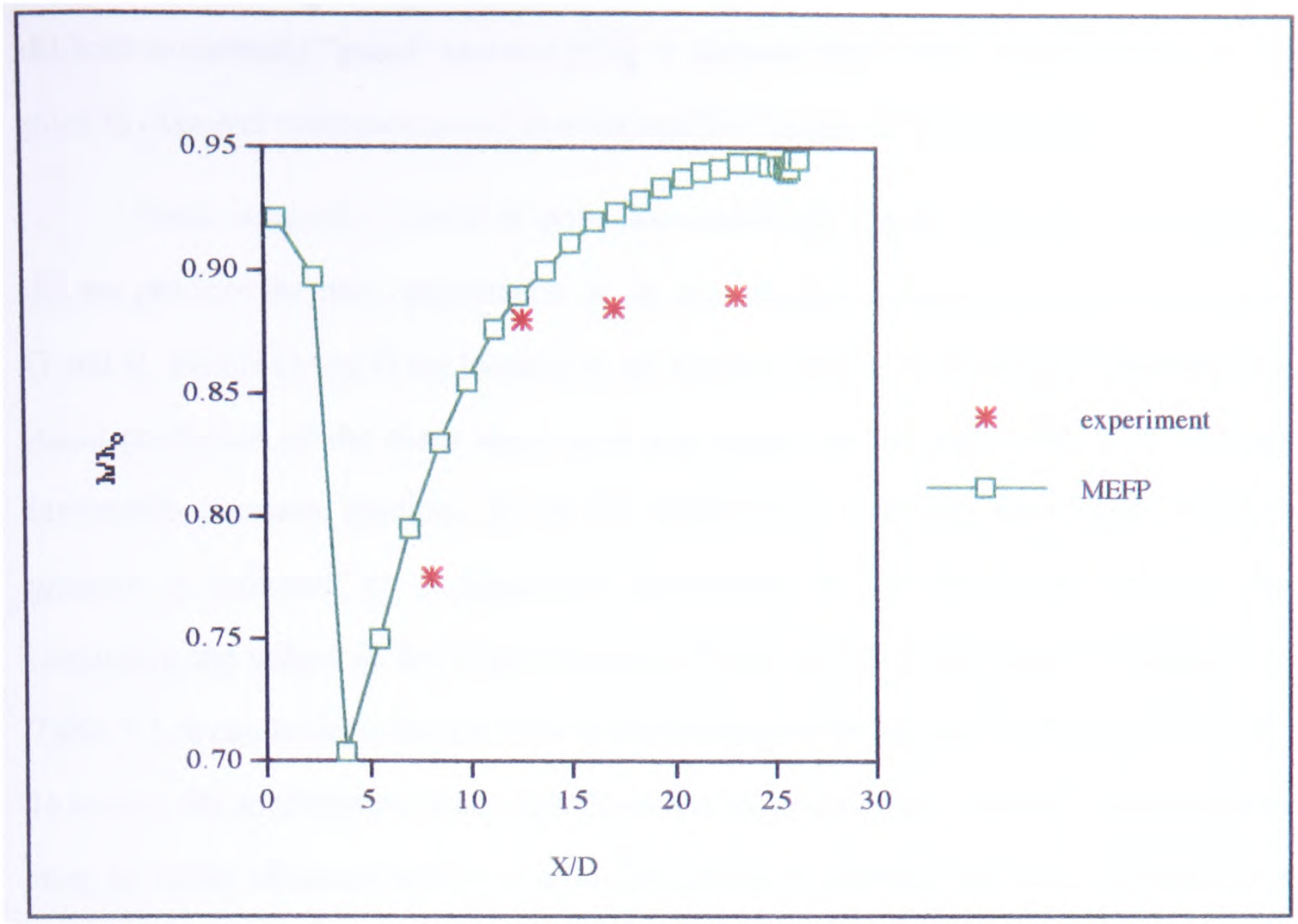


Graph 7.14 Optimized Build C h/h_o (G=0.36)

Graph 7.15 and Graph 7.16 show the heat transfer enhancement ratio at the second position along the pressure surface of the blade. Once again, a large, noticeable improvement is not seen when comparing the results from each graph. However, the optimized parameters do generate a small improvement, and the final agreement that is seen in Graph 7.16 is quite good. Due to the fact that Build D is located close to the trailing edge of the pressure surface, there were very few experimental data points to use for the purpose of comparison. A data point located closer the point of injection would be helpful in indicating whether or not the heat transfer enhancement ratio directly downstream of the row of holes is predicted correctly.



Graph 7.15 Original Build D h/h_o (G=0.36)



Graph 7.16 Optimized Build D h/h_o (G=0.36)

Table 7.3 shows the final RT27A optimization values for the test cases presented above. The values for Builds B, C, and D were successful "first guesses". That is to say that the initial or first estimate of the mass shed ratio (and consequently, the pitch to diameter ratio) from the corresponding ILPT data was the best. The values for each of the two injection rates of Builds G and H were successful "second guesses" that were arrived at by comparing the correlation with the experimental values and the values from the "first guess".

The "first guess" values for the pitch to diameter ratio for Builds G and H (in the order that they are presented in Table 7.3) were 3.0, 3.5, 1.5, and 2.0. It can be seen that the eventual optimized values for Build H fall between the experimental values and the "first guess" values. The optimized values for Build G are lower than the experimental values and the "first guess" values. While the difference in the pitch to diameter ratios may seem significant, the difference in the mass shed ratios is not. It can be seen from Graph 6.19 that at high injection rates, a large change in the injection rate corresponds to a small change in the mass shed ratio. Therefore, it can said that it is

difficult to correctly "guess" an exact pitch to diameter ratio when small changes in the pitch to diameter ratio correspond to even smaller changes in the mass shed ratio.

There is another source of error that could help explain why the "first guess" did not produce the best optimization of the heat transfer enhancement ratio for Builds G and H. Builds G and H are located on the suction surface of the blade, therefore, the initial prediction of the mass shed ratio was based on the ILPT data for a strong favourable pressure gradient. It can be recalled that a strong favourable pressure gradient is indicated by a significant acceleration in the freestream velocity. By consulting the values of the local freestream Mach number at the point of injection in Table 7.1, it can be seen that the flow is accelerating in the regions of Builds G and H. However, the acceleration is not significant and as a result, the surface in these regions may be better characterized by a mild favourable pressure gradient as opposed to a strong favourable pressure gradient.

BUILD	INJECTION RATE (G)	PITCH TO DIAMETER RATIO	MASS SHED RATIO (K)
B	0.92	2.0	0.3259
C	0.36	1.25	2.873
D	0.36	1.25	2.713
G	1.07	2.0	0.4966
G	1.44	3.0	0.2225
H	0.71	3.0	0.2162
H	1.07	3.0	0.1301

Table 7.3 RT27A Optimization Values

7.3 CONCLUSIONS

It is clear that the mass shed ratio optimization values from the ILPT flat plate test cases are very valuable. There was concern before the commencement of this particular analysis that the values would only be correct for test cases under the same set of testing parameters as the ILPT test cases. This has been proven to be not true. It can be recalled that the ILPT testing parameters included an injection angle of 30 degrees and a local freestream Mach number at the point of injection of 0.5. It has been shown here that the mass shed ratio optimization values can be used over a wide range of injection angles and local freestream Mach numbers with great success and improvement of the predictions. For instance, the testing parameters for Build B, which showed the best experimental correlation, as well as the most improvement in the accuracy of the predictions, consisted of an injection angle of 40 degrees and a local freestream Mach number at the point of injection of 0.8. In fact, it would appear as if pressure gradient is the most significant testing parameter. The injection angle and the freestream Mach number at injection can be significantly different from the ILPT testing parameters with no ill effects. However, if the pressure gradient shows a serious departure from that used in the ILPT test cases, then the mass shed ratio optimization values will not be exact.

The RT27A test cases have increased the database of knowledge that can be drawn upon in the examination and MEFP prediction of even more complex film cooling schemes and blade geometries. They confirm that the ILPT data can be used with great success in a large number of situations, and refinement of the data is only needed in a corresponding small number of situations. Furthermore, the RT27A data can be used as a valuable guideline for the refinement of the ILPT data under those situations where the pressure gradient profile may differ.

CHAPTER 8. CHTT TURBINE BLADE CFD CASES

8.1 TEST CASES

The CHTT or Cold Heat Transfer Tunnel is a 1.5 scale annular cascade which consists of thirty five transonic nozzle guide vanes. The tunnel is able to correctly simulate engine representative Reynolds numbers and Mach numbers. For a full description of the CHTT and how it works, Martinez-Botas et al. **(ref.58)** should be consulted.

The CHTT test case provided an excellent platform for a CFD study of an actual turbine geometry with all the characteristics of three-dimensional flow and film cooling. The geometry was defined in three dimensions and the entire CFD computation was performed in three dimensions, which made this test case the most complex and difficult to date. MEFP was used to calculate the heat transfer on the pressure surface, the suction surface and the leading edge of the blade geometry both with and without film cooling present.

An initial non-film cooled test case was programmed to run for 50 passes and the solution from this test case was used as an "initial guess" or restart dataset for each of the film cooled test cases. Each film cooled test case was subsequently programmed to run for 100 passes. The non-film cooled test case took approximately two days to complete and the film cooled test cases took approximately four to five days to complete on a Silicon Graphics Iris Indigo2 computer. This total number of passes was chosen because it was found to give adequate convergence of the relevant parameters in all cases, while still maintaining as low a computing time as possible.

Figure 8.1 shows a scale representation of the CHTT turbine blade. The locations on the blade surface that are marked and designated by row number correspond to the film cooling locations. They are further labeled according to whether they are located on the suction surface, the pressure surface, or the leading edge.

Experimental testing was performed initially with all of the cooling holes blowing air. Later, successive rows were blocked off in a regular pattern and further data were collected. The experimental test matrix includes ten different test conditions or configurations where the number of rows that were blocked off ranged from zero to thirteen. The computational test matrix only examines a few of these possible configurations, which are discussed and presented later in this section.

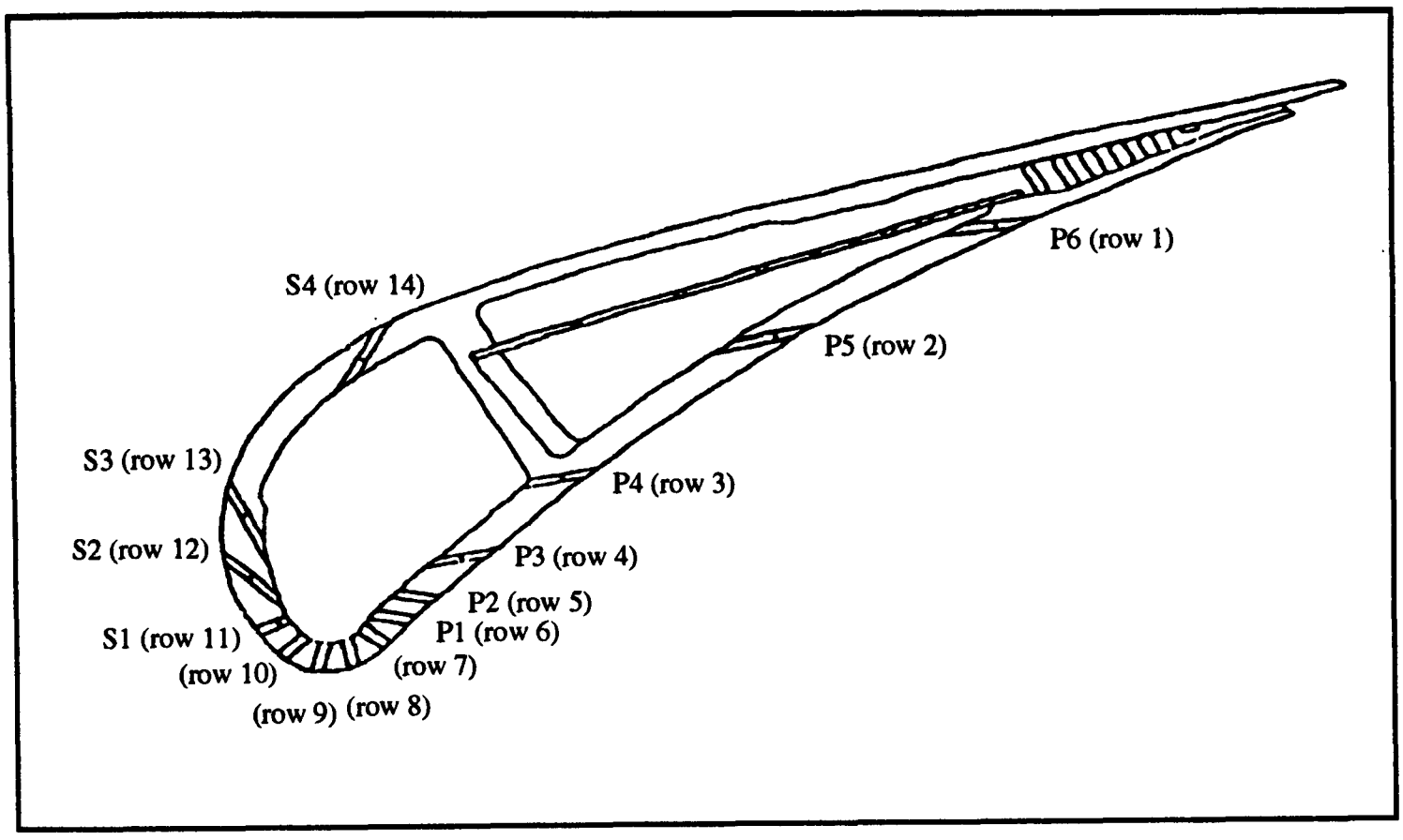


Figure 8.1 CHTT Cascade Geometry

8.2 Discussion of Results

8.2.1 Non-Film Cooled Results

Shengmin Guo performed all the MEFP calculations for the non-film cooled CHTT test cases. His thesis (to be presented) should be consulted for a full presentation and discussion of these results. Guo's predictions verified that MEFP gave satisfactory results in a uncooled setting, so film cooling was added using the improved treatment that was developed based on the ILPT data, and proven using the RT27A turbine data. This treatment was discussed in detail in a previous section. The uncooled results of Guo also examine the effects of roughness on the heat transfer. This analysis

should be useful when the experimental film cooling data are collected with the use of liquid crystals.

It must be noted that there is a presentation of non-film cooled data later in this section. It is shown simply for the purpose of comparison with the film cooled results. The values that are shown here is the solution of the 50 pass dataset that was used as the restart dataset for the film cooled test cases. The results that are depicted show good agreement with the results of Guo, although his results should be consulted for a thorough treatment of this subject.

8.2.2 Film Cooled Results

The boundary and initial conditions for the film cooled test cases were chosen to coincide exactly with those used in the experimental CHTT testing, and these testing conditions were representative of those found in real gas turbine engines. The film cooling parameters in the calculations were chosen to coincide with the scaled engine representative values from Rolls Royce, which were different from the experimental CHTT test conditions but identical in non-dimensional terms.

In order to match the scaled engine representative test conditions, the corresponding experiment would need to be able to generate a freestream to coolant temperature difference of approximately 119 degrees Kelvin. However, there is a much easier method for simulating these test conditions and the density differences that are inherent in flows with such different temperatures in a laboratory setting. This method includes using a foreign gas with a different gas constant from air which allows for a much smaller freestream to coolant temperature difference. This method was used in the experimental CHTT testing. A foreign gas of SF_6 (30.2 percent by mass) and Argon (69.8 percent by mass) served as the coolant and was injected at a temperature of approximately 45 degrees Celsius, allowing for a temperature difference of only thirty degrees Kelvin. This use of this foreign gas mixture gave the correct coolant to freestream density ratio.

At the moment, MEFP is unable to correctly simulate foreign gas injection, where the value of the gas constant for the coolant is different from that of air. Therefore, the original engine representative values were used in all of the datasets. This discrepancy should produce no noticeable difference in the final results, because each of the methods attempt to model the same flow characteristics and testing conditions.

A simple summary of the MEFP/engine to experimental modeling proves that the end result should be identical. The coolant densities and velocities are the same, therefore, the momentum flux is also the same. The fact that the velocity field is identical in each case means that the same turbulent mixing properties of the coolant with the freestream can be expected. The reason why the modeling of the mixing properties is the most important factor will be addressed later in this chapter. The only differences in the modeling are in the values of each respective gas constant and coolant temperature. The fact that the temperature field is not identical in each case is not a problem. While the heat transfer rate will be different because of the different coolant temperatures, the heat transfer coefficient will not be if it is defined with respect to the adiabatic wall temperature. This particular definition of heat transfer coefficient is also addressed later in this chapter. Table 8.1 shows the temperature boundary conditions for the CFD CHTT test cases.

T_{t_∞}	Tti	Tw
288.2 °K	169.5°K	388.2 °K

Table 8.1 Temperature Boundary Conditions

Table 8.2 shows the values of the relevant film cooling parameters for all fourteen cooling rows on the film cooled CHTT test blade. These values represent the original or pre-optimization parameters that were used in the experimental testing, and

were used for the initial MEFP predictions. The results of the initial MEFP predictions using these original parameters are found later in this section.

ROW #	SURFACE	HOLE DIAMETER	# OF HOLES	PITCH TO DIAMETER RATIO
1	pressure	0.9 mm.	26	3.23
2	pressure	0.9 mm.	25	3.23
3	pressure	0.9 mm.	27	3.23
4	pressure	0.9 mm.	28	3.23
5	pressure	1.05 mm.	30	2.966
6	pressure	1.05 mm.	31	2.966
7	leading edge	1.05 mm.	20	2.37
8	leading edge	1.05 mm.	21	2.37
9	leading edge	1.05 mm.	21	2.37
10	leading edge	1.05 mm.	21	2.37
11	suction	0.9 mm.	27	2.938
12	suction	0.9 mm.	25	3.752
13	suction	0.9 mm.	24	3.752
14	suction	0.9 mm.	14	5.091

ROW #	INJECTION RATE	ALPHA	BETA	LOCAL MACH #	X/S
1	1.3012	20.86°	0°	0.41	0.705342
2	1.6243	20°	7°	0.21	0.509367
3	2.2287	28.06°	0°	0.12	0.30101
4	2.7277	30.37°	0°	0.09	0.179068
5	3.1979	58.31°	0°	0.073	0.111177
6	3.3054	58.31°	0°	0.07	0.082064
7	4.5441	89.99°	60°	0.05	0.056235
8	1.5557	88.79°	60°	0.155	0.010713
9	1.6342	83.9°	60°	0.19	0.006309
10	1.0859	82.88°	60°	0.35	0.033862
11	1.2117	78.19°	0°	0.38	0.056235
12	1.3264	39.43°	0°	0.49	0.143610
13	1.1083	40.39°	0°	0.705	0.217457
14	1.1576	30.42°	6°	1.04	0.344431

Table 8.2 CHTT Film Cooling Parameters

The optimization technique that was used in the CHTT MEFP testing proved to be very successful in the case of the RT27A MEFP testing. Therefore, the test case that was run using the original parameters as in Table 8.2 was used only as a baseline case for means of comparison with the test case that was run using the optimized parameters. Table 8.3 shows the final CHTT optimization values for the test cases presented above. These values were computed based on the values for the ILPT flat plate test cases and further refined based on the values for the RT27A turbine test cases.

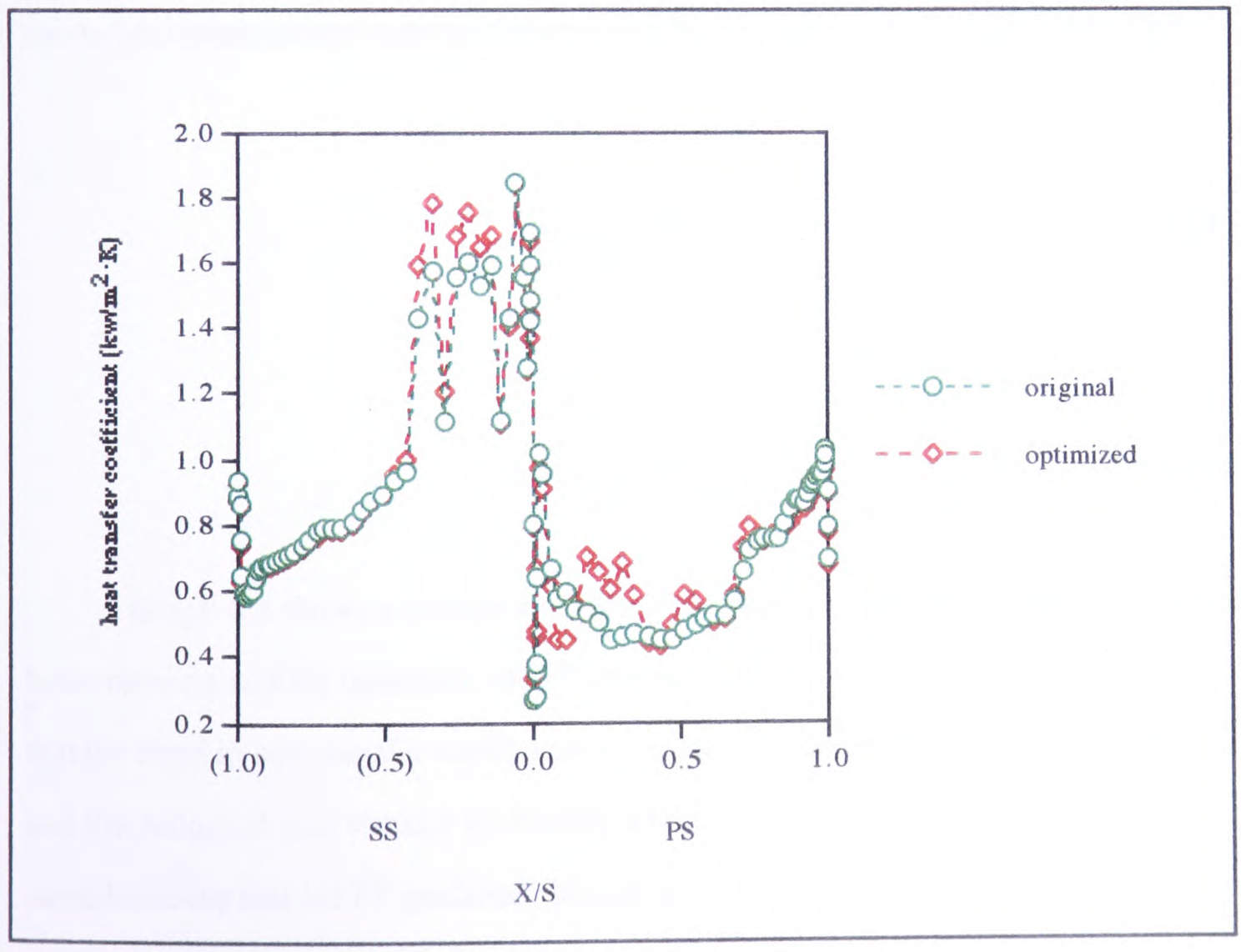
By referring to Table 8.3, it can be seen that the mass shed ratio was not changed or optimized in the case of rows seven through eleven. Leading edge film cooling or cooling in the showerhead region, as it is commonly called, presents a unique problem. These rows have a near tangential alpha, which is the angle of the coolant jet to the surface, and a large beta, which is the angle of the coolant jet to the freestream when projected on a plane parallel to the surface. This particular scenario has not been encountered to date. An experiment that is meant to simulate the conditions and geometry of the leading edge of a turbine blade with coolant injection can not be modeled using a flat plate rig. Furthermore, in spite of the wealth of RT27A experimental data, there was no leading edge film cooling testing performed at the extreme angles that were seen here. Due to the uncertainty in knowing exactly how to change the mass shed ratio in the showerhead region in order to improve the predictions, it was left unaltered with the original values. This is a definite area where future development and improvement of the film cooling model would be invaluable.

ROW #	PITCH TO DIAMETER RATIO	MASS SHED RATIO (K)
1	1.75	0.2308
2	1.45	0.2266
3	1.80	0.2154
4	2.00	0.2089
5	3.50	0.1999
6	3.60	0.1923
7	unchanged	0.7244
8	unchanged	0.6340
9	unchanged	0.4895
10	unchanged	0.5014
11	unchanged	0.4659
12	2.67	0.2093
13	3.00	0.2088
14	2.05	0.2265

Table 8.3 CHTT Optimization Values

Graph 8.1 shows the heat transfer results for the CHTT test case using the original parameters that completely define the properties and the geometry of a cooling row in comparison with the optimized parameters that define the cooling rows. The data were collected at the fifty percent midspan location of the turbine blade. All of the CHTT data that are presented here were collected at this location for exact comparison with the experimental thin film heat transfer gauge data.

It can be seen that the heat transfer results for each case are similar. The results are exactly the same in the region of the leading edge, where none of the parameters were altered. The results are also the same in the regions where there were no cooling holes, such as the last half of the suction surface and the last quarter of the pressure surface. These results correspond with the expected outcome. It is clear that the optimization makes only small changes and those changes occur locally to the film cooling rows with little downstream effect. This statement can be confirmed by comparing the X/S values from Table 8.2 (which are the locations of coolant injection) with the peaks in heat transfer coefficient in Graph 8.1. It is encouraging to note that MEFP correctly predicts the changes in heat transfer coefficient that occur with particular changes in the mass shed ratio. For instance, when the mass shed ratio was increased, then MEFP predicted an increase in the heat transfer coefficient and vice versa. It can also be said that a greater change in the mass shed ratio resulted in a greater change in the heat transfer coefficient.



Graph 8.1 Film Cooled Heat Transfer Comparison

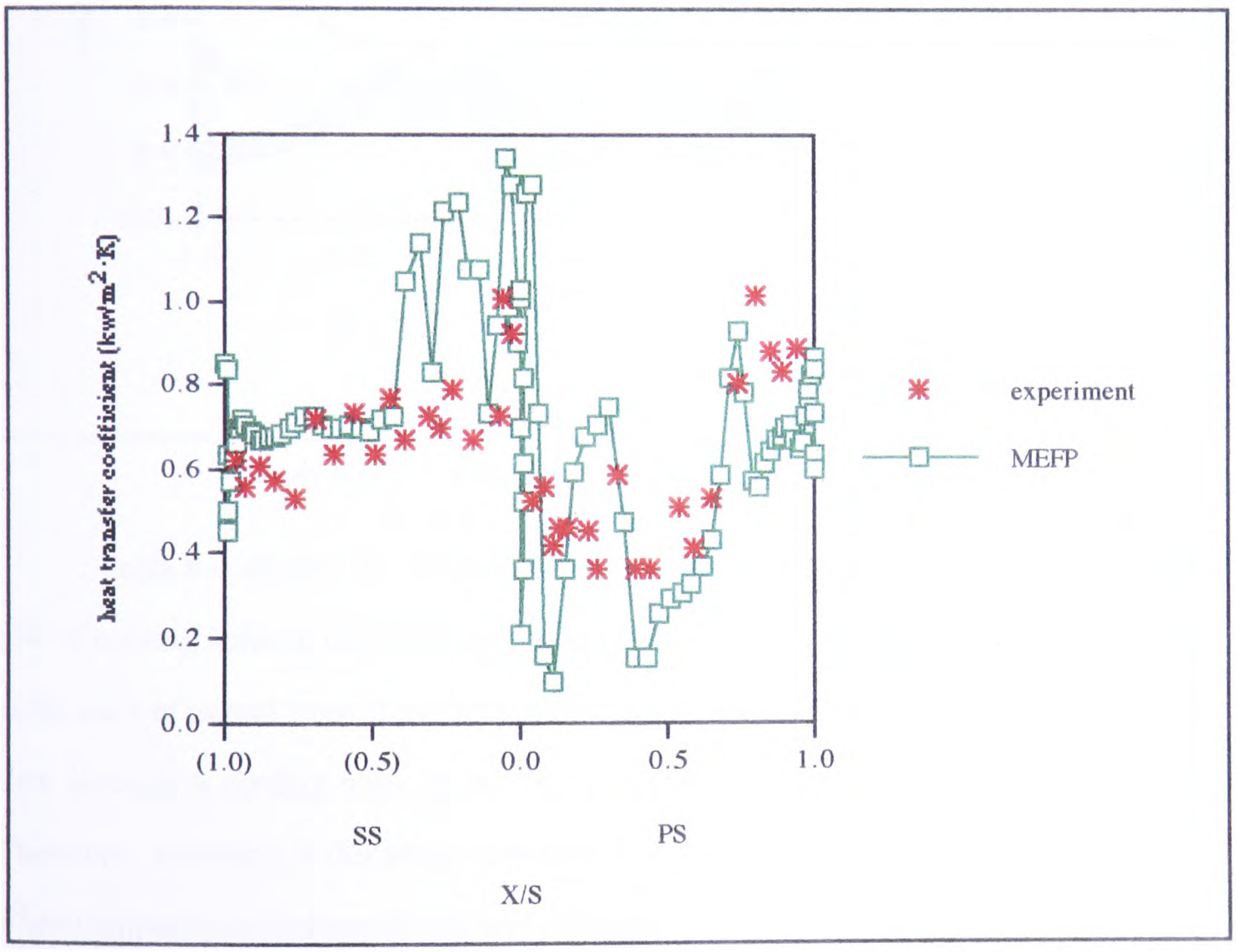
There are numerous definitions of heat transfer coefficient. Throughout this investigation, whenever heat transfer coefficient is referred to, it is meant to be defined as in Eqn.8.1. The only exceptions to this are the RT27A turbine data where the experimental heat transfer coefficient was defined according to Eqn.7.1 and the CHTT experimental data where the heat transfer coefficient was defined according to Eqn.8.2. In each case, the MEFP data were then altered to match each definition. All of the CHTT data plots presented in this chapter use Eqn.8.1 as the definition for heat transfer coefficient for ease of comparison with the other data presented in this study. The experimental and computational data that are presented in Graphs 8.2 and 8.4 use Eqn.8.2 as the definition for heat transfer coefficient. In order to resolve this difference, heat transfer rate data were collected at an alternate wall temperature. When the two values of heat transfer rate (at a given X/S value) are plotted versus their respective wall temperatures, a linear slope that is h, as defined by Eqn.8.2, is generated. The conversion of the other heat transfer data in such a manner was deemed not necessary due to the absence of other experimental data at this time, as well as the enormous computational resources that would be required to accomplish such a task.

$$h = \frac{\dot{q}}{(T_{r\infty} - T_w)} \tag{8.1}$$

$$h = \frac{\dot{q}}{(T_{aw} - T_w)} \tag{8.2}$$

Graph 8.2 shows a comparison plot of the experimental CHTT data with all the holes blowing and the optimized MEFP data with all the holes blowing. It can be seen that the trend in heat transfer coefficient is similar when comparing the results. The high and low values of heat transfer are located where they are expected and there are in the same locations that MEFP predicted. However, it can be seen that there are significant differences in the peak levels of heat transfer coefficient in some locations. Upon

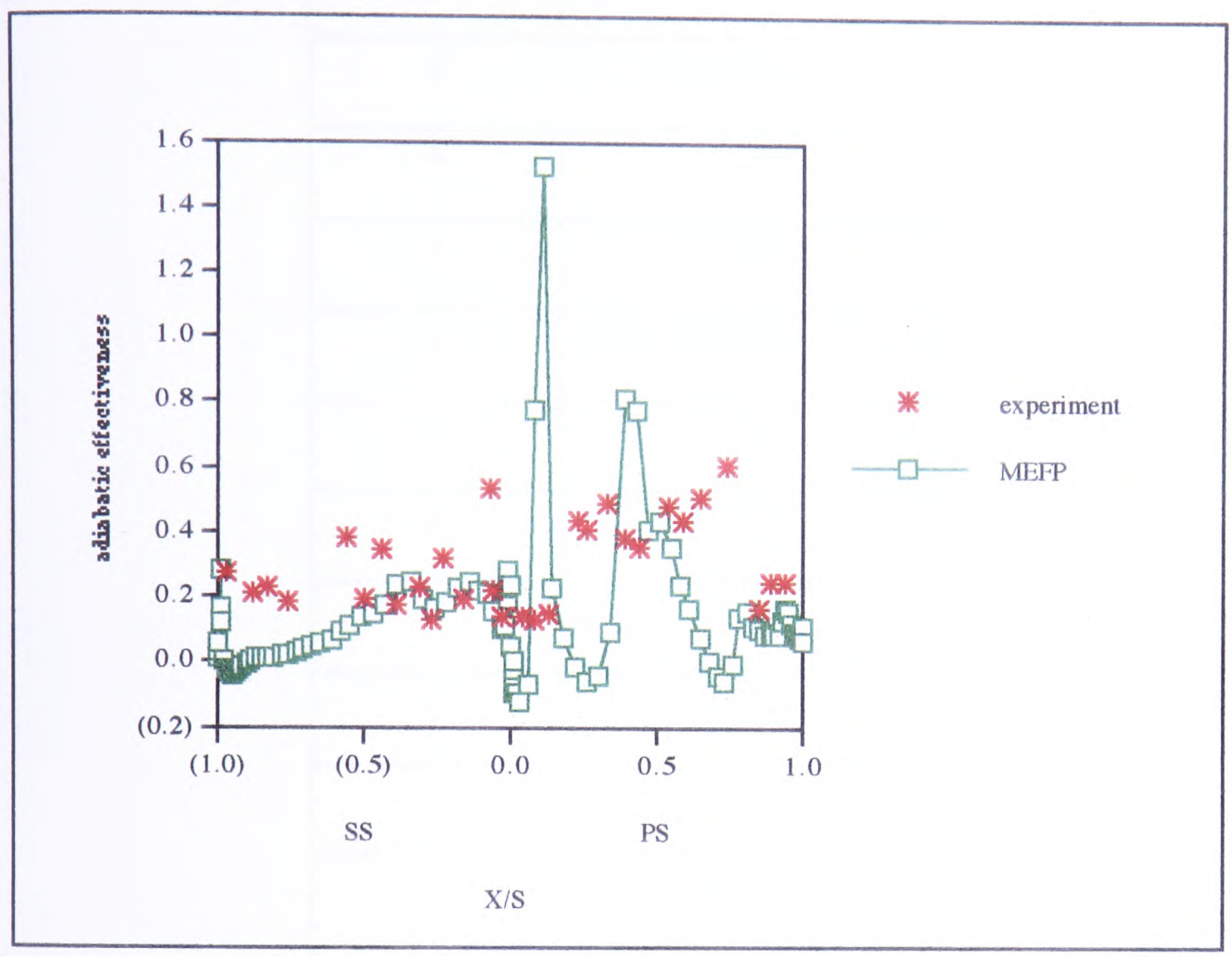
discussion with the CHTT experimental group, these differences were resolved. The MEFP calculations were carried out assuming a discharge coefficient of one, or assuming an ideal exit of the coolant flow through the holes. In reality, these assumptions can not be made, as the discharge coefficient has been measured experimentally to be less than one. This discrepancy results in a greater coolant mass flow through the holes in the ideal or computational case in comparison with the experimental case. Therefore, the peak levels of heat transfer that MEFP predicts are higher than they should be. In the regions where there is no injection, such as on the last half of the suction surface and on the trailing edge of the pressure surface, the MEFP and experimental results are the most similar. In these areas the difference in coolant mass flow would not be significant.



Graph 8.2 Heat Transfer Coefficient Comparison

Graph 8.3 shows a plot of the adiabatic effectiveness data as defined in Eqn.5.7. The results that are shown are a comparison between the experimental results

and the MEFP predictions using the same computation as in Graph 8.2. Once again, the trend in cooling effectiveness is similar when comparing the results. However, the peak values are not correct due to the differences in coolant mass flow in the experimental and computational test cases.



Graph 8.3 Adiabatic Effectiveness Comparison

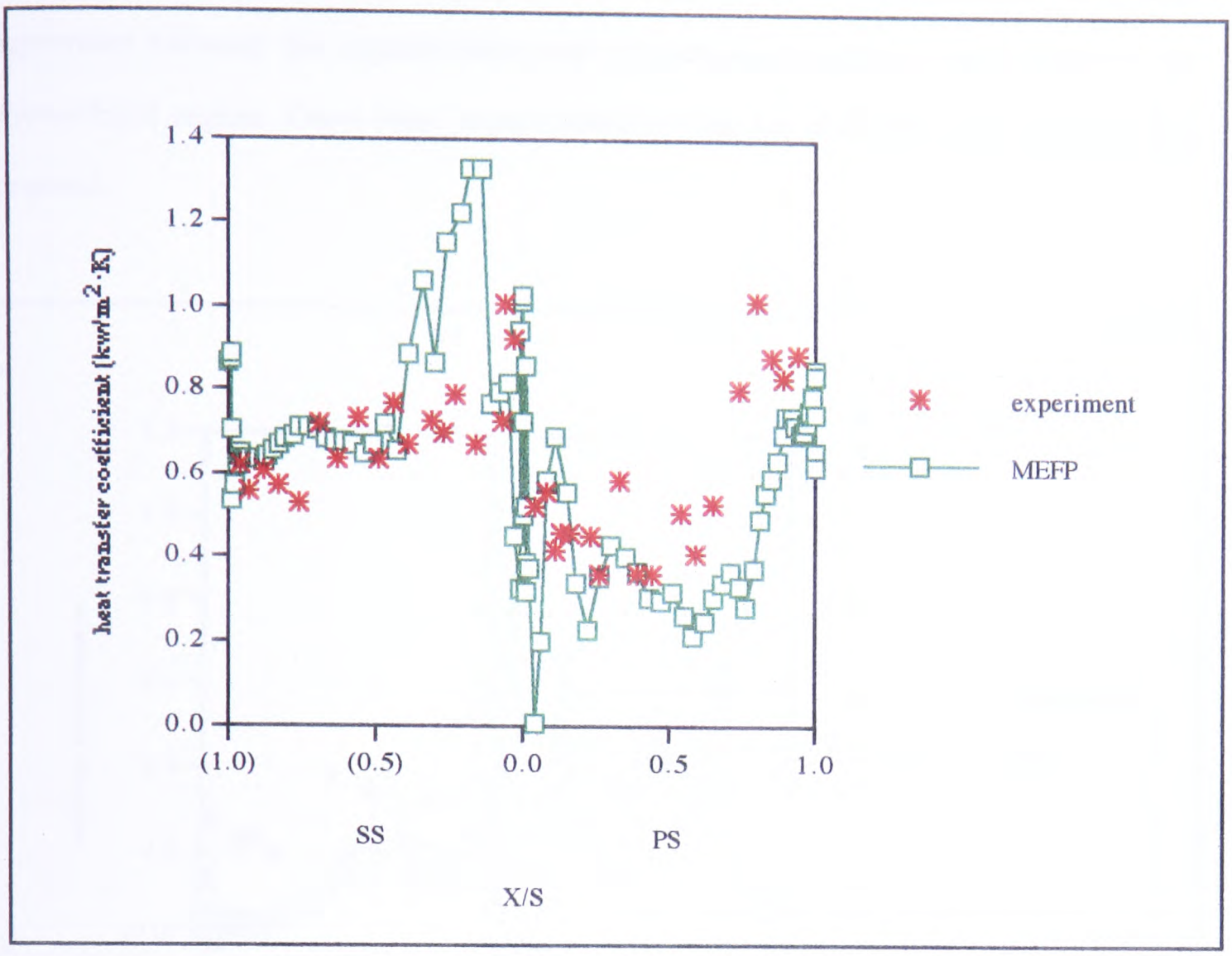
Table 8.4 shows the experimentally measured discharge coefficients for each row of cooling holes in the absence of crossflow. Discharge coefficient may be defined as the ratio of actual mass flow through a cooling hole to the ideal or theoretical mass flow through a cooling hole. It can be seen that these values are all less than one. Therefore, assuming a discharge coefficient of one can lead to major discrepancies when comparing experimental data and computational predictions.

ROW #	DISCHARGE COEFFICIENT (C_D)
1	0.640
2	0.595
3	0.590
4	0.570
5	0.660
6	0.740
7	0.720
8	0.750
9	0.720
10	0.725
11	0.633
12	0.605
13	0.630
14	0.700

Table 8.4 Discharge Coefficient Values

Graph 8.4 shows a comparison plot of the experimental CHTT data and the optimized MEFP data with all the holes blowing and using a realistic discharge coefficient. On the suction surface, it can be seen that the peak levels of heat transfer coefficient are slightly lower than in Graph 8.2. This is the expected outcome. In the showerhead region, the peak levels of heat transfer coefficient are also noticeably lower. However, the most profound improvements can be seen in the predictions on

the pressure surface. It is clear that the trend in heat transfer coefficient is far more reasonable when decreased mass flow through the holes is assumed.

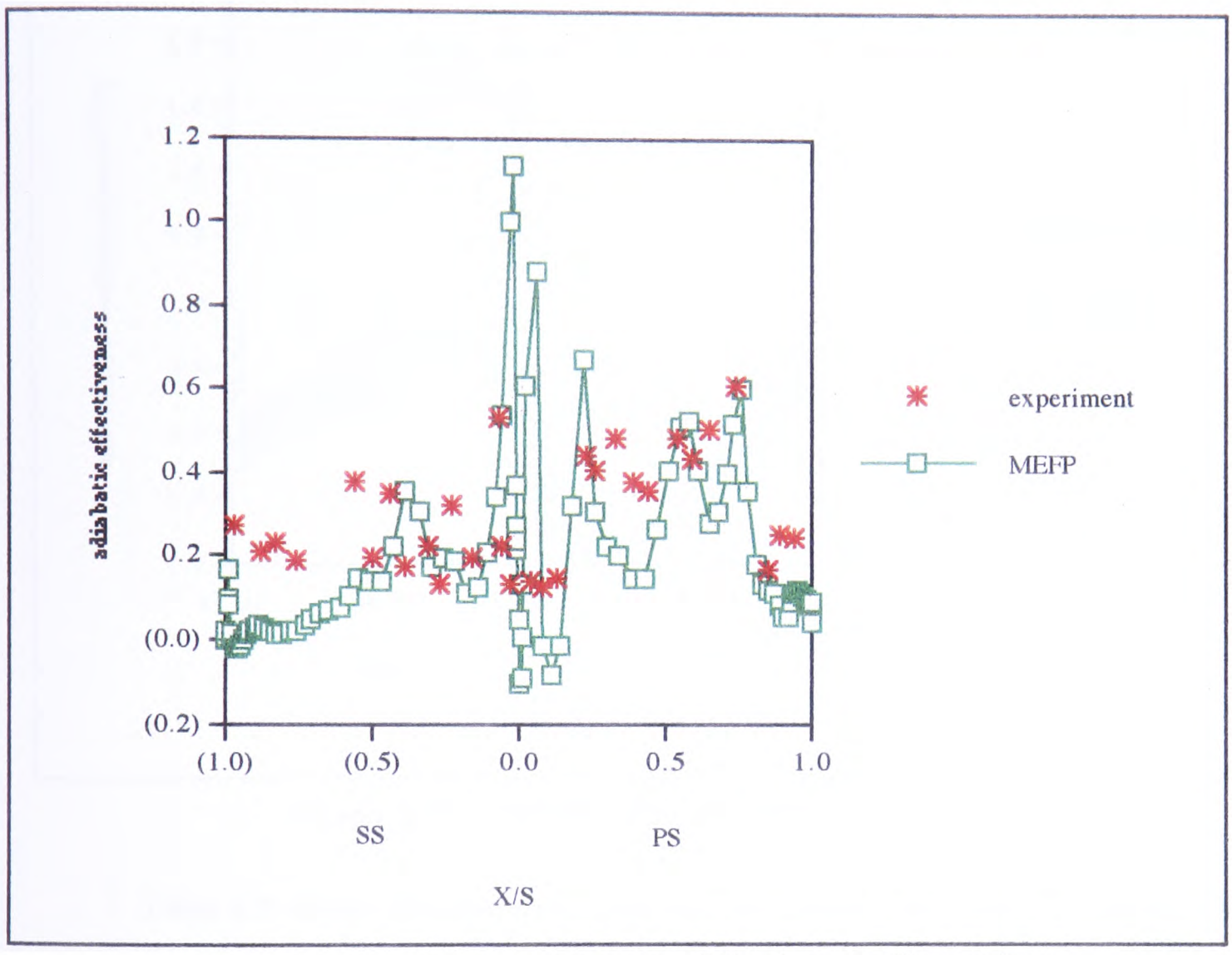


Graph 8.4 Updated Heat Transfer Comparison

Graph 8.5 shows an updated comparison plot of the adiabatic effectiveness data using the realistic discharge coefficients. On the suction surface, it can be seen that there is some minor improvement in the predictions in the region of the coolant injection. The effectiveness in the area of the leading edge is still overpredicted, but its magnitude is much more reasonable than that shown in Graph 8.3. On the pressure surface, the improvement is quite apparent. The peaks in adiabatic effectiveness are predicted far more accurately than what was previously seen.

The improvements in the predictions are clearly visible when the discharge coefficients from Table 8.4 are used. However, even further improvements are possible. At this time only the discharge coefficients without crossflow are available. Discharge coefficients with crossflow present are needed to completely and realistically

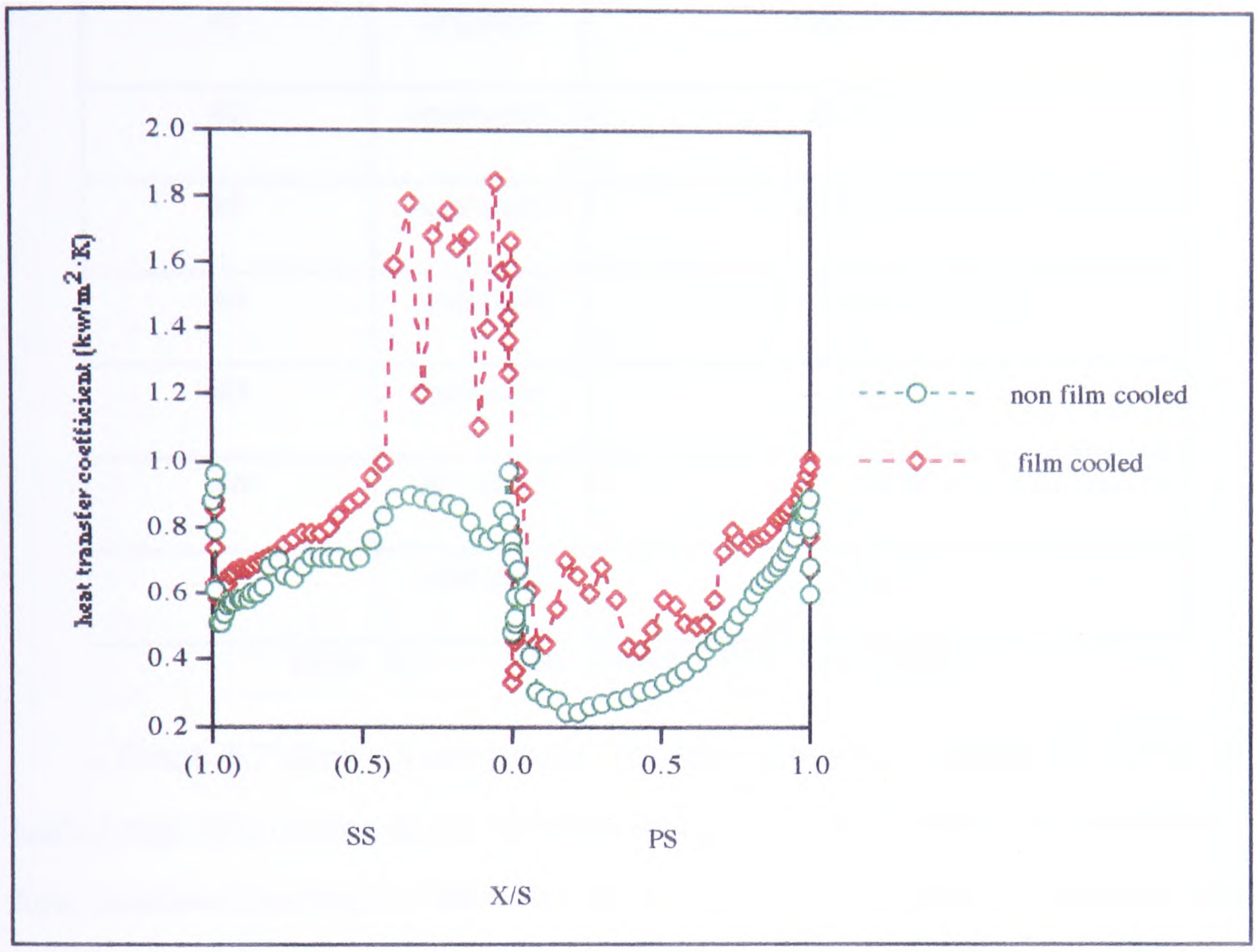
simulate the experimental testing conditions. Generally, the values of the discharge coefficient with crossflow are slightly lower than those without crossflow. Even lower computed mass flows through the rows of cooling holes can only generate even better agreement between the experimental and computational results, particularly in the showerhead region. Once these experimental values are available, this analysis will proceed.



Graph 8.5 Updated Adiabatic Effectiveness Comparison

Graph 8.6 shows a plot comparing the uncooled heat transfer level with the film cooled, optimized heat transfer level. It is clear that the film cooled heat transfer coefficient is higher than the uncooled heat transfer coefficient, particularly in the region of a row of cooling holes. It can be confirmed by consulting Table 8.2 that the locations of the peaks correspond to the locations of the cooling rows on the blade. Furthermore, all of the CHTT injection rates are above one. Therefore, it can be assumed that the coolant stream has separated from the surface of the blade. The flow in the

neighbourhood of the cooling rows would then be highly three-dimensional and turbulent, more so than at any other location along the blade. Nirmalan and Hylton **(ref.67)** reported similar increases in heat transfer, particularly when downstream film cooling was accompanied by leading edge film cooling at high injection rates.



Graph 8.6 MEFP Heat Transfer Comparison

Table 8.5 shows the test matrix for the film cooled CHTT MEFP testing. The results from the first two test cases were presented and discussed above. These test cases were the only two test cases where all of the film cooling rows were blowing air. It was mentioned earlier in this section that in subsequent experimental testing successive rows of holes were eliminated. Rows of holes were eliminated one at a time, but in this analysis rows of holes were eliminated two at a time due to the large amount of computational time that was required to run each MEFP test case. These particular cases are labeled test case number four through seven. Test case number three was included in the test matrix in an attempt to quantify the cooling effect of the showerhead region. Downstream differences in the heat transfer solution were examined both with

and without leading edge film cooling to accomplish this goal. These results are presented next.

TEST CASE #	VALUES	ACTIVE FILM COOLING ROWS
#1	original	all (1 - 14)
#2	optimized	all (1 - 14)
#3	optimized	1 - 6 and 12 - 14
#4	optimized	1 - 6 and 11 - 12
#5	optimized	1 - 6
#6	optimized	3 - 6
#7	optimized	5 - 6

Table 8.5 Film Cooled CHTT Test Matrix

Graph 8.7 shows a comparison plot that is meant to quantify the effect of leading edge film cooling on the heat transfer coefficient both locally and downstream from the showerhead region. There was never any planned experimental test that would quantify this effect so this plot serves to accomplish this task on a purely computational level. The film cooled results both with and without showerhead injection or leading edge film cooling are compared with the non-film cooled results so that any differences in the overall solution can be easily noted. The vertical lines on the plot represent the boundaries of the showerhead region.

An analysis of the differences that the showerhead injection produces is to follow. On the suction surface it can be seen that far downstream of the last row of cooling holes (past X/S=0.4), the three solutions merge. This is the expected effect. It was stated previously that leading edge film cooling produces a large amount of turbulence which would generate considerably higher local values of heat transfer coefficient in comparison with the uncooled solution. It would stand to reason that there

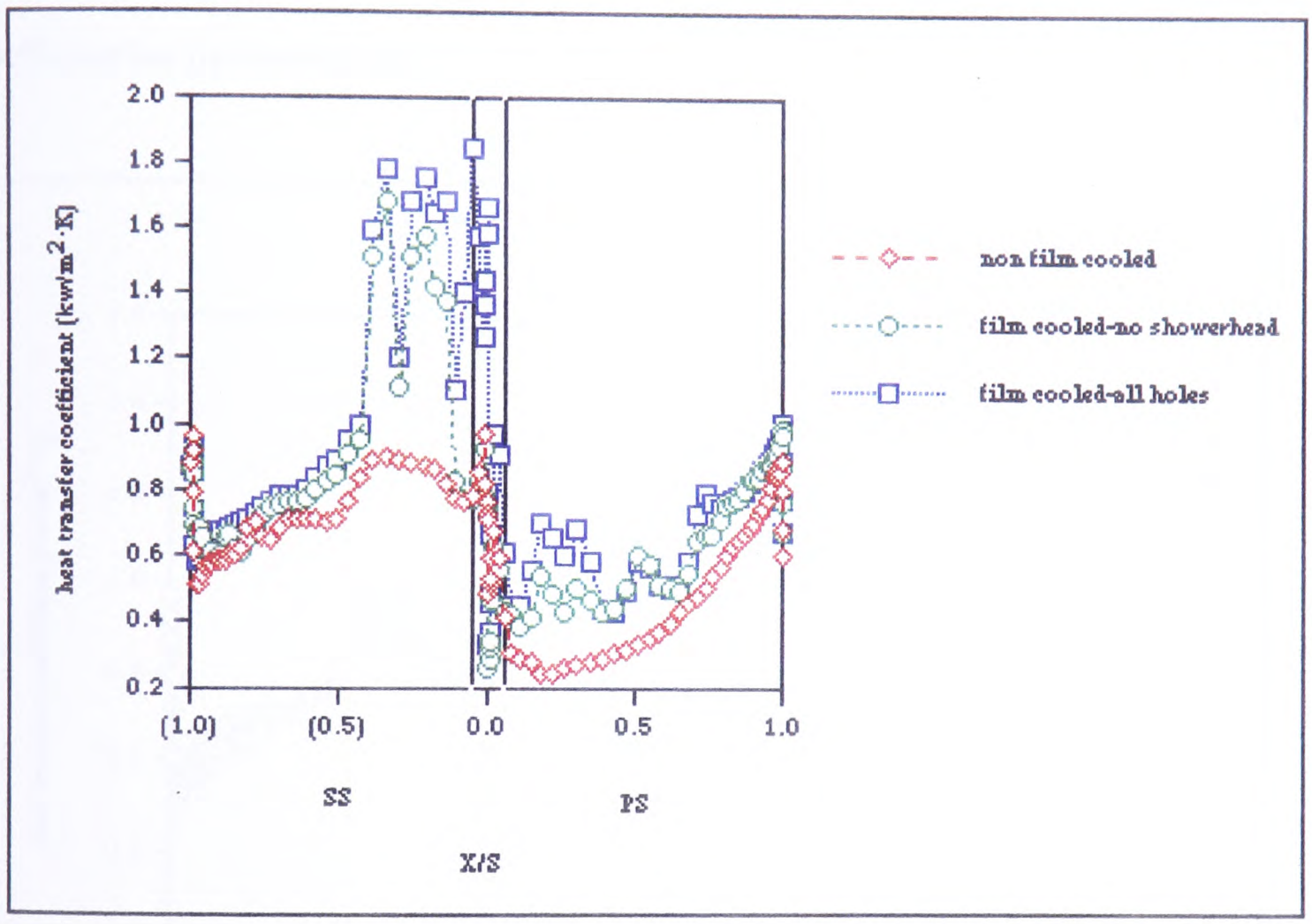
would be some downstream effect of this increased turbulence due to the presence of the leading edge film cooling. It can be seen that there is some downstream effect if the film cooled results both with and without showerhead injection are compared. By noting the difference in the peak levels of heat transfer coefficient on the suction surface in Graph 8.7 it can be seen that the difference due to the showerhead injection amounts to approximately ten to fifteen percent.

On the pressure surface, it can also be seen that far downstream of the last row of cooling holes (past X/S=0.7) the three MEFP solutions merge. It can be seen that in the absence of the increased turbulence from the leading edge coolant injection, the heat transfer solution is approximately twenty percent lower. On the suction surface there was no injection past X/S=0.4, so it was difficult to gauge how far downstream the effects of the leading edge film cooling persist. There is no such difficulty on the pressure surface as there is a point of injection closer to the trailing edge. It can be seen by comparing the peaks in heat transfer coefficient that the effects of the increased turbulence from the showerhead injection damp out past a downstream distance of X/S=0.4. Therefore, if there were any points of injection past this X/S location on the suction surface, identical film cooled results would be expected.

In the leading edge region that is bounded by the vertical lines, the similarities between the uncooled and the film cooled solution with no showerhead cooling can be noted. The film cooled heat transfer level with showerhead cooling is considerably higher, but that is to be expected. It is also obvious that the most pronounced effect of the leading edge film cooling is local to the injection. This is a region where major advancements and benefits are possible if a CFD code was known to accurately predict the heat transfer levels.

Based on the results of this computational survey of the effects of showerhead injection, important conclusions can be drawn. The optimization procedure that was carried out on the pressure and suction surfaces of the blade yielded a ten to twenty percent difference in the heat transfer coefficient local to the point of injection. This

indicates that there is the possibility of a significant improvement in the heat transfer coefficient predictions in the region of the leading edge or showerhead. However, it can also be said that the heat transfer coefficient results downstream of the leading edge are not likely to change more than approximately five percent. This judgment has been made based on the film cooled results both with and without showerhead cooling as it pertains to the downstream cooling locations. Therefore, the veracity of the downstream results can be confirmed, and future improvements in the prediction of heat transfer in the showerhead region are eagerly anticipated.

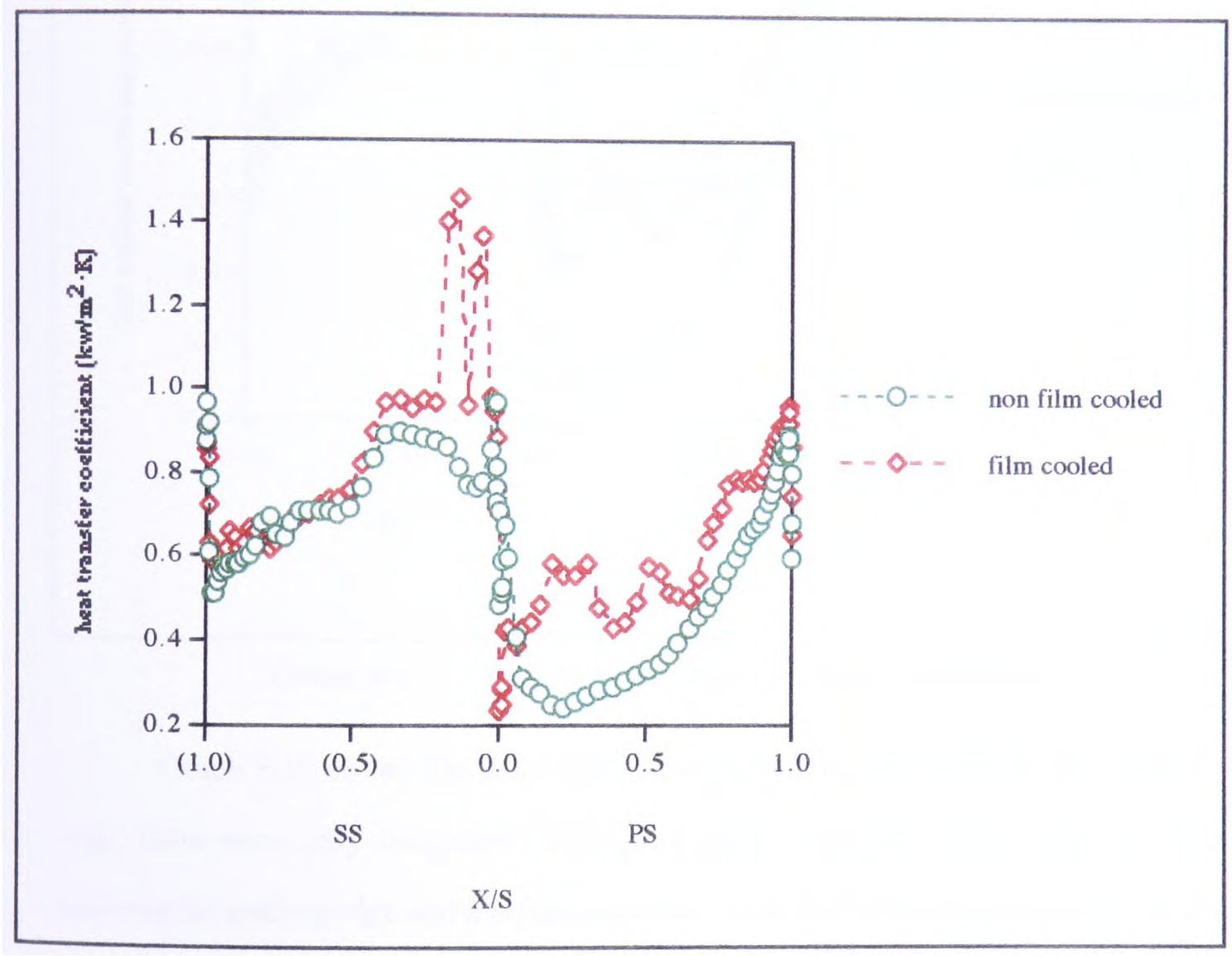


Graph 8.7 Effect of Showerhead Region on Heat Transfer

Graph 8.8 shows the heat transfer coefficient data for test case #4. In the absence of the corresponding experimental data, the film cooled data are presented in comparison with the non-film cooled data. Due to the fact that the data are presented in such a manner, it is very easy to note the locations of the cooling rows. For instance, there were only two rows of holes that were blowing on the suction surface which can be proven by noting that there are only two peaks in the heat transfer coefficient. It can

be seen that the cooling effects generated by these two rows are predominantly localized, but there is some small effect further downstream as well.

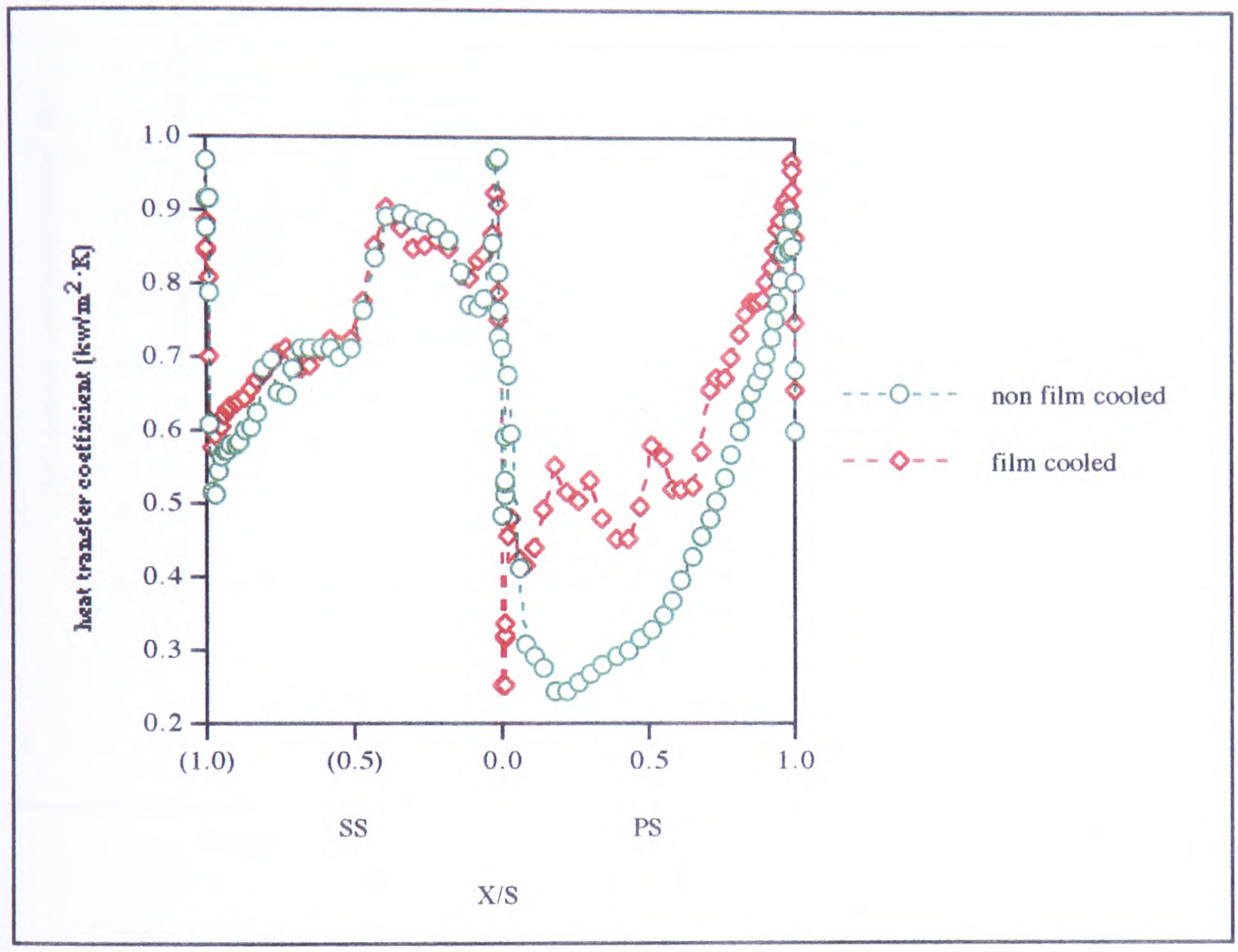
All six rows of holes that were located on the pressure surface were blowing. As expected, it is slightly harder to locate all the peaks in heat transfer coefficient on this surface. It can be seen from previous plots that the increase in heat transfer on the pressure surface is noticeably lower than the increase in heat transfer on the suction surface. As in the case of the suction surface, it can be seen that the cooling effects generated by the cooling rows on the pressure surface are predominantly localized. The only exception to this statement would be in the region where the uncooled heat transfer coefficient has its lowest value.



Graph 8.8 Test Case #4 Heat Transfer Coefficient

Graph 8.9 shows the heat transfer coefficient data for test case #5. Once again, due to the absence of the corresponding experimental data, the film cooled data are presented in comparison with the non-film cooled data. In this test case, only the

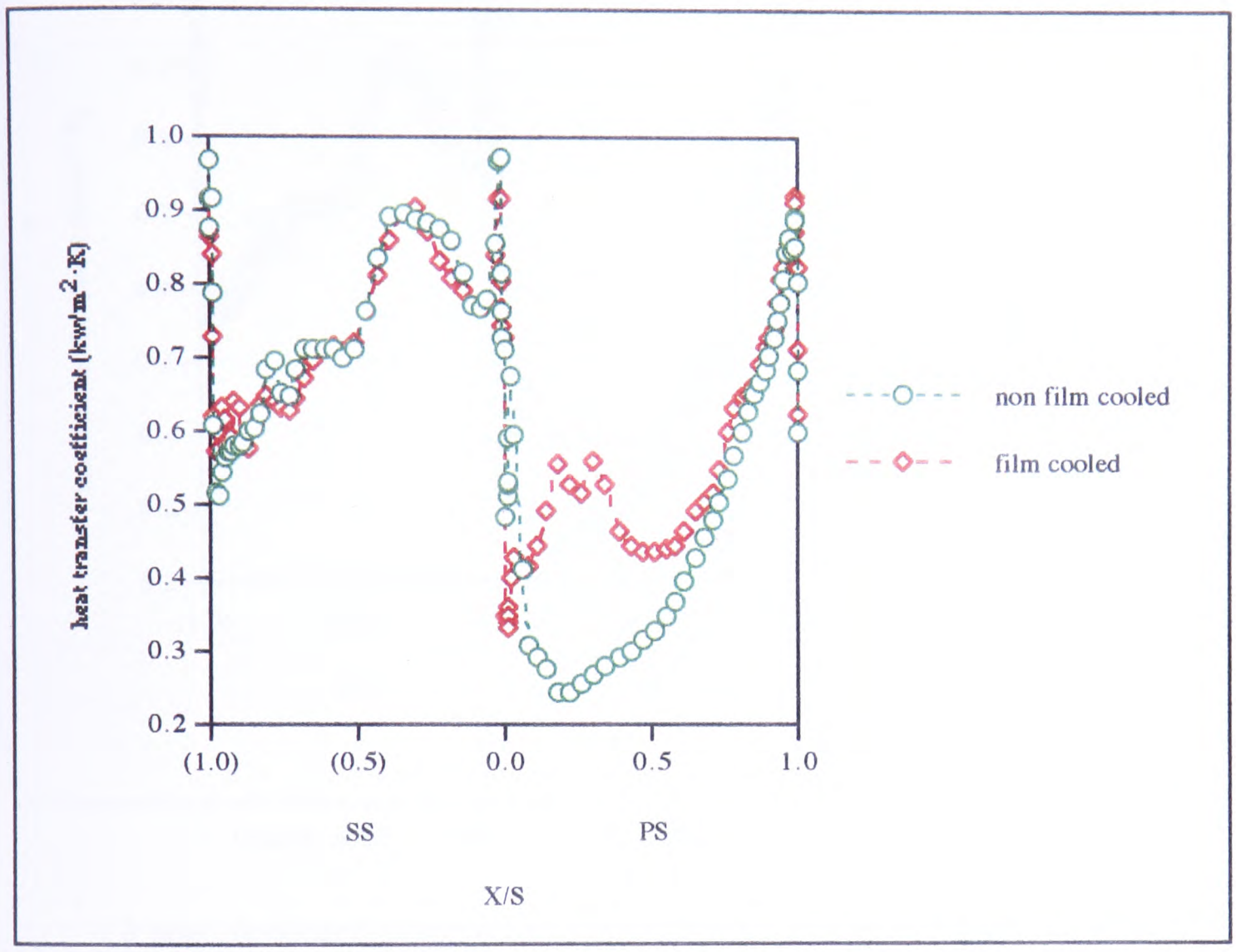
pressure surface cooling rows were active. This can be easily confirmed by looking at the plot. Furthermore, the heat transfer levels are similar in each of the cases up to this point where the leading edge film cooling has been eliminated. This fact can be confirmed by comparing Graphs 8.7 - 8.9. Also, since there is no cooling present on the suction surface of the blade, the film cooled heat transfer result should match the uncooled result in this region. This fact is also confirmed.



Graph 8.9 Test Case #5 Heat Transfer Coefficient

Graph 8.10 shows the heat transfer coefficient data for test case #6. In this test case, there were only four rows of cooling holes remaining. They were all located between the leading edge and a point that includes the X/S=0.3 location on the pressure surface. Two of these rows were located close to the stagnation point so only two peaks are strikingly noticeable in comparison with the non-film cooled data. Once again, it can be easily determined that the heat transfer levels are similar in each of the cases up to this point where the leading edge film cooling has been eliminated. There

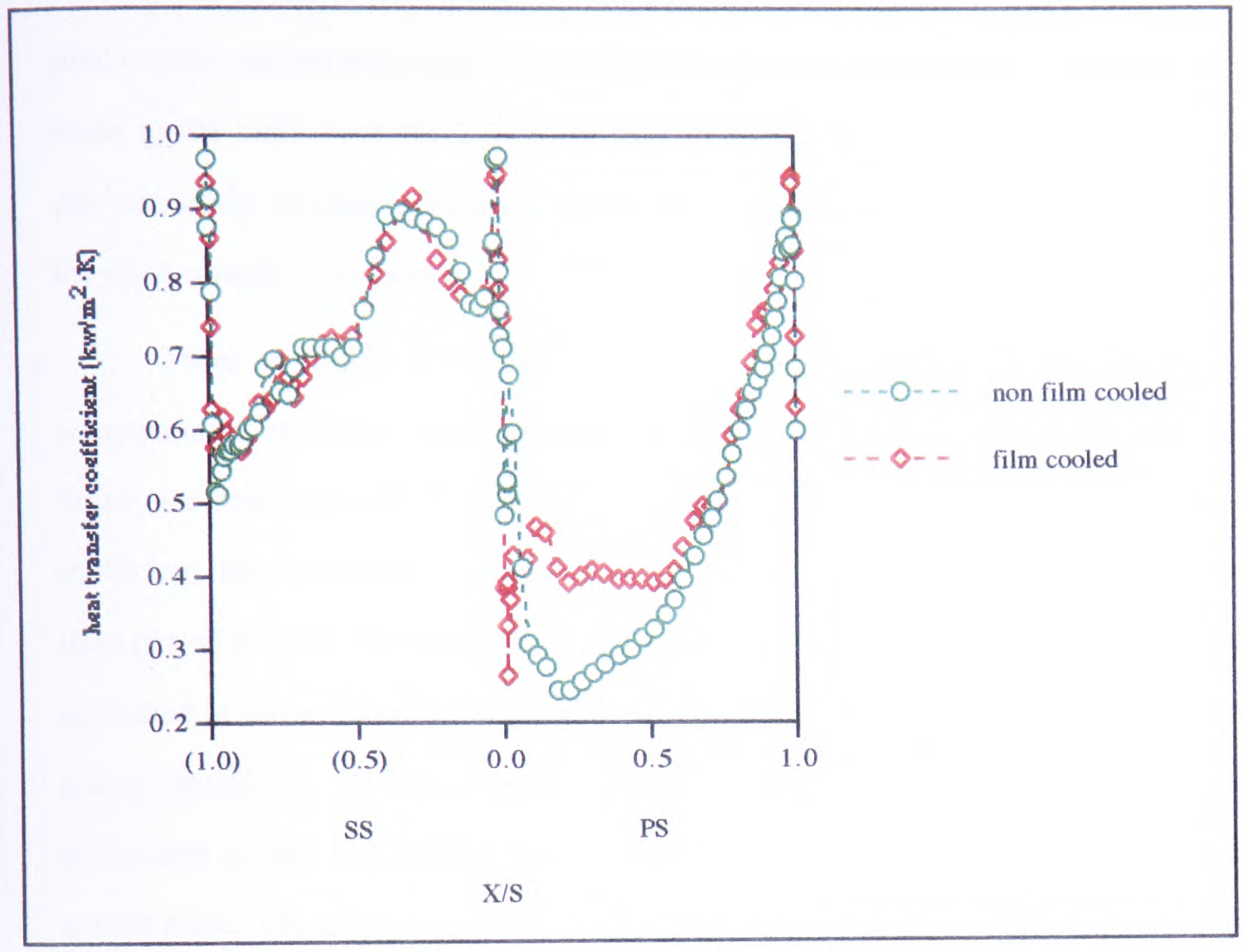
was no cooling present on the suction surface of the blade, or on the second half of the pressure surface of the blade. It would be expected that the film cooled heat transfer result should match the uncooled result in these regions. This fact is also easily determined by looking at the plot.



Graph 8.10 Test Case #6 Heat Transfer Coefficient

Graph 8.11 shows the heat transfer coefficient data for test case #7. In this test case, there were only two rows of cooling holes which were located close to the stagnation point on the pressure surface. At least one peak in the heat transfer coefficient is noticeable and the increased heat transfer level persists for a significant downstream distance before it meets the uncooled heat transfer level. It can be easily determined that the heat transfer levels are similar in each of the cases up to this point where the leading edge film cooling has been eliminated. It can also be easily determined that the film cooled heat transfer level matches the uncooled heat transfer

level more closely than in any of the previous plots because the fewest rows of cooling holes were blowing in this test case.



Graph 8.11 Test Case #7 Heat Transfer Coefficient

It was mentioned in an earlier chapter that the density of the grid in any CFD problem can have a profound effect on the final outcome. In all of the MEFP test cases presented in this analysis, from the flat plate ILPT test cases to the three-dimensional CHTT turbine test cases, there was a sufficient degree of experimentation with the grid density. A suitable grid density was selected based on the criterion of having sufficient spatial resolution while still maintaining as low a computing time as possible. Experimentation in the form of doubling of the grid density in each case was undertaken to determine if the final solution changed significantly. None of the results presented in this investigation changed more than five percent, which is an acceptable margin.

8.3 CONCLUSIONS

The predictions that MEFP has made in this three-dimensional turbine test case are very encouraging. The trends in heat transfer coefficient can be explained and the final results confirm the expected outcome. It is clear that the refinements that have been made to the code over the course of this investigation are valuable and allow for predominantly accurate predictions of the relevant parameters even when presented with the most complex test cases.

There is further work that can be done on this series of test cases. The computational resources were limited for the purpose of this analysis. In the near future, the resources will be available to convert all of the computational heat transfer coefficient data to the same format as the experimental heat transfer coefficient data in a short period of time. The differences in the coolant mass flow can also be more easily addressed at some future point so that the predictions reflect the actual experimental testing conditions. The final area that requires future attention is to ensure that accurate predictions of the heat transfer can be made in the showerhead region of a cooled turbine blade. The discrepancy that the difference in the discharge coefficients generates may or may not account for the difference that can be noted when comparing the computational and experimental heat transfer predictions in this region.

CHAPTER 9. FILM COOLING EXPERIMENTS

9.1 Experimental Facility

A series of film cooling experiments were performed using an existing facility at the Osney laboratory. The experimental facility consisted of a number of important elements that were necessary to create true engine representative testing conditions. For any film cooling test, a driving temperature difference is needed between the freestream and the coolant flow. This was provided by a heater mesh that was located at the inlet of the test section. The mesh was electrically heated by current from an arc welding transformer in order to provide a freestream temperature of approximately 42°C. The need for a freestream temperature of 42°C is discussed later in this section. In order to achieve this freestream temperature, a current of approximately 230A was required.

It was also important to be able to simulate realistic engine boundary layer conditions. For this purpose, there was a boundary layer bleed near the inlet of the test section followed by a boundary layer trip. A 5mm slot inclined at a 45° angle to the surface of the test section served as the boundary layer bleed, and a wire with a diameter of 500 microns served as the boundary layer trip. In this way it was possible to ensure that the same approach boundary layer conditions existed for every test. The coolant air was then injected at room temperature either through a set of four holes or through a slot located downstream of the boundary layer bleed and trip.

The test section itself was manufactured from perspex and measured 58mm by 58mm in cross section and 0.6m in length. The main flow was provided by suction to a 1000 cubic foot capacity vacuum tank, and the coolant flow was supplied via a British Standard orifice meter from the laboratory compressed air supply. Thermocouples were also placed in the test section to measure the freestream temperature, the surface temperature, and the coolant temperature. Figure 9.1 is a photograph of the test section configured with the four film cooling holes. Figure 9.2 is a photograph of the test section configured with the trench slot cooling geometry.

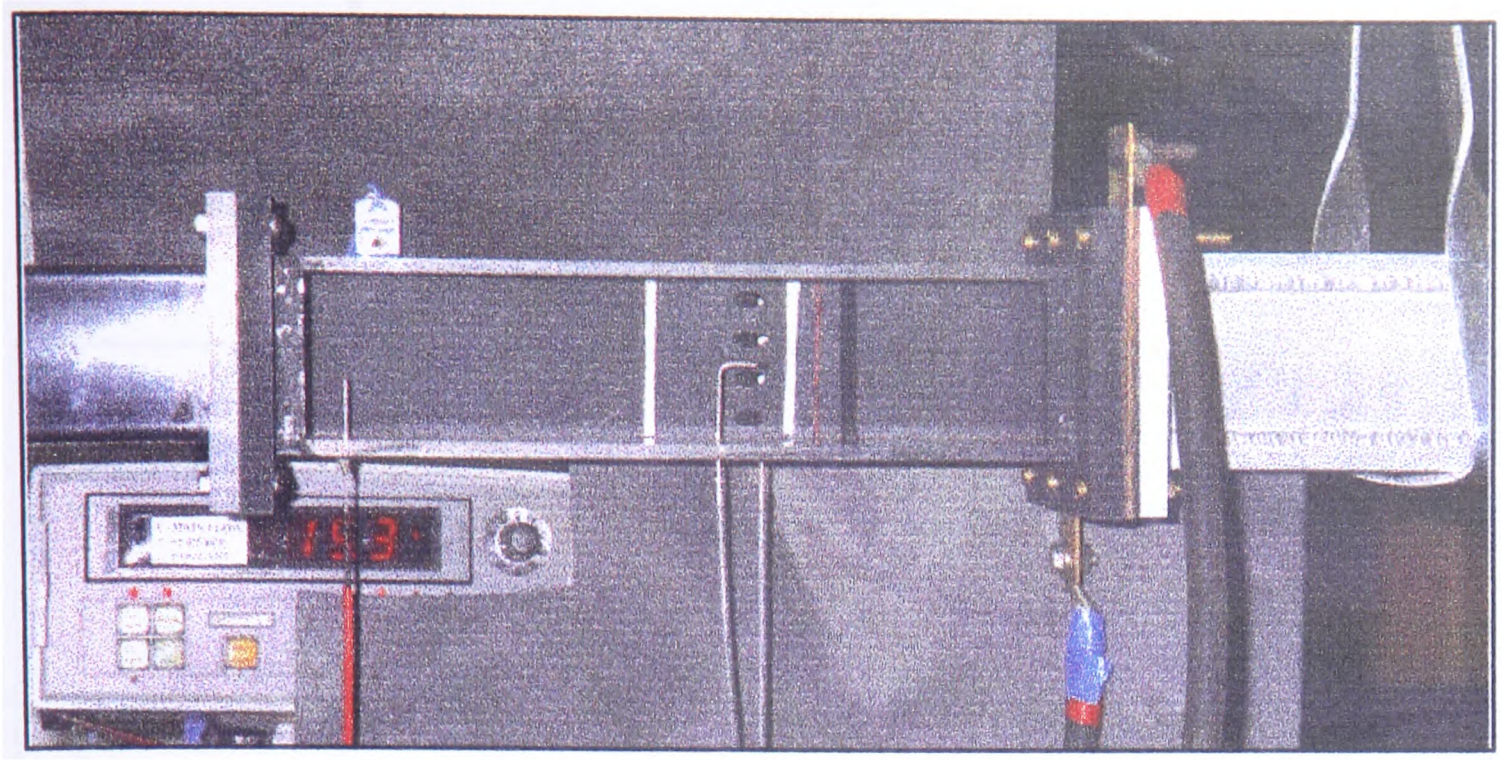


Figure 9.1 Experimental Test Section with Holes

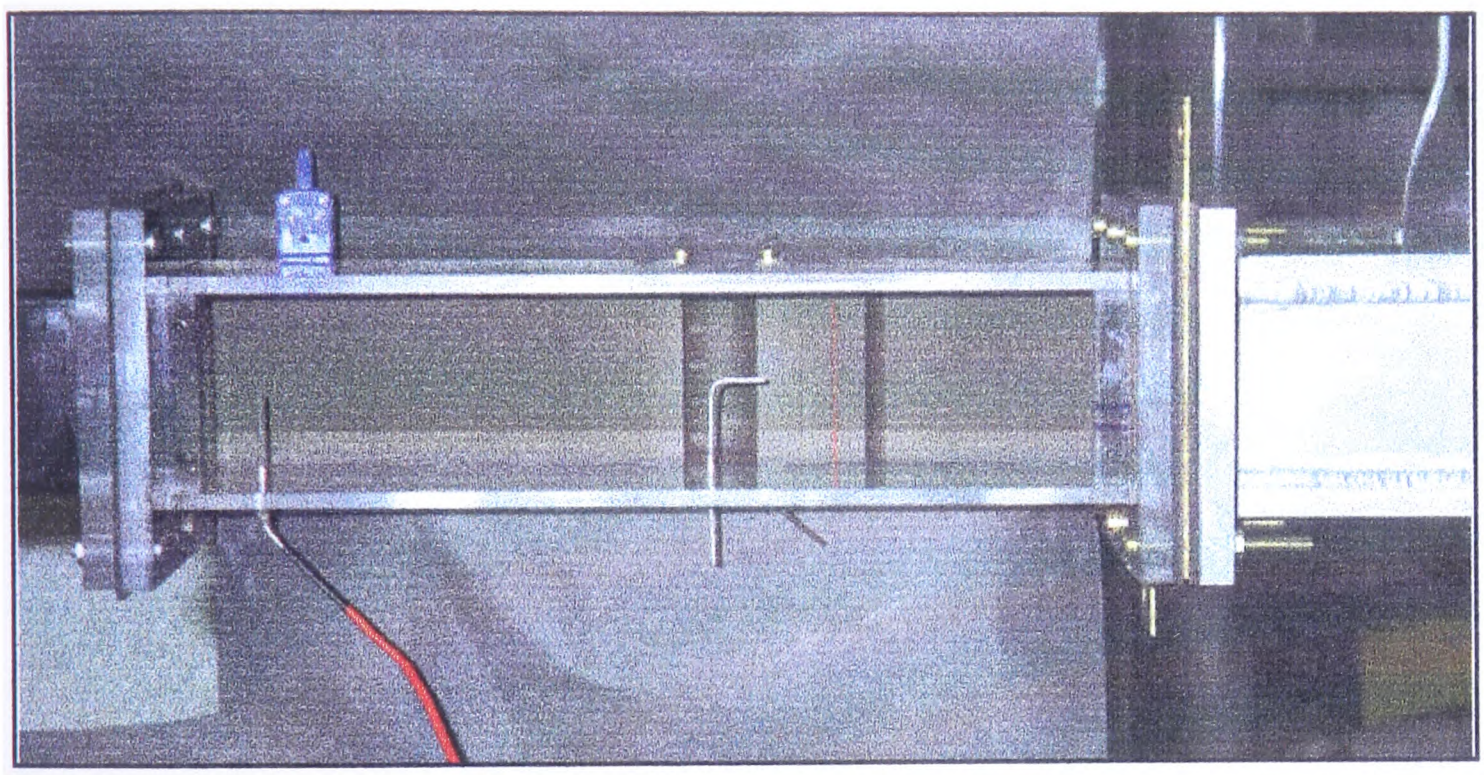


Figure 9.2 Experimental Test Section with Slot

The figures that follow show the film cooling configurations that were tested in more detail. Figure 9.3 shows the basic film cooling configuration with a single row of four cooling holes. The pitch to diameter ratio for the tests involving this particular geometry was 2.5 and the diameter of each hole was 5.8mm. The holes were inclined at a 30° angle with respect to the wall or the surface of the test section. This specific pitch to diameter ratio was chosen because it is a common spacing. An additional test was initially performed with a flat insert without film cooling holes. This was done to confirm that the experiment produced reliable results, and also to confirm that the

experimental results could be easily compared to the theoretical results for heat transfer on a flat plate. The non-film cooled data were also used at a later point to non-dimensionalize the film cooled heat transfer coefficient.

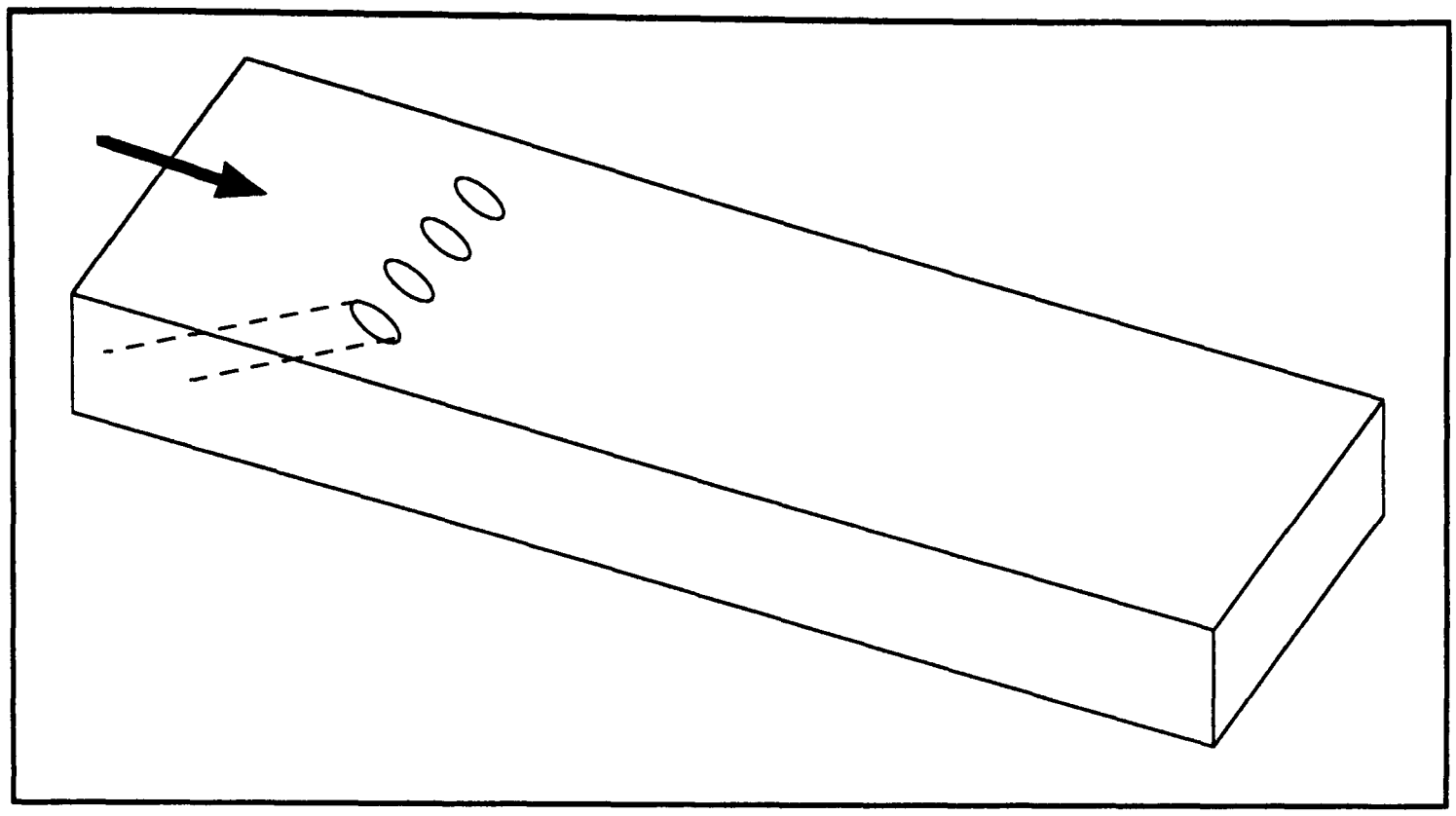


Figure 9.3 Basic Film Cooling Geometry

It was mentioned previously that even though film cooling through a slot as opposed to a row of holes is the most effective means of cooling a blade surface, it is very difficult to manufacture a turbine blade with such a configuration and implement it in a working engine. However, with the push for greater turbine inlet temperatures to increase engine efficiency, the benefits of slot cooling can not be abandoned altogether. Rolls Royce devised two hybrid slot-hole configurations in the hope that they would prove to have the cooling efficiency of a simple slot and yet be manufacturable using existing manufacturing technology. Figures 9.4 and 9.5 show these experimental configurations. The pitch to diameter ratio for the holes in each slot-hole configuration was 2.0 and the diameter of each hole was 5.8mm. Therefore, for the vortex slot and trench vortex geometries, five holes delivered the coolant to the vortex cavity. Figures 9.6 and 9.7 show photographs of the vortex slot and trench vortex test section inserts respectively.

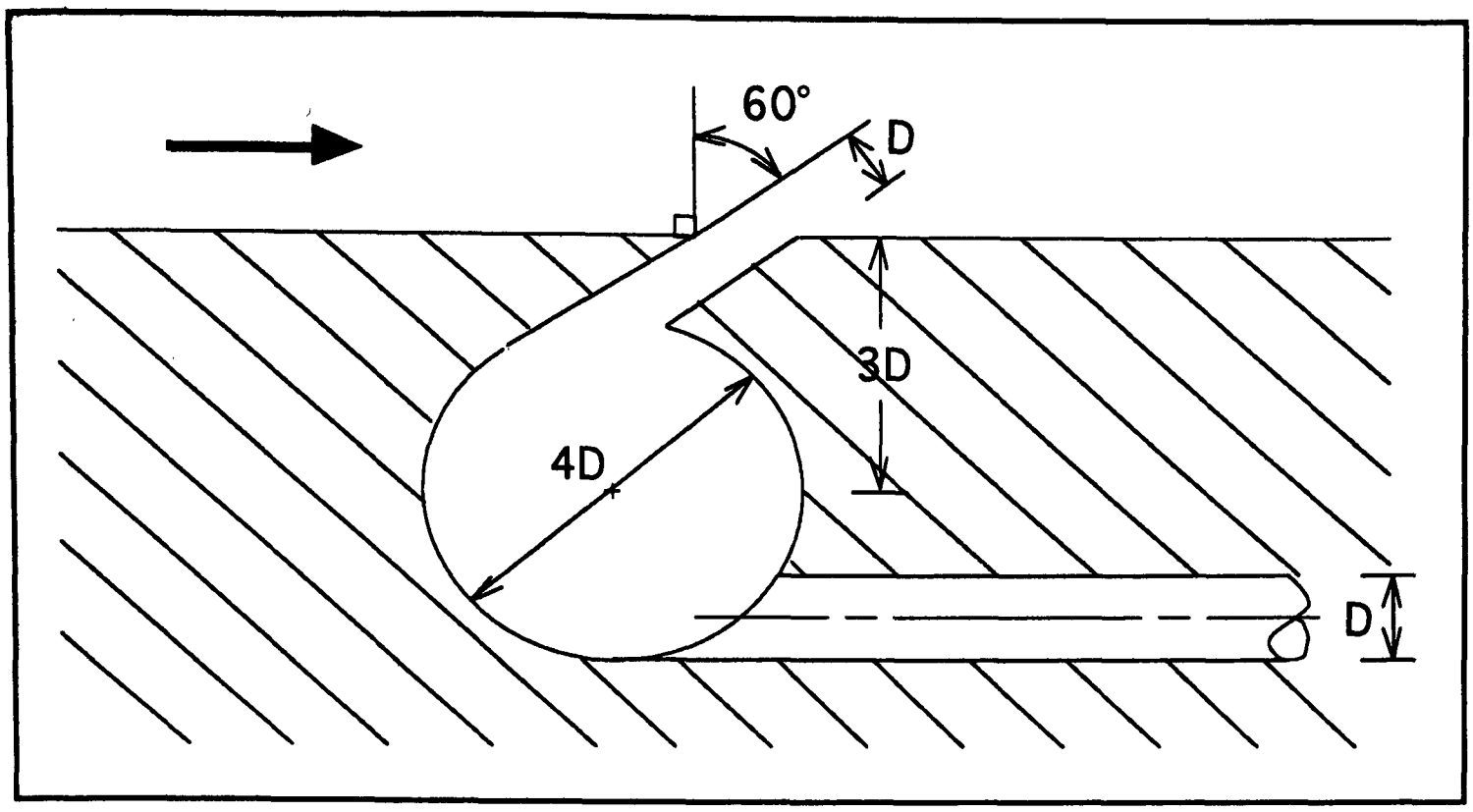


Figure 9.4 Vortex Slot Geometry

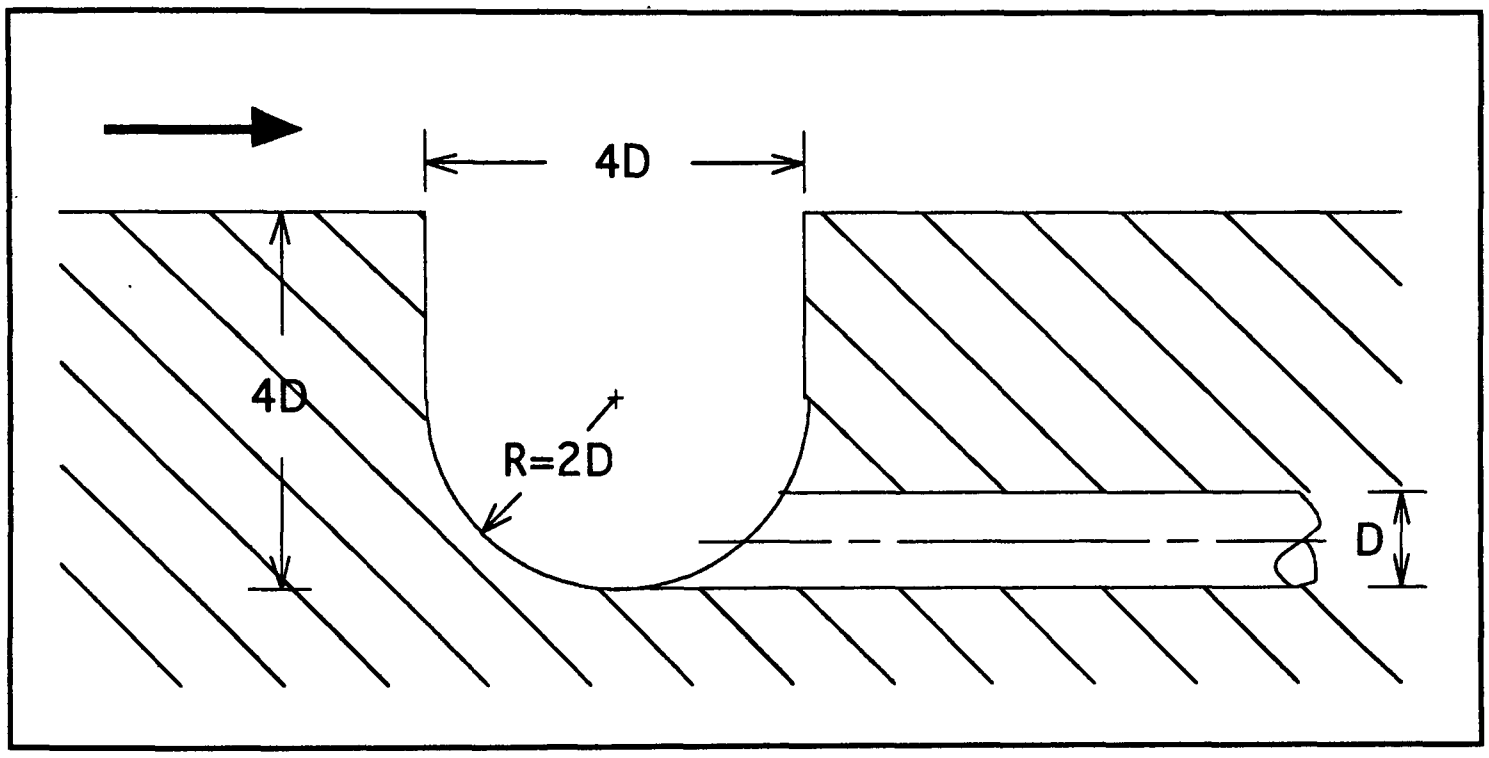


Figure 9.5 Trench Vortex Geometry

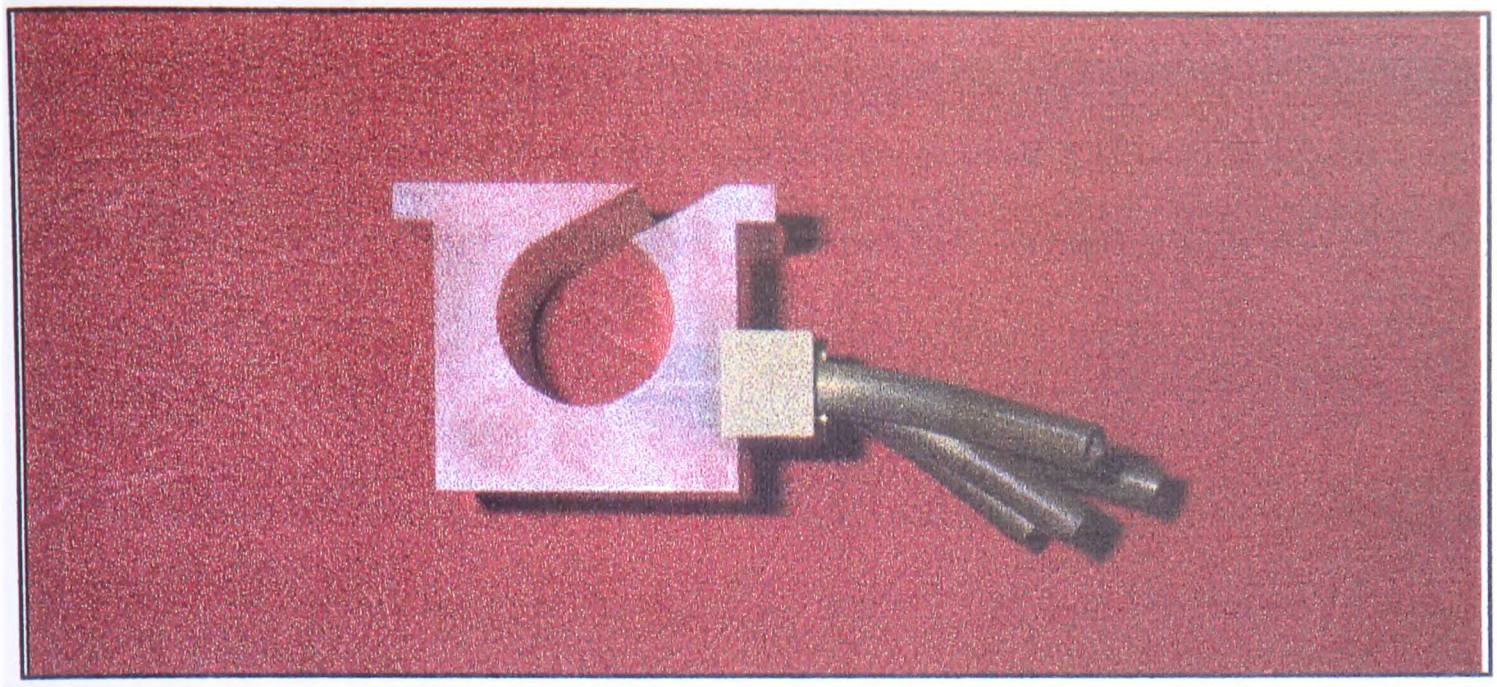


Figure 9.6 Vortex Slot Test Section Insert

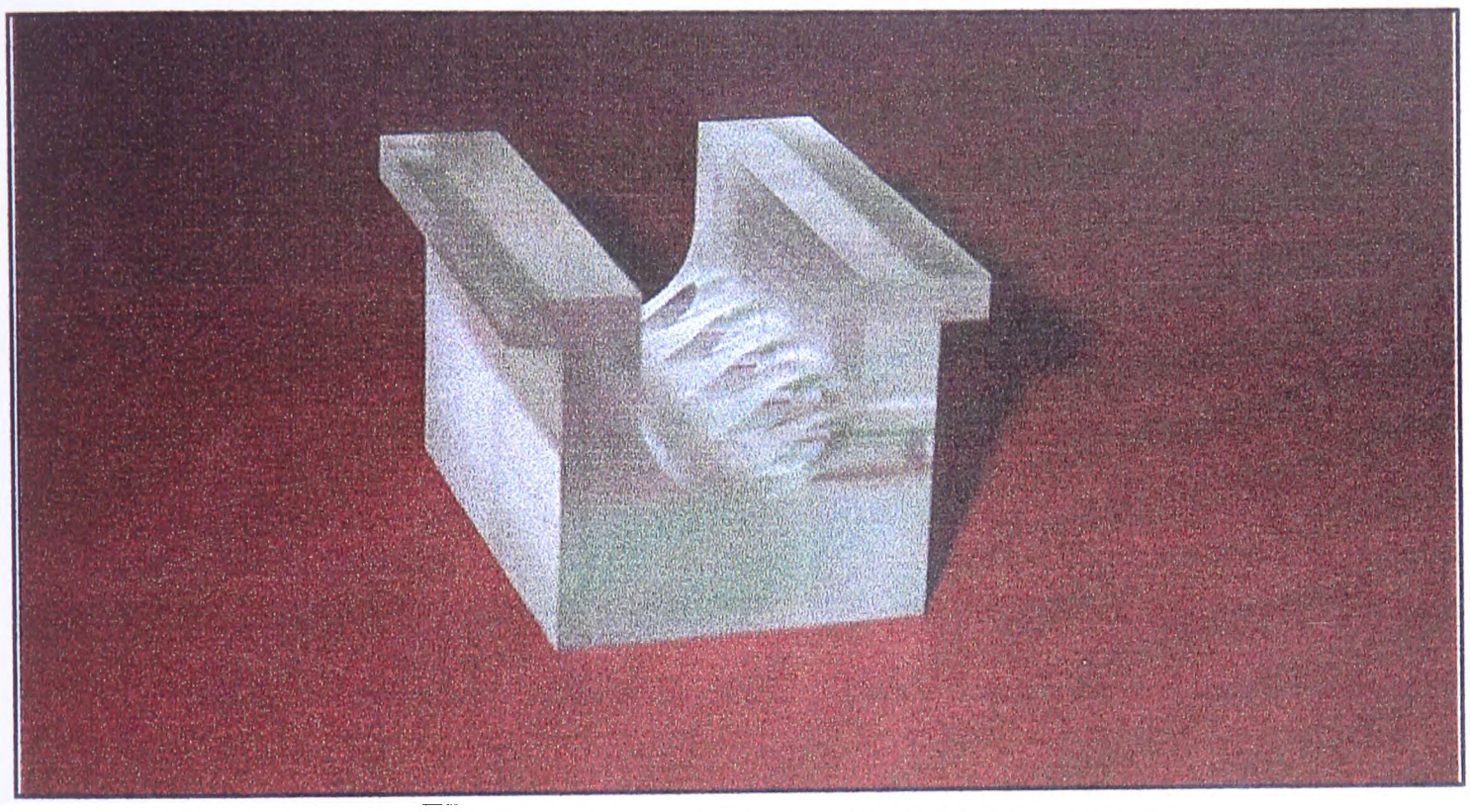


Figure 9.7 Trench Vortex Test Section Insert

Figures 9.8 and 9.9 show schematics of the test section. The heated mesh is pictured at the inlet to the section, as is the boundary layer bleed, and the exit for the coolant flow. The relative position of the video camera is also depicted. The arrow shows the direction of flow for the freestream. It is clear that there is a difference in the configuration of the settling plenums in the case of injection through a row of holes (Figure 9.8) and in the case of injection through the slot-hole combination (Figure 9.9). A simple plenum was sufficient for the case of cooling by holes alone. It can be said that the flow distribution through each of the four holes was judged to be sufficiently

uniform. Even if this was not the case, then any decreased amount of coolant flow that might pass through the outermost film cooling holes could be easily explained by a lack of uniformity in the repeating spanwise pattern of heat transfer coefficient and film cooling effectiveness. This can be confirmed by referring to the results presented in a later section.

It was very important to ensure that the flow through each of the five holes of the slot-hole configurations was uniform. This consideration was much more important in the case of the slot-hole configurations than in the case of the hole configuration because a completely uniform flow is needed at the slot exit to correctly simulate the desirable properties of slot cooling. As in the case of the film cooling holes, success in this aspect can be confirmed by inspection of any inconsistencies in heat transfer coefficient and film cooling effectiveness in a spanwise direction.

It can be seen in Figure 9.9 that instead of the coolant being injected from the initial settling plenum directly into the insert, that there is a set of long tubes located between the initial settling plenum and the insert. The criterion that was used for ensuring uniform flow through each of the holes was that the pressure drop in the plenum was less than five percent of the head loss along the length of the tubes. The pressure drop in the plenum was defined as the difference in pressure between the point where the velocity is greatest (at the entrance to the plenum along the centerline) and a point where the velocity has a value of zero. Darcy's equation (Eqn.9.1) was used to calculate head loss for the flow in the tubes. Assuming there are five holes each with a diameter of 5.8mm, then the tubes leading from the initial settling plenum to the insert need to be slightly greater than 3m in length. The dimensions of the test section were constant for all tests, therefore the five holes were at a pitch to diameter ratio of 2.0. This particular configuration was judged to be a likely engine configuration.

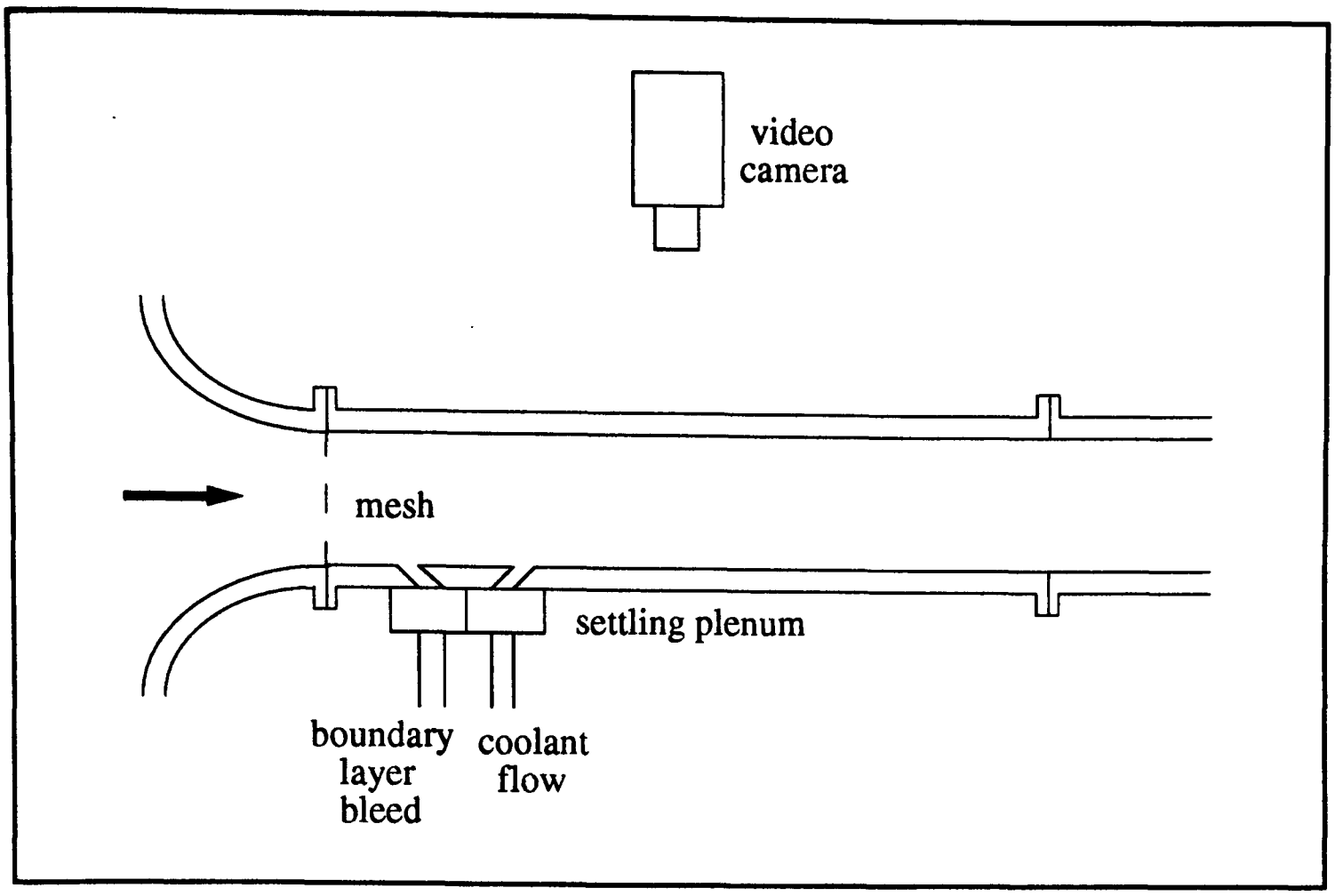


Figure 9.8 Test Section Schematic with Holes

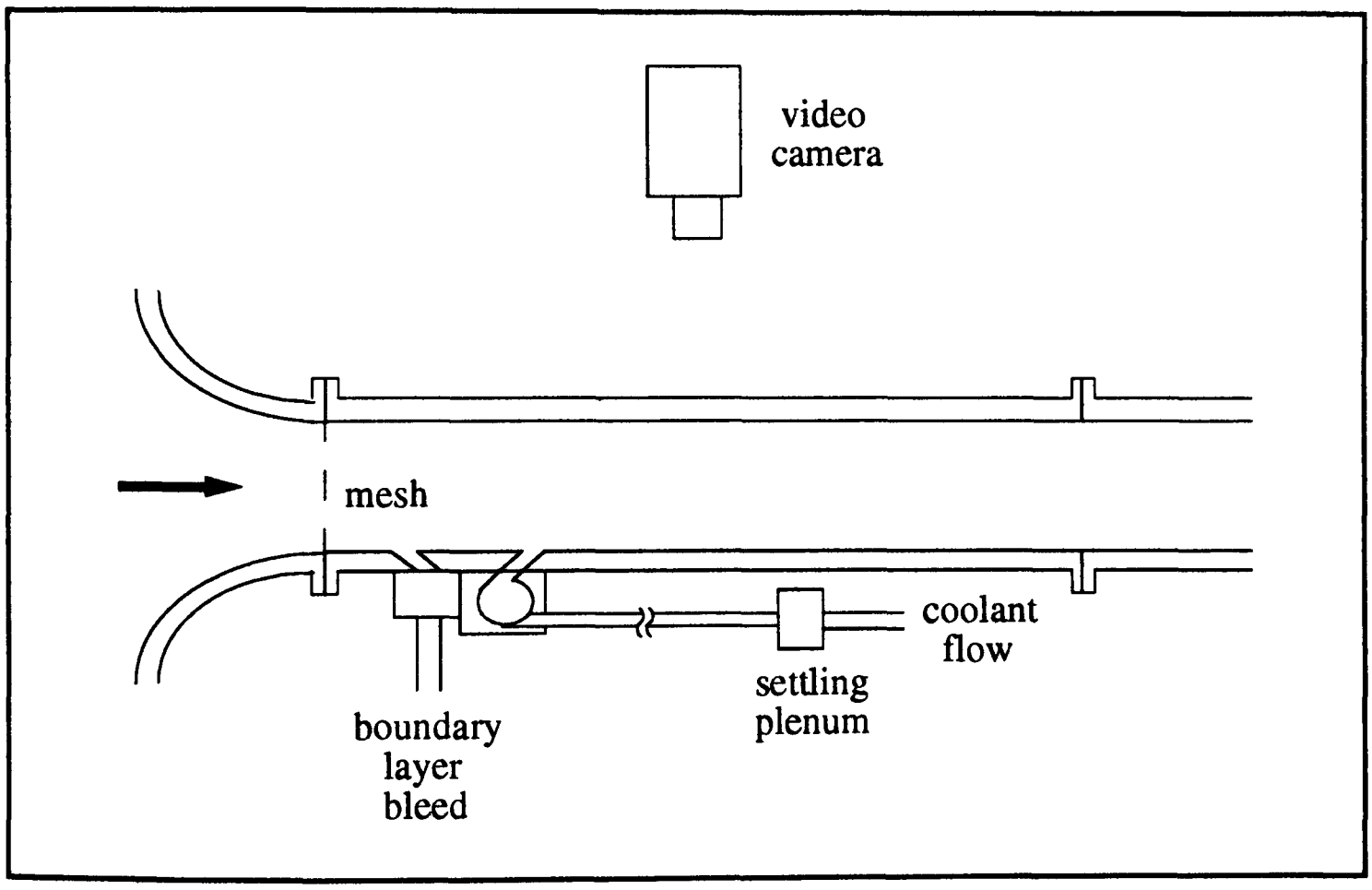


Figure 9.9 Test Section Schematic with Slot

$$h_L = f\frac{Lv^2}{4rg} \qquad (9.1)$$

9.2 Data Processing

In all of the film cooling experiments, complete surface temperature distributions were measured using encapsulated thermochromic liquid crystals. The entire area downstream of the row of cooling holes and the slot was sprayed with black paint and then overlaid with a thin layer of crystals. The type of crystals that were used were wide band liquid crystals that have a continuous colour play over a wide range of temperatures. The colour play progresses from clear or colourless to red, green, blue-green, and then blue before returning to a clear or colourless state. In this case, the crystals were sensitive to temperature changes in the range of approximately 22°C to 38°C. Experience with the experimental facility has consistently shown that during a typical hole cooling test, the maximum surface temperature at the end of a run was approximately 4°C less than the recorded freestream temperature. Therefore, in order to take advantage of the full range of crystal colour play, a freestream temperature of approximately 42°C was needed.

The colour play is defined in terms of values of hue. Throughout the experiments, the test section is lit with a pair of fluorescent strip lights placed above and below the test section, and the colour play of the crystals is recorded with a standard video camera and VHS video recorder. Using a video processing system developed by Wang **(ref.94)** and a calibration curve, the hue values can then be converted to temperature values. This technique is described in a later section. One of the main advantages of using wide band liquid crystals as opposed to narrow band liquid crystals is that a number of temperature or hue values can be collected over a significant time period.

During each test, it was necessary to know the exact time that had elapsed from the activation of the heater. A digital timer was connected to the video system and was

switched on simultaneously with the mesh current at the inlet to the test section. In this way it was very easy to label the beginning and end of each test. The video processing system samples the recorded video image every 0.04 seconds for a two minute run or every 0.02 seconds for a one minute run. Therefore, for each of the thousands of frames that are eventually processed, a hue value can be determined for each pixel.

The experiments described here are all transient tests, which means that the surface of the liquid crystals is exposed to a step change in the driving gas temperature. In this application, the mesh time constant, the liquid crystal response time (3 milliseconds), and the video sampling period (0.04 seconds) are all small in comparison to the perspex surface response time (**ref.11**). Therefore, it is assumed that the test surface is initially at a uniform temperature at all depths, and that the surface response can be described using a semi-infinite heat transfer model according to Eqns.9.2 and 9.3. The condition that the thickness of the wall must be greater than the thermal penetration depth also be met for this model to be valid, as it was for these tests. The data processing generates values of surface temperature at particular points in time (and space), so since all the other terms in Eqns.9.2 and 9.3 have known values, the heat transfer coefficient and the adiabatic wall temperature can be evaluated. Therefore, it was possible to measure the local values of heat transfer coefficient and film cooling effectiveness over the entire length of the test section downstream of the holes or the slot and over the entire width of the test section.

$$\frac{T_w - T_i}{T_{aw} - T_i} = 1 - e^{\beta^2}\,\mathrm{erfc}(\beta) \qquad \textbf{(9.2)}$$

$$\beta = h\frac{\sqrt{t}}{\sqrt{\rho C_p k}} \qquad \textbf{(9.3)}$$

9.3 Discussion of Results

9.3.1 Calibration Test Results

The liquid crystal data are very sensitive to the type of camera being used, the crystals that are being used, and the light and camera position. Therefore, for each set of tests with a new camera or different light position, a new calibration curve had to be constructed. The calibration curve simply defines a specific temperature value for a specific hue value.

For these sets of experiments, the liquid crystals were slowly heated using a hair dryer placed at the inlet of the test section. This proved to be a very efficient way of controlling the temperature rise, as opposed to using the mesh to heat the freestream. The temperature range that was recorded was the range of temperatures over which the crystals showed a colour change, which was mentioned previously to be approximately 22°C to 38°C. Using the image processing system, an average hue value was determined over a small region located just upstream of the surface thermocouple. Hue values were collected for each increment in temperature over the specified range. The resulting hue/temperature curve was then smoothed or filtered using a Butterworth filter in Matlab®. Figure 9.10 shows a sample plot of the raw hue versus temperature data that were collected in the manner described above. It is clear from this graph that the data outside the temperature range of 22°C to 38°C are not useful. Figure 9.11 shows a typical smoothed calibration curve that was used for data reduction in these experimental test runs. It is imperative that the resulting curve has a steep slope with no regions where the slope of the curve is close to zero. This is done to ensure that each hue value represents one specific or distinct temperature, as opposed to representing a possible range of temperatures.

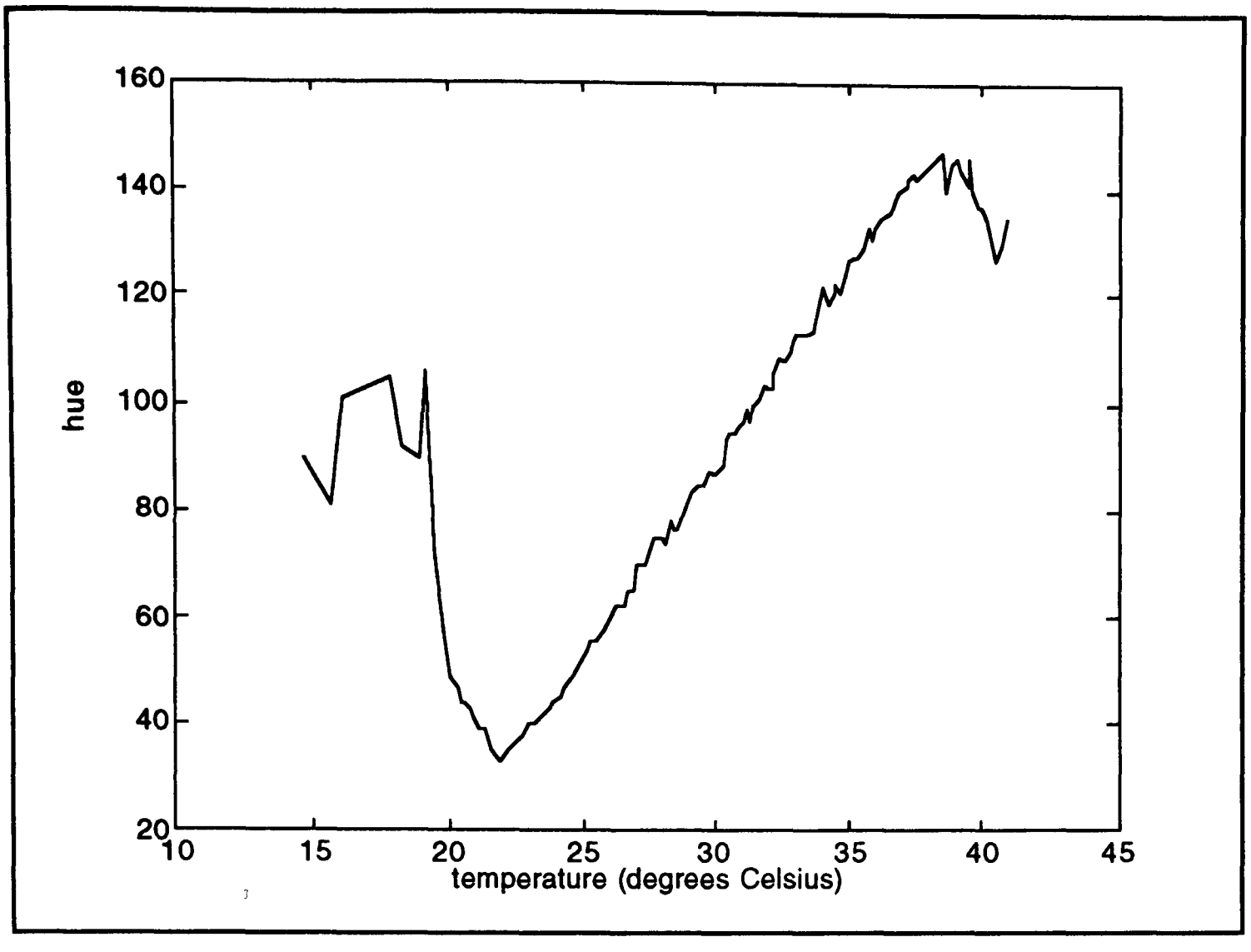


Figure 9.10 Raw Hue vs. Temperature Data

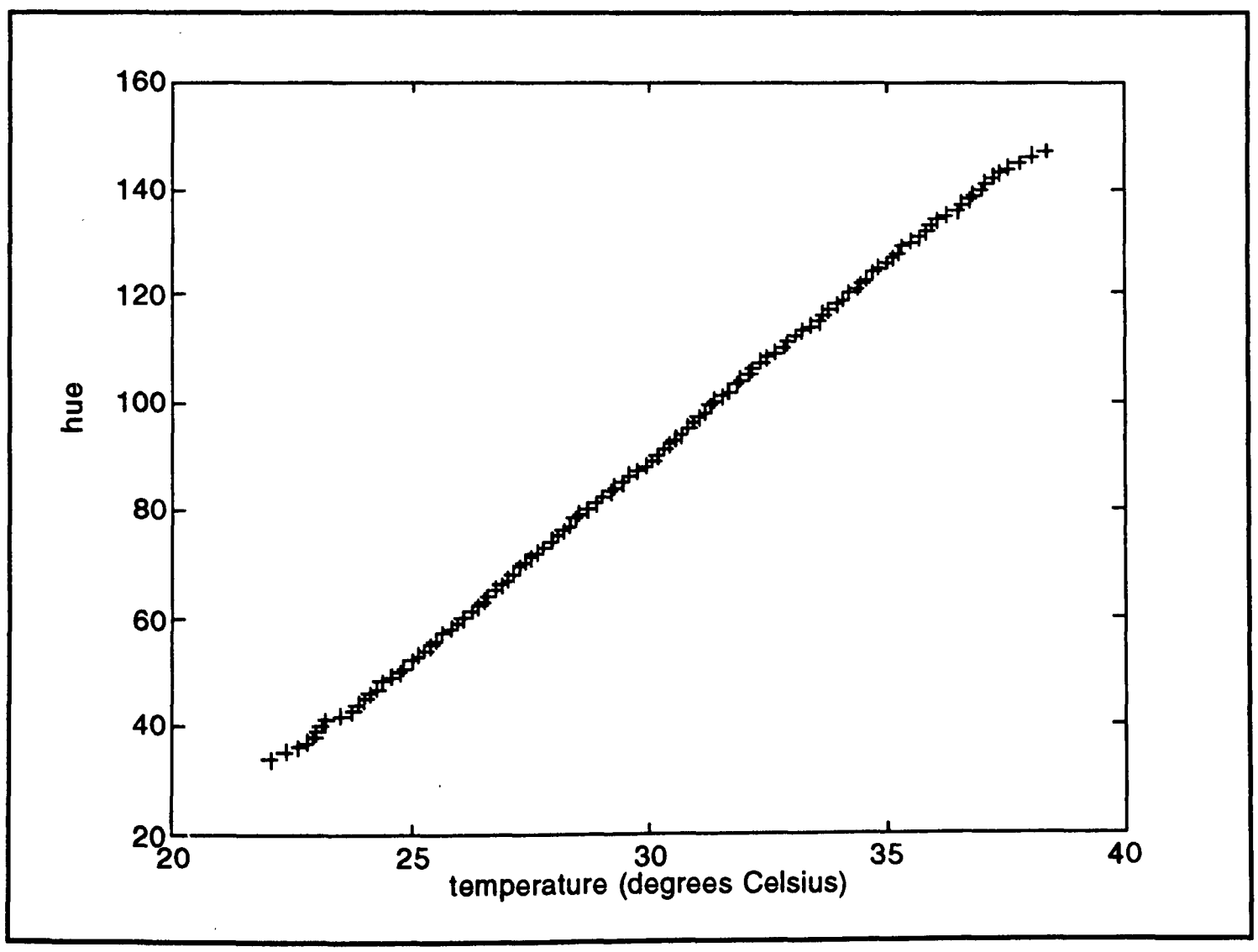


Figure 9.11 Smoothed Calibration Curve

9.3.2 Non-Film Cooled Results

It is impractical to analyze the hue data from every single pixel over the entire test section. Therefore, it was decided that for all of the tests in this study, data would be collected only at various predetermined downstream locations (from the cooling holes or slot). For this study, X/D values of three, five, eight, twelve and sixteen were used, where X is the downstream distance measured from the trailing edge of the holes or slot and D is the diameter of the holes. This set of values was thought to give enough data so that an accurate picture of the flow throughout the test section could be constructed. It was also believed that twenty spanwise data points at each of the X/D locations would give sufficient resolution of the required parameters. This chosen matrix was similar to that of other researchers who had conducted related experiments so that the results from this study could be compared to the results from other studies.

The image processing system saves the hue values for each specified pixel to a Matlab® file. In this case, there were five Matlab® files containing the data at each of the X/D locations that are described above for each experimental run. Each of these files was then loaded individually, along with the calibration data, into a program written by David Gillespie for further data reduction. Gillespie's program converts the raw hue signal into a temperature signal over the time of the run according to the calibration curve and then achieves a least squares regression fit of the resulting data to Eqns.9.2 and 9.3. A value for the heat transfer coefficient and the adiabatic wall temperature are arrived at by minimizing the sum of the squares of the differences between the surface temperature as determined from the raw hue signal and the surface temperature as calculated from Eqn.9.2. Figure 9.12 shows a sample plot of the raw temperature signal at one particular X/D location over a thirty second run time. The '+' symbols correspond to the numerous, discrete points selected by the program and used in the least squares regression. In practice, the adiabatic wall temperature would be the final surface temperature reached for a test of infinite duration. The value of the heat transfer

coefficient dominates the slope of the curve at the start of the experiment. The steeper the initial slope, the greater the value of the heat transfer coefficient.

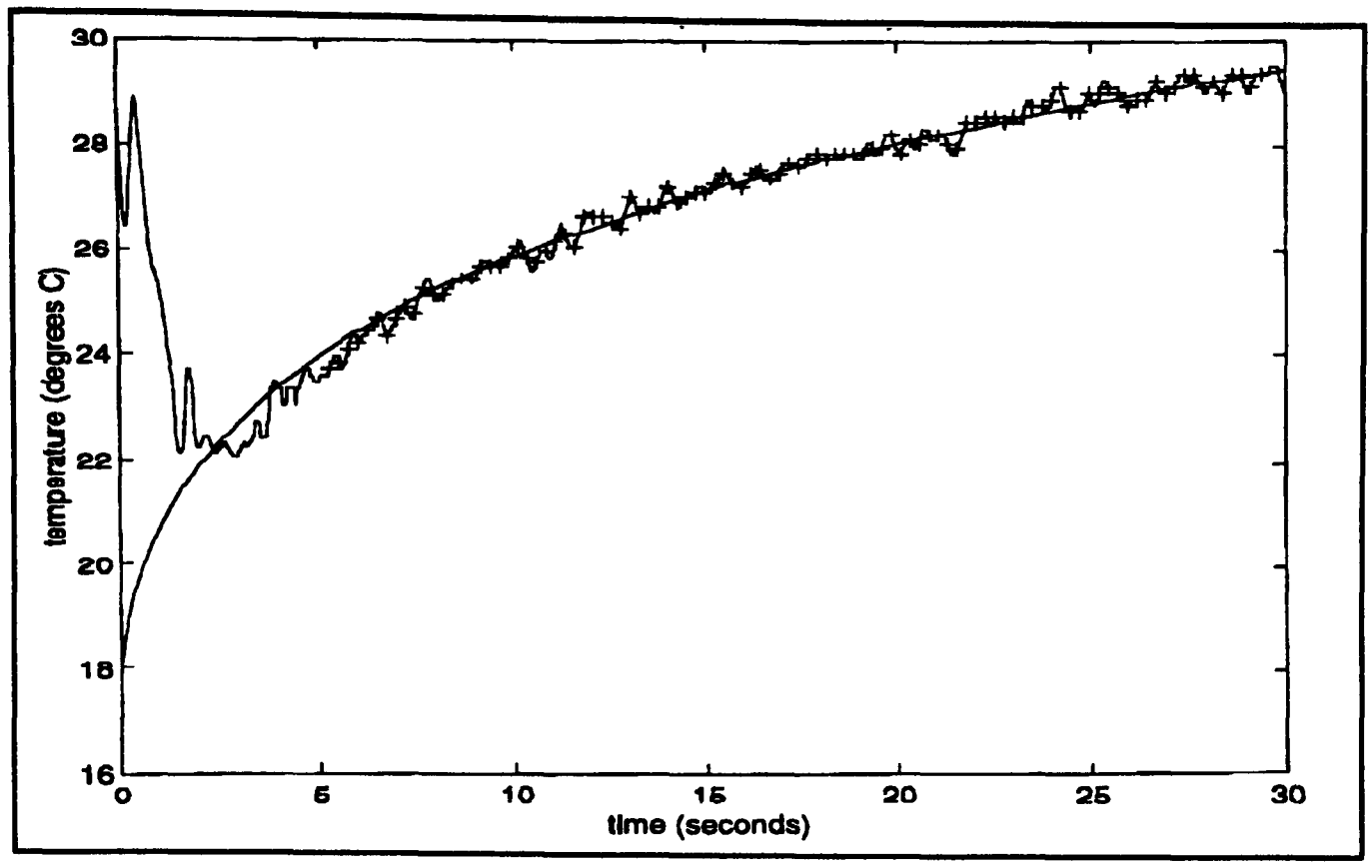
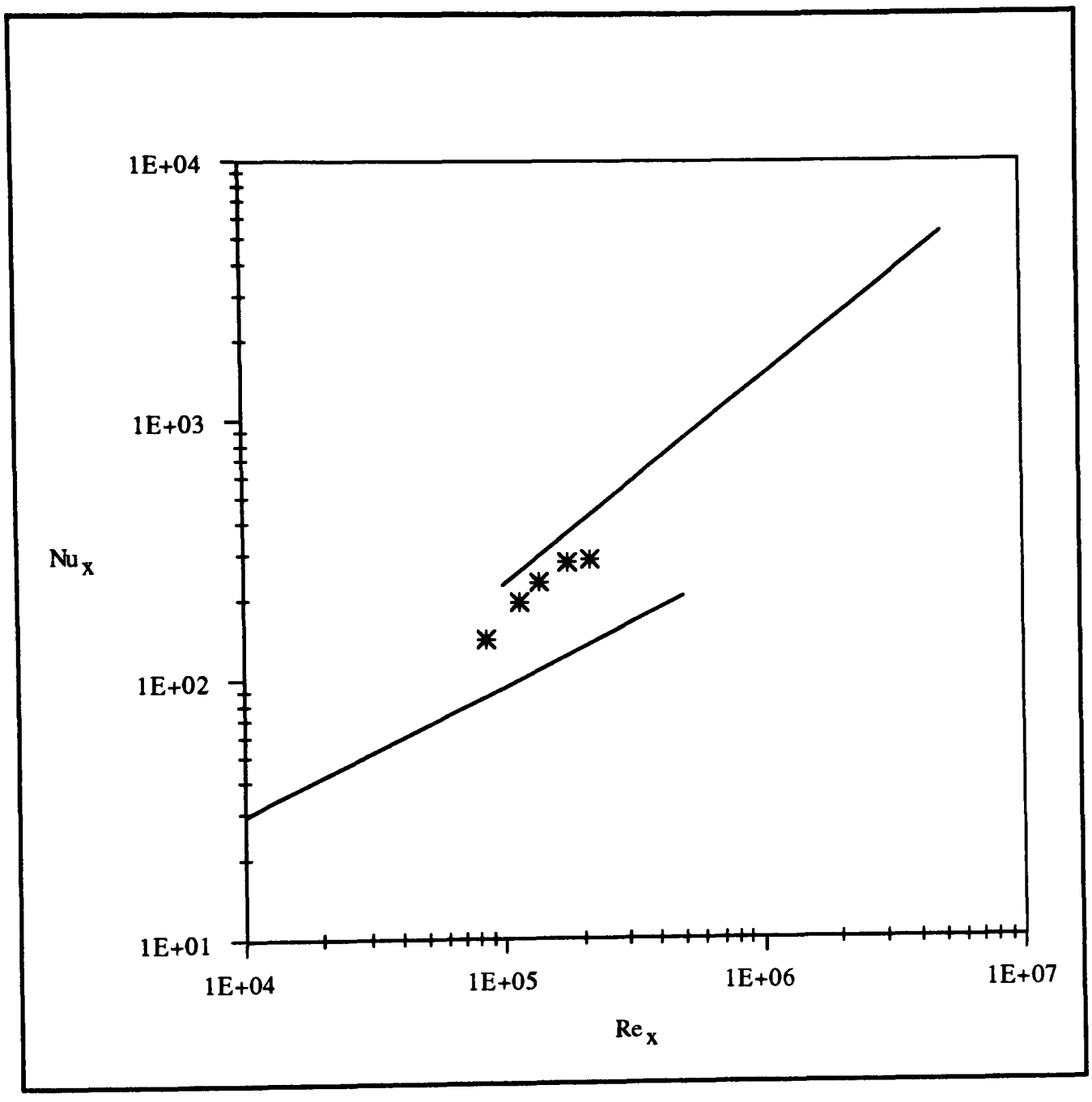


Figure 9.12 Raw Temperature Signal with Curve Fit

The program described above generates values for the heat transfer coefficient and the adiabatic wall temperature at each spanwise position and X/D location. For the non-film cooled test case only, the adiabatic wall temperature was held constant at a value that corresponded to the maximum freestream temperature recorded during the run in order to make the data reduction both faster and easier. As was expected for this test case, there was no significant spanwise variation in the heat transfer coefficient, so all of the spanwise values were averaged to give one heat transfer coefficient for each X/D location. The test conditions were all known, therefore, the Nusselt number and the Reynolds number were easily calculated. Graph 9.1 shows the experimental results in comparison to the theoretical results assuming both fully laminar and fully turbulent flow under the same test conditions. The top line on the graph represents the theoretical turbulent flow calculation and the bottom line on the graph represents the theoretical laminar flow calculation. Each data point on the graph corresponds to one of the X/D locations that was mentioned earlier. These results are consistent with a slightly earlier

onset of turbulent flow due to the presence of a grid that produces a turbulence intensity on the order of 0.5 percent. Figure 9.13 shows a plot of the theoretical Nusselt number versus the Reynolds number over the entire range of laminar, transitional, and turbulent flow on which Graph 9.1 is based. Eqns.9.4 and 9.5 show the equations used for the theoretical laminar and turbulent Nusselt numbers respectively.



Graph 9.1 Nusselt Number vs. Reynolds Number

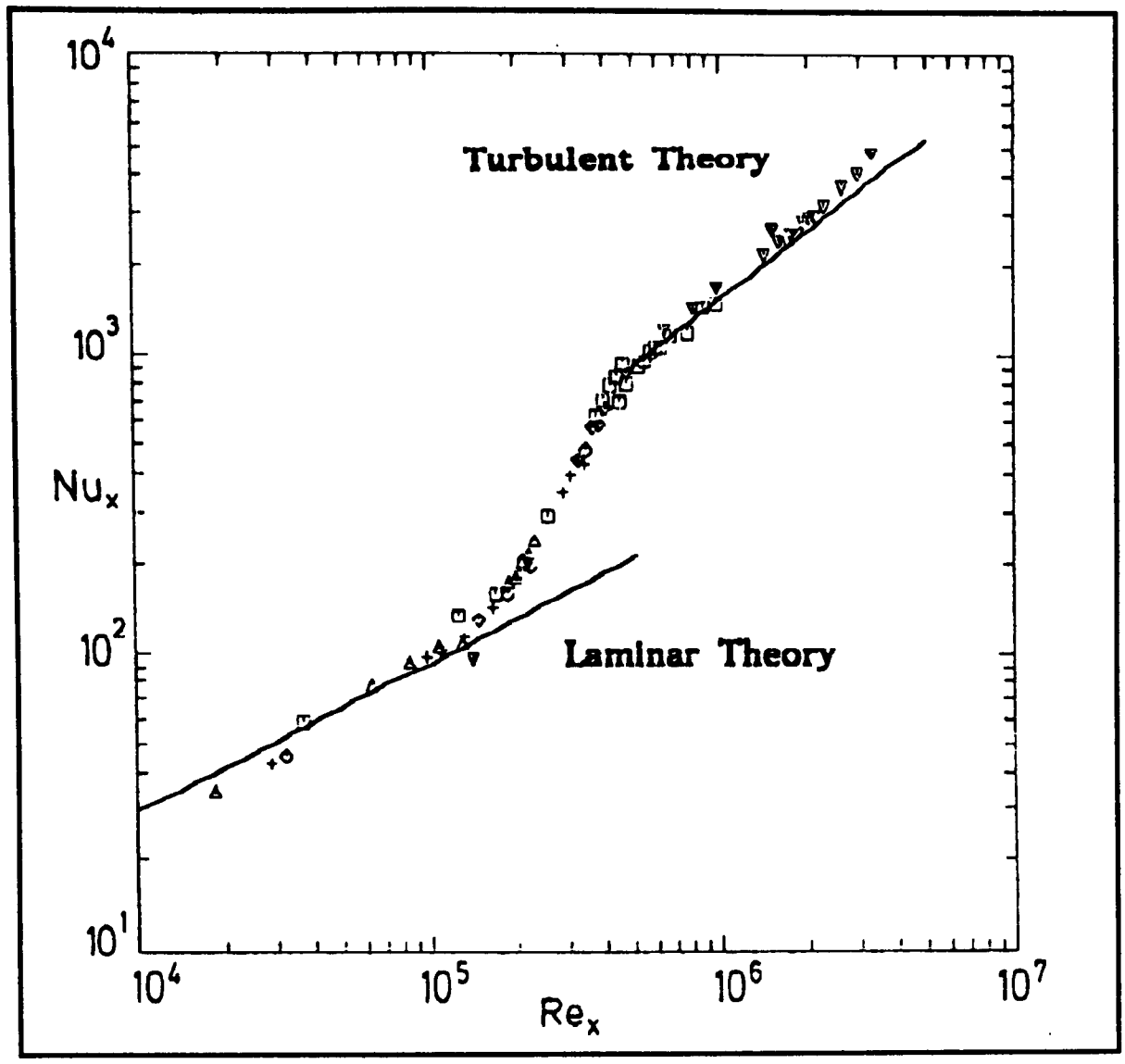


Figure 9.13 Theoretical Nu_x vs. Re_x
(reference: D. Phil. Thesis by Arnold J. Teekaram, 1989)

$$Nu_{laminar} = 0.332\, Re^{1/2}\, Pr^{1/3} \tag{9.4}$$

$$Nu_{turbulent} = 0.0287\, Re^{0.8}\, Pr^{0.6} \tag{9.5}$$

9.3.3 Hole Cooling Results

Film cooling experiments were carried out with the basic film cooling geometry as depicted in Figure 9.3 at the injection rates shown in Table 9.1. The velocity of the freestream was 30m/s, so the velocity of the coolant flow varied from 6m/s to 30m/s. A freestream velocity of 30m/s was chosen because it achieved a Reynolds number close to engine values. A run time of 30 seconds was found to be sufficient for the non-film cooled runs. Not only did this amount of time allow for an adequate collection of data, but it could also be said that at the end of the run, the surface temperature changes were

small. However, a run time of 60 seconds was needed for the film cooled runs in order to collect an adequate amount of data. At the end of this 60 seconds, the entire range of the crystal colour play had been recorded.

TEST NUMBER	INJECTION RATE (G)
#1a	0.2
#2a	0.4
#3a	0.6
#4a	0.8
#5a	1.0

Table 9.1 Experimental Test Matrix (Holes)

Recording the data on video tape was not only necessary for the data reduction process, but it was also very useful as a visual record of the experiment. These experiments are so short that it was often difficult to make visual observations while the experiment was being conducted. In a study of this kind, qualitative visual observations are just as important as quantitative numerical data in providing a greater understanding of complex flow behavior in a film cooling situation. What follows is a presentation and discussion of these two elements.

Figures 9.14 and 9.15 show video frame captures from the VHS video tape of the actual film cooling run at the injection rate of 0.2. It is the lowest injection rate considered here, therefore, the coolant would be expected to have a small effect. This is confirmed by consulting Figure 9.14. After only 1.39 seconds of a sixty second run, only faint cooling stripes can be seen. The colour change is essentially uniform in the spanwise direction and any noticeable effect of the coolant disappears almost immediately. Figure 9.15 shows the bright blue-green shade that is typically seen at the end of these experiments and characterizes the end of the colour play range. Once

again, it is not surprising to find that the colour looks uniform at this point and that there is little evidence of cooling.

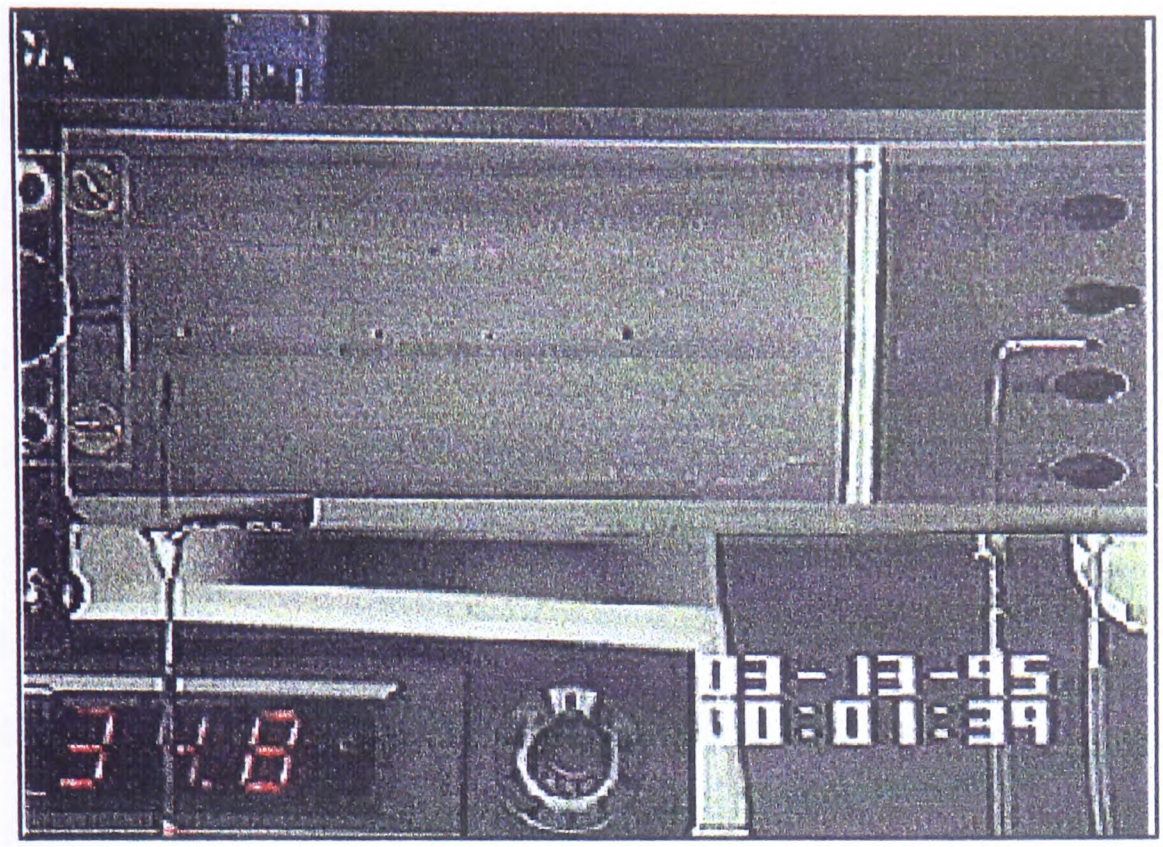


Figure 9.14 G=0.2 at t=1.39 sec.

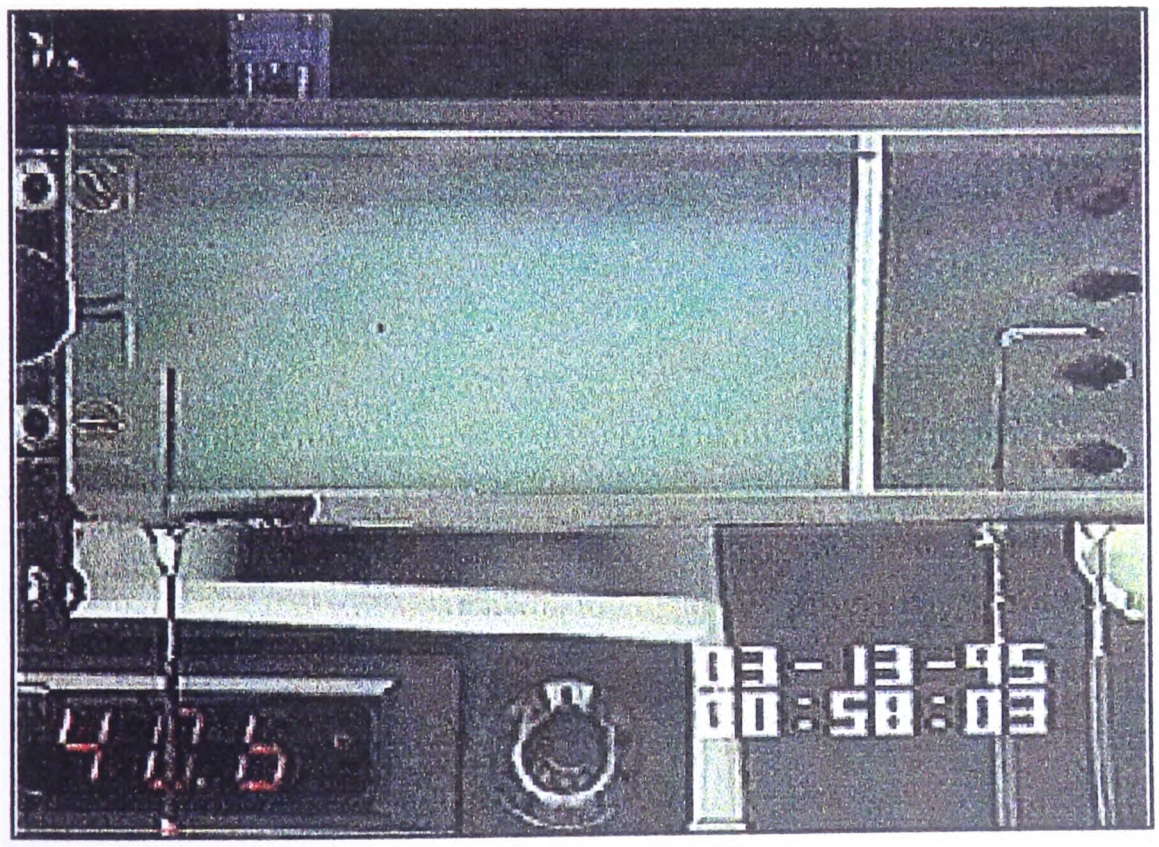
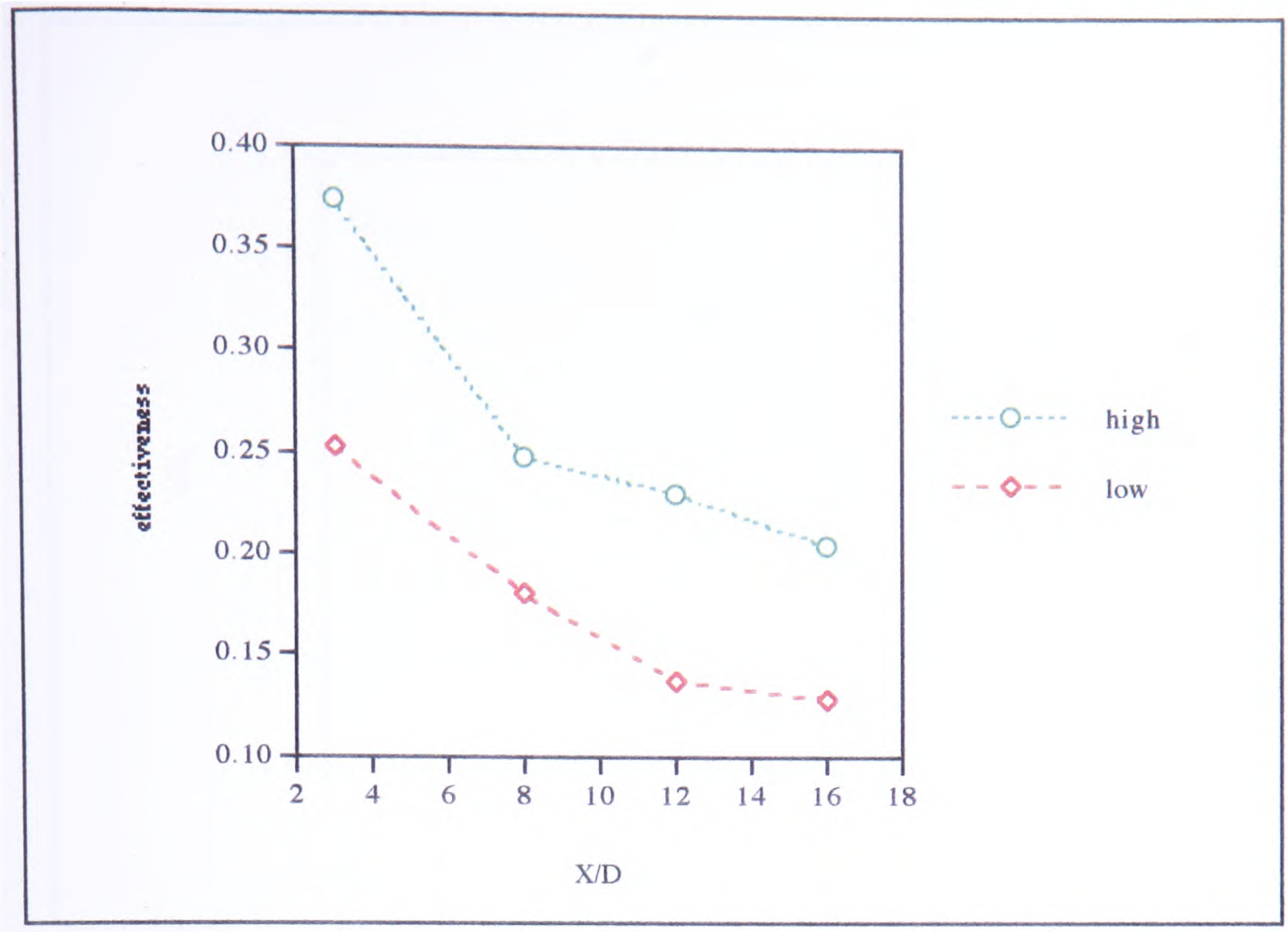


Figure 9.15 G=0.2 at t=58.03 sec.

The plots that follow depict the hole film cooling results at each injection rate. The data are not presented in the common form shown in Figures 9.31-9.35. Instead the magnitude of the peaks and troughs that are found in Figures 9.31-9.35 are plotted

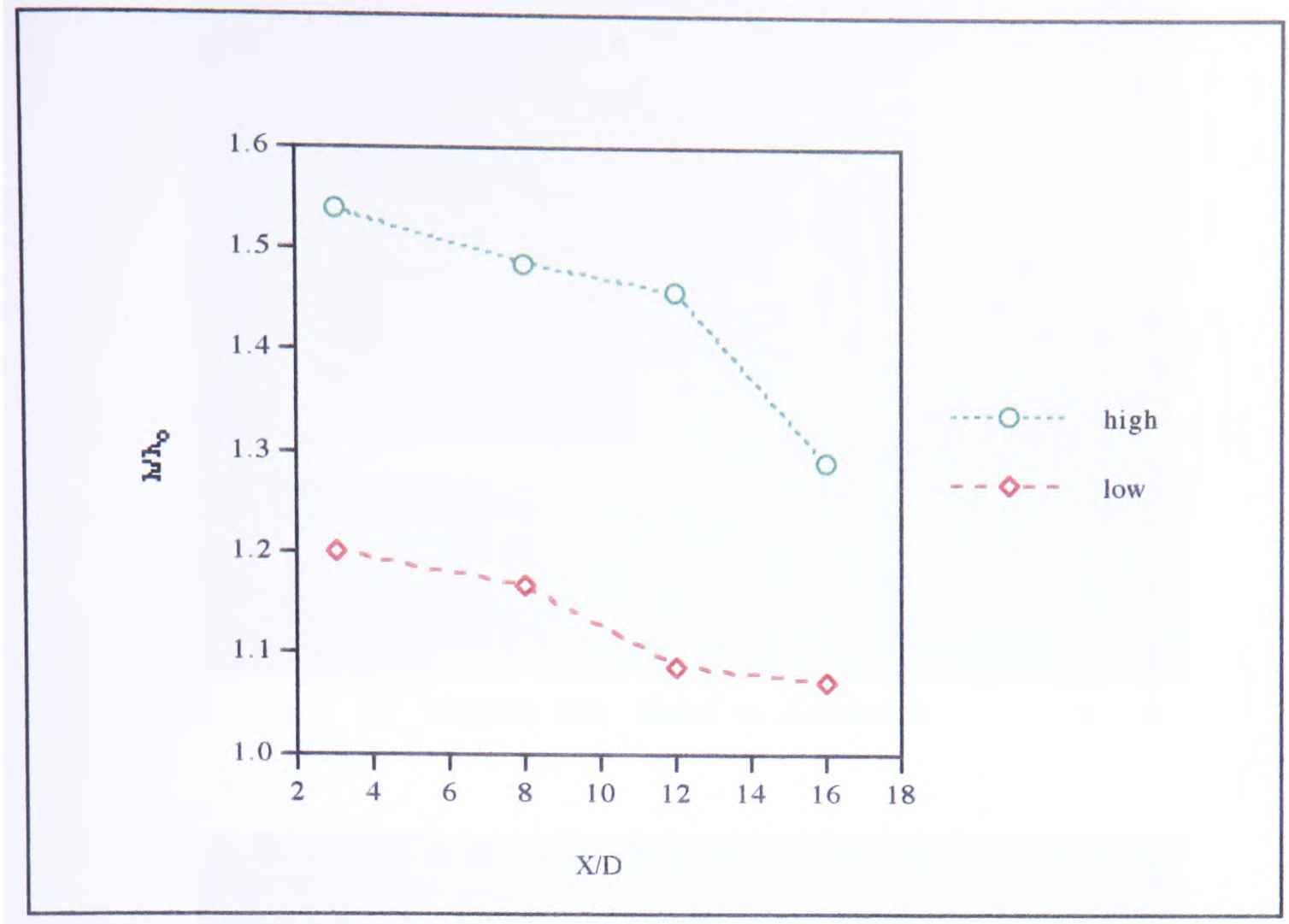
as a function of their downstream position from the row of cooling holes. The peaks are the "high" values and the troughs are the "low" values. These values can be related to a particular spanwise position. The high values are located in a line leading from the center of the film cooling hole where the effectiveness is at a maximum. The low values are located in a line leading from a point that is halfway between neighbouring film cooling holes where the effectiveness is at a minimum. This plotting format was chosen for the ease of comparison with other results. Both Teekaram's experimental results (Fig.9.36) and the slot cooling results are presented in this fashion. It is also easier to compare the hole cooling results between different injection rates.

Graph 9.2 shows the film cooling effectiveness data at the lowest injection rate tested. Both the high and low data points begin at a maximum value and decrease with a similar slope with increasing downstream distance. It would be logical to assume that there would not be any evidence of separation at such a low injection rate. This is confirmed by noting that the point where the effectiveness is highest is the point that is closest to the row of cooling holes. If Figure 9.36 is consulted, then it is also confirmed that the magnitude of the effectiveness is similar to that which is reported by Teekaram **(ref.89)**.



Graph 9.2 η vs. X/D (G=0.2)

Graph 9.3 shows the heat transfer data at the lowest injection rate that was tested. It can be seen that the heat transfer enhancement ratio decreases with increasing downstream distance. This is what is expected with the decreasing effectiveness that is seen in the previous plot. In each subsequent heat transfer enhancement plot, the base level heat transfer or h_o was defined as the theoretical turbulent heat transfer value in the absence of film cooling. The values of the heat transfer enhancement ratio are also similar to the values reported later in this section by Teekaram (**ref.89**) and, Vedula and Metzger (**ref.92**).



Graph 9.3 h/h_o vs. X/D (G=0.2)

Figures 9.16-9.20 show video frame captures from the VHS video tape of the film cooling run at the injection rate of 0.4. These figures are noticeably different from those at the previous injection rate of 0.2. There is a strong and noticeable cooling effect that is characterized by the presence of cooling stripes. These cooling stripes not only persist for the entire sixty second run time, but during this time, they continue to be visible over the entire length of the test section. The region that is directly downstream of the cooling holes resisted any colour change, or temperature change within the colour play range, until approximately ten seconds into the run. This can be confirmed by looking at Figure 9.18. Even at the end of the run (Figure 9.20), it can be seen that the coolant does its job by preventing the temperature of the surface directly in its path from rising as much as the surrounding surface areas. The diminishing potency of the injected flow in a downstream direction from the holes can be clearly seen in each of the video frame captures as well.

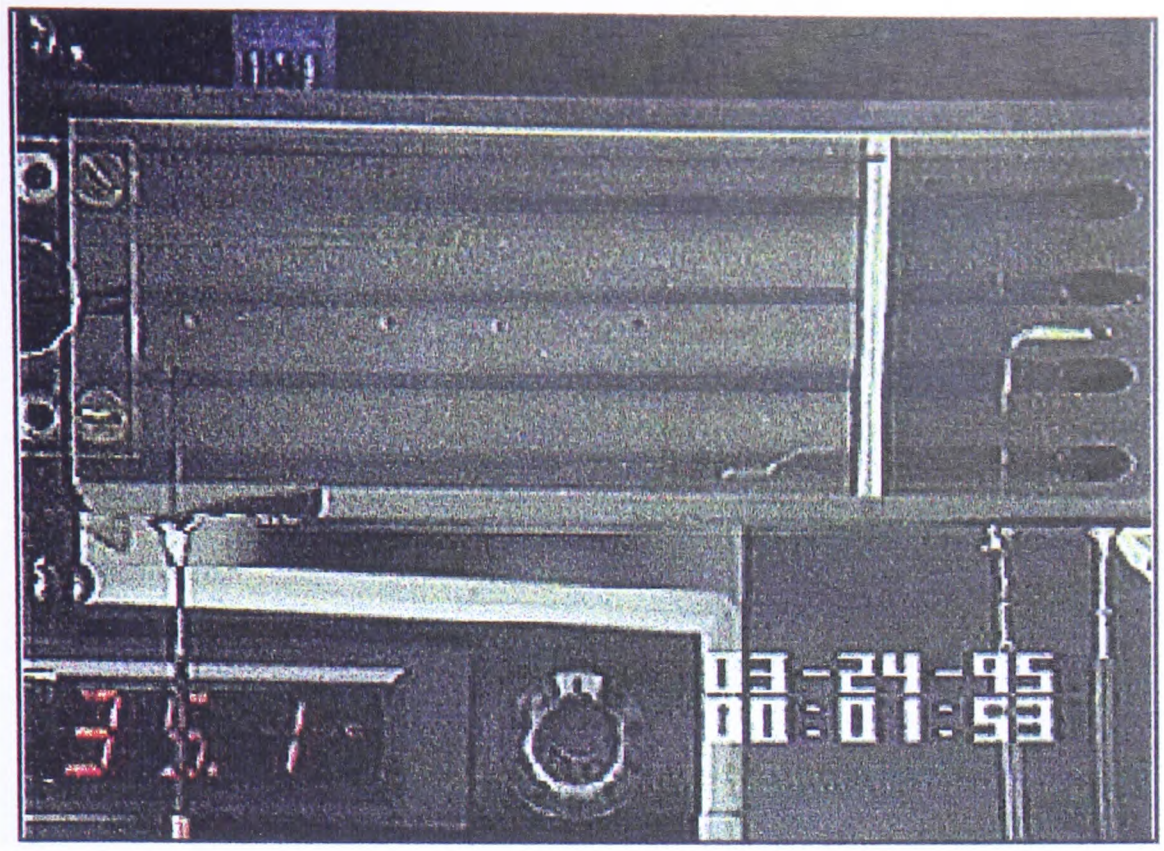


Figure 9.16 G=0.4 at t=1.53 sec.

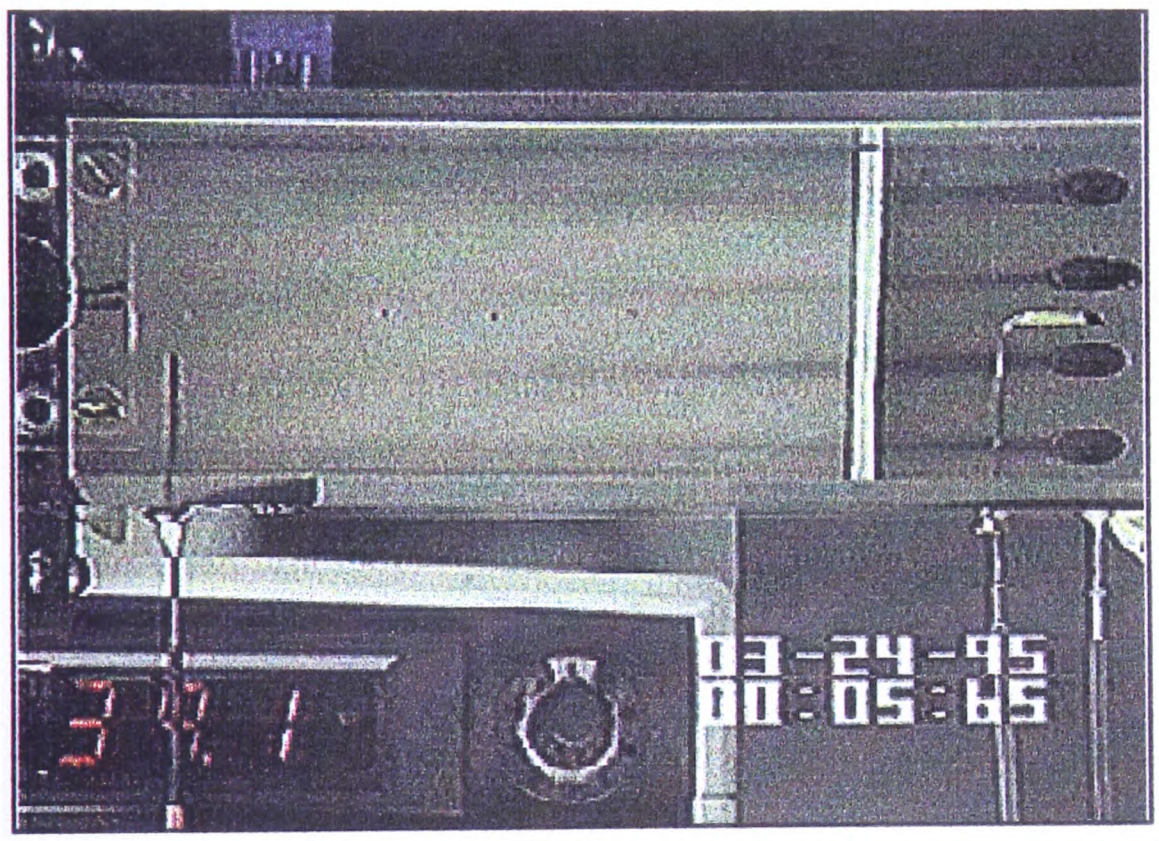


Figure 9.17 G=0.4 at t=5.65 sec.

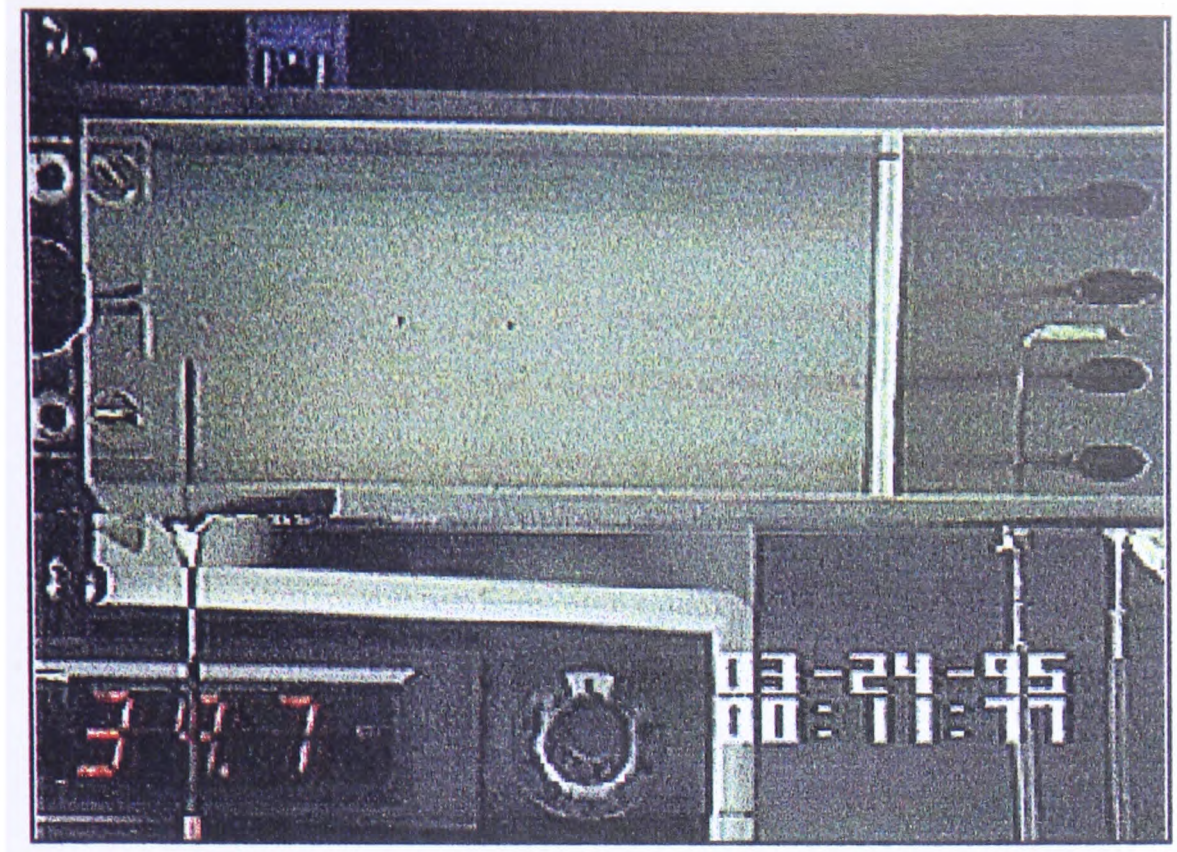


Figure 9.18 G=0.4 at t=11.77 sec.

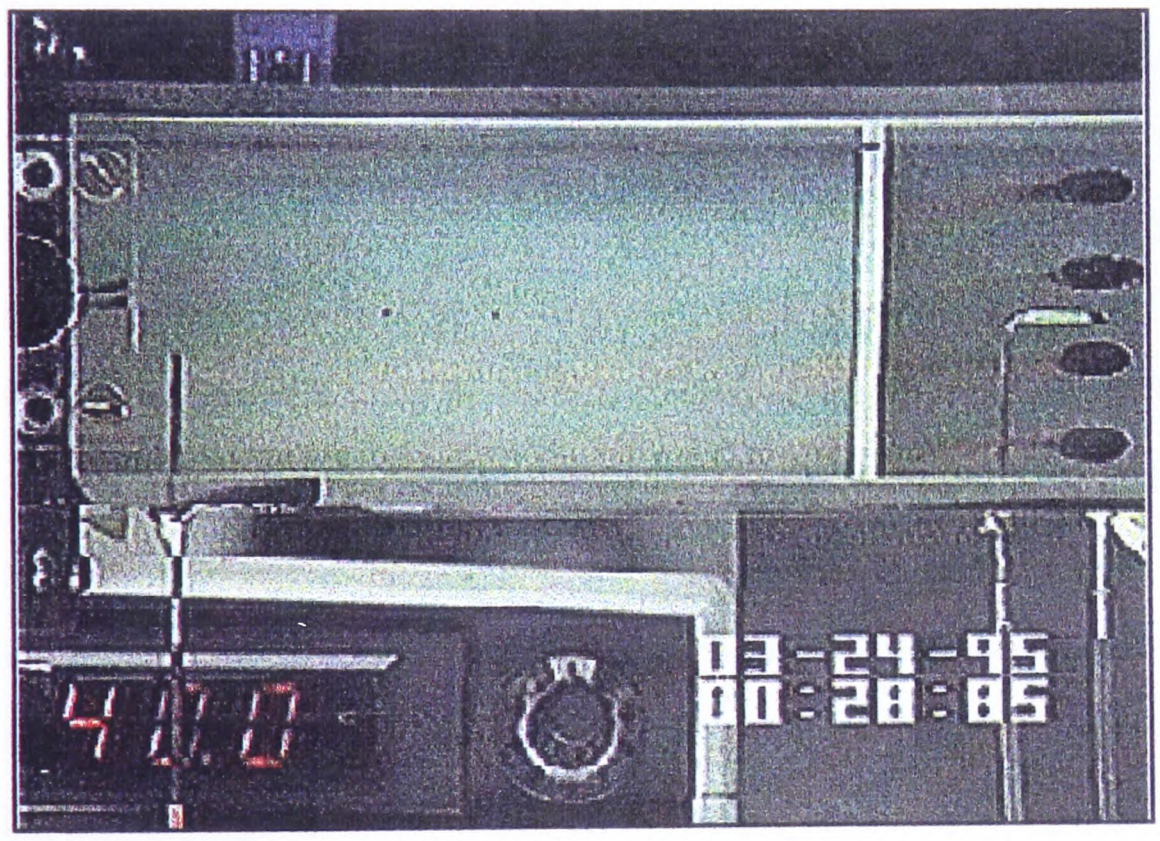


Figure 9.19 G=0.4 at t=28.85 sec.

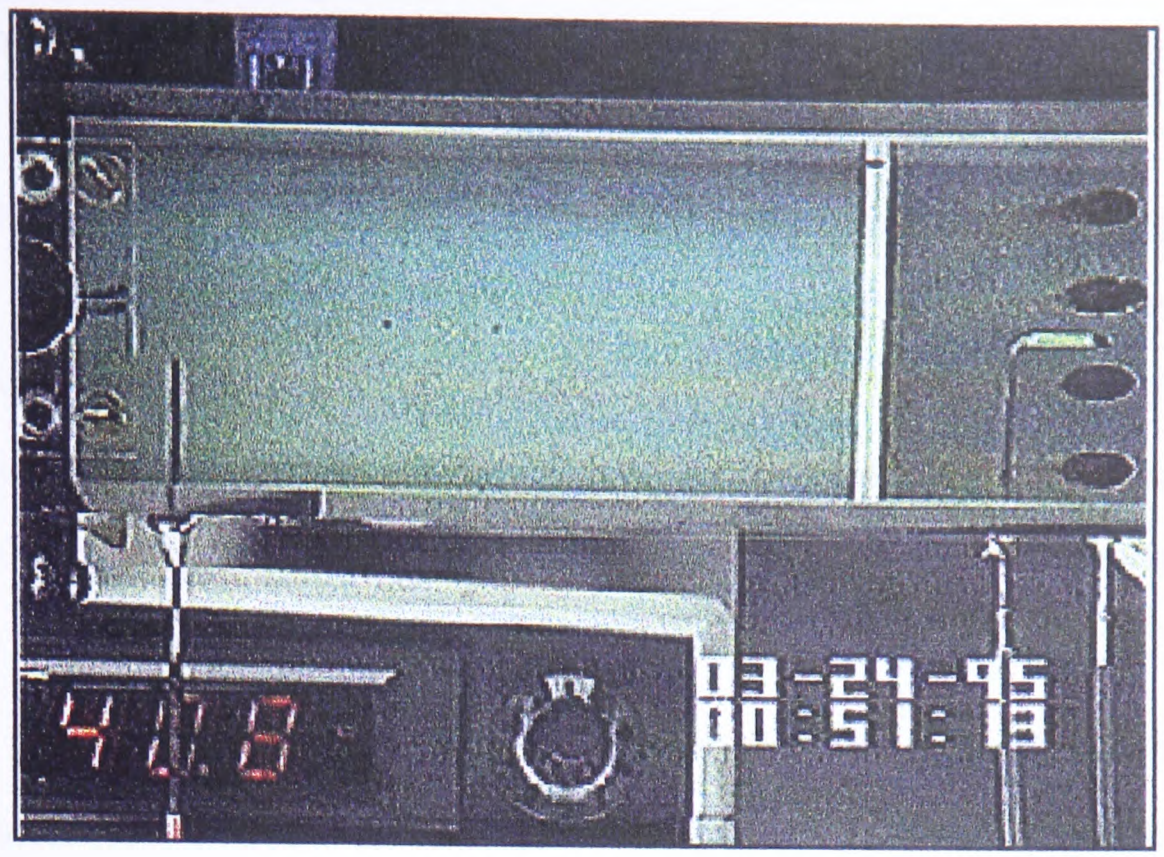


Figure 9.20 G=0.4 at t=51.13 sec.

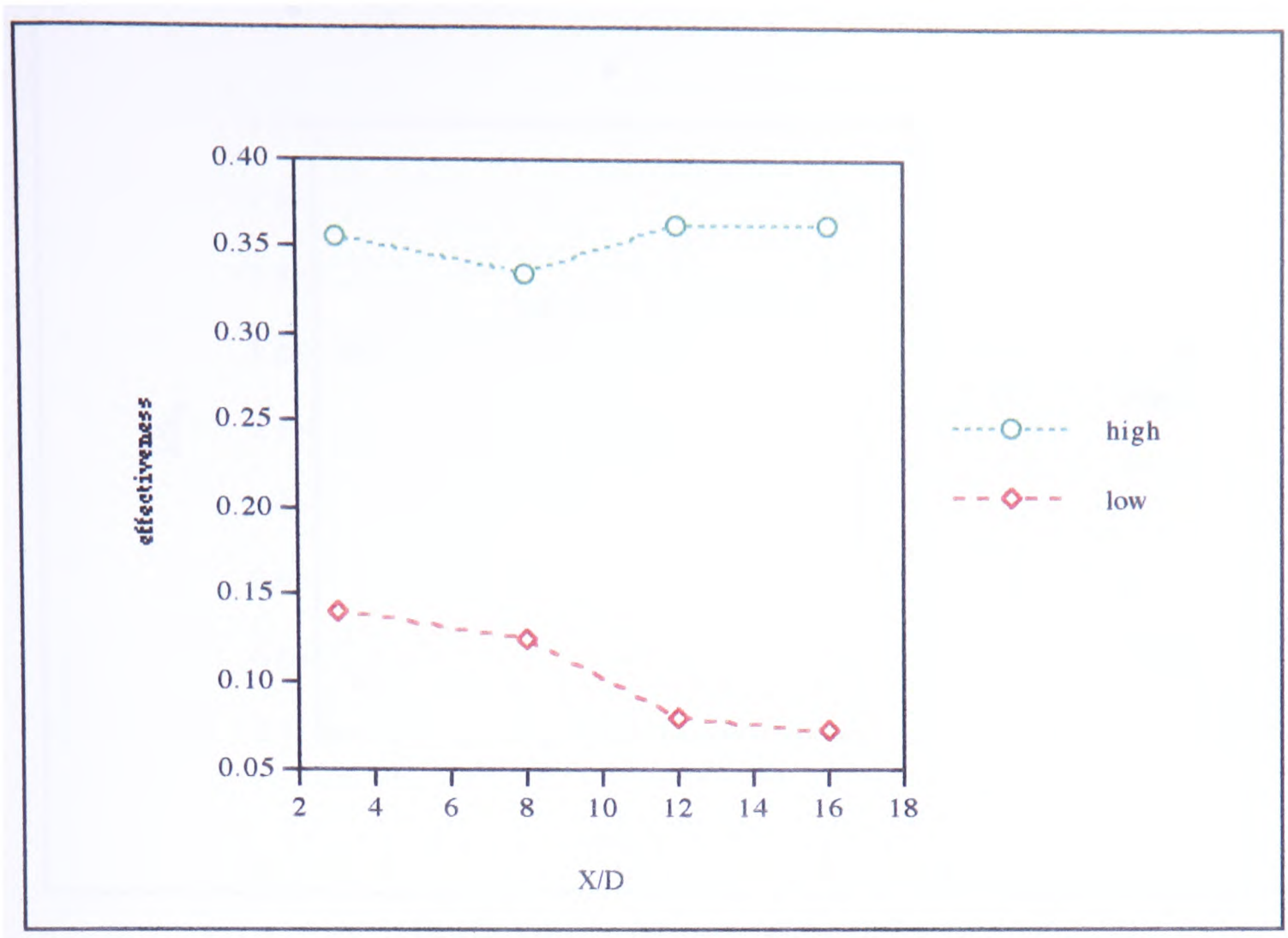
Graph 9.4 shows the film cooling effectiveness for the injection rate of 0.4. From the earlier discussion of hole cooling experiments in the literature, it can be recalled that for a flat plate with zero pressure gradient and an injection angle close to 30°, evidence of separation is clear at an injection rate of approximately 0.5. In this case, it is easy to see the first signs of the onset of coolant flow separation. The low values still show a maximum at the point nearest to the row of holes, but the effectiveness does not decrease with increasing downstream distance at the same rate as was seen in the previous injection rate. The high values also appear to maintain a constant value. This is the trend that would be expected as the point of separation is approached where the highest value of the effectiveness would no longer be located closest to the row of cooling holes.

If Figure 9.36 is consulted then it can be seen that these results are not identical to the results that Teekaram reported (**ref.89**). His results show that at an injection rate of 0.35, the effectiveness is still at a maximum at the first data point and decreases with increasing downstream distance. It is only at an injection rate of 0.59, that the effectiveness curve appears to begin leveling off. This noticeable difference can be attributed in part, to a discrepancy in the temperature or density ratios in each set of

experimental results, where these ratios are defined as the coolant temperature or density divided by the freestream temperature or density. Teekaram reported a temperature ratio of 0.82 in each of his experimental tests, which corresponds to a density ratio of approximately 1.22. Conversely, the experiments conducted in this study were conducted with a temperature ratio of 0.92, or a density ratio of 1.08. The consequence of this difference is that the point at which the effectiveness data begin to flatten out or show signs of early separation, occurs at a lower injection rate than that seen in Teekaram's data.

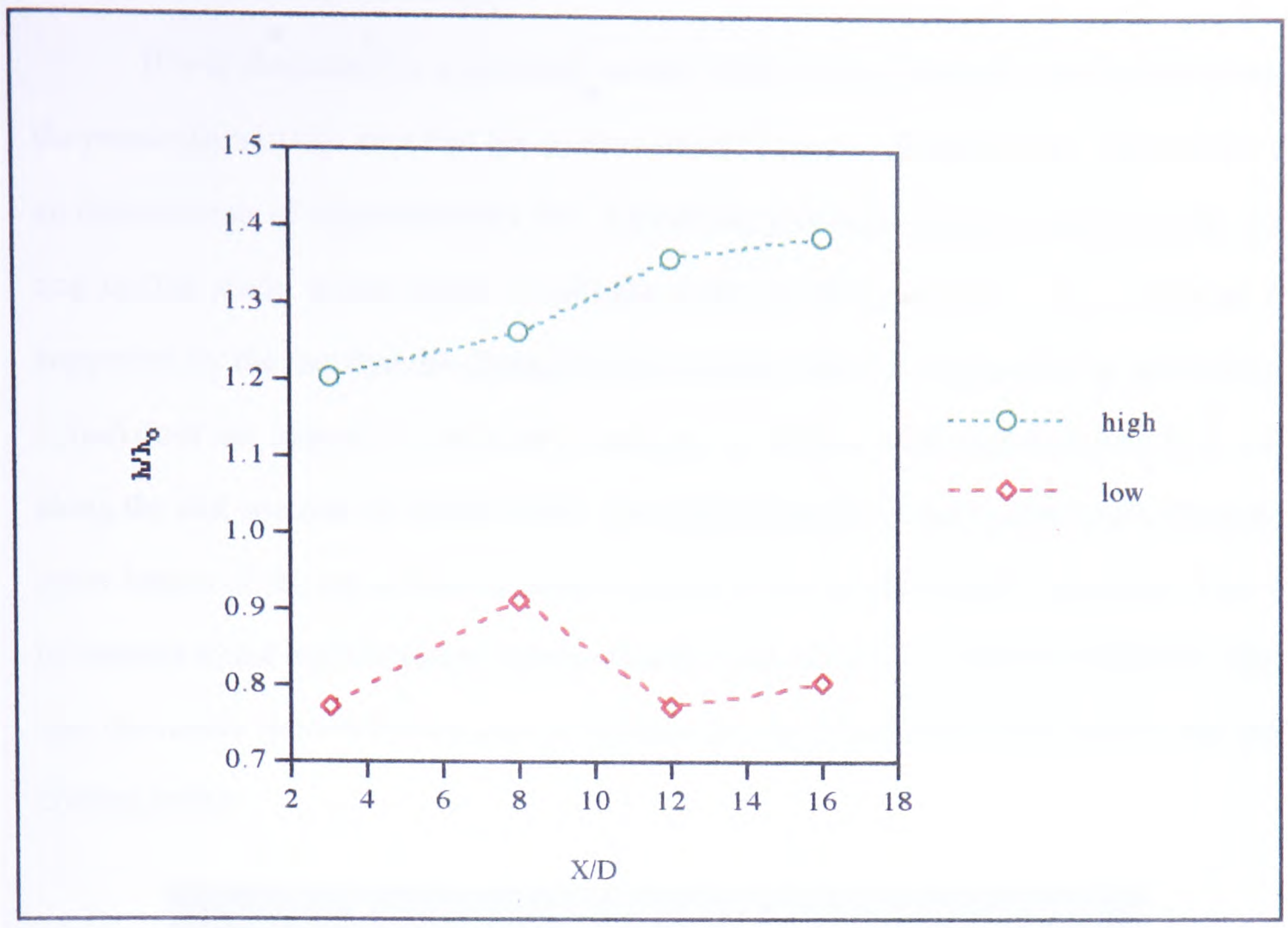
More specifically, the flow field in this case is, to the first order, defined by the momentum flux ratio. This ratio is defined in Eqn.9.6. It can be said that separation of the coolant flow from the surface of the wall or test section occurs at a particular value of the momentum flux ratio. Therefore, for two tests that are conducted at two different density ratios, it would be logical to expect the earliest signs of separation occurring at two different injection rates.

$$\text{momentum flux ratio} = \frac{\rho_i u_i^2}{\rho_\infty u_\infty^2} = \frac{G^2}{\rho_i / \rho_\infty} \qquad \textbf{(9.6)}$$



Graph 9.4 η vs. X/D (G=0.4)

Graph 9.5 shows the heat transfer enhancement ratio for the injection rate of 0.4. The low value data points appear to be decreasing slightly as the effectiveness decreases. This decrease is small however, which is logical and predictable. The high value data points are seen to increase slightly which is consistent with the trend that is evident as the injection rate increases. Once again, the magnitude of the data points are comparable to the data that are presented later in this section.



Graph 9.5 h/h_o vs. X/D (G=0.4)

Figures 9.21-9.23 show video frame captures from the VHS video tape of the film cooling run at the injection rate of 0.6. Even though the figures from this run look similar to the figures from the previous run, there are some major differences that are expected, and that can be confirmed, when the injection rate is increased even more. For instance, it is clear that the cooling effect is even stronger. Once again, the cooling stripes can be seen, the only difference is that they appear to be even more pronounced than before, particularly at the beginning of the run. The increased cooling effect can also be proven by looking at the end of the test section. Here, the stripes begin to diffuse or spread out, instead of merely diminishing or dying out. The coolant also shields the surface more effectively from the hot freestream at this higher injection rate. This point is clear if the video frame captures from this run and the previous run are compared at a run time of approximately six seconds. In the case of Figure 9.22, the cooling stripes are still visible and have successfully prevented any colour change, or temperature change, even at the end of the test section. This is not the same situation as seen in Figure 9.17 at the lower injection rate.

It was discussed in a previous section that it is a commonly held belief among the researchers in this area that the coolant should begin to separate from the surface at an injection rate of approximately 0.5. Therefore, this injection rate should be the first one in this study where there is definite evidence of separation. This statement is supported by the fact that the coolant stream (made visible at the surface by the coolant stripe) does not appear to diminish in strength or diffuse until approximately half way along the test section. In other words, the colour change in the coolant path along the entire length of the test section is more uniform than has previously been seen. This is in contrast to the injection rates where separation would not be expected and the coolant was obviously more effective only in the area directly downstream and close to the film cooling holes.

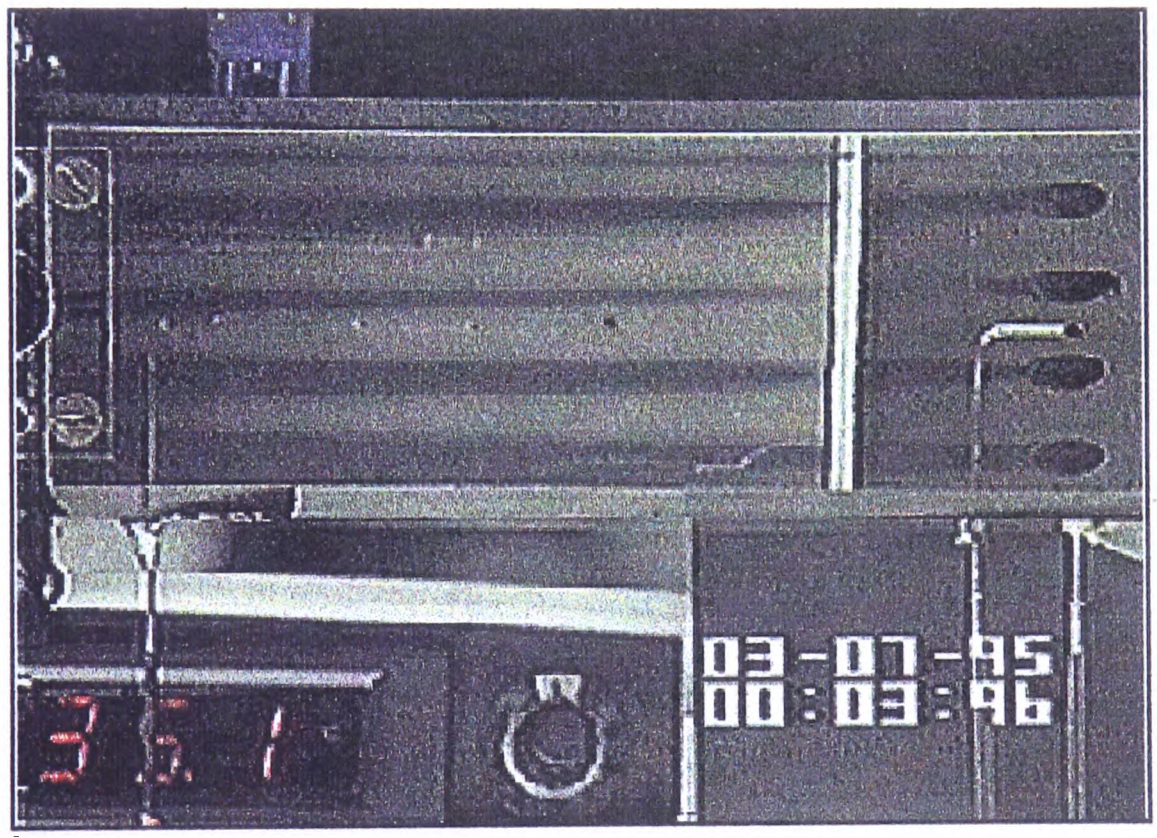


Figure 9.21 G=0.6 at t=3.96 sec.

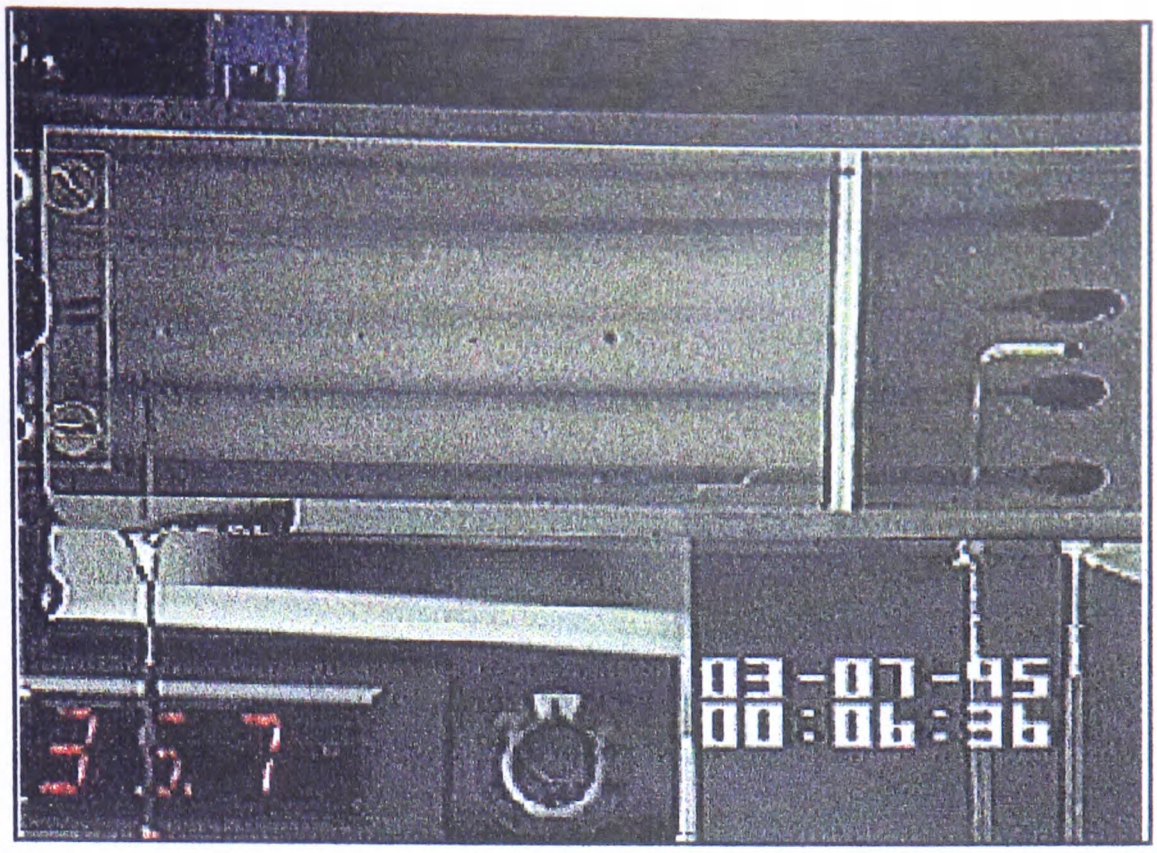


Figure 9.22 G=0.6 at t=6.36 sec.

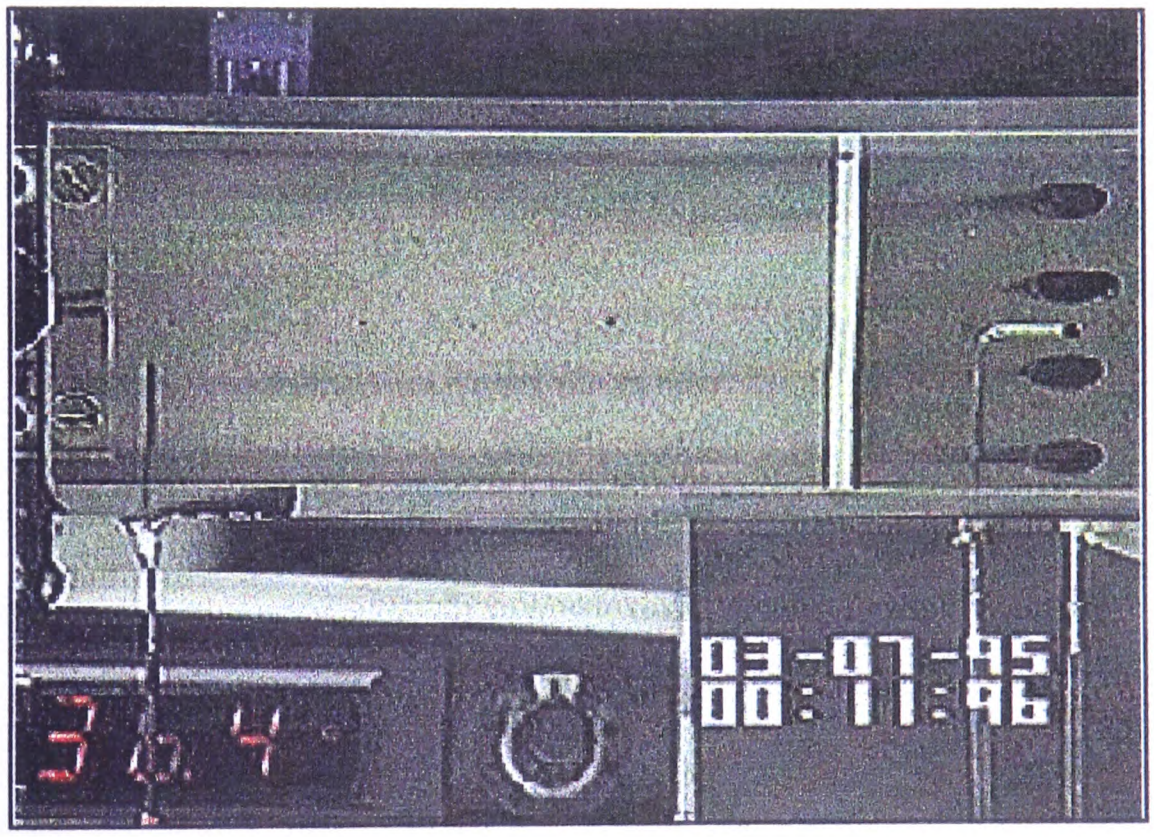
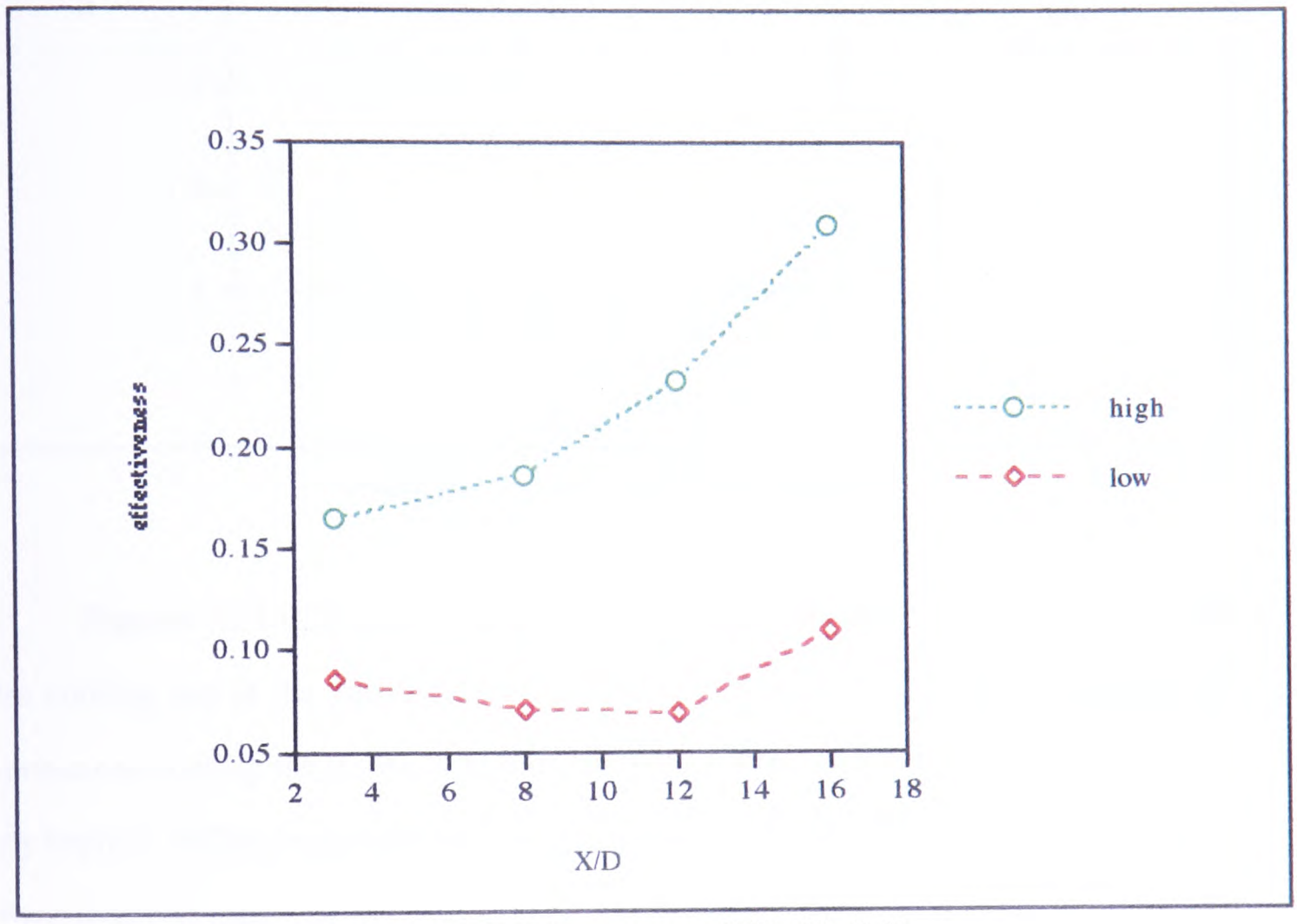


Figure 9.23 G=0.6 at t=11.96 sec.

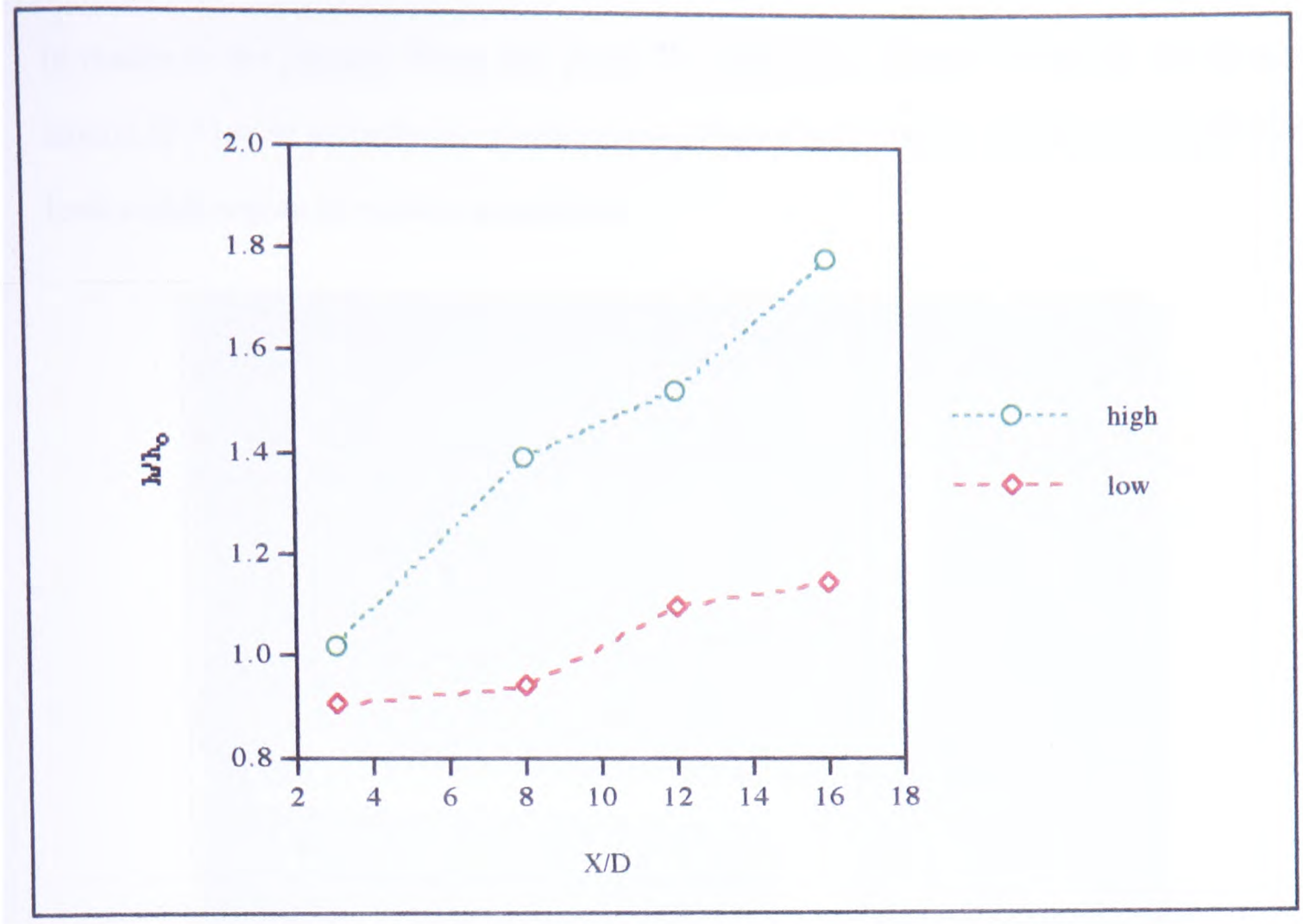
Graph 9.6 shows the film cooling effectiveness data at an injection rate of 0.6. At this injection rate, it is expected that there would be definite evidence of separation. This is easily confirmed by noting that the maximum value is not located directly downstream of the cooling holes. Furthermore, the maximum value would be expected to be located where the coolant jet reattaches to the surface. It can be seen that the low

values show a slight increase in effectiveness with increasing downstream distance, which is consistent with the trend from the previous plots. It can also be seen that the high values show a noticeable increase with increasing downstream distance, which is consistent with both the current trend and the expectation of separation. However, the actual magnitude of the values are more consistent with a slightly higher injection rate according to Teekaram and Figure 9.36.



Graph 9.6 η vs. X/D (G=0.6)

Graph 9.7 shows the corresponding heat transfer data for this injection rate. Based on the trends that are evident in the presentation of the data up to this point, a slight increasing trend would be expected in the low value data points and a noticeable increasing trend would be expected in the high value data points. Both of these trends are confirmed by consulting the following graph. However, the value of the heat transfer enhancement ratio tends to be slightly higher than that reported in the literature far downstream of the cooling holes.



Graph 9.7 h/h_o vs. X/D (G=0.6)

Figures 9.24-9.26 show video frame captures from the VHS video tape of the film cooling run at the injection rate of 0.8. Once again, there is the presence of pronounced cooling stripes that continue to the end of the test section just before which they begin to diffuse or spread out. This injection rate could be characterized as quite a strong injection rate, and as such there is evidence of separation beginning at the hole exit in the case of the two middle holes. The topic of unequal exit velocity in each of the four holes was previously discussed. Numerical evidence supports this prediction and it is no surprise that a greater hole exit velocity is apparent in the two middle holes. It can be seen that there is a hot area bounded by two cool areas. This is indicated by the two black stripes emanating from the holes where no colour play has begun, and a region in between that has begun to show some colour change. It is my contention that a similar situation is occurring to that depicted in Figure 5.2. The bulk of the coolant is separated from the surface and the two outside cool stripes are formed by the contra-rotating kidney vortices where they touch the surface. The reattachment point of the coolant stream can be clearly seen as being just beyond the vertical strip of tape that

is visible in the picture. From this point, its behavior is similar to that of an injected stream of a lower velocity (or injection rate). Figure 9.27 shows a closer, more detailed look at this region of coolant separation.

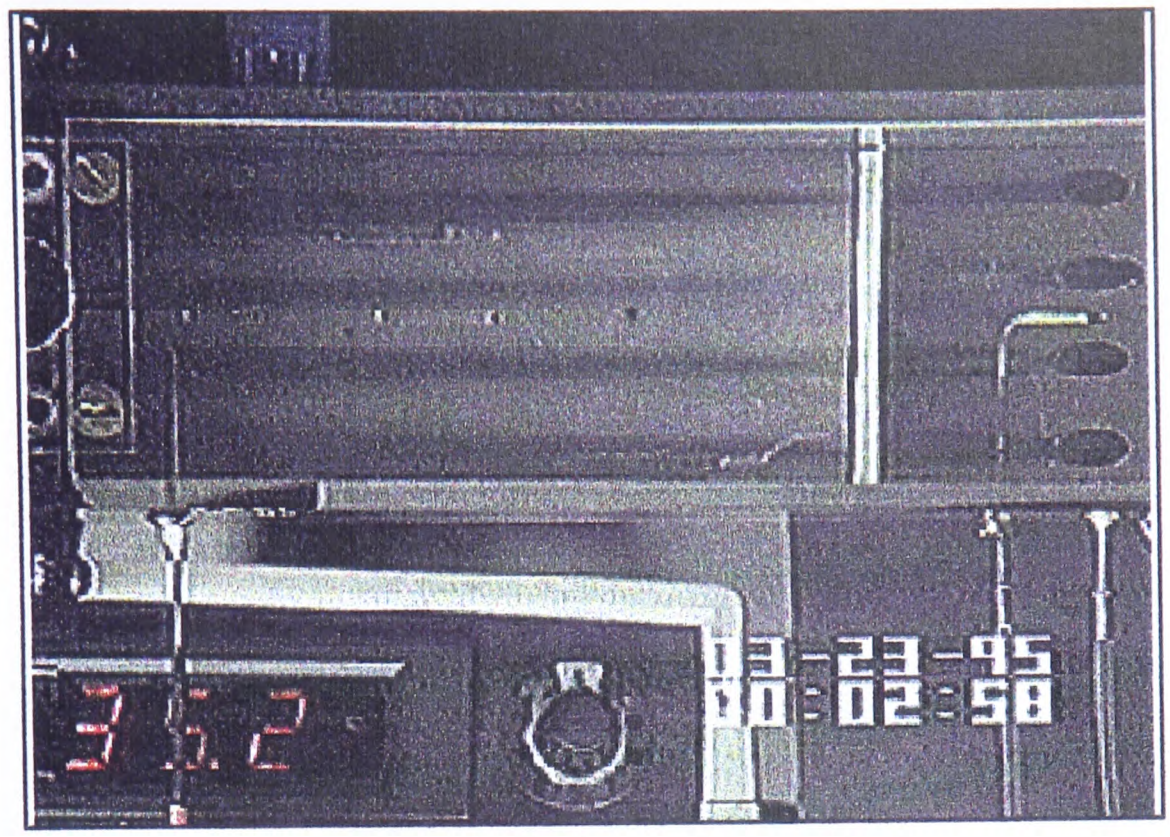


Figure 9.24 G=0.8 at t=2.58 sec.

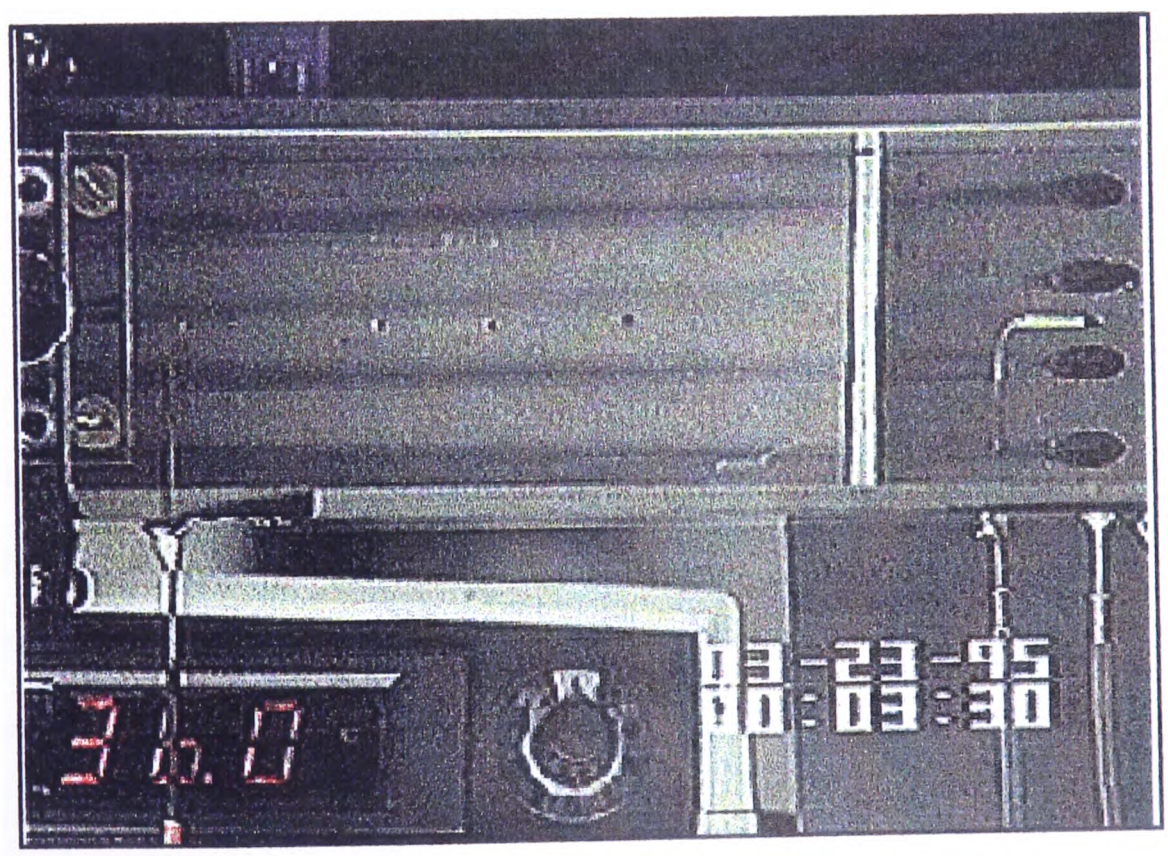


Figure 9.25 G=0.8 at t=3.30 sec.

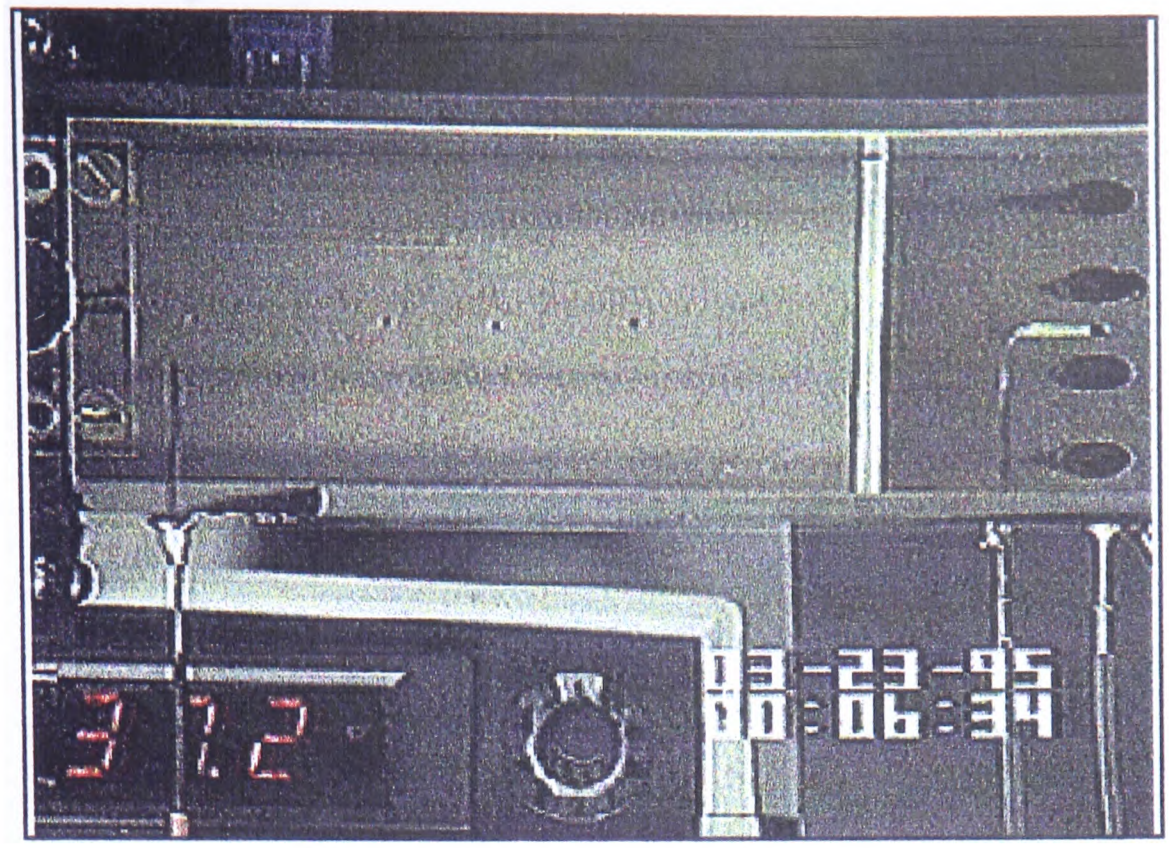


Figure 9.26 G=0.8 at t=6.34 sec.

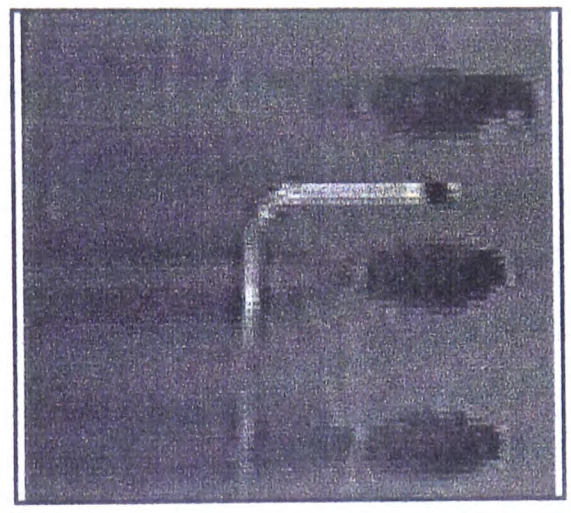
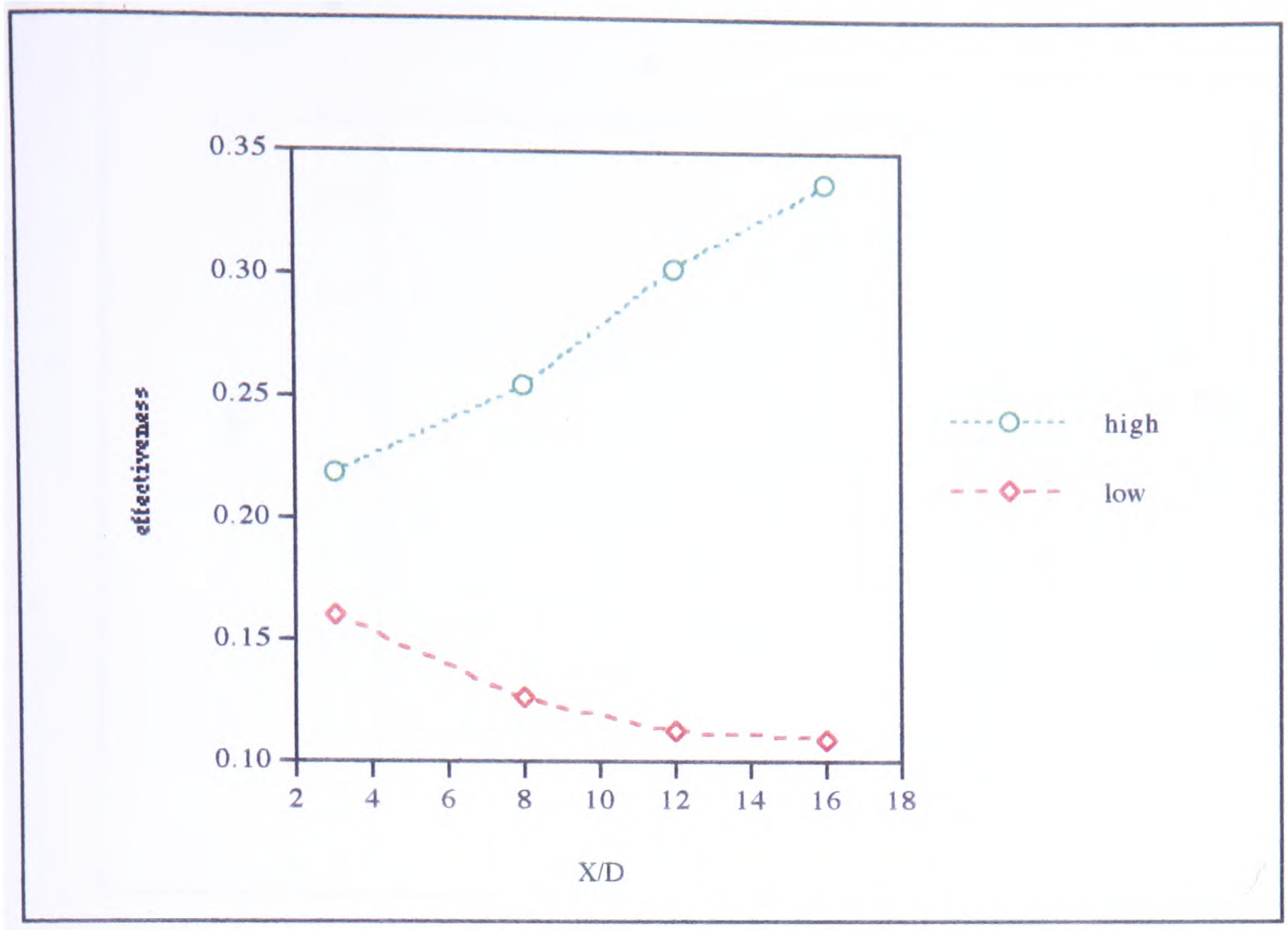


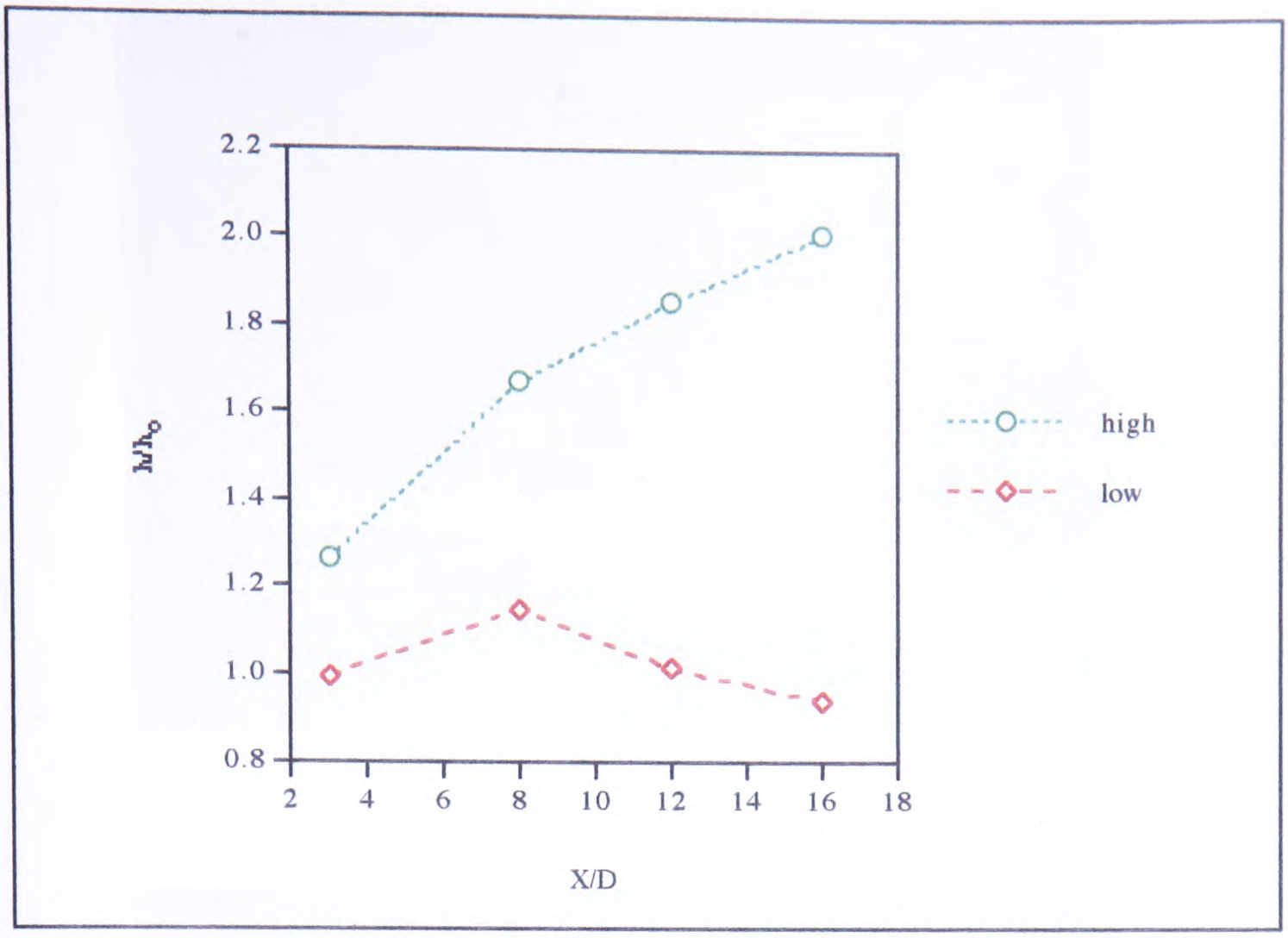
Figure 9.27 Coolant Separation

Graph 9.8 shows the film cooling effectiveness data at the high injection rate of 0.8. It can be seen that this plot looks very similar to the previous film cooling effectiveness plot at the injection rate of 0.6. It can be seen that the magnitude of the effectiveness is slightly higher at all points downstream of the cooling holes. This would be expected with a higher injection rate. It can also be seen that these values are in close agreement with the experimental values in Figure 9.36. However, it is interesting to note that the low value data points decrease with increasing downstream distance. This particular trend is consistent with a reattachment of the contra-rotating kidney vortices where they touch the surface.



Graph 9.8 η vs. X/D (G=0.8)

Graph 9.9 shows the heat transfer data at the injection rate of 0.8. Based on the effectiveness data, the noticeable increase of the high values data points and the slight decrease of the low value data points is understandable. Due to the increased magnitude of the film cooling effectiveness at this higher injection rate, the high value data points that are far downstream of the coolant injection are higher than those for the injection rate of 0.6. These points are once again higher than those normally reported in the literature.



Graph 9.9 h/h_o vs. X/D (G=0.8)

Figures 9.28-9.30 show video frame captures of the film cooling run at the injection rate of 1.0. Once again, the separation phenomenon at the exit of the cooling holes that was described for the previous injection rate can be seen. In fact, the bottom hole now shows signs of this separation. It is consistent with a higher injection rate that this effect would still be evident and that it would encompass more cooling holes in light of the unequal hole exit velocities.

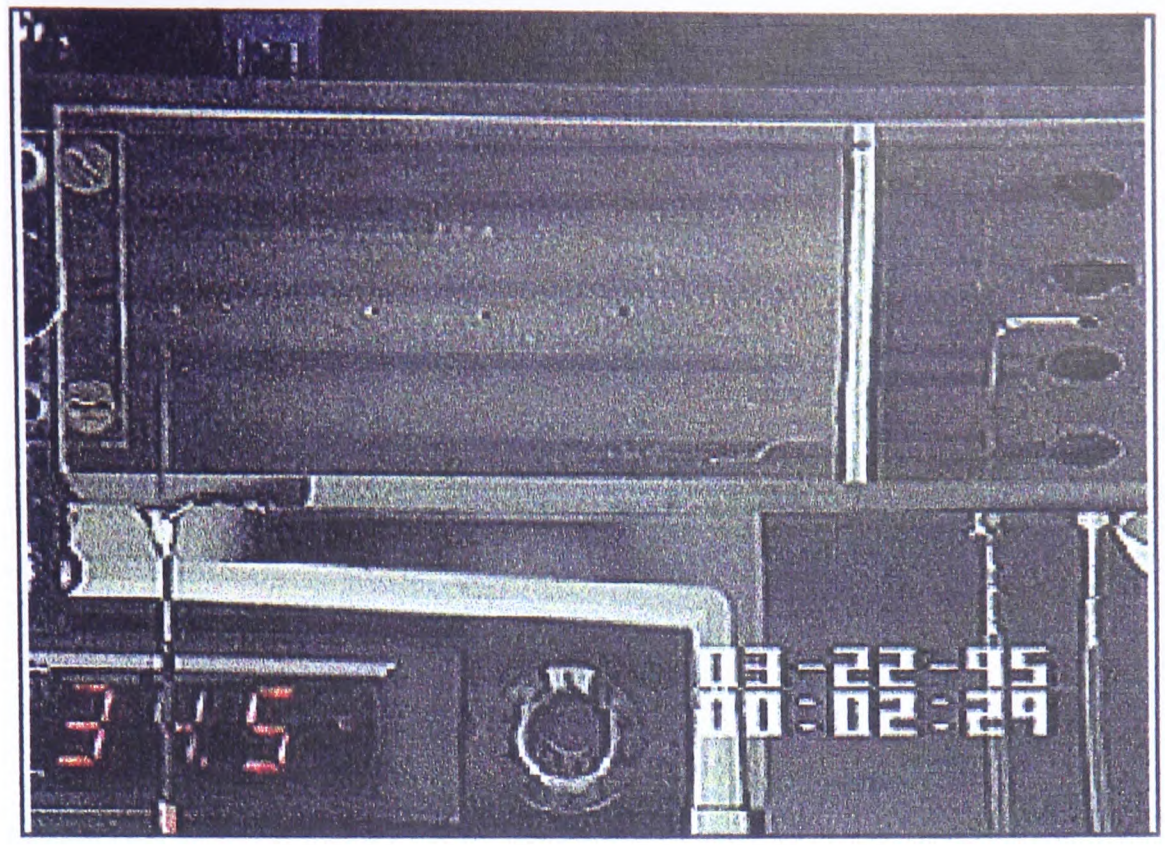


Figure 9.28 G=1.0 at t=2.29 sec.

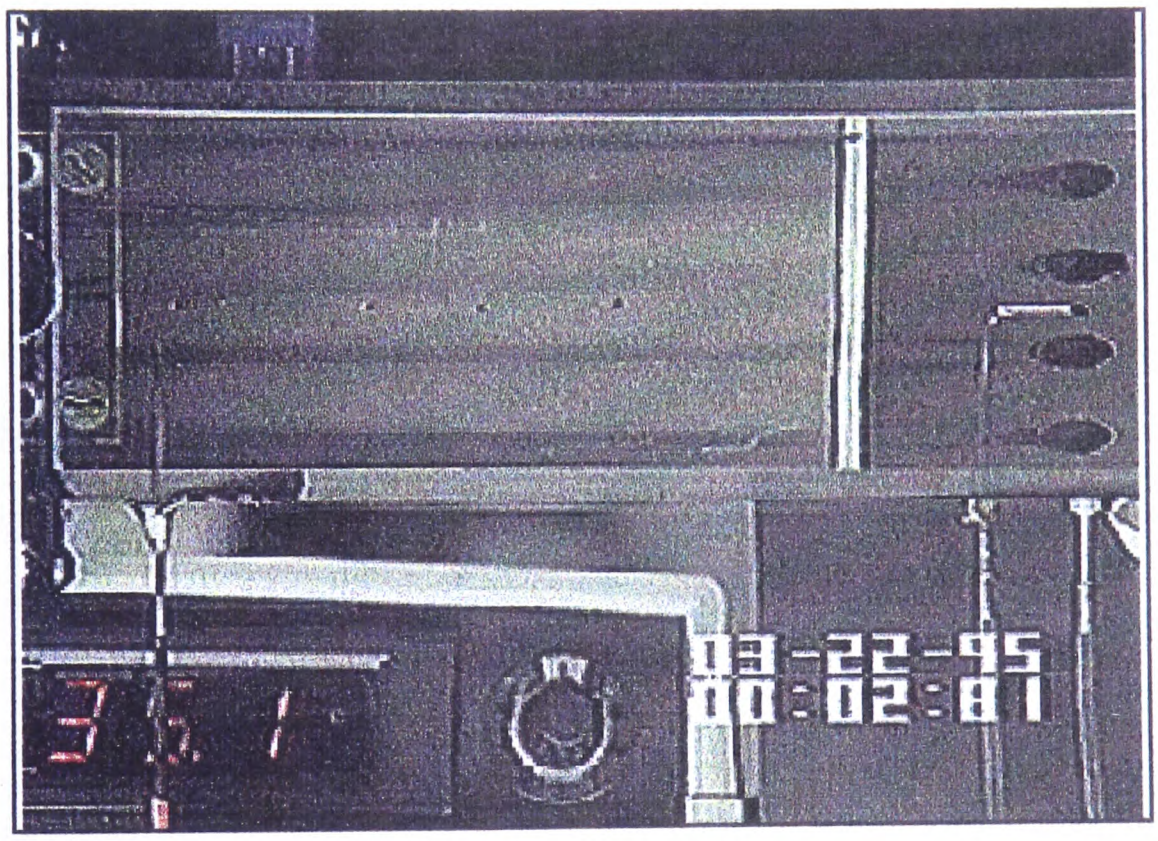


Figure 9.29 G=1.0 at t=2.81 sec.

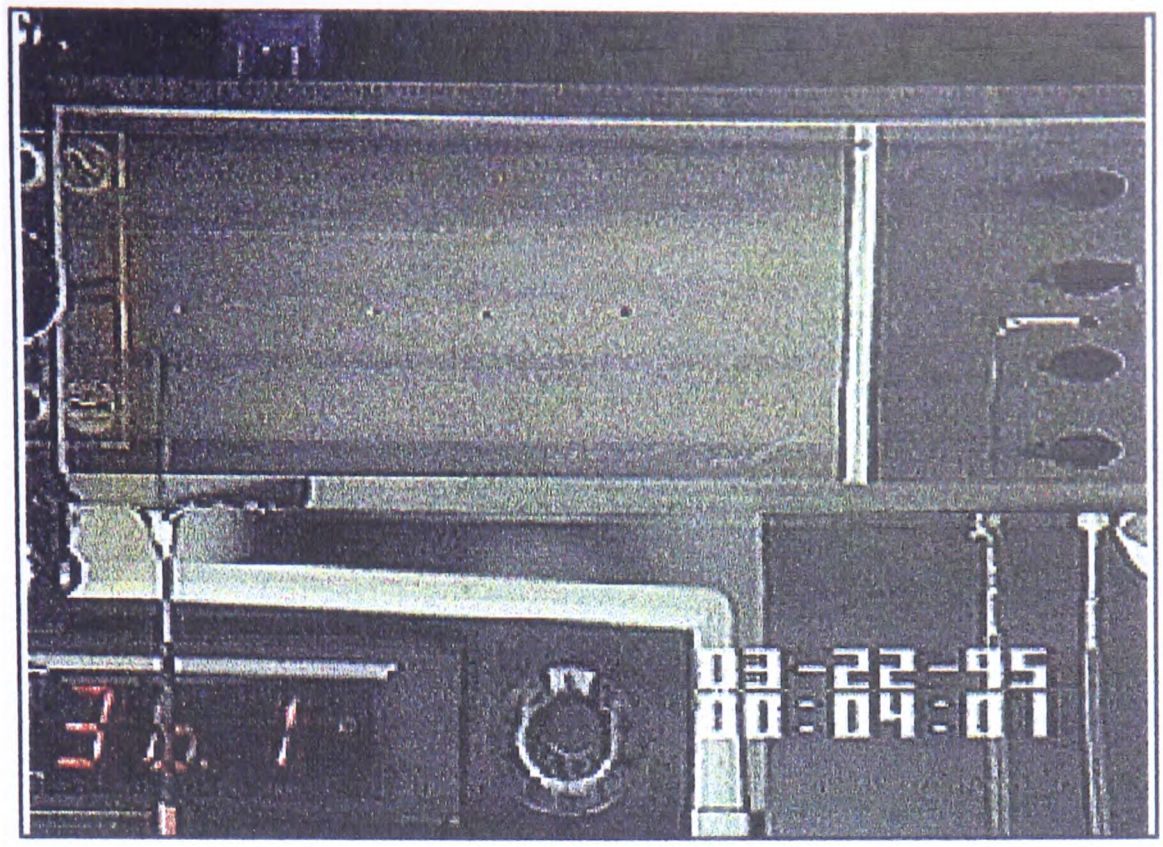
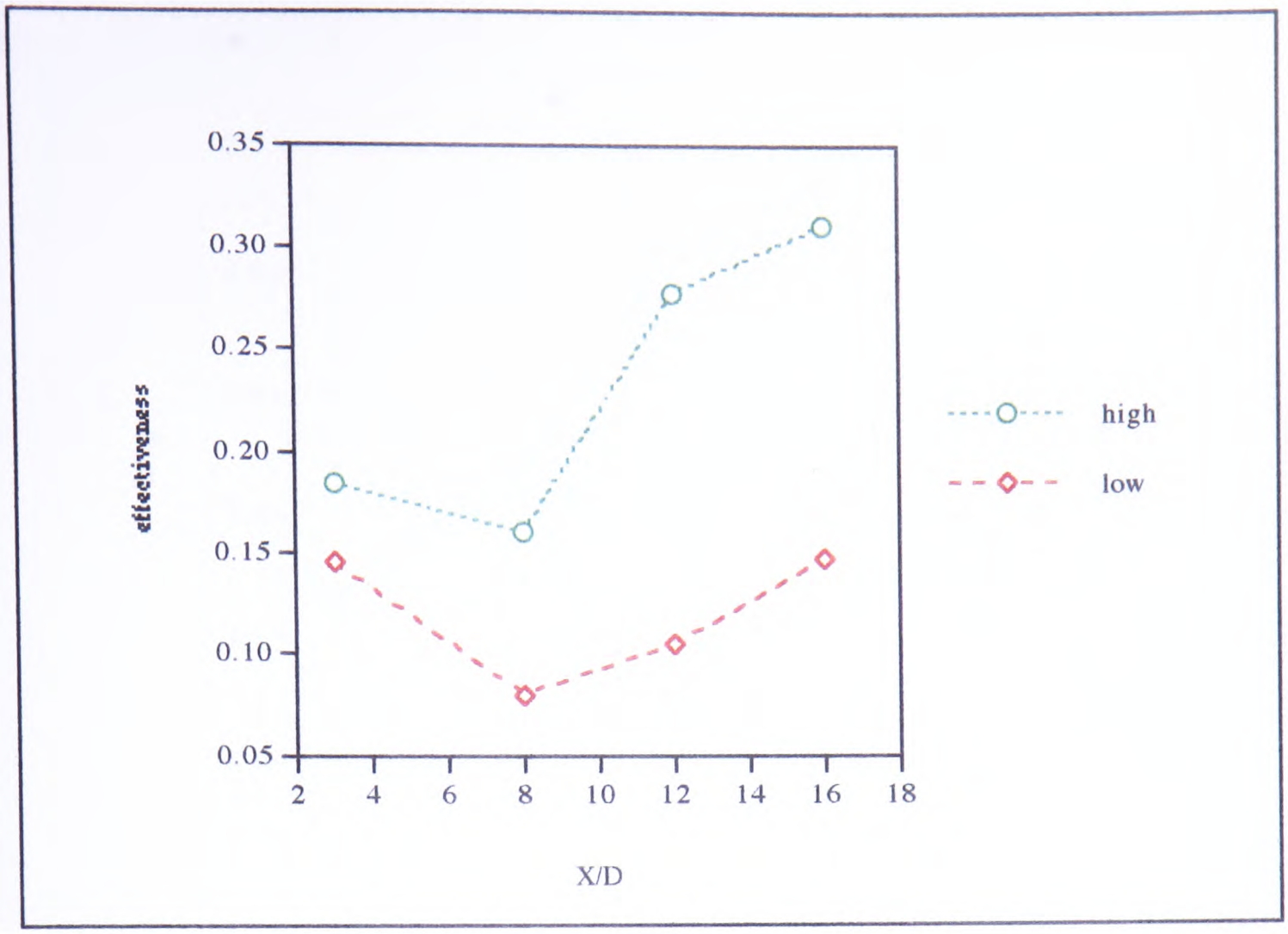


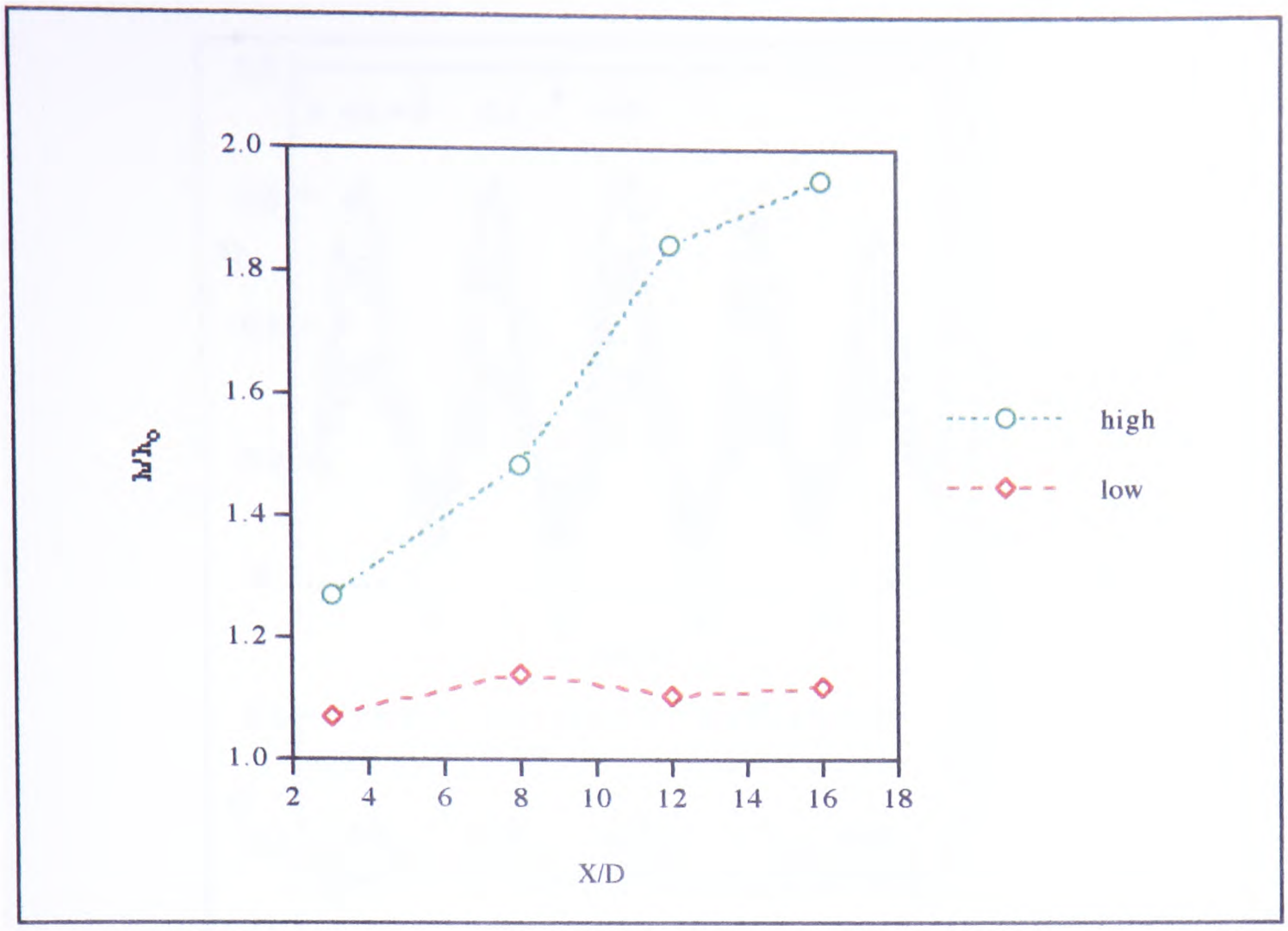
Figure 9.30 G=1.0 at t=4.01 sec.

Graph 9.10 shows the film cooling effectiveness data at the highest injection rate that was tested. It can be seen that this plot looks similar to the previous film cooling effectiveness plots at the injection rates of 0.6 and 0.8. The magnitude of the effectiveness at all points downstream of the cooling holes is approximately the same as it was for the injection rate of 0.8. However, the lowest value can be found at the second data point instead of the first data point which could be an indication of even stronger separation. Once again, these values are in close agreement with the experimental values in Figure 9.36.



Graph 9.10 η vs. X/D (G=1.0)

Graph 9.11 shows the heat transfer data at the highest tested injection rate. Based on the film cooling effectiveness data, the noticeable increase of the high values data points and the near constant level of the low value data points is understandable. Like the effectiveness results, the heat transfer results are very similar to the results that were presented for the injection rate of 0.8. Therefore, it is predictable that the values are again higher than what is normally reported in the literature, especially far downstream of injection.



Graph 9.11 h/h_o vs. X/D (G=1.0)

9.3.3.1 Comparison of Results

Other researchers have conducted similar experiments to those discussed above. One such source of data that can be used as a basis for comparison is a paper by Vedula and Metzger (**ref.92**). In this paper they also compare their work to the work of other researchers. Figures 9.31 and 9.32 show the film cooling effectiveness and heat transfer results of Vedula and Metzger. These results were obtained using an injection rate of 0.6. Therefore, they can easily be compared to the results presented previously at this injection rate which are shown in Graphs 9.6 and 9.7.

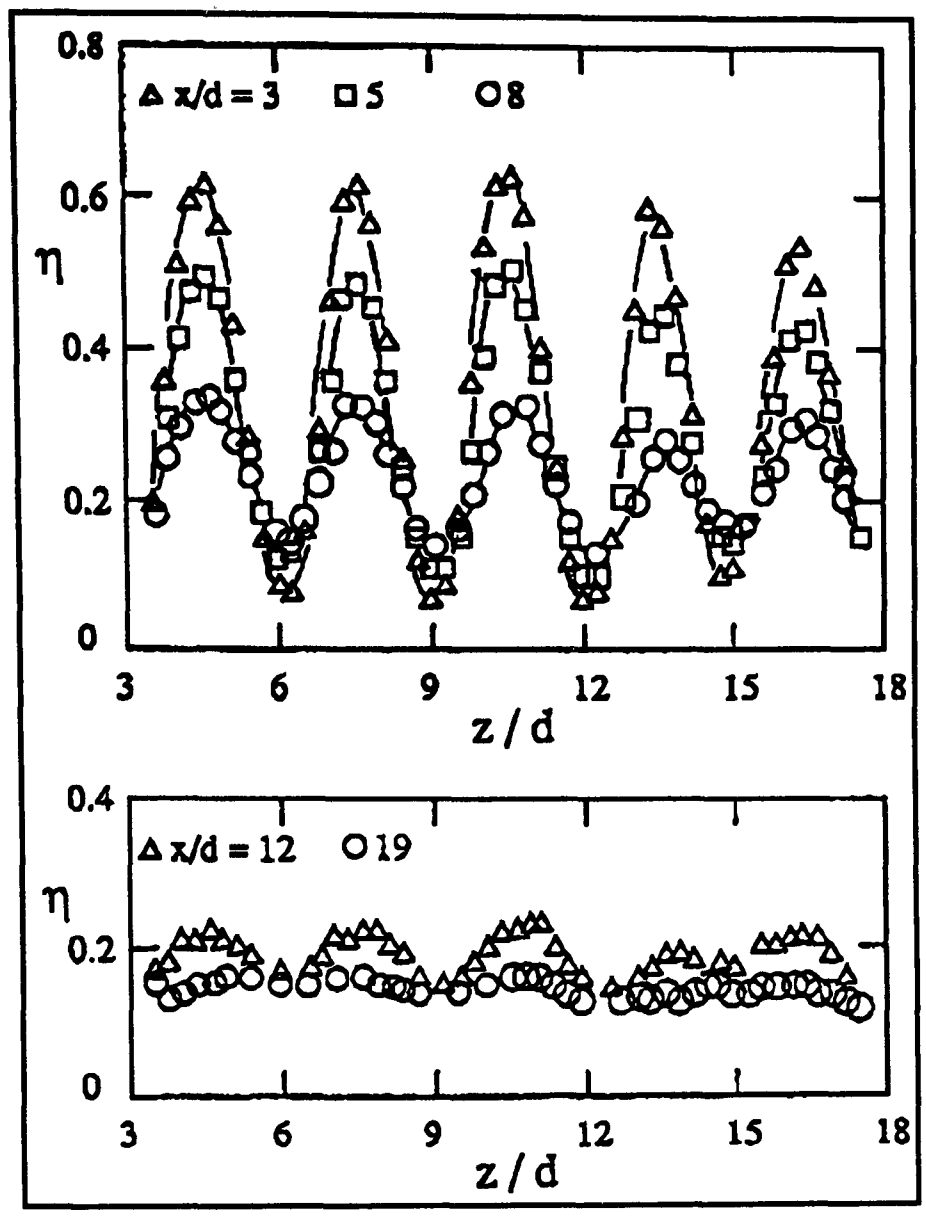


Figure 9.31 η vs. Z/D
(reference: "A Method for the Simultaneous Determination of Local Effectiveness and Heat Transfer Distributions in Three-Temperature Convection Situations" by R.J. Vedula and D.E. Metzger, 1991)

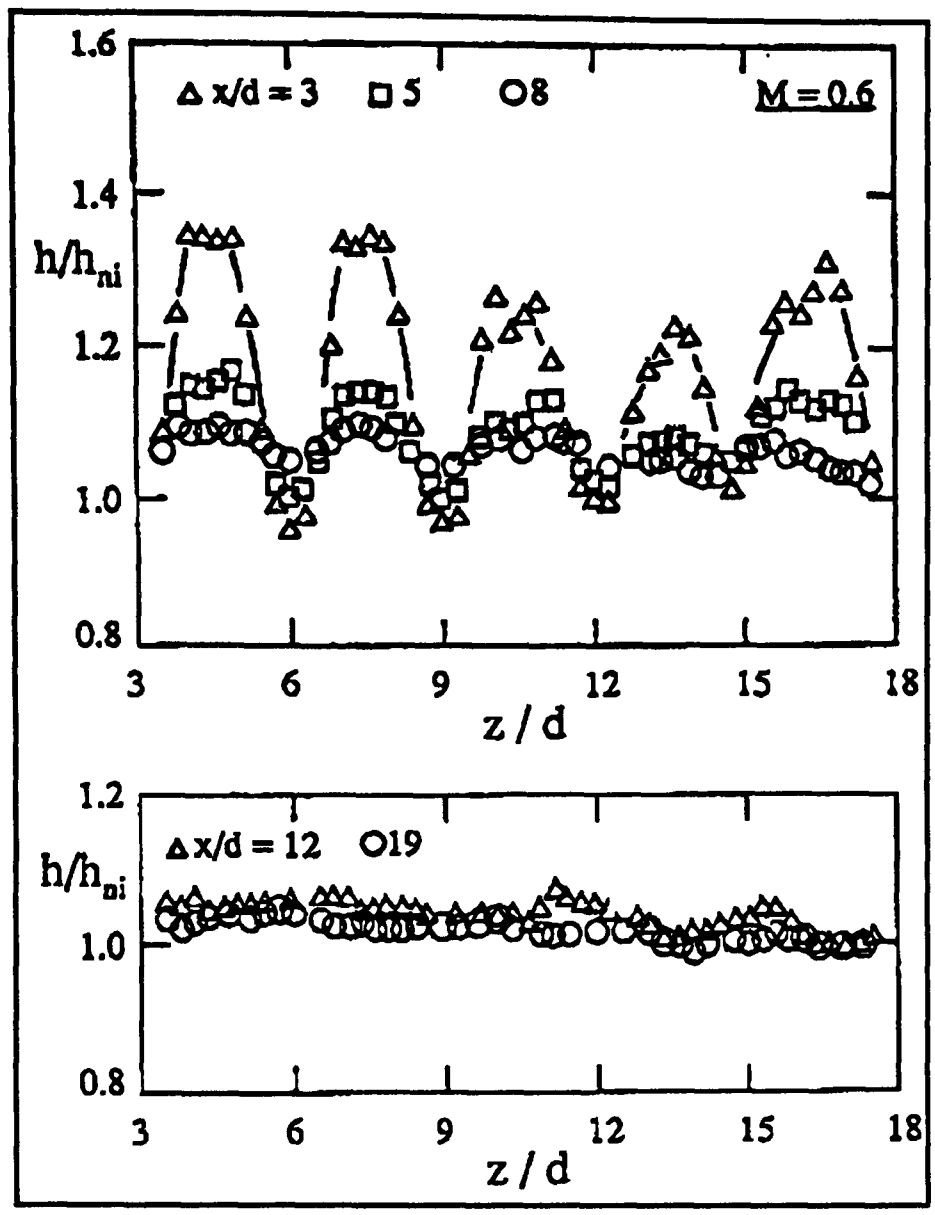


Figure 9.32 h/h_o vs. Z/D
(reference: "A Method for the Simultaneous Determination of Local Effectiveness and Heat Transfer Distributions in Three-Temperature Convection Situations" by R.J. Vedula and D.E. Metzger, 1991)

While the experiments that Vedula and Metzger conducted were the most similar to the experiments conducted in this study, there were some fundamental differences. A liquid crystal technique was used in both cases, but the geometry that Vedula and Metzger tested was different enough to potentially cause dissimilar results. Their study was conducted using five film cooling holes at a 35 degree injection angle and a pitch to diameter ratio of 3.0. It was previously stated that the present study was conducted using four film cooling holes at a 30 degree injection angle and a pitch to diameter ratio of 2.5. Vedula and Metzger also estimated that the uncertainty in their effectiveness predictions was ±12 percent. Wang et al. **(ref.94)** reported an estimated uncertainty in the value of heat transfer coefficient using the equipment and technique at the Osney laboratory of ±7.5-8.5 percent. Furthermore, the uncertainty that Wang et al. estimated in the prediction of the value of T_{gas} is ±1.5-2.1 percent. These estimates of uncertainty

are significantly less than the corresponding prediction of uncertainty by Vedula and Metzger. These facts should be kept in mind when comparing the results from each liquid crystal film cooling study.

As previously discussed in the paper of Vedula and Metzger, their results were compared to the results of other researchers. Figure 9.33 shows a comparison of the effectiveness data at an injection rate of 0.6. Figure 9.34 shows a comparison of the heat transfer data at an injection rate of 0.6 and Figure 9.35 shows a comparison of the heat transfer data at an injection rate of 1.2. According to Vedula and Metzger, the comparison of other researchers data with their own data was "quite reasonable" and "good correspondence" was seen all around.

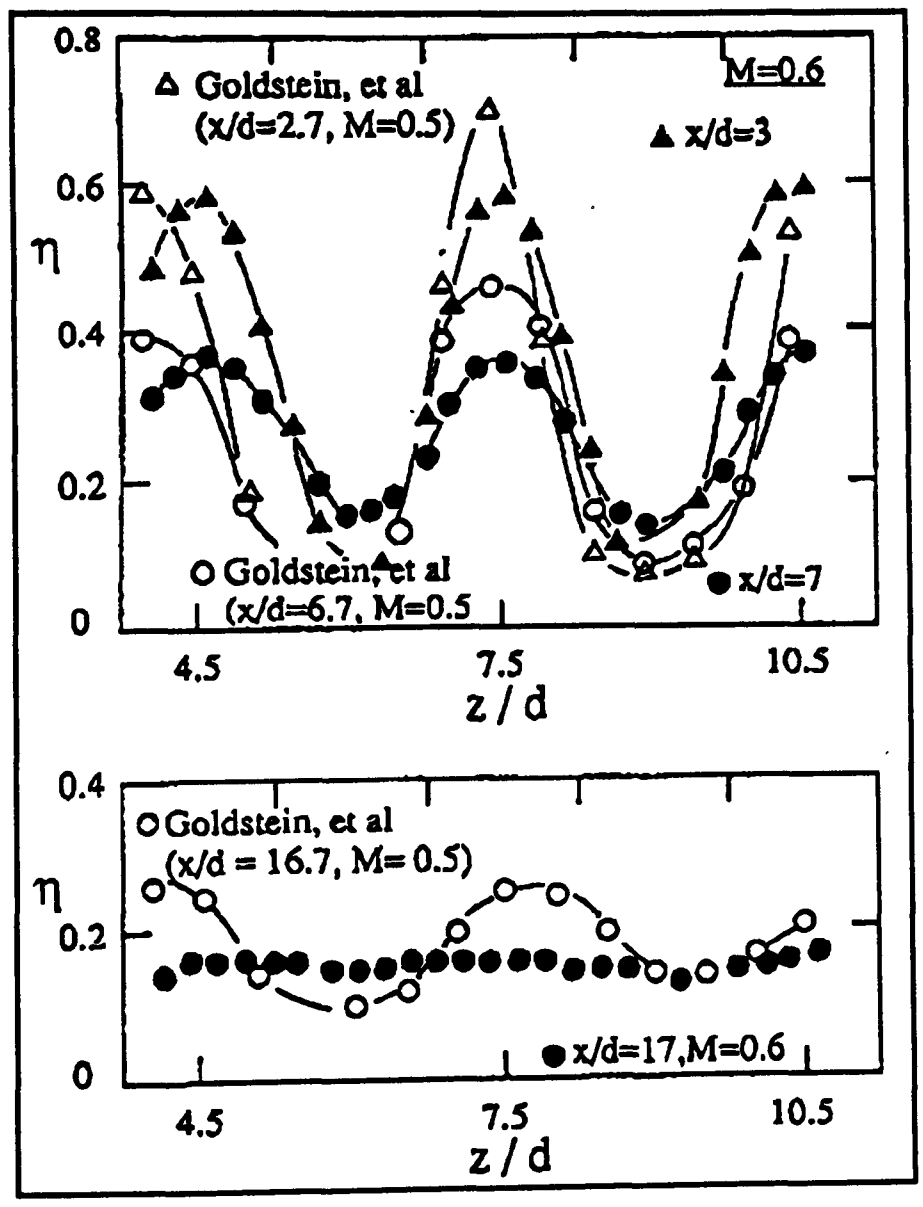


Figure 9.33 Effectiveness Data at G=0.6
(reference: "A Method for the Simultaneous Determination of Local Effectiveness and Heat Transfer Distributions in Three-Temperature Convection Situations" by R.J. Vedula and D.E. Metzger, 1991)

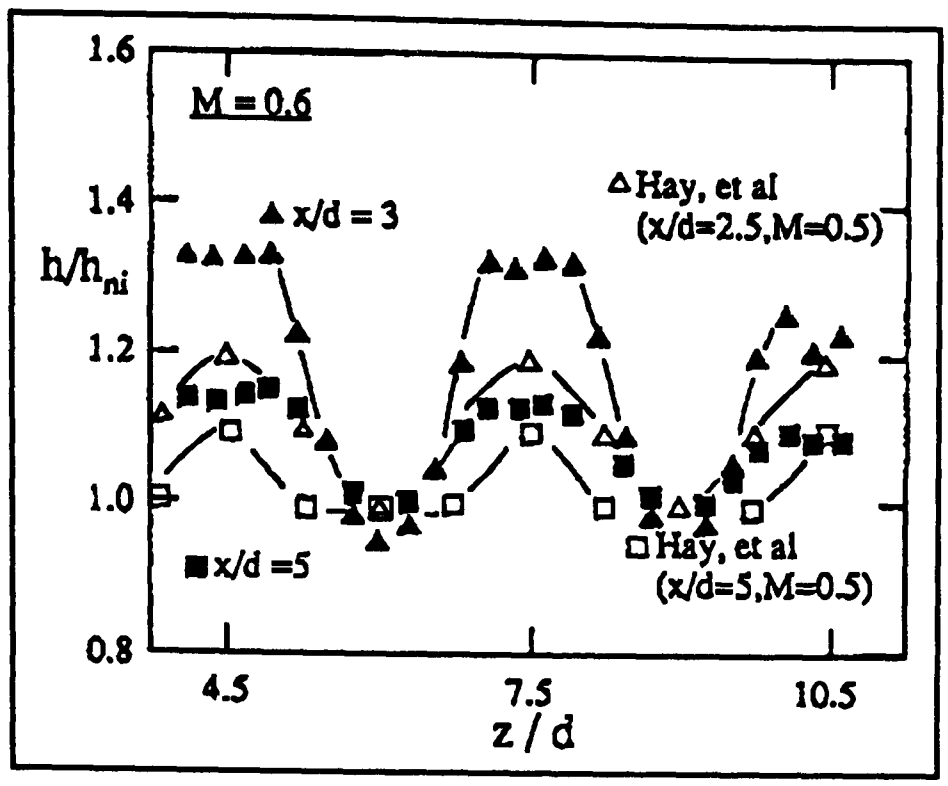


Figure 9.34 Heat Transfer Data at G=0.6
(reference: "A Method for the Simultaneous Determination of Local Effectiveness and Heat Transfer Distributions in Three-Temperature Convection Situations" by R.J. Vedula and D.E. Metzger, 1991)

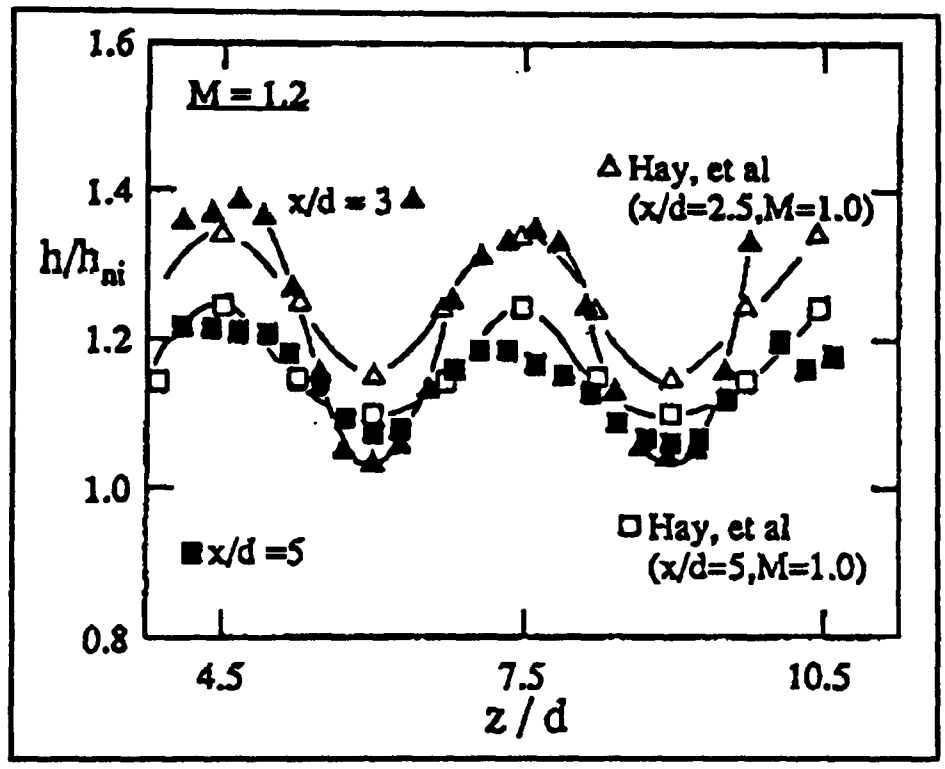


Figure 9.35 Heat Transfer Data at G=1.2
(reference: "A Method for the Simultaneous Determination of Local Effectiveness and Heat Transfer Distributions in Three-Temperature Convection Situations" by R.J. Vedula and D.E. Metzger, 1991)

Teekaram's results provide yet another source of comparative data **(ref.89)**. Table 9.2 shows the film cooling effectiveness data that were reported at various X/D positions and injection rates by Teekaram. There were no spanwise data reported, only the streamwise data shown here. The effectiveness values shown here are averaged in a spanwise direction. Table 9.3 shows the heat transfer data that were reported at various

X/D positions and injection rates. Once again, there is only streamwise data and the values that are shown here are averaged in the direction parallel to the row of holes.

INJECTION RATE (G)	X/D	η
0.2	2	0.453
	8	0.135
	14	0.076
0.4	2	0.594
	8	0.400
	14	0.312
0.6	2	0.416
	8	0.318
	14	0.300
0.8	2	0.235
	8	0.206
	14	0.245
1.0	2	0.159
	8	0.147
	14	0.200

Table 9.2 Comparative Hole Effectiveness Data

INJECTION RATE (G)	X/D	h/h_o
0.2	2	1.475
	14	1.104
0.4	2	1.424
	14	1.150
0.6	2	1.325
	14	1.148
0.8	2	1.289
	14	1.244
1.0	2	1.331
	14	1.298

Table 9.3 Comparative Hole Heat Transfer Data

Figure 9.36 shows a plot of the film cooling effectiveness data that are presented in Table 9.2. Figure 9.36 shows the exact experimental injection rates that were used, as opposed to the interpolated data that are presented in Table 9.2. It is presented again in this slightly different form for the sake of clarity and easy comparison with the experimental results found in previous plots. It is also a very useful plot because it is easy to confirm that Teekaram **(ref.89)** found that the coolant flow does separate from the surface of the wall directly downstream of the cooling holes in the case of the higher injection rates. No such evidence can be found in the presented results of Vedula and Metzger **(ref.92)** even at the highest injection rate.

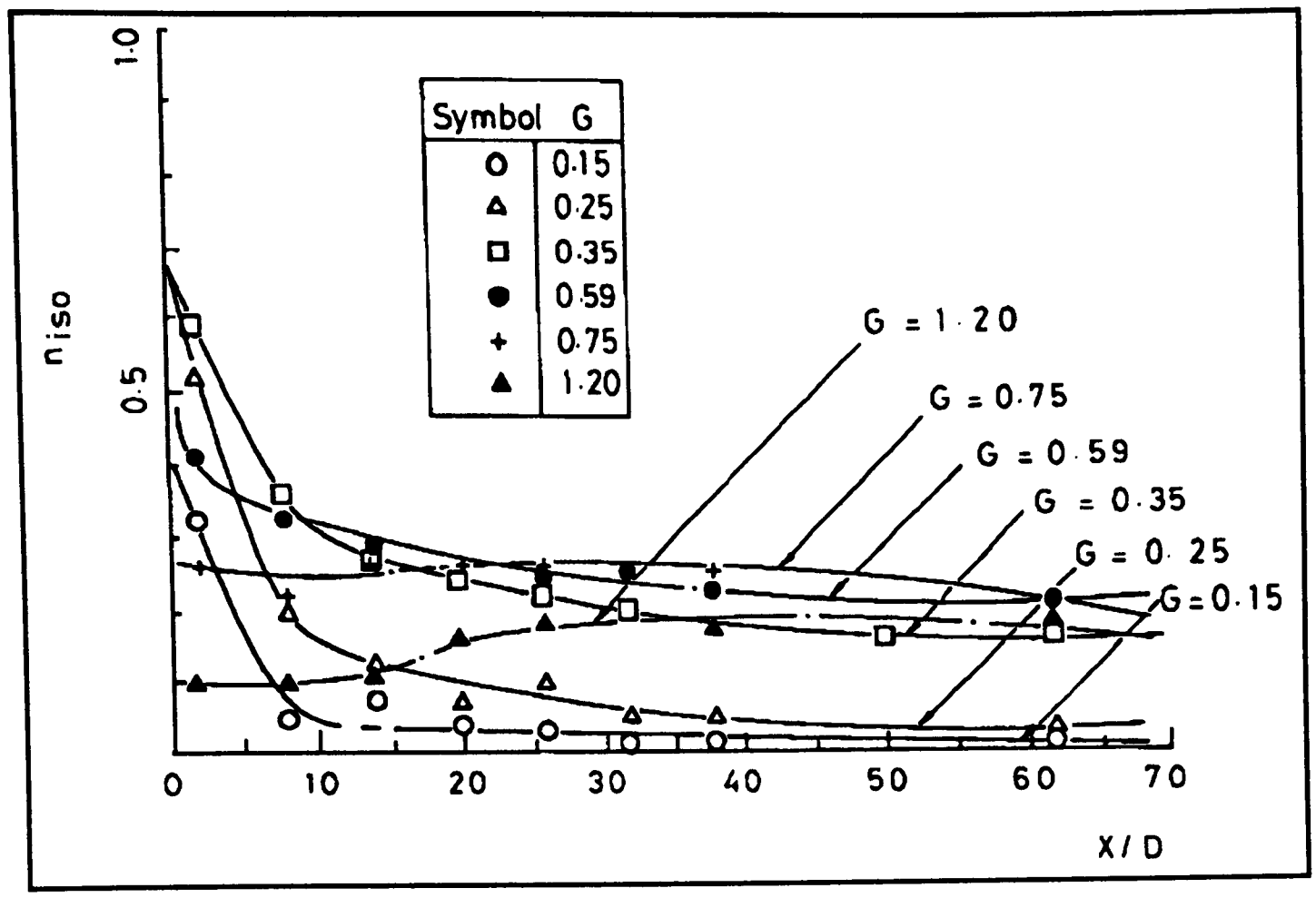
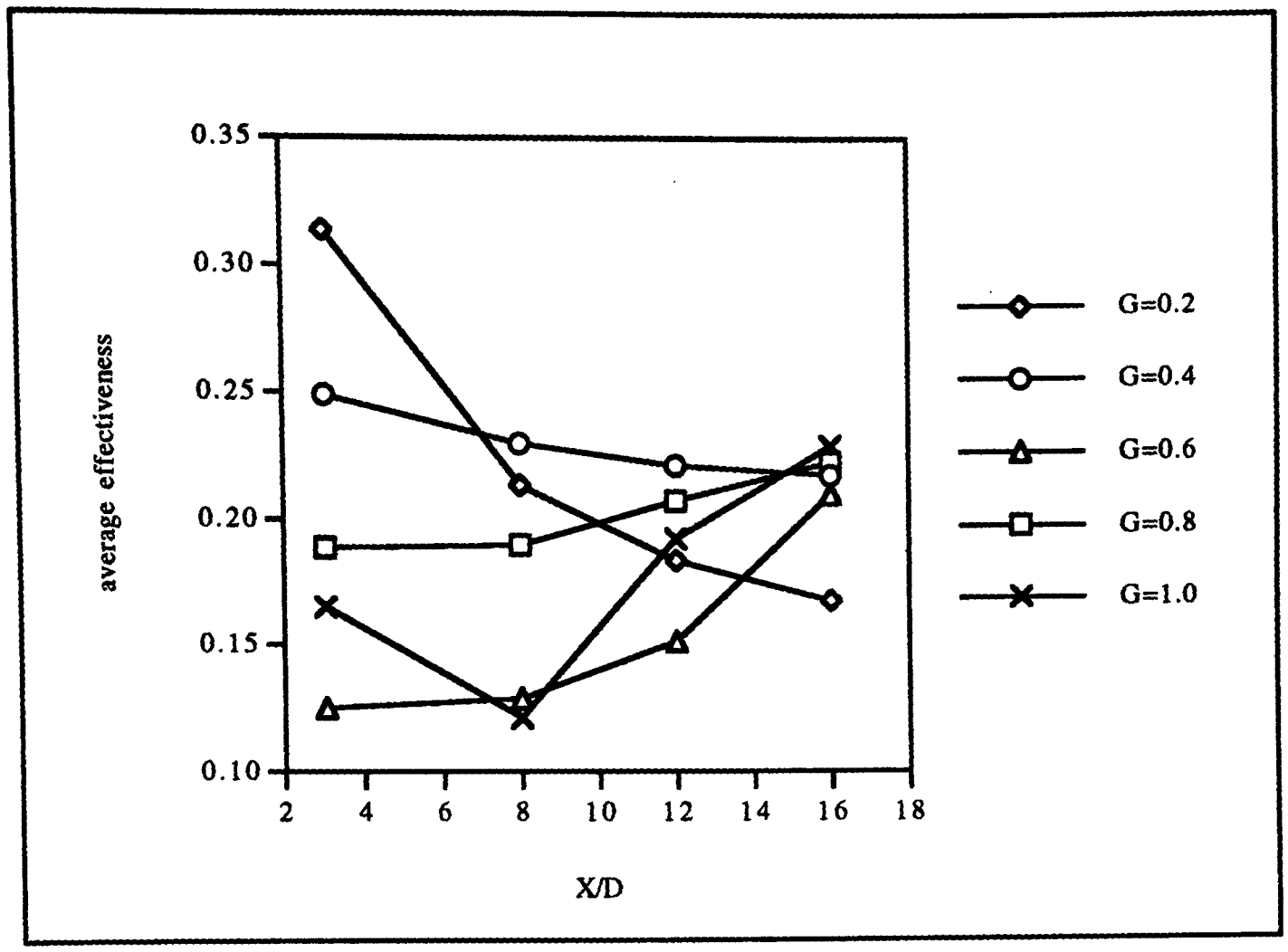


Figure 9.36 Comparative Hole Cooling Data (reference: D. Phil. Thesis by Arnold J. Teekaram, 1989)

Graph 9.12 is a review of the data presented in Graphs 9.2, 9.4, 9.6, 9.8 and 9.10. The high and the low values on each of these plots were averaged so that the data from each injection rate could be presented on the same plot. It is also presented in exactly the same manner as Teekaram's averaged data in Figure 9.36 for a convenient and easy comparison.



Graph 9.12 Average Hole Cooling Data

All of the above values do not agree at every point or at every injection rate. Different test conditions and parameters were used for each of the tests but the results are not so contradictory as to be useless. All of the data are useful in that more information about flow phenomena in a simulated turbine environment is uncovered. Furthermore, the data provide strong guidelines (as opposed to exact values) for the values of certain relevant parameters.

9.3.4 Slot Cooling Results

9.3.4.1 Vortex Slot Results

Vortex slot cooling experiments were carried out with the geometry depicted in Figure 9.4 at the injection rates shown in Table 9.4. All of the relevant test parameters were the same for these tests as for the hole film cooling tests. As stated previously, the freestream velocity was 30m/s and the experiments lasted for 60 seconds. The low injection rates were eliminated from the test matrix for the vortex slot geometry because it was thought that they would be less effective. A high injection rate was required with

an accompanying high injection velocity, so as to ensure sufficient mixing in the vortex region that would produce the desired uniform film of cool injection air at the slot exit.

TEST NUMBER	INJECTION RATE (G)
#1b	0.6
#2b	0.8
#3b	1.0

Table 9.4 Experimental Test Matrix (Vortex Slot)

Figure 9.37 shows a video frame capture of a vortex slot cooling run at an injection rate of 0.8. This injection rate was chosen because it is typical of all the vortex slot tests that were performed. Unlike the hole cooling runs, there are no cooling stripes that become more or less distinct depending on the injection rate. All of the vortex slot runs look similar, as it is hard for the human eye to distinguish slight differences in colour from one experimental run to the next in the region downstream of the slot.

It is easy to see from this video frame capture, which is taken near the end of a test, that the coolant and the geometry have performed their jobs very effectively. For instance, no cooling stripes can be seen at the exit of the slot. It can be argued that the flow was in fact mixed by the presence of the vortex region so that the coolant formed a uniform layer of cool air upon exiting from the slot. It is also apparent that there is a significant colour difference between the region upstream of the slot and the region downstream of the slot. By the end of the test, the region upstream of the slot has already passed through its entire colour play and has returned to a clear colour (the isotropic phase) while the region downstream of the slot has only just begun to enter the blue-green colour phase. This indicates a significant temperature difference between the two regions at the end of the experiment. Also in the case of the slot tests, the cooling effect diminishes far less as it proceeds in the downstream direction than in the

case of the hole tests. It could be argued that it is easier to see cooling stripes spreading out and disappearing in the downstream direction during a hole cooling test than it is to see a slight colour difference during a slot cooling test. This observation is confirmed by comparison of the effectiveness results at progressively larger X/D values.

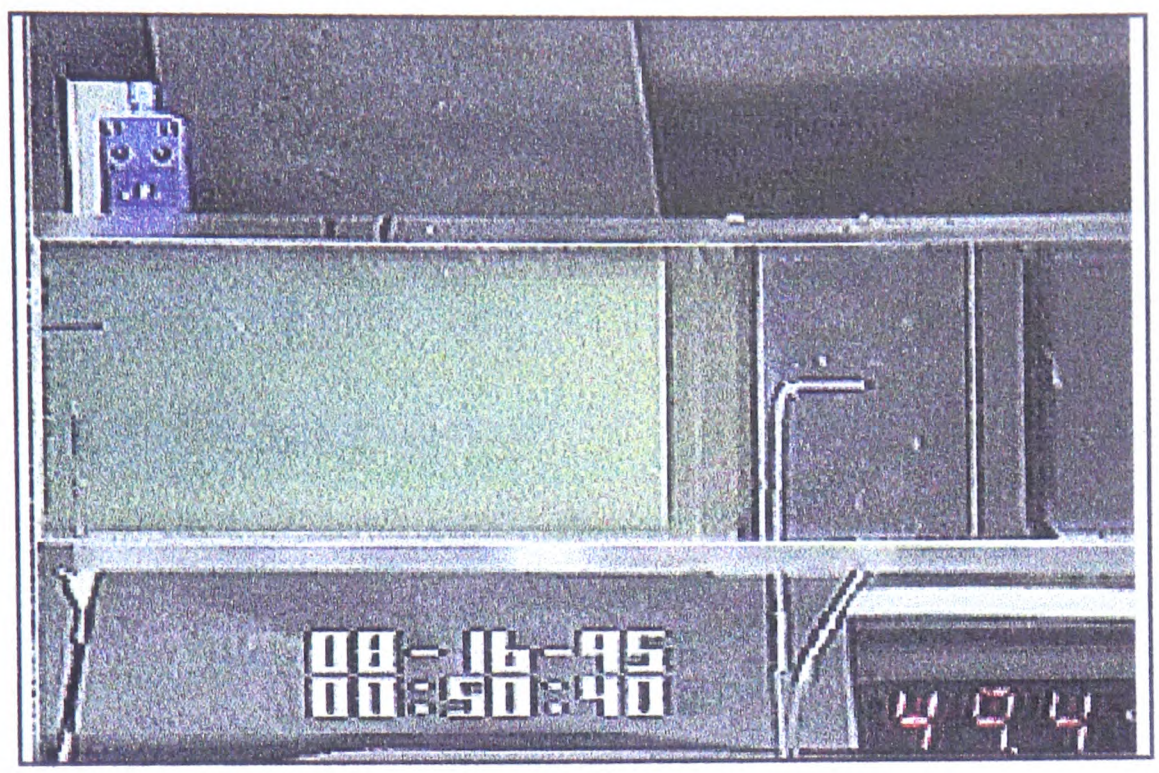
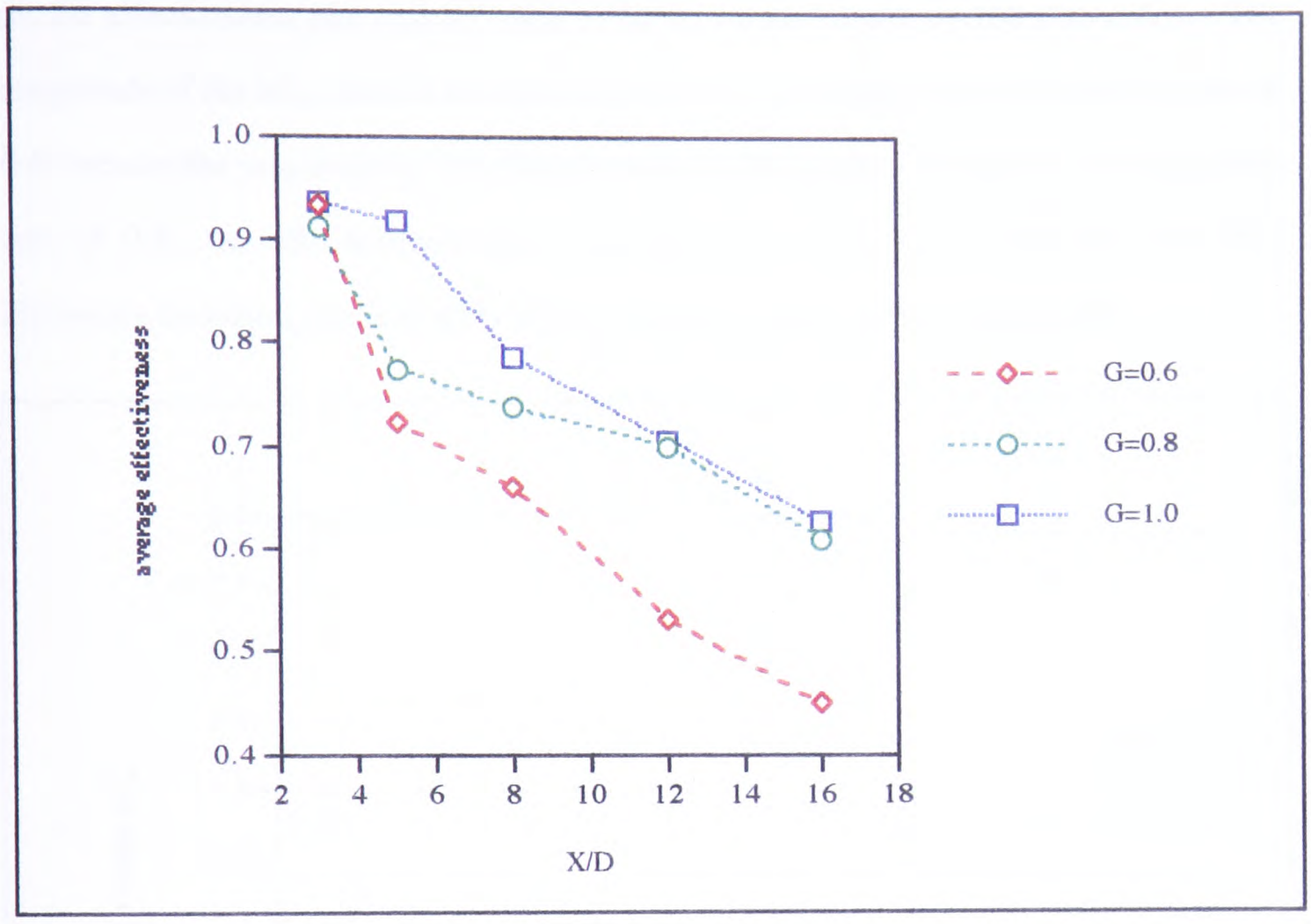


Figure 9.37 Video Capture of Vortex Slot Run

Graph 9.13 shows the average film cooling effectiveness data presented at various downstream positions and at the three injection rates tested. In this case, the effectiveness may be averaged at each downstream location because little or no spanwise variation in the wall temperature was expected. The results for this geometry were found to confirm this observation. This also implies that the vortex region of this geometry was successful in sufficiently mixing the flow from the coolant holes in order to simulate the geometry of a simple slot at the exit to the freestream.

If Teekaram's experimental data (**ref.89**) are consulted for comparison (Table 9.6), then it is easy to confirm that the numerical data also suggest that this geometry successfully simulates a simple slot at the exit. The effectiveness values at each injection rate are close to one at a downstream position very close to the slot exit. The only significant difference between Teekaram's experimental data (simple slot) and the experimental data presented here (vortex slot) exists far downstream of the injection.

Teekaram shows that the high effectiveness levels are maintained over a greater distance for a simple slot than those measured here. The mixing that takes place in the vortex region of the vortex slot geometry seems to decrease or dissipate the cooling effect at greater distances from the slot exit.

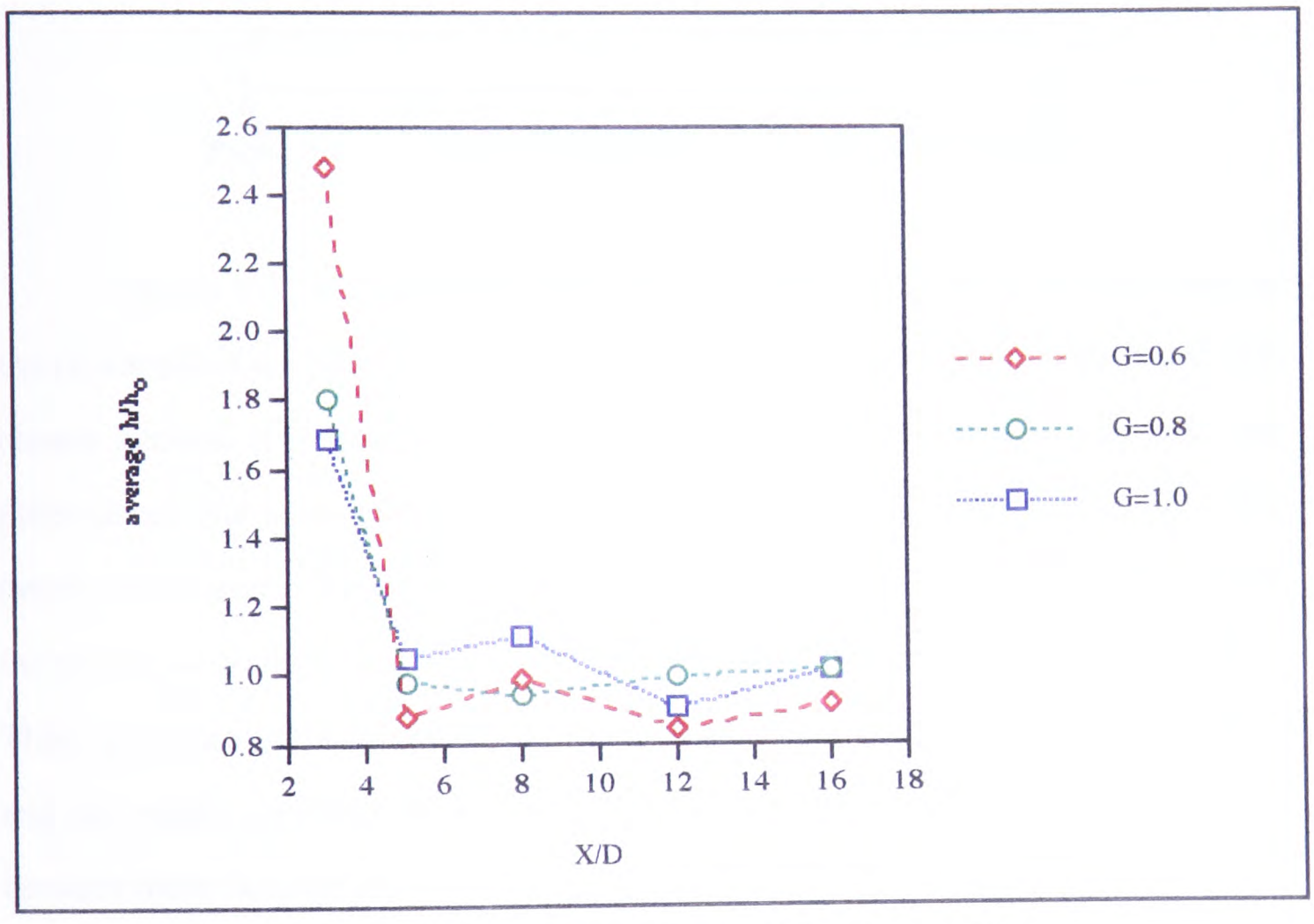


Graph 9.13 Average η vs. X/D (Vortex Slot)

Graph 9.14 shows the average h/h_o data presented at various downstream positions and at the three injection rates that were tested. Once again, the values of heat transfer coefficient were averaged in the spanwise direction because there was little or no spanwise variation present in the results. If Teekaram's experimental data (**ref.89**) are consulted for comparison (Table 9.7), then the high values of h/h_o are further evidence that this geometry successfully simulates a simple slot at the exit. However, Teekaram's values are slightly higher at the point of injection and are noticeably higher downstream of the injection. Teekaram shows that the high values of h/h_0 are maintained much further downstream than what is shown here. The mixing that takes

place in the vortex region of the vortex slot geometry obviously has some effect on the magnitude of the heat transfer with distance from the slot exit as well.

It can be seen that the h/h_o profiles also resemble the effectiveness profiles in the case of the injection rates of 0.6 and 1.0. These two injection rates have similar slopes on the effectiveness plot and are seen to have similar slopes on the plot below. The magnitude of the h/h_o data for the injection rate of 1.0 is higher than the injection rate of 0.6 because the magnitude of the effectiveness is also higher. However, at an injection rate of 0.8, the effectiveness does not decrease at the same constant rate. This difference translates into a slightly increasing heat transfer enhancement ratio.



Graph 9.14 Average h/h_o vs. X/D (Vortex Slot)

9.3.4.2 Trench Vortex Results

Trench vortex cooling experiments were carried out with the geometry depicted in Figure 9.5 at the injection rates shown in Table 9.5. Once again, the runs lasted for 60 seconds and the freestream velocity was 30m/s. As in the case of the vortex slot, the

low injection rates were eliminated in the test matrix for the trench vortex geometry because it was thought that they would be less effective. A high injection rate was required with an accompanying high injection velocity, so as to ensure sufficient mixing in the vortex region that would produce the desired uniform film of cool injection air at the trench exit.

TEST NUMBER	INJECTION RATE (G)
#1c	0.6
#2c	0.8
#3c	1.0

Table 9.5 Experimental Test Matrix (Trench Vortex)

Figures 9.38 and 9.39 show video frame captures from the VHS video tape of trench vortex cooling runs at an injection rate of 0.8. Once again, this injection rate was chosen because it is typical of all the trench vortex tests that were performed. The observations that were made concerning the vortex slot runs can also be made about the trench vortex runs. There are no distinct cooling stripes at the exit of the trench, therefore, the coolant flow was in fact mixed by the presence of the vortex region. There is also a significant colour difference between the region upstream of the trench and the region downstream of the trench indicating a large temperature difference between these two regions.

It is easy to see when comparing Figures 9.37, 9.38 and 9.39 that the colour has progressed to a hue that would indicate a higher surface temperature in the case of the trench vortex runs. Higher surface temperatures translate into lower values of film cooling effectiveness which can be confirmed by comparing the results from the vortex slot runs with the results from the trench vortex runs. It was expected that the values of effectiveness would be higher in the case of the vortex slot runs as opposed to the

trench vortex runs due to their different geometries. The vortex slot geometry obviously provided a more effective and traditional slot at the exit, and was able to mix the flow coming from the five cooling holes in the vortex region to a greater extent.

Finally, by comparing the two video frame captures, it is easy to see the progress of the colour play in the region upstream of the trench over time. During this same period of time, there appears to be little colour change in the region downstream of the slot. The effect of the boundary layer trip upstream of the injection is also clear, particularly in Figure 9.38.

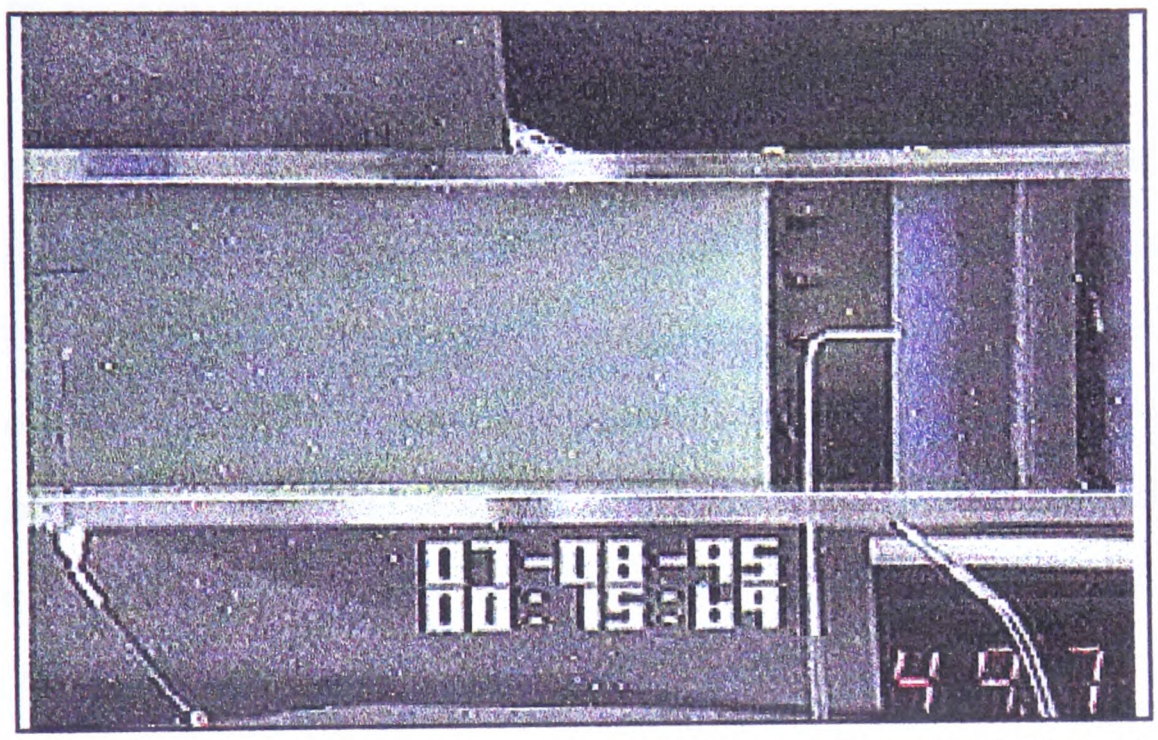


Figure 9.38 Video Capture of Trench Vortex Run (t=15.69 sec.)

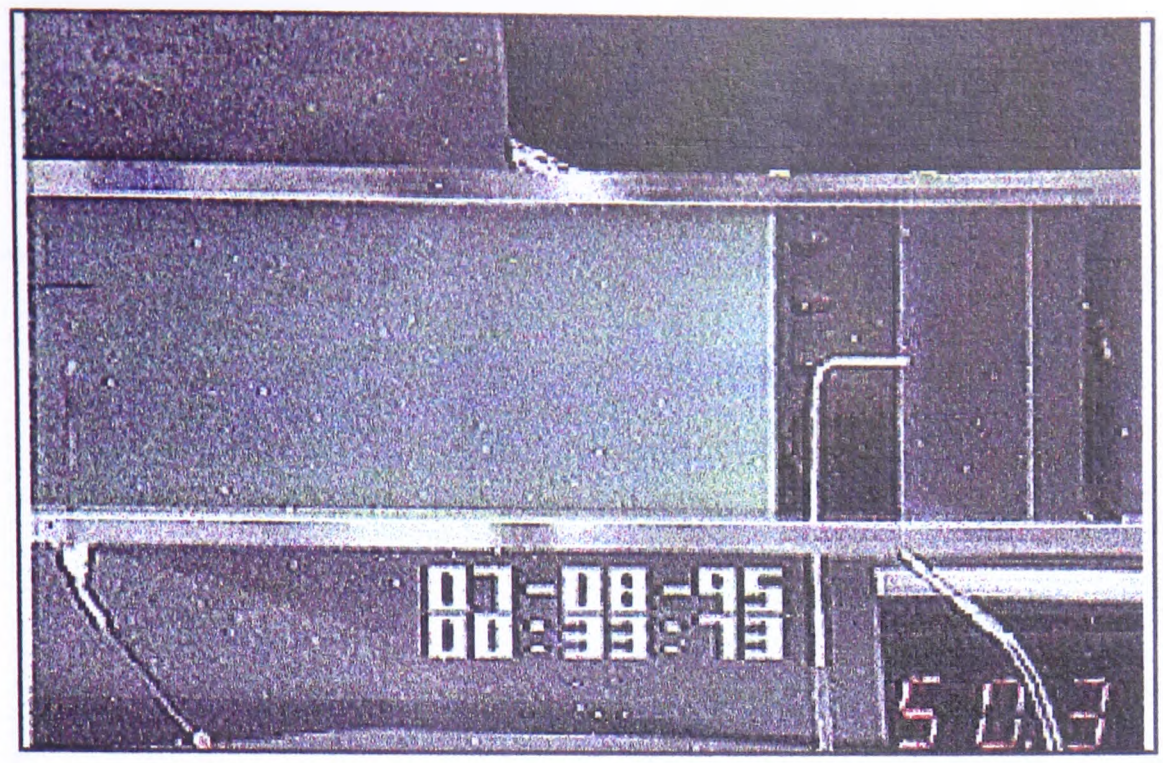
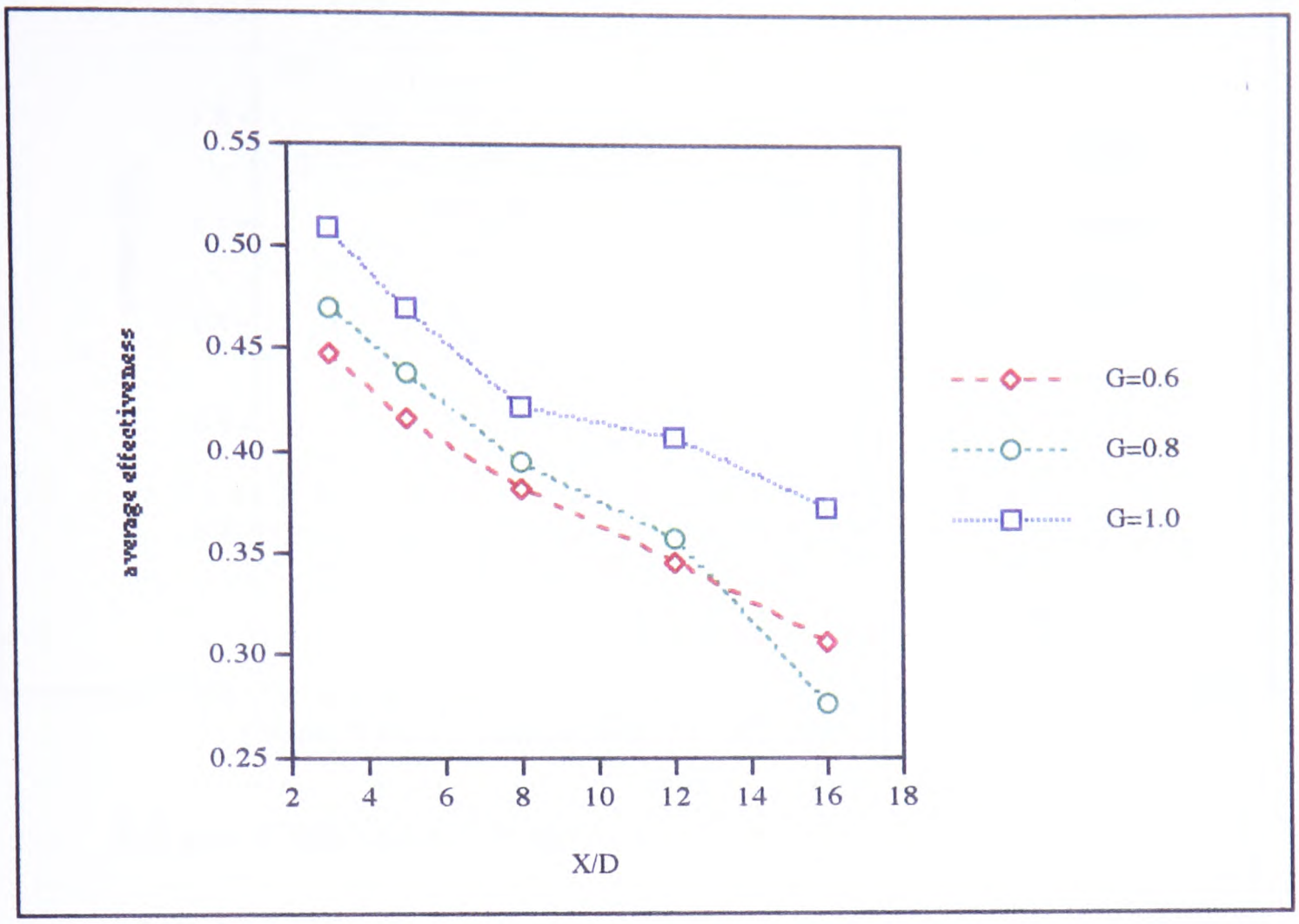


Figure 9.39 Video Capture of Trench Vortex Run (t=33.73 sec.)

Graph 9.15 shows the average film cooling effectiveness data presented at various downstream positions and at the three injection rates that were tested. Once again, the film cooling effectiveness was averaged at each downstream location because little or no spanwise variation in the wall temperature was expected or recorded. This implies that the vortex region of this geometry was successful in sufficiently mixing the flow from the coolant holes in order to simulate the uniform film of coolant air that the geometry of a simple slot would provide at the exit into the freestream.

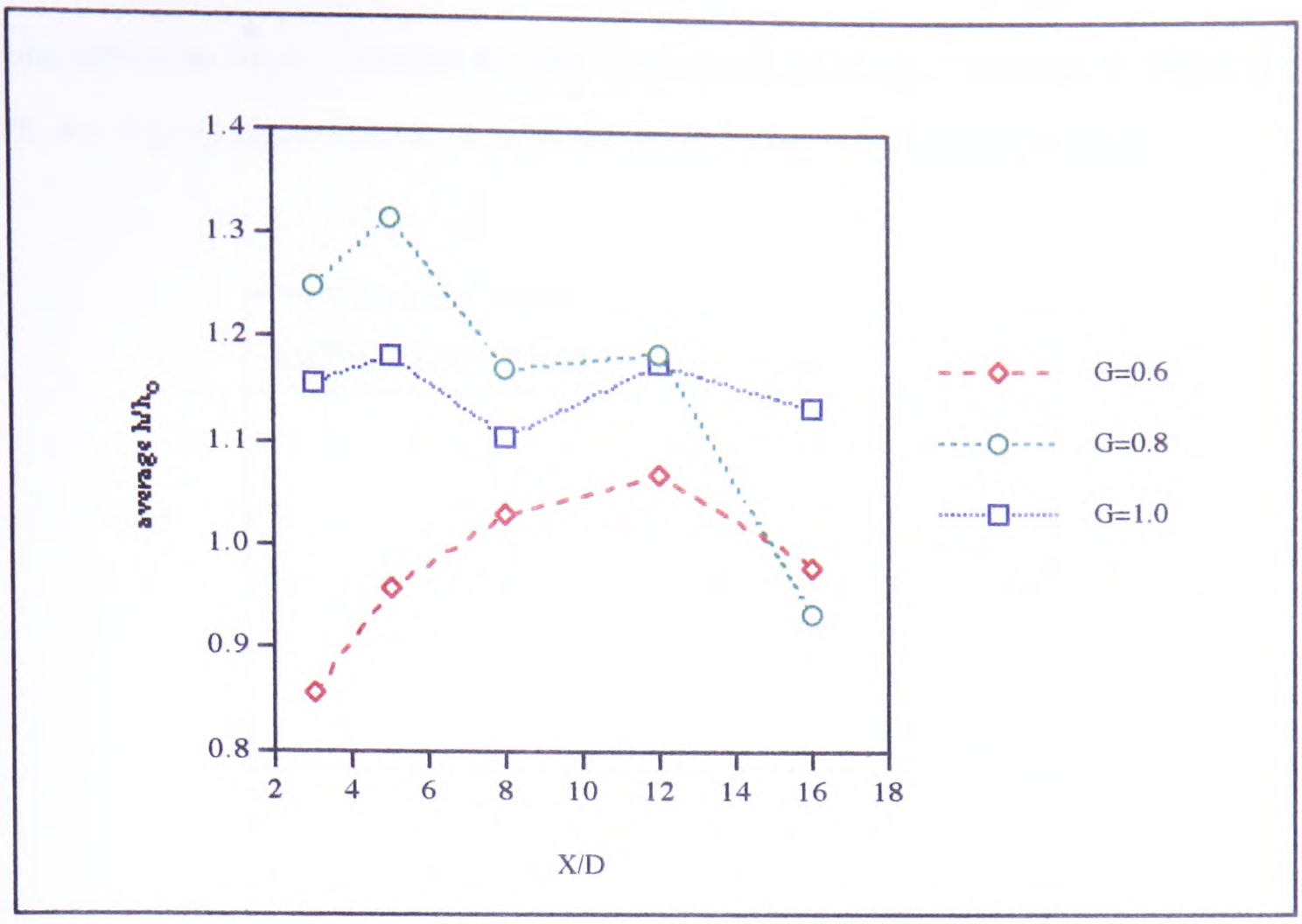
If Graph 9.15 is compared to Graph 9.13, then it is obvious that the magnitude of the film cooling effectiveness is much lower in the case of the trench vortex than in the case of the vortex slot at any injection rate. Therefore, the numerical results suggest that the trench vortex geometry was less successful at emulating a simple slot. It can be seen that the maximum values at each injection rate and downstream position are lower than the in the case of the vortex slot, as are the minimum values. There is, however, less of a difference between the maximum value and the minimum value in the case of the trench vortex, meaning the effectiveness does not decrease with downstream distance as much as with the vortex slot geometry. Of course, this may be due to the fact that the effectiveness starts out at a much lower value. In general, the film cooling effectiveness values do appear to increase with increasing injection rate in more of a

constant, predictable fashion (except far downstream of injection) than was previously seen.



Graph 9.15 Average η vs. X/D (Trench Vortex)

Graph 9.16 shows the average h/h_o data presented at various downstream positions and at the three injection rates that were tested. Once again, the values of heat transfer coefficient were averaged in the spanwise direction because there was little or no spanwise variation present in the results. Comparison of Graph 9.16 to Graph 9.14, shows that at the point of injection, the trench vortex does not demonstrate the same high values of h/h_o that the vortex slot and a simple slot demonstrate. In fact, the magnitude of the heat transfer enhancement ratio that was observed some distance downstream of injection in the case of the vortex slot was similar to the magnitude of the heat transfer enhancement ratio that is observed at all points downstream of injection in the case of the trench vortex. It can also be seen that the h/h_o profiles resemble some of the trends in the corresponding effectiveness profiles.



Graph 9.16 Average h/h_o vs. X/D (Trench Vortex)

9.3.4.3 Comparison of Results

There have been other researchers who have conducted similar experiments to the experiments conducted in this investigation. Unlike a literature survey in hole film cooling, there is less of a chance that there will be any discrepancy in the slot cooling results presented by one researcher in comparison with another. This may be due to the fact that slot cooling is a simpler problem to investigate than hole cooling. In the case of slot cooling, there is no spanwise variation in the relevant parameters that needs to be addressed. Cooling by means of slots is characterized by very high levels of film cooling effectiveness. In fact, a value of effectiveness very close to one is generally reported directly downstream of injection. These high levels of effectiveness also tend to be maintained for significant distances downstream of the slot.

Teekaram's results provide an excellent source of comparative slot cooling data (**ref.89**). His effectiveness and heat transfer data at comparable injection rates are presented in Tables 9.6 and 9.7. For the most part, the values that are presented are

quite similar to those presented by other researchers. However, Teekaram's values of h/h_o are slightly higher than those reported in the literature by other researchers.

INJECTION RATE (G)	X/D	η
0.6	8	0.914
	14	0.805
0.8	8	0.964
	14	0.836
1.0	8	0.989
	14	0.885

Table 9.6 Comparative Slot Effectiveness Data

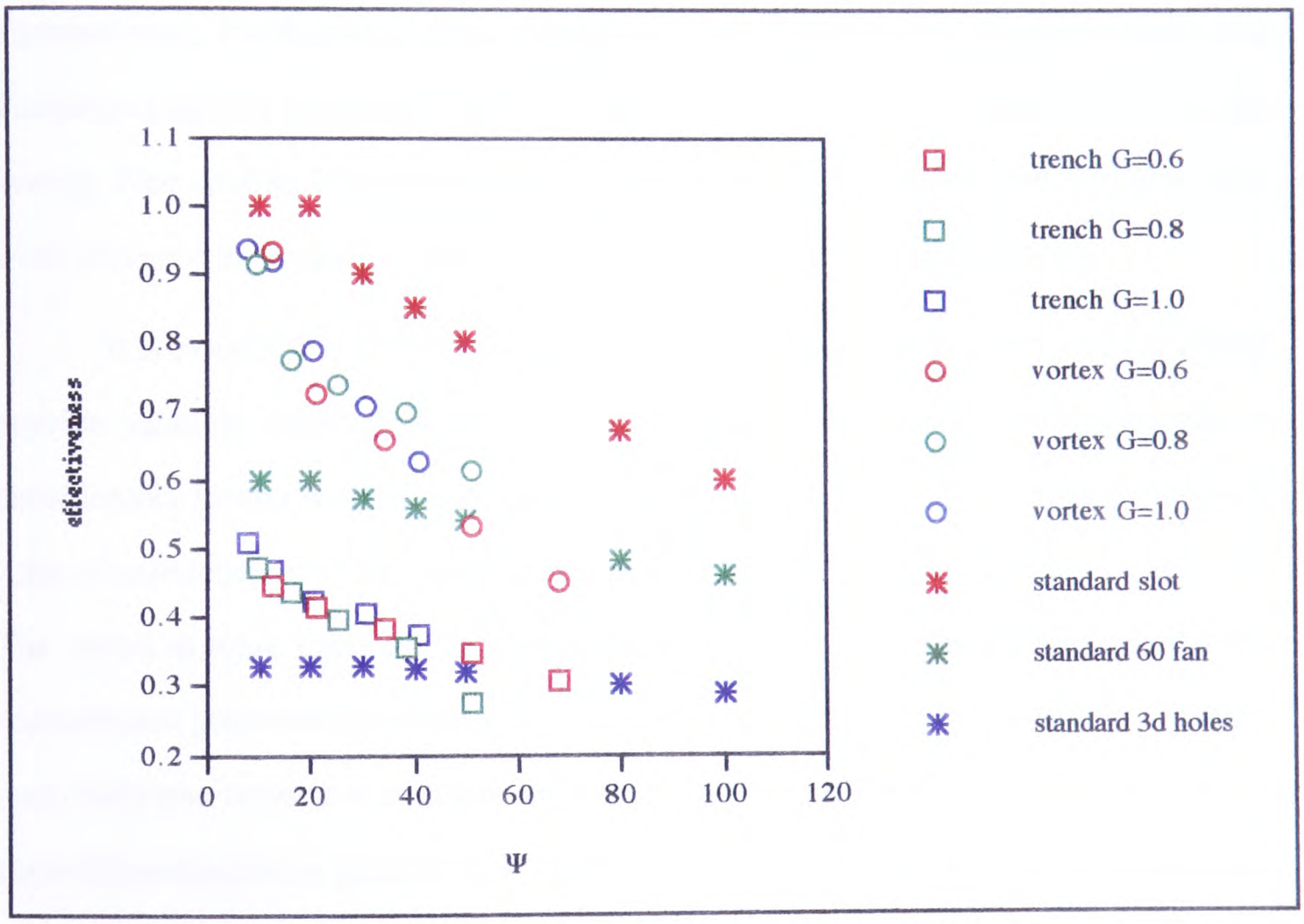
INJECTION RATE (G)	X/D	h/h_o
0.6	2	2.886
	14	1.179
0.8	2	3.425
	14	1.336
1.0	2	3.857
	14	1.429

Table 9.7 Comparative Slot Heat Transfer Data

Graph 9.17 is a comparison plot of the film cooling effectiveness achieved by various turbine cooling schemes. The data that are included in this plot consist of the

trench vortex and the vortex slot cooling data that were presented earlier, as well as standard Rolls Royce data of common cooling geometries and configurations. The comparison of the cooling data is invaluable because the performance of the slot-hole geometries can be gauged with respect to cooling schemes that are in use in gas turbine engines today. The parameter Ψ that is seen in the plot is a non-dimensional parameter that is defined according to Eqn.9.7. This parameter provides a universal downstream distance which can be used in the comparison of experimental data that were even collected at different pitch to diameter ratios.

$$\Psi = \frac{4(\text{pitch to diameter ratio})(X/D)}{\pi G} \qquad (9.7)$$



Graph 9.17 Comparison of Cooling Schemes

9.4 CONCLUSIONS

The results confirm that the experimental technique is both very powerful in the extent of the information that it provides, as well as very flexible in that it has been rapidly applied to three complex film cooling geometries. It is also very useful in that it can be used to test a further range of cooling geometries. The experimental rig was easily alterable and the results were easily repeatable. The repeatability of the experiment using the full range of geometries was confirmed by selectively choosing test cases to be re-run and re-processed. This also served to prove the reliability of the software and the hardware used at every step.

The hole cooling results showed consistent and logical trends that are most evident when looking at the data from the perspective of either increasing or decreasing injection rate. Furthermore, these trends are very similar to the overall results that Teekaram reported using heat transfer gauges in the ILPT. The numerical values for the average film cooling effectiveness at various downstream locations and injection rates were also seen to be quite accurate in comparison to the data in the literature.

It is evident that further hole cooling experimentation with a different rig would provide valuable information. Without the benefit of data taken at a distance that is considerably further downstream from the cooling holes, it is hard to predict where the point of reattachment of the coolant flow is for the injection rates of 0.6, 0.8 and 1.0. The values at these injection rates are needed to confirm the expected outcome of the reattachment point moving further downstream with increasing injection rate. The new data could also be used to correlate the results with Teekaram's experimental data which show the reattachment point at these higher injection rates beyond the downstream limit of the rig used in this study.

The slot cooling results confirmed the predictions that were made as to how each geometry would perform relative to each other, and in comparison to simple hole cooling and simple slot cooling. The vortex slot was seen to behave in a way that is most like a simple slot. This is logical in light of the fact that the vortex slot geometry is

the most like that of a simple slot. The magnitude of the relevant parameters was consistent with slot data reported in the literature at the exit, but not further downstream. The performance of the trench vortex can be ranked in between that of simple hole cooling and cooling by means of the vortex slot. These results can be confirmed by consulting Graph 9.17.

RECOMMENDATIONS FOR FURTHER WORK

It is the author's hope that this computational and experimental examination of turbine cooling flows is useful in that it provides a stepping stone for the pursuit of further work in this area. This investigation saw the initial implementation and parameter adjustment of the film cooling portion of MEFP. Further work in this area is needed if even greater improvements are sought. Further use of the code in the comparison of theoretical and experimental results with computational results can only be advantageous.

Improvements to the film cooling subroutine can follow several different paths. It was previously seen that the code encountered difficulty when presented with adverse pressure gradients. It was suggested that this was due to the fact that MEFP used the mixing length turbulence model throughout this investigation. One possible course would be to experiment with the use of alternate turbulence models to see whether the accuracy of the predictions is increased or decreased.

Analyzing different test cases would be another viable option, facilitating the development and improvement of the code. In the cases presented here, most of the cooling was done by holes at an injection angle that fell within a small range of values. Choosing test cases with injection rates that fell within a small range was the logical course, since this is the typical range of injection angles in real gas turbine engines. Nevertheless, this course of action tends to provide only limited information. Furthermore, the coolant was generally only angled in one direction, that direction being with respect to the surface of the plate or the blade. It would be valuable if different test cases were chosen where the injection angle varied with respect to the direction of the freestream as well. A detailed analysis of the film cooling optimization parameters for these test cases would provide valuable insight, especially if it could be determined how much these values differ from those values presented here. An investigation of this kind would also be valuable if applied to the showerhead region or the leading edge of a turbine blade where coolant injection is present.

A third and definitely more time consuming option is to change the film cooling model. A trajectory model was mentioned earlier as a possible, more complex option for defining the process of film cooling. It was decided in this investigation not to abandon the stripping model altogether, but merely to improve it. This approach was successful, but a future approach could analyze the viability of implementing a trajectory film cooling model in MEFP. This would be a natural course to follow due to the fact that a trajectory model would more accurately represent what happens when coolant is injected into the freestream.

The film cooled CHTT experimental runs are continuing and in the future even more experimental data will be available. The experimental data that were collected with the thin film heat transfer gauges at the fifty percent midspan location were presented here, but the experimental data that were collected with the liquid crystals were not. The non-film cooled datasets with the simulated liquid crystal roughness are in existence. The film cooled datasets for a smooth surface with data collection at the fifty percent midspan location are also in existence. Therefore, it is a relatively easy task to construct film cooled datasets with the simulated roughness characteristics and with data collection over the entire surface using the optimized film cooling parameters.

There are particular areas that possess great potential for improvement in the prediction of the three-dimensional film cooled turbine blade case, like the CHTT. One promising area consists of using the thermal paint data that were collected in Rolls Royce test engines and rigs. Thermal paint could provide additional fluid dynamic and heat transfer turbine data that could be used as a guideline for the implementation of certain key parameters, or the optimization of film cooling parameters.

The experimental part of this investigation was very successful, but further work in this area can only be beneficial. For instance, it was mentioned previously that conducting the same tests with a different experimental test rig that provides a greater downstream distance over which data can be collected would be very helpful. The liquid crystals provided data that agreed with other experimental results in the near

field, close to the cooling holes or slot, but information in the far field was not available.

The experiments with the hybrid slot-hole configurations were the first of their kind. Therefore, any additional information that could be collected would be advantageous. An example of this would be data taken in the vortex or mixing region of the slots. The velocity could be sampled at the exit of each hole to confirm that the velocity was in fact the same across the entire row of holes. Any positive or negative effects that the differences in coolant hole exit velocity produce could be studied with greater ease if the coolant hole exit velocity was known for each hole. Other information could also be gathered to determine how efficiently the coolant is mixed in the vortex region. This factor is particularly important in determining if the flow at the exit of the slot, correctly models the uniform "blanket" of cool air that is found at the exit from a simple slot. An initial step would be to make use of the various flow visualization methods in this region.

APPENDIX

What is presented here are the two Matlab® programs written by David Gillespie that were used to determine the heat transfer coefficient and the adiabatic wall temperature for the film cooled experimental test cases.

```
%       HUE2HTC.M is an m file to convert the hue signal from  Z.Wang's Image
%       Processing system to the heat transfer coefficient and Adiabatic Wall
%       temperature for each point processed.
%       For each test a history*.mat file, a calibration of HC(a row vector)
%       vs TC (a column vector of the same length) saved in matlab format
%       (***.mat).

%       Other data required to run the program :
%       Tjet=   Driving Gas Temperature
%       Tinit=  Substrate Initial Temperature
%       ttransport = time for gas to reach the starting point from the mesh
%       tvideo     = the extra time shown on the last video frame grabbed
%       sfrm,efrm  = start and end frame of the run
%       sm,em      = range of points in history file to be processed
%       Thighcut,Tlowcut = Range of calibration to be used for processing

clear
% Initial Data %
% 1 Data Calibration and Reference Cooordinate files %
load c:\matlab2\carrie\run10\history2.mat;          %from realmode program
load c:\matlab2\carrie\calib2\calib.mat             %from calibration

% 2 Initial temperatures, time corrections %
Tjet=39.2
Tinit=14.35
ttransport=0.00
tvideo=0.00
butterfilter=.1
butterfilterw=.01
ifw=inter_frame_wait+1
number_of_steps=100
```

```
% start/end frames,matlab matrix data %
Tlowcut=22.1
Thighcut=38.3
Tbreak=Tlowcut
% Make greater than Tlowcut to ignore data below this temperture when full history is
available %
sfrm=1
efrm=3000
sm=1
em=20
z=data(sfrm:efrm,sm:em);
clear data;

% Make Butterworth Filter components %
[C,D]=butter(4,butterfilterw); %4,.01 filter to find max;
[A,B]=butter(4,butterfilter); %4,.1 filter for processing data;

% Convert to Diameter coordinates %
[E,F]=size(coord);
for i=1:1:F,
        final(i,1)=coord(1,i);
        final(i,2)=coord(2,i)*2;
end

% This portion converts the hue data to temperature data using the calibration loaded
% previously TC is the calibrated temperature curve HC is the hue values associated
% with TC %
for i=1:1-sm+em,

% This portion takes the data and sets all values below HC(1) equal to HC(1) %
% Creates a cal_temp file to use later %
[N,M]=size(TC);
clear c;
c=find(z(:,i)<HC(1));
cal_temp=TC(1)*ones(1:300,i);

% The data is then smoothed using the butterworth filter %
z2(:,i)=filtfilt(A,B,z(:,i));

% The smoothed data is then checked for values less than HC(1) and adjustments made %
```

```
clear c1;
c1=find(z2(:,i)<HC(1));
[cm1,cn1]=size(c1);
checkc1=isempty(c1);
if checkc1 == 0,
                    for j=1:cm1,
                                z2(c1(j),i)=HC(1);
                    end
end

% creates calibration file and sets upper limit of data equal to calibration file
% and puts temperatures into cal_temp %
cal_temp(M:N,i)=TC;
clear c2;
c2=find(z2(:,i)>HC(N));
checkc2=isempty(c2);
if checkc2 == 0;
          [cm2,cn2]=size(c2);
          for j=1:cm2,
                    z2(c2(j),i)=HC(N);
          end
end

% Transforms the hue data into Temperature by subtracting HC(1) from data hue values and
looking up the corresponding TC value in cal_temp directly (adding one so the value is never
zero for the first case This number then is the index for TC file starting at one %
          e(:,i)=cal_temp((z2(:,i)-HC(1))+1,i);
          e2(:,i)=filtfilt(C,D,e(:,i));
end
clear z
clear z2

% This portion creates a time base corrected for video and transport %
timecorrection=fix((ttransport-tvideo)*50/ifw);
ttotal=-timecorrection*ifw/50:0.02*ifw:(efrm-timecorrection-1)*ifw/50;

% This portion picks off a number_of_steps and matches h and T to it %
final(1,3:4)=[0,0];
for i=1:em-sm+1
sm+i-1;
Sfrm(i)=99+fix(mean(find(e(100:efrm,i)==min(e(100:efrm,i)))));
if max(e2(Sfrm(i):efrm,i))<Thighcut,
```

```
Efrm(i)=Sfrm(i)-1+fix(min(find(e2(Sfrm(i):efrm,i)>max(e2(Sfrm(i):efrm,i)-0.001))));
else
Efrm(i)=Sfrm(i)-1+fix(min(find(e2(Sfrm(i):efrm,i)>Thighcut)));
end
Ifrm(i)=Sfrm(i)+fix(mean(find((e2((Sfrm(i)+1):efrm,i)>Tbreak-0.5)&(e2((Sfrm(i)+1)
:efrm,i)<Tbreak+0.5))));
        if (Sfrm(i)-timecorrection < 0) | (Sfrm(i)>Efrm(i))
                Sfrm(i)=timecorrection;
        end
        if Ifrm(i)>=Efrm(i)|isnan(Ifrm(i))==1|Ifrm(i)<Sfrm(i)
                Ifrm(i)=Sfrm(i);
        end;
        Index=fix((Efrm(i)-Ifrm(i)).*(1/number_of_steps:(1/number_of_steps):1));
        time=(Ifrm(i)-timecorrection+Index)*ifw/50;
        Data=e(Ifrm(i)+Index,i)';
        Guess=[100,Tjet];
        options(1)=0;
        options(2)=0.001;
        options(14)=500;
        global Tinit time Data q
        final(sm+i-1,3:4)=fmins('stepfit2',Guess,options);

% The next bit is just for plotting purposes %
        [k,l]=find(ttotal>0);
        Tw2=Tinit+(final(sm+i-1,4)-Tinit).*(1-exp(final(sm+i-1,3).^2.*ttotal(l(1):efrm).
/(569^2)).*(1-erf(final(sm+i-1,3).*sqrt(ttotal(l(1):efrm))./569)));
        plot(ttotal,e(:,i),time,Data,'+',ttotal(l:efrm),Tw2,'b')
        text(0,0,['h = ',num2str(final(sm+i-1,3)),' Taw = ',num2str(final(sm+i-1,4))])
        xlabel('time (seconds)')
        ylabel('temperature (degrees C)')
        title(['Time vs Temperature History '])
        pause
end
final(sm:em,:)
```

```
function q=stepfit2(guess)
global Tinit time Data q
h=guess(1);
T=guess(2);
beta=h.*sqrt(time)./569;
q=Tinit+(T-Tinit).*(1-exp(beta.*beta).*(1-erf(beta)))-Data;
q=sum(q.^2);
```

REFERENCES

1. Abuaf, N. et al., "Heat Transfer and Film Cooling Effectiveness in a Linear Airfoil Cascade", ASME 95-GT-3.

2. Afejuku, W.O. et al., "The Film Cooling Effectiveness of Double Rows of Holes", Journal of Engineering for Power, Transactions of the ASME, volume 102, 1980.

3. Amer, A.A. et al., "Comparison of Different Two-Equation Turbulence Models for Prediction of Film Cooling From Two Rows of Holes", Numerical Heat Transfer, Part A, volume 21, 1992, pg. 143-162.

4. Anderson, Dale A. et al., Computational Fluid Mechanics and Heat Transfer, Hemisphere Publishing Corporation, 1984.

5. Bergeles, G. et al., "The Turbulent Jet in a Cross Stream at Low Injection Rates: A Three-Dimensional Numerical Treatment", Numerical Heat Transfer, volume 1, 1978, pg. 217-242.

6. Bergeles, G. et al., "Double-Row Discrete-Hole Cooling: An Experimental and Numerical Study", Journal of Engineering for Power, Transactions of the ASME, volume 102, April 1980, pg. 498-503.

7. Bonsell, J.J. and J.W. Chew, "2D Testing of the MEFP-SC03 Link", Rolls Royce plc, Aerothermal Methods Report #DNS16703, December 1994.

8. Bradley, C.C., "Computer Systems Report - GRAFFITI (JH01) Input Dataset Format - Version 3", Rolls Royce plc, report #CSR5068, February 1992.

9. Bradley, C.C., "Computer Users Guide Silicon Graphics 3D Output Processor", Rolls Royce plc, report #CUGJH01, February 1992.

10. Brown, A., "A Theoretical and Experimental Investigation Into Film Cooling", The Queen's University of Belfast, Belfast, Northern Ireland, Department of Mechanical Engineering, 1967.

11. Buckley, John, 4th Year Report, University of Oxford, Oxford, U.K., Department of Engineering Science, 1994.

12. Camci, C. and T. Arts, "Short-Duration Measurements and Numerical Simulation of Heat Transfer Along the Suction Side of a Film-Cooled Gas Turbine

Blade", Journal of Engineering for Gas Turbines and Power, Transactions of the ASME, volume 107, October 1985, pg. 991-997.

13. Chew, J.W., "Implementation of a 'Crawford-Type' Film Cooling Model in MEFP", Rolls Royce plc, Theoretical Science Group report #TSG0580, November 1991.

14. Chew, J.W., Rolls Royce plc, Theoretical Science Group, Private Communication, 1993-present.

15. Chin, J.H. et al., "Adiabatic Wall Temperature Downstream of a Single, Tangential Injection Slot", ASME No. 58-A-107.

16. Choi, D., "A Navier-Stokes Analysis of Film Cooling in a Turbine Blade", AIAA-93-0158.

17. Cohen, H. et al., Gas Turbine Theory, third edition, New York, U.S.A.: John Wiley & Sons, Inc., 1987.

18. Coupland, J. and P. Stow, "Turbulence Modeling for Turbomachinery Flows", 2nd International Symposium on Engineering Turbulence Modeling and Measurement, Florence, 31 May - 2 June, 1993.

19. Crawford, M.E. et al., "Full Coverage Film Cooling Part II: Heat Transfer Data and Numerical Simulation", Journal of Engineering for Power, Transactions of the ASME, volume 102, October 1980, pg. 1006-1012.

20. Demuren, A.O., "Numerical Calculations of Steady Three-Dimensional Turbulent Jets in Cross Flow", Computer Methods in Applied Mechanics and Engineering, volume 37, 1983, pg. 309-328.

21. Demuren, A.O. et al., "Systematic Study of Film Cooling With a Three-Dimensional Calculation Procedure", Journal of Turbomachinery, Transactions of the ASME, volume 108, July 1986, pg. 124-130.

22. Dibelius, G.H. et al., "Numerical Prediction of Film Cooling Effectiveness and the Associated Aerodynamic Losses With a Three-Dimensional Calculation Procedure", ASME 90-GT-226.

23. Dring, R.P. et al., "An Experimental Investigation of Film Cooling on a Turbine Rotor Blade", Journal of Engineering for Power, Transactions of the ASME, volume 102, January 1980, pg. 81-87.

24. Eckert, E.R.G. and R.C. Birkebak, "The Effects of Slot Geometry on Film Cooling", Heat-Mass Transfer and Thermodynamics, 1964.

25. Ekkad, S.V. et al., "Heat Transfer Coefficients Over a Flat Surface With Air and CO_2 Injection Through Compund Angle Holes Using a Transient Liquid Crystal Image Method", ASME 95-GT-10.

26. Ekkad, S.V. et al., "Film Effectiveness Over a Flat Surface With Air and CO_2 Injection Through Compund Angle Holes Using a Transient Liquid Crystal Image Method", ASME 95-GT-11.

27. Ferri, A. et al., "Investigation of Slot Cooling at High Subsonic Speeds", AIAA Journal, volume 14, No. 7, July 1976, pg. 880-885.

28. Fitt, A.D. et al., "Temperature Ratio Effects in Compressible Turbulent Boundary Layers", International Journal of Heat and Mass Transfer, volume 29, number 1, 1986, pg. 164-167.

29. Fletcher, C.A.J., Computational Techniques for Fluid Dynamics, volume I, New York, U.S.A.: Springer-Verlag, 1988.

30. Fletcher, C.A.J., Computational Techniques for Fluid Dynamics, volume II, New York, U.S.A.: Springer-Verlag, 1988.

31. Forth, C.J. Patrick, "An Investigation of Scaling Parameters Governing Film-Cooling", Oxford University, D. Phil. Thesis, 1985.

32. Garg, V.K. and R.E. Gaugler, "Heat Transfer in Film-Cooled Turbine Blades", ASME 93-GT-81.

33. Garg, V.K. and R.E. Gaugler, "Effect of Velocity and Temperature Distribution at the Hole Exit on Film Cooling of Turbine Blades", ASME 95-GT-2.

34. Goldsmith, E.L. and J. Seddon, Practical Intake Aerodynamic Design, London, U.K.: Blackwell Scientific Publications Ltd., 1993.

35. Goldstein, R.J., "Film Cooling", Advances in Heat Transfer, New York, U.S.A. and London, U.K.: Academic Press, volume 7, 1971.

36. Goldstein, R.J. and T. Yoshida, "The Influence of a Laminar Boundary Layer and Laminar Injection on Film Cooling Performance", ASME 81-HT-38.

37. Goldstein, R.J. et al., "Film Cooling With Injection Through Holes - Adiabatic Wall Temperatures Downstream of a Circular Hole", Journal of Engineering for Power, Transactions of the ASME, volume 90, October 1968, pg. 384-395.

38. Haas, W. et al., "The Influence of Density Difference Between Hot and Coolant Gas on Film Cooling by a Row of Holes: Predictions and Experiments", ASME 91-GT-255.

39. Harnett, J.P. et al., "Velocity Distributions, Temperature Distributions, Effectiveness and Heat Transfer for Air Injected Through a Tangential Slot Into a Turbulent Boundary Layer", Journal of Heat Transfer, Transactions of the ASME, August 1961, pg. 293-306.

40. Hay, N. et al., "Effects of the Condition of the Approach Boundary Layer and of Mainstream Pressure Gradients on the Heat Transfer Coefficient on Film-Cooled Surfaces", Journal of Engineering for Gas Turbines and Power, Transactions of the ASME, volume 107, January 1985, pg. 99-104.

41. Hay, N. et al., "Discharge Coefficients of Holes Angled to the Flow Direction", ASME 92-GT-192.

42. Herring, H.J., "A Method of Predicting the Behavior of a Turbulent Boundary Layer With Discrete Transpiration Jets", Journal of Engineering for Power, Transactions of the ASME, April 1975, pg. 214-224.

43. Hill, Philip and Carl Peterson, Mechanics and Thermodynamics of Propulsion, second edition, New York, U.S.A.: Addison-Wesley Publishing Company, Inc., 1992.

44. Horton, F.G., "Aerodynamics and Heat Transfer of Turbine Blading", Oxford University, D. Phil. Thesis, 1985.

45. Horton, F.G. et al., "Heat Transfer Measurements With Film Cooling on a Turbine Blade Profile in Cascade", ASME 85-GT-117.

46. Ito, S. et al., "Film Cooling of a Gas Turbine Blade", Journal of Engineering for Power, Transactions of the ASME, volume 100, July 1978, pg. 476-481.

47. Jones, T.V., "The Scaling of Film Cooling", University of Oxford, Oxford, U.K., Department of Engineering Science, unpublished lecture notes.

48. Jones, T.V., "Turbine Heat Transfer", University of Cambridge, Cambridge, U.K., Programme for Industry lecture notes, June 1994.

49. Jones, T.V. and T.W. Walton, "Reynolds Analogy in Film Cooling", University of Oxford, Oxford, U.K., Department of Engineering Science.

50. Kadotani, K. and R.J. Goldstein, "On the Nature of Jets Entering a Turbulent Flow: Part B, Film Cooling Performance", Proceedings of the Tokyo Gas Turbine Congress, 1977.

51. Kays, W.M. and M.E. Crawford, Convective Heat and Mass Transfer, third edition, New York, U.S.A.: McGraw-Hill Inc., 1993.

52. Kerrebrock, Jack L., Aircraft Engines and Gas Turbines, Cambridge, MA, U.S.A.: MIT Press, 1992.

53. Kulisa, P. et al., "Computation of a Wall Boundary Layer With Discrete Jet Injections", ASME 91-GT-143.

54. Lakshminarayana, Budugur, Fluid Dynamics and Heat Transfer of Turbomachinery, New York, NY, U.S.A.: John Wiley & Sons, Inc., 1996.

55. Lee, S.W. et al., "Experimental Study on the Flow Characteristics of Streamwise Inclined Jets in Crossflow on a Flat Plate", ASME 92-GT-181.

56. Liess, C., "Experimental Investigation of Film Cooling With Ejection From a Row of Holes for the Application to Gas Turbine Blades", Journal of Engineering for Power, Transactions of the ASME, 1974, pg. 1-7.

57. Leylek, J.H. and R.D. Zerkle, "Discrete-Jet Film Cooling: A Comparison of Computational Results With Experiments", ASME 93-GT-207.

58. Martinez-Botas, R.F. et al., "A Cold Heat Transfer Tunnel for Gas Turbine Research on an Annular Cascade", ASME 93-GT-248.

59. Mayle, R.E. and F.C. Kopper, "Adiabatic Wall Effectiveness of a Turbulent Boundary Layer With Slot Injection", Journal of Heat Transfer, Transactions of the ASME, May 1976, pg. 240-244.

60. Mehendale, A.B. and J.C. Han, "Influence of High Mainstream Turbulence on Leading Edge Film Cooling Heat Transfer", ASME 90-GT-9.

61. Metzger, D.E. et al., "Heat Transfer With Film Cooling Near Nontangential Injection Slots", Journal of Engineering for Power, Transactions of the ASME, April 1968, pg. 157-163.

62. Miller, K.L. and M.E. Crawford, "Numerical Simulation of Single, Double, and Multiple Row Film Cooling Effectiveness and Heat Transfer", ASME 84-GT-112.

63. Moran, Jack, An Introduction to Theoretical and Computational Aerodynamics, New York, U.S.A.: John Wiley & Sons, Inc., 1984.

64. Moore, Joan G. and John, "A Computational Study of Tip Leakage Flow and Losses in a Linear Turbine Cascade", AGARD CP 510, February 1992.

65. Moore, Joan G. and John, "The Moore Elliptic Flow Program for Turbomachinery Flow Calculations 1990 Users Guide", February, 1990.

66. Muska, J. F. et al., "The Additive Nature of Film Cooling From Rows of Holes", Journal of Engineering for Power, Transactions of the ASME, October 1976, pg. 457-464.

67. Nirmalan, V. and L.D. Hylton, "An Experimental Study of Turbine Vane Heat Transfer With Leading Edge and Downstream Film Cooling", ASME 89-GT-69.

68. Norton, R.J.G. et al., "Turbine Cooling System Design - Volume I - Technical Report", Aero Propulsion Laboratory, Wright Patterson Air Force Base, Ohio, U.S.A., AFAPL-TR-89, March 1989.

69. Page et al., Fortran 77 for Humans, third edition, St. Paul, MN, U.S.A.: West Publishing Co., 1986.

70. Papell, S.S., "Effect on Gaseous Film Cooling of Coolant Injection Through Angled Slots and Normal Holes", NASA Technical Note D-299, 1960.

71. Papell, S.S. and A.M. Trout, "Experimental Investigation of Air Film Cooling Applied to an Adiabatic Wall by Means of an Axially Discharging Slot", NASA Technical Note D-9, 1959.

72. Patankar, Suhas V., Numerical Heat Transfer and Fluid Flow, New York, U.S.A.: Hemisphere Publishing Company, 1980.

73. Patankar, S.V. et al., "Prediction of the Three-Dimensional Velocity Field of a Deflected Turbulent Jet", Journal of Fluids Engineering, Transactions of the ASME, December 1977, pg. 758-762.

74. Ramette, P.H. and J.F. Louis, "Analytical Study of the Thermal and Fluid Mechanical Evolution of a Cooling Film Injected From a Single Line of Inclined Round Holes", International Journal of Turbo and Jet Engines, volume 1, number 1, 1983-1984, pg. 7-28.

75. Rastogi, A.K. and J.H. Whitelaw, "Procedure for Predicting the Influence of Longitudinal Curvature on Boundary Layer Flows", ASME 71-WA/FE-37.

76. Roache, J., Computational Fluid Dynamics, Albuquerque, N.M., U.S.A.: Academic Press, Inc., 1976.

77. Rodi, W. and S.K. Srivatsa, "A Locally Elliptic Calculation Procedure for Three-Dimensional Flows and its Application to a Jet in Cross-Flow", Computer Methods in Applied Mechanics and Engineering, volume 23, 1980, pg. 67-83.

78. Rohsenow, W.M. et al., Handbook of Heat Transfer Applications, second edition, New York, U.S.A.: McGraw-Hill, Inc., 1985.

79. Salcudean, M. et al., "Leading Edge Film Cooling of a Turbine Blade Model Through Single and Double Row Injection: Effects of Coolant Density", ASME 94-GT-2.

80. Schönung, B. and W. Rodi, "Prediction of Film Cooling by a Row of Holes With a Two-Dimensional Boundary-Layer Procedure", ASME 87-GT-122.

81. Seban, R.A., "Heat Transfer and Effectiveness for a Turbulent Boundary Layer With Tangential Fluid Injection", Journal of Heat Transfer, Transactions of the ASME, November 1960, pg. 303-312.

82. Seban, R.A. and L.H. Back, "Velocity and Temperature Profiles in Turbulent Boundary Layers With Tangential Injection", ASME Journal of Heat Transfer, volume 84, 1962, pg. 45-54.

83. Seban, R.A. et al., "Heat Transfer to a Turbulent Boundary Layer Downstream of an Injection Slot", ASME No. 57-A-36.

84. Shaw, C.T., Using Computational Fluid Dynamics, London, U.K.: Prentice Hall International (UK) Ltd., 1992.

85. Simoneau, R.J. and F.F. Simon, "Progress Towards Understanding and Predicting Heat Transfer in the Turbine Gas Path", International Journal of Heat and Fluid Flow, volume 14, number 2, June 1993, pg. 106-128.

86. Smith, A.D., "Program Operating Practice for JH01 - GRAFFITI", Rolls Royce plc, report #POPJH01, February 1993.

87. Smith, A.D., "CFDS / MEFP Version 2 and How it Works", Rolls Royce plc, report #TRE90228, September 1993.

88. Tafti, D.K. and S. Yavuzkurt, "Prediction of Heat Transfer Characteristics for Discrete Hole Film Cooling for Turbine Blade Applications", ASME 89-GT-139.

89. Teekaram, Arnold J.H., "Film-Cooling in the Presence of Mainstream Pressure Gradients and Foreign Gas Injection", Oxford University, D. Phil. Thesis, 1989.

90. Van Treuren, K.W., "Impingement Flow Heat Transfer Measurements of Turbine Blades Using a Jet Array", Oxford University, D. Phil. Thesis, 1994.

91. Van Treuren, K.W. et al., "Local Heat Transfer Coefficient and Adiabatic Wall Temperature Measurement Beneath Arrays of Staggered and Inline Impinging Jets", ASME 94-GT-181.

92. Vedula, R.J. and D.E. Metzger, "A Method for the Simultaneous Determination of Local Effectiveness and Heat Transfer Distributions in Three-Temperature Convection Situation", ASME 91-GT-345.

93. Wang, Z. et al., "An Advanced Method of Processing Liquid Crystal Video Signals From Transient Heat Transfer Experiments", ASME 93-GT-282.

94. Wang, Z. et al., "A Colour Image Processing System for Transient Liquid Crystal Heat Transfer Experiments", ASME 94-GT-290.

95. Wieghardt, K., "Hot-Air Discharge for De-Icing", AAF Translation No. F-TS-919-RE, August 1946.

96. Wilson, D.J. et al., "Predicting Heat Transfer Coefficients With Film Cooling From a Row of Holes", Journal of Heat Transfer, Transactions of the ASME, May 1974, pg. 258-260.

97. Young, A.D., Boundary Layers, London, U.K.: Blackwell Scientific Publications Ltd., 1989.

98. Zhou, J. et al., "Prediction of Film Cooling by Discrete-Hole Injection", ASME 93-GT-75.

99. CFDS SZ02 User Guide, Rolls Royce plc, Theoretical Science Group, 1993.